



THE UNIVERSITY *of* EDINBURGH

This thesis has been submitted in fulfilment of the requirements for a postgraduate degree (e.g. PhD, MPhil, DClinPsychol) at the University of Edinburgh. Please note the following terms and conditions of use:

- This work is protected by copyright and other intellectual property rights, which are retained by the thesis author, unless otherwise stated.
- A copy can be downloaded for personal non-commercial research or study, without prior permission or charge.
- This thesis cannot be reproduced or quoted extensively from without first obtaining permission in writing from the author.
- The content must not be changed in any way or sold commercially in any format or medium without the formal permission of the author.
- When referring to this work, full bibliographic details including the author, title, awarding institution and date of the thesis must be given.

Massive Galaxies at $1 < z < 3$

Victoria A. Bruce



Doctor of Philosophy
The University of Edinburgh
2013

Lay Summary

The work presented in this thesis explores the evolution of the most massive galaxies from ~ 7 to 11 billion years ago. During this key era in cosmic time these most massive galaxies are observed to undergo dramatic changes in their shape and structure, as well as ceasing to form new stars. The physical processes which are responsible for these transformations are still not well understood within the context of our current models of galaxy formation and evolution, and there is continued debate over whether the mechanisms which cause these changes are in fact linked. By studying both the shapes of the most massive galaxies and how actively they are forming stars, this work addresses these issues.

Galaxies observed in the present-day Universe appear to have shapes that are well described by either round bulge-dominated structures or flat disks, but it is not known at which era in cosmic time massive galaxies relaxed into these well-defined structures. Thus, in order to provide new insight into the evolution of these massive galaxies I have decomposed the shapes of the galaxies in my sample into their separate bulge and disk components and have determined the masses and rates of on-going star-formation for both components separately. This has revealed that these galaxies are more disk-dominated further back in cosmic time, and become increasingly mixed bulge+disk systems towards the present day. Although even at most recent cosmic eras studied in this work, the pure bulges which are comparable to present-day massive galaxies are yet to emerge in significant numbers.

In addition to this, I also find that the sizes of both the bulge and disk components are more compact further back in time compared to the present-day sizes of similarly massive galaxies. This confirms previous observations and is consistent with some of the proposed galaxy evolution models which suggest that the sizes of galaxies grow as they accrete stars from less massive galaxies and satellites, which add material to the outskirts of the massive galaxies but leave the central

regions unchanged.

Finally, by examining the rates of on-going star-formation in the separate bulge and disk components I have been able to place constraints on the viability of the competing models for galaxy evolution as I find that the trends between the rates of star-formation and galaxy shape are more consistent with current models which describe a mild evolution of galaxies in isolation rather than those which propose that galaxy evolution within this regime is driven by the violent mergers of massive systems.

Abstract

This thesis explores the evolution of massive galaxies ($M_* > 10^{11} M_\odot$) by conducting the largest multiple-component Sérsic light-profile fitting study to date of the rest-frame optical and ultra-violet morphologies of galaxies at redshifts $1 < z < 3$. Despite many of the recent advances in galaxy formation and evolution models, the physical processes which are responsible for driving morphological transformations and star-formation quenching remain unclear. By undertaking a detailed study of the individual bulge and disk components of these massive systems, the work presented in this thesis addresses these outstanding issues by exploring not only how the sizes of the individual components evolve with redshift, but also how the overall bulge and disk fractions evolve, and how these trends are connected to star-formation quenching of the separate components.

In order to perform this analysis, I have combined the latest high-resolution near-infrared HST WFC3/IR and ACS imaging provided by the CANDELS survey in the UDS and COSMOS fields and have presented a robust procedure for morphological multiple-component Sérsic light-profile model fitting across the $0.6\mu\text{m}$ to $1.6\mu\text{m}$ wavelength range sampled by CANDELS. This procedure is discussed in depth along with the tests I have undertaken to assess its reliability and accuracy. This approach has enabled me to generate separate bulge and disk component model photometry, allowing me to conduct individual component SED fitting in order to determine decomposed stellar-mass and star-formation rate estimates for the separate bulge and disk components.

The results presented in this work reveal that the sizes of the bulge and disk components lie both on and below the local size-mass relations, confirming that the size evolution required by the previously reported compact sizes of high-redshift galaxies extends to both galaxy components. However, I find evidence that the bulge components display a stronger size evolution with redshift than the disks as, at $1 < z < 3$, the bulges are a median factor of 3.09 ± 0.2 times

smaller than similarly massive local early-type galaxies, whereas the disks are a median factor of 1.77 ± 0.1 times smaller than similarly massive local late-type galaxies. By including decomposed star-formation rates for the individual bulge and disk components, this work also reveals that while the growth of individual components through, for example, inside-out processes such as minor merging, are consistent with the size evolution of these systems, the addition of larger newly quenched systems to the galaxy population, for the disk components at least, may also play an important role in the observed size evolution of massive galaxies.

By exploring the evolution of the bulge and disk-dominated fractions with redshift, I find that $1 < z < 3$ marks a key transition era in cosmic time where these most massive galaxies appear to be undergoing dramatic structural transformations. Within this redshift range there is a decline in the population of disk-dominated galaxies and a gradual emergence of increasingly bulge-dominated systems. However, despite the rise of S0-type galaxies, even by $z = 1$ I do not yet find a significant fraction of “pure” bulges comparable to the giant ellipticals which comprise the majority of the local massive galaxy population.

In addition to studying how the overall bulge and disk dominated fractions evolve with redshift, by incorporating the star-formation rate and stellar-mass estimates for the separate components and imposing new, highly conservative criteria, I confirm that a significant fraction of passive galaxies are disk-dominated ($18 \pm 5\%$) and a significant fraction of star-forming galaxies are bulge-dominated ($11 \pm 4\%$). The presence of passive disks and star-forming bulges has interesting implications for the models of galaxy evolution as they suggest that the processes which quench star-formation may be distinct from the mechanisms which cause morphological transformations.

Finally, the detailed morphological analysis presented in this work has also allowed me to explore the axial ratio distributions of these most massive high-redshift galaxies, which provides additional insight into the structure of the passive and star-forming bulge and disk-dominated sub-populations. Whilst the overall axial ratio distributions for star-forming disks are peaked, I find tentative evidence that the largest and most active star-forming disks are flatter. I have also been able to further demonstrate that by selecting the most active star-forming disks and comparing to extreme star-forming (sub-)mm selected galaxies, the axial ratio distributions of the two samples appear to be comparably flat, thus reconciling the observed structures of these populations.

Declaration

I declare that this thesis was composed by myself, that the work contained herein is my own except where explicitly stated otherwise in the text, and that this work has not been submitted for any other degree or professional qualification except as specified.

Parts of this work have been published in Bruce et al. (2012).

(Victoria A. Bruce, 2013)

This thesis is dedicated to my family.

Acknowledgements

Poets say science takes away from the beauty of the stars - mere globs of gas atoms. I, too, can see the stars on a desert night, and feel them. But do I see less or more ? - Richard P. Feynman

The time I've spent during my PhD has been full of ups and downs, so it's only fitting that I get this opportunity to thank everyone who has helped me through them all.

First of all I'd like to thank my supervisors: Jim, Ross and Michele, for all their help and patience, and without whom I would probably still be writing up. They've provided me with the best possible training and I'm extremely lucky to have had the chance to work with them. I'd also like to thank Jim for giving me the opportunity to take the next step in my career and to carry on my work with him.

Before I start my personal thank yous I think it's important for me to acknowledge the contribution from others who have provided the public code which have made the work done during my PhD substantially easier. So thank you to the developers of GALFIT and SExtractor who have already been credited, and to those in the wider community who have contributed to IDL and IRAF routines used by many of us. Finally, a special mention to the author of and the contributors to Topcat, without whom this work would have taken a lot longer and who are often undercited.

The next people on my list to thank are my office-mates, past and present, for putting up with a lot while I was "smashing out the science". In particular Jack for imparting a wealth of random facts and culinary advice, Vinod for the constant supply of biscuits, chocolate and patience with my ranting and Alasdair for helping with the seemingly never-ending supply of YouTube procrastination. Also a mention to the Vista Huts Gang for the moral support, letting me thaw out in their offices and of course for providing the, mostly horrendous, chat - you know who you are. And to Will for maintaining some standards. Thanks to Dave too for the ... , em, well just being you. And to Alice who helped keep me calm in the final days before my Viva.

I'd also like to thank everyone else at the ROE for making this such a nice place to work. Especially Paula, Eric and John, to name just a few.

A huge thank you to all my friends for lending an ear over the years. Especially to Cassie and Ciara for helping to keep me sane when times were tough and providing a link to the real world. Not to mention all the cocktails when they were needed the most.

Finally, of course, I'd like to thank my family. Grandpa, for being so interested in everything I do, and Grandma and Auntie Sheila for always cheering me up and supplying me with magazines and lasagne.

Most importantly I'd like to thank my Mum for her endless love and support, and my Dad for passing on a love for science and giving me the inspiration and encouragement to get this far, as well as a head start with the tutorials on electron "party" behaviour.

Contents

Lay Summary	i
Abstract	iii
Declaration	v
Acknowledgements	vii
Contents	ix
List of Figures	xiv
List of Tables	xx
1 Introduction	1
1.1 Background	1
1.2 Λ CDM Cosmology Overview.....	2
1.2.1 Evidence in favour of Λ CDM cosmology and parameter refinements	3
1.2.2 Failures of the Λ CDM model	5
1.3 Synopsis of Galaxy-Formation Models.....	6
1.4 Observational Constraints and Updates to Models.....	10
1.4.1 Luminosity function	10

1.4.2	The star-formation history of the Universe	13
1.4.3	Downsizing	16
1.4.4	Morphological and size evolution.....	18
1.5	Current State of Galaxy models: Progress and Outstanding Issues .	27
1.5.1	<i>K</i> -band luminosity function and sub-mm populations	27
1.5.2	IMF	28
1.5.3	Fundamental plane.....	30
1.5.4	Galaxy sizes	31
1.6	Introduction to Photometric Techniques.....	32
1.7	Introduction to SED fitting	37
1.8	Outline of Thesis and Impact.....	44
2	The Sizes of Massive High-redshift Galaxies	46
2.1	Introduction	46
2.2	Data and Sample Selection.....	48
2.2.1	HST imaging and basic sample definition	48
2.2.2	Supporting multi-wavelength data	49
2.2.3	Photometric redshifts	49
2.2.4	Stellar masses	50
2.2.5	Star-formation rates	54
2.2.6	Final sample selection.....	57
2.3	Morphologies: 2-D modelling	57
2.4	Single Sérsic models.....	60
2.4.1	PSF dependence.....	60

2.4.2	Background dependence	64
2.5	Conclusions	71
3	The Evolution of Galaxy Morphologies	75
3.1	Introduction	75
3.2	Data Overview	77
3.3	Morphology Fitting Procedure	77
3.4	Multiple-Component Models.....	78
3.4.1	Bulge-only and disk-only models	79
3.4.2	Double-component bulge+disk models.....	80
3.4.3	Introduction of an additional point-source	80
3.5	Final Galaxy Models.....	82
3.5.1	Selection of the best model	82
3.5.2	Model fit refinement	84
3.6	Science Results.....	91
3.6.1	The size-mass relation.....	91
3.6.2	Evolution of morphological fractions	95
3.6.3	Star-forming and passive disks.....	97
3.6.4	Axial ratio distributions	100
3.7	Conclusions	103
3.7.1	Galaxy growth	103
3.7.2	Morphological evolution	107
3.7.3	Star-forming and quiescent galaxies	109
3.7.4	Passive disks and quenching.....	114

4	Multiple-Component SED Fitting	118
4.1	Introduction	118
4.2	Data	118
4.2.1	Supporting multi-wavelength data	119
4.2.2	Sample selection	120
4.3	Multiple-Component Morphology Fitting.....	123
4.3.1	Extension to additional bands	124
4.4	Double-Component SED Fitting.....	136
4.4.1	Refinement of photometry	137
4.4.2	The effect of stellar template choice on stellar-mass estimates and ages.....	141
4.4.3	Separate component star-formation rates	143
4.5	Correlation Between Single and Multiple-Component Model Morphologies	147
4.6	Size-Mass Relations	149
4.7	Comparison to Literature.....	164
4.8	Discussion	168
5	Morphological and Star-formation Evolutionary Trends	174
5.1	Introduction	174
5.2	Morphological Evolution	175
5.2.1	Trends with redshift	177
5.3	Star-Formation Evolution	187
5.3.1	Star-formation and morphology	188
5.3.2	Passive disks.....	193

5.3.3	Star-forming bulges	197
5.4	Axial Ratios	203
5.4.1	Passive disks.....	204
5.4.2	Star-forming disks.....	206
5.5	Comparison with Sub-mm Galaxies.....	215
5.6	Summary & Discussion.....	219
6	Conclusions and Future Work	227
6.1	Conclusions	227
6.2	Future Work	235
6.2.1	AGN hosts	235
6.2.2	HST grism spectroscopy	237
6.2.3	KMOS follow-up.....	237
	References	239
	Publication List	256

List of Figures

1.1	CMB power spectrum from Planck	4
1.2	Hubble tuning fork	7
1.3	Outline of semi-analytical galaxy evolution models.	8
1.4	Schematic representation of the hierarchical growth of dark matter haloes.	9
1.5	Comparison of modelled dark matter and observed galaxy luminosity functions.	10
1.6	Reconciliation of modelled luminosity functions with observations.	12
1.7	Updated Madau-Lilly plot for the star-formation rate density evolution.	13
1.8	Stellar-mass function.	17
1.9	Local size-mass relation from SDSS.	20
1.10	Compilation of size-mass results for $1 < z < 3$	21
1.11	Evidence for inside-out growth.	26
1.12	Comparison of the IMFs.	29
1.13	Lyman break galaxies.	34
1.14	BzK diagram.	36
1.15	SED of an SSP model	39
1.16	Comparison between photometric and spectroscopic redshifts	40
1.17	TP-AGB track in the HR diagram.	42
2.1	Comparison between $SFR_{UV,dust\ corrected}$ and SFR_{UV+IR}	56

2.2	Comparison of the radial profiles of alternative H_{160} PSFs.	62
2.3	Difference image of the stacked empirical PSF – the Tiny Tim model.	63
2.4	Comparison of background estimations.	65
2.5	Errors in and degeneracies between the fitted effective radius and Sérsic index n , also showing the effect of a varying background.	68
2.6	Size-mass relations for the maximum and minimum effective radii fitted.	69
2.7	Comparison of fitted parameters derived using the different background estimations.	71
2.8	Size-mass relations from previous studies compared with the results from my full background grid search analysis.	74
3.1	Objects with additional structure which failed the initial fitting acceptability criteria.	85
3.2	Examples of the χ^2 -masks.	87
3.3	Residual maps of the objects which after masking still failed the χ^2 acceptability criterion.	88
3.4	Distributions of minimum χ^2 achieved by the modelling.	89
3.5	Comparison between the fitted parameters returned for the initial and the first χ^2 -masked fits.	90
3.6	Comparison of the multiple component bulge to total light fractions with the single Sérsic index fits.	92
3.7	Size-mass relations split into the separate bulge and disk components.	94
3.8	Redshift evolution of the morphological fractions.	96
3.9	Specific star-formation rate versus morphological type.	98
3.10	Axial-ratio distributions displayed by the dominant disk components in the disk-dominated galaxies.	101
3.11	Comparison of disk-dominated galaxy axial ratio distributions with literature results.	102
3.12	$24\mu\text{m}$ images of the pure-disk objects.	110
3.13	Image stamps and fits of star-forming disks.	113
3.14	High-resolution models of the passive disks.	115

4.1	Schematic of the WFC3 and ACS coverage in the UDS and COSMOS fields.	120
4.2	Comparison of mass-redshift distribution between fields.	122
4.3	Comparison of co-moving number densities between fields.	123
4.4	Comparison of the χ^2 statistics of models with and without fixed parameters.	126
4.5	Comparison of the fitted magnitudes of the fixed-parameter models for both components in relation to the H_{160} model fits.	127
4.6	Comparison of the fitted magnitudes of the free-parameter models for both components in relation to the H_{160} model fits.	128
4.7	Relation between the sum of the best-fit multiple-component model magnitudes and the measured iso-magnitude of each object for the different models.	129
4.8	Comparison of the fitted sizes of individual components between the fixed and free-parameter models.	130
4.9	Image stamps of an example fit for a pure bulge object.	131
4.10	Image stamps of an example fit for a pure disk object.	132
4.11	Image stamps of an example fit for a bulge+disk object with $B/T < 0.5$	133
4.12	Image stamps of an example fit for a bulge+disk object with $B/T > 0.5$	134
4.13	Image stamps of an example fit for a bulge+disk object with $B/T = 0.5$	135
4.14	Iso-magnitude and aperture photometry comparisons to the sum of the integrated model-fit photometry in the H_{160} and v_{606} -bands.	138
4.15	SED models for example fits	140
4.16	Stellar-mass estimates from single and double-component models.	141
4.17	Comparison between the age distributions of the single-component models and old population of the double-component models.	143
4.18	Age distribution of the young components from the double-burst fits over-plotted with $24\mu\text{m}$	144
4.19	Ages of the young double-burst models against the SFR from the single-component SED fit.	146

4.20	Bulge/Total light fractions vs single-Sérsic index fits.	148
4.21	Bulge/Bulge+Disk light fractions vs single-Sérsic index fits.	148
4.22	Bulge/Total mass fractions vs single-Sérsic index fits.	149
4.23	Size-mass by H_{160} light fractions, UDS.	151
4.24	Size-mass by H_{160} light fractions, COSMOS.	152
4.25	Size-mass by H_{160} light fractions, Combined UDS + COSMOS. . .	153
4.26	Size-mass by SED component mass, combined	155
4.27	Size-mass by SED mass and component sSFRs, combined.	156
4.28	Fractional ETG and LTG size evolution	161
4.29	Fractional bulge and disk size evolution	162
4.30	Fractional bulge and disk size evolution for bulge and disk- dominated objects.	163
4.31	Fractional bulge and disk size evolution compared with literature results	166
4.32	Distribution of the time each passive disk component has been quenched.	169
4.33	Fractional bulge and disk component size evolution including the relation for progenitors of the passive disks	170
4.34	Distributions of the masses of the passive and star-forming disks. .	171
4.35	Bulge/Total mass fraction evolution	173
5.1	Co-moving number densities by light fractions	178
5.2	Co-moving number densities by SED mass fractions	179
5.3	Morphological fractions determined from H_{160} light fractions. . . .	181
5.4	Morphological fractions determined from decomposed mass fractions.	182
5.5	Redshift distributions of the bulge and disk dominated components in the UDS and COSMOS.	183
5.6	Comparison of my redshift distribution in the UDS with the Dahlen et al. (2013, in preparation) redshifts.	185
5.7	SEDs fitted with the Dahlen et al. redshifts.	186

5.8	Sérsic index and bulge/total H_{160} light fractions against sSFR for the UDS sample.	189
5.9	Sérsic index and bulge/total H_{160} light fractions against sSFR for the COSMOS sample.	191
5.10	Sérsic index and bulge/total H_{160} light fractions against sSFR for the combined UDS+COSMOS sample.	192
5.11	Example fit of one of the genuinely passive disk-dominated galaxies.	195
5.12	A second example fit of one of the genuinely passive disk-dominated galaxies.	196
5.13	The first of three genuinely star-forming bulge-dominated galaxies.	199
5.14	The second of three genuinely star-forming bulge-dominated galaxies.	200
5.15	The third genuinely star-forming bulge-dominated galaxy.	201
5.16	Redshift distribution of the passive disks and star-forming bulges.	202
5.17	Axial ratio distributions for the star-forming and passive bulges and disks.	205
5.18	The axial ratio distributions for low and high-redshift ETGs from Chang et al. (2013a)	207
5.19	The single-Sérsic axial ratio distributions for the passive and star-forming galaxies.	208
5.20	Axial ratio distributions for the star-forming disks, split by specific and absolute star-formation rate.	210
5.21	Axial ratio distributions for the star-forming disks, split by redshift and disk size.	212
5.22	Axial ratio distributions for star-forming disks split above and below 25% and 75% quartile sizes.	213
5.23	Axial ratio distributions for star-forming disks, plotted by their decomposed properties.	214
5.24	Magnitudes of the passive and star-forming disks.	216
5.25	Properties of the (sub-)mm galaxies.	217
5.26	Size distributions of the (sub-)mm galaxies.	218
5.27	Axial ratios of the (sub-)mm galaxies.	220

5.28 Axial ratio distributions of the extreme star-forming disks in comparison with the (sub-)mm selected sample.	221
--	-----

List of Tables

3.1	Percentages of the final sample of 192 objects with multiple-component best-fits corresponding to each of the six fitted models.	90
4.1	The fractions of components which lie on (or above) their respective local relations within the $1 - \sigma$ scatter and below the $1 - \sigma$ scatter of their relations, where masses for each component have been estimated separately from the multiple-component SED fitting.	157
4.2	The fractions of components which lie on or below their respective local relations, where masses for each component have been estimated separately from the multiple-component SED fitting, split further into their star-forming and passive populations using the individual component sSFRs.	158
4.3	Offsets from local relations	160
5.1	The percentages of the original UDS sample of 192 objects with multiple-component best-fits corresponding to each of the six fitted models.	176
5.2	The percentages of the re-selected UDS sample of 184 objects with multiple-component best-fits corresponding to each of the six fitted models.	176
5.3	The percentages of the final COSMOS sample of 163 objects with multiple-component best-fits corresponding to each of the six fitted models.	176
5.4	The percentages of the combined UDS+COSMOS samples of 347 objects with multiple-component best-fits corresponding to each of the six fitted models.	177
5.5	The fractions of passive galaxies which are disk-dominated, split by field and using both the single-Sérsic and multiple-component classifications.	193

5.6	The fractions of star-forming galaxies which are bulge-dominated, split by field and using both the single-Sérsic and multiple- component classifications.	193
-----	--	-----

Chapter 1

Introduction

1.1 Background

The formation and evolution of galaxies is one of the most fundamental research areas in astronomy. How and when the first galaxies formed, and how they have transformed over the past several giga-years into the well-classified local population that we see today is still not properly understood. The advent of 4–10 metre class telescopes and space-based instruments over the last several decades has enabled a profusion of scientific breakthroughs in all areas of astrophysics, from planetary formation to the establishment of generally accepted cosmological models underpinning the very nature of the Universe in which we live. The field of galaxy formation is no exception. The wide availability of multi-wavelength data now ranging from the X-ray to the radio has opened up new windows into the most crucial epochs of galaxy evolution, allowing evolutionary models to be extensively tested against observations probing increasingly further back in cosmic time. By focussing on the constraints imposed on these models by the observed properties of the most massive galaxies at high redshift, this thesis demonstrates that these rare objects provide invaluable insights into the physical processes responsible for the formation and evolution of galaxies throughout cosmic time.

1.2 Λ CDM Cosmology Overview

The birth of modern observational cosmology and extragalactic astronomy can be traced to 1913 when Slipher measured the first redshifts due to recessional velocities along the line of sight. This was followed by the work of Hubble, who in 1926 used the Period-Luminosity relationship for Cepheid variable stars (Leavitt 1908) to deduce the existence of extragalactic systems from standard-candle distance measurements. Motivated by the work of Slipher, in 1929 Hubble used the redshift of these galaxies to demonstrate their relationship with distance: $v = H_0 D$, where H_0 is the Hubble constant and was first measured by Hubble to be $500 \text{ kms}^{-1} \text{ Mpc}^{-1}$. As a result, Hubble is credited with being the first to discover that the Universe is expanding with a recessional velocity proportional to distance. At the time, these results lent strong support to the idea of Big Bang cosmology (e.g. Lemaître 1927) which was then competing with the favoured model of a steady state Universe (e.g. Jeans 1928, Hoyle 1948).

In the 1940s the Big Bang model was developed further by Gamow, Alpher and Herman (e.g. Gamow 1946, Alpher et al. 1948, Alpher & Herman 1948) who presented the first models of Big Bang Nucleosynthesis and predicted the Cosmic Microwave Background (CMB): an isotropic background of radiation with a spectrum close to a near perfect black body that arose from the surface of last scattering, when photons decoupled from matter as the Universe cooled. The first unequivocal evidence in favour of this model came in 1965 when Penzias & Wilson directly observed the CMB and support began to increase for this model of cosmology.

It was also in 1965 that Peebles put forward the first generation of large scale structure models and theorised that, as the Universe cools, any primordial perturbations in the density field following the Big Bang lead to the growth of over and under-dense regions, which later form the large scale structure of voids and galaxy clusters observed in the Universe. It is in the over-densities that dark matter haloes form from gravitational interactions and provide the sites of galaxy formation.

These fundamental principles underpin our current framework for cosmological and galaxy-evolution models, as they are capable of producing important predictions for mass assembly. In recent years, much effort in observational cosmology has not only proved that many of these theories yield predictions

which are consistent with observational constraints, but has also driven key steps towards accurately measuring the six different parameters by which the Lambda Cold Dark Matter (Λ CDM) model can be primarily described: the physical baryon ($\Omega_b h^2$, where h is the dimensionless reduced Hubble constant given by $h = H_0/100 \text{ kms}^{-1}\text{Mpc}^{-1}$), dark-matter ($\Omega_c h^2$) and dark energy ($\Omega_\Lambda h^2$) density parameters, the scalar spectral index (n_s), curvature fluctuation amplitude (Δ_R^2) and reionisation optical depth (τ).

1.2.1 Evidence in favour of Λ CDM cosmology and parameter refinements

CMB Fluctuations

In 1967 Sachs & Wolfe posited that any primordial perturbations in the density field of the Universe at the surface of last scattering would manifest as temperature variations in the observed signal of the CMB due to general relativistic effects of photons interacting with gravitational potentials. These fluctuations were first observed by the COBE satellite (Smoot et al. 1992) in the early 1990s, and since then have been observed with increasingly high angular resolution and sensitivity by WMAP (Larson et al. 2011), and most recently Planck (Planck Collaboration et al. 2013a). By measuring these peaks in the CMB power spectrum it is possible to constrain the cosmological model parameters.

Power spectrum of galaxy clustering

In addition to the small scale power spectrum contributions from the CMB, support for the Λ CDM model can also be found from the power spectrum of galaxy clustering which manifests as acoustic peaks at larger scales. The pioneering large area studies of the local Universe conducted by SDSS (York et al. 2000) and 2dFGRS (Colless et al. 2001) confirmed the detection of the Baryonic Acoustic Oscillation (BAO) signals predicted in the Λ CDM model due to interactions between photons, dark matter and baryons in the early Universe. These interactions create acoustic waves which result in oscillations in the power spectrum of the distribution of galaxies at set scales (the sound horizon), which can be observed with galaxy clustering surveys. This signal was detected by e.g.

Percival et al. (2001) and Cole et al. (2005). Due to the pre-determined scale of these oscillations they can be used as standard rulers for cosmology, thus the local surveys by SDSS and 2dFGRS were additionally used to tighten constraints on, and break degeneracies between, cosmological model parameters.

Most recently, the sensitivity of WMAP and Planck at increasingly large scales has allowed the peaks in the power spectrum from the CMB and BAOs to be measured with greater accuracy, which has led to refined constraints on the cosmological model parameters. The latest power spectrum from Planck is shown in Fig. 1.1. The current estimates from Planck show that the baryonic fraction of the critical density (Ω_b) is approximately 0.049, whereas dark matter (Ω_c) makes up 0.314 ± 0.02 and dark energy (Ω_Λ) comprises 0.686 ± 0.02 (Planck Collaboration et al. 2013b). In the context of previous studies, these latest measurements find marginally higher dark matter and baryon density fractions, and yield a slightly lower value for H_0 of $67.3 \pm 1.2 \text{ kms}^{-1} \text{ Mpc}^{-1}$.

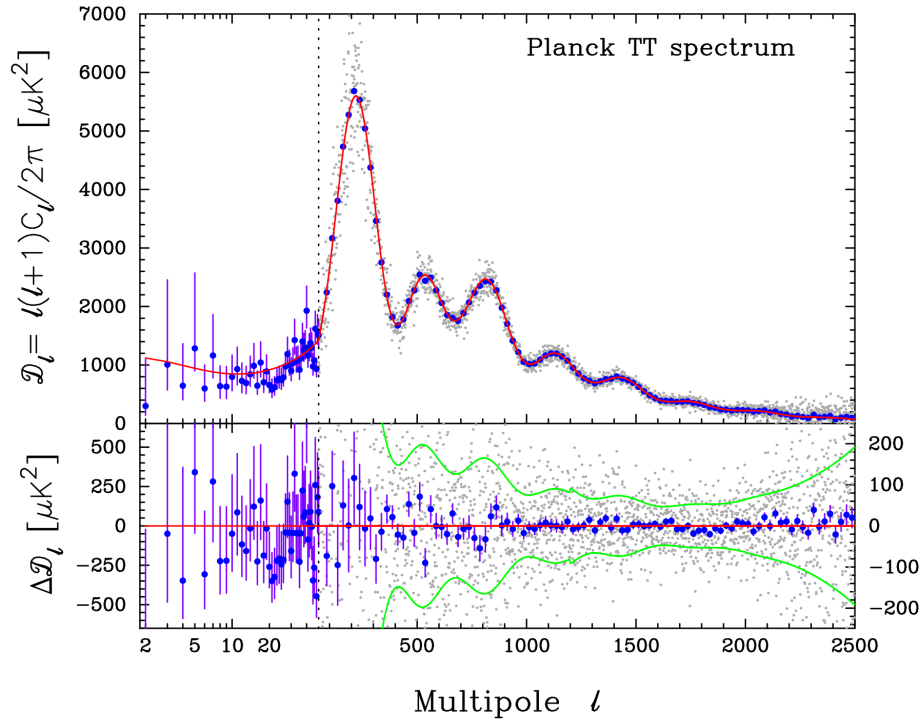


Figure 1.1 *The temperature power spectrum from the latest Planck results Planck Collaboration et al. (2013b) over-plotted in red with the temperature spectrum for the best-fit Λ CDM cosmology model. The lower panel is the residual of the power spectrum with respect to this cosmological model, where the green lines show the $1\text{-}\sigma$ errors on the individual power spectrum estimates.*

Dark energy

Finally, the remaining compelling support in favour of the Λ CDM model comes from the observation of accelerating expansion provided by Riess et al. (1998) and Perlmutter et al. (1999). These studies used type-1A supernovae, which are used as standard candles as they occur in stellar binary systems where a white dwarf is accreting material from a giant until the white dwarf reaches the Chandrasekhar mass at $1.38M_{\odot}$ and undergoes a supernova explosion. As this process occurs at a fixed mass limit, type-1A supernovae have a peak luminosity which correlates with the decline rate of the light curve, thus these cosmological studies used type-1A supernovae to derive distance measurements to $z \leq 0.35$ galaxies. The results revealed that the expansion of the Universe is accelerating, thus necessitating the inclusion of dark energy in the concordance cosmology model and placing the first constraints on the dark energy density of the Universe. However, the nature of dark energy remains one of the main open questions in cosmology with competing models including, for example, the cosmological constant, or vacuum energy, which has an equation of state with $w = -1$, or scalar field models such as quintessence in which $w \neq -1$.

1.2.2 Failures of the Λ CDM model

Despite the strong evidence outlined above in favour of the currently adopted Λ CDM model for cosmology, there remain some key disparities between model predictions and observations, namely the “missing satellite” (Klypin et al. 1999, Moore et al. 1999a) and “cuspy core” (e.g. Flores & Primack 1994, Moore et al. 1999b) problems. The former refers to the issue that models seem to over-predict the number of bound systems at very low masses compared to the number of satellite galaxies observed around the Milky Way and other local galaxies. This may in part be due to the observational limits associated with detecting such faint objects or, conversely, there may be physical processes which act to disrupt any star formation in such low-mass haloes (e.g. Benson et al. 2002). In addition, it has also been proposed that the “missing satellite” problem could be resolved if dark matter is not cold but instead warm (e.g. Bode et al. 2001), however at present this is an issue of continued debate. The latter potential failure of the current cosmological model is the prediction from CDM models that dark matter density distributions should be “cuspy”, i.e. dwarf galaxies should have steeper inner density profiles than those observed. Again this issue remains an

active area of research with some groups suggesting that these discrepancies can be explained by a better understanding of star formation and feedback processes which may, at least temporarily, disrupt cuspy cores (e.g. Governato et al. 2012), while other groups propose that these problems require additions to the current cosmological model (e.g. Spergel & Steinhardt 2000, McGaugh 2005).

Finally, one might argue that whilst the evidence for significant components of dark matter and dark energy in the Universe strengthens the arguments in favour of Λ CDM cosmology, the fact that candidate particles for both of these constituents remain elusive may constitute a non-trivial obstacle for our current model. Despite these arguments for and against Λ CDM cosmology, at present it provides the best available framework upon which our current models for galaxy formation and evolution are based.

1.3 Synopsis of Galaxy-Formation Models

Prior to the now widespread adoption of hierarchical models of galaxy evolution based on Λ CDM cosmology, one of the first generations of galaxy-formation models posited by Eggen et al. (1962) and Larson (1975) proposed a monolithic model. In this picture galaxy formation is described by a high-redshift epoch of formation during which galaxies form rapidly by gravitational collapse and undergo a single burst of star formation, thereafter evolving purely secularly. This model proposed that galaxies initially collapse into spheroidal systems which gradually relax into disks, and hence describes an evolutionary sequence for the Hubble tuning fork (Fig. 1.2) established in 1926 (see also Hubble 1936), which classifies local galaxies into these two broad categories using their morphologies.

However, by the 1980s this model of monolithic collapse was being replaced by a model of hierarchical galaxy evolution based upon the CDM model (Peebles 1980, Blumenthal et al. 1984, Davis et al. 1985). These first cold dark matter models were founded upon the principle that any perturbations in the density field of the Universe at early times will grow through gravitational instabilities to form cosmic structures. The first calculations of the number of bound structures of a certain mass that would arise from a given density field were conducted by Press & Schechter (1974), who used a spherical top-hat function (which describes the evolution and collapse of spherically-symmetric over-densities in a non-linear growth regime through application of the Friedman equation), an approach which

was later updated by, for example, Peacock & Heavens (1990). This technique was later combined with the first estimates of the density field expected from a CDM cosmology by the perturbation theory presented in Peebles (1982) and was extended by the work of Blumenthal et al. (1984) and Davis et al. (1985) to provide the first model of hierarchical growth in a CDM Universe.

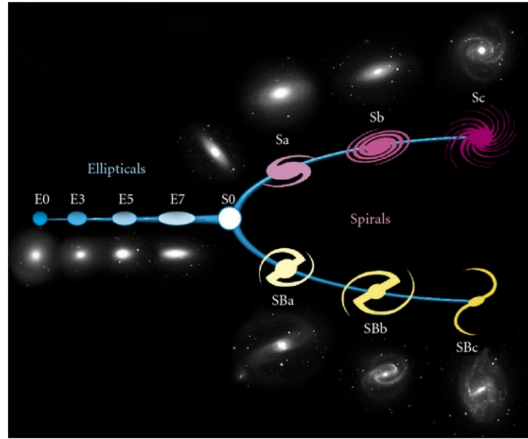


Figure 1.2 *An updated version of the Hubble Tuning Fork illustrating how the galaxy population can be clearly split into elliptical (E) and spiral (S) classes, with spirals being additionally divided into barred (SB) and un-barred (S) morphologies. The Hubble classification further describes elliptical galaxies by their axial ratios ranging from spherical E0 systems, to more elongated E7's. In the case of barred or un-barred spiral galaxies the extent to which the spiral arms are wound is characterised by the notation (S or SB)a-d, where e.g. Sa galaxies have more tightly wound spiral arms than Sd systems. The tuning fork also identifies a class of lenticular (S0) galaxies which despite being disks display no current evidence of spiral arm structure. Image credit NASA and ESA.*

At the same time, White & Rees (1978) combined the first predictions for the growth of dark matter haloes with the models of Rees & Ostriker (1977) and Silk (1977), which described the processes governing the cooling of gas within galaxies, to deliver the first two-phase model of galaxy evolution. This model also made use of the much earlier, fundamental, work of Hoyle (1953) suggesting that the rotation of a galaxy is determined by the tidal torques acting upon it during its collapse, and that galaxy mass is governed by the time taken for the gas to cool. It was noted early on by White & Rees (1978) that their model predictions for the luminosity function of galaxies (the function describing the number of galaxies per unit luminosity per unit volume) over-estimated the number of faint galaxies observed, and so they proposed that there must be some physical mechanisms

which disrupt star formation in low luminosity (and thus low-mass) galaxies.

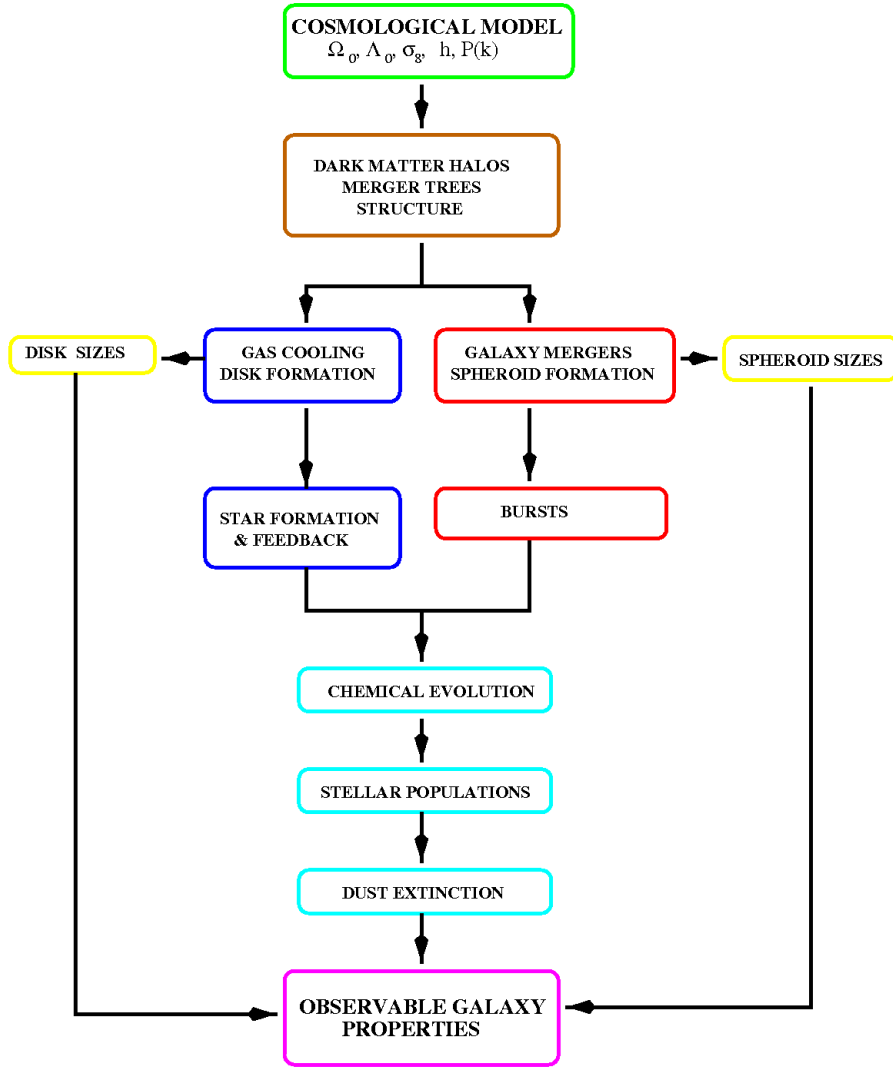


Figure 1.3 *An overview of the general construction of semi-analytic models for galaxy-formation models, taken from Baugh (2006) and originally adapted from Cole et al. (2000).*

By the early 1990s White & Frenk (1991), Cole (1991) and Lacey & Silk (1991) had published the first semi-analytical models of galaxy evolution, which incorporated the hierarchical build-up of dark matter haloes, the cooling of gas within such haloes and prescriptions for star formation and feedback within galaxies. An overview of how such codes are constructed is presented in Fig. 1.3. In these early models feedback at low masses was associated with gas ejection from supernova winds.

In the following years effort was concentrated on improving the merger trees

of dark matter haloes (Kauffmann et al. 1993) such as those illustrated in Fig. 1.4 , the prescriptions for gas cooling (Kauffmann & Charlot 1994), supernova feedback (Cole et al. 1994) and the development of hydrodynamical codes. Since then the most significant advancements in galaxy-formation and evolution models have been driven by the endeavour to reproduce observations by improving prescriptions for baryonic physics.

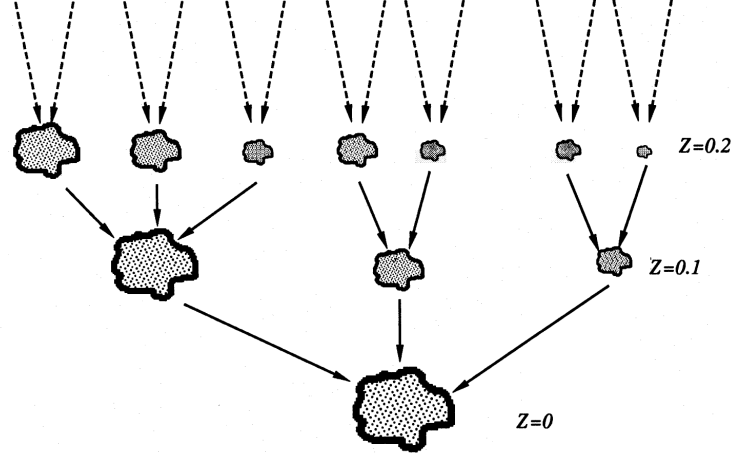


Figure 1.4 *A schematic diagram from Kauffmann et al. (1993) illustrating the merging history of dark matter haloes in a hierarchical Λ CDM cosmology. This diagram clearly demonstrates the bottom-up formation scenario.*

Broadly speaking, modern galaxy-formation and evolution models can now be split into two different approaches: the semi-analytic model technique discussed above (e.g. White & Frenk 1991, Kauffmann et al. 1993, Baugh et al. 2005, Croton et al. 2006, Guo et al. 2011b) which is based on N-body simulations of dark matter haloes (such as the Millennium simulation Springel et al. 2005) and overlays prescriptions for baryonic physics which can be fine-tuned to reproduce observations; and smoothed-particle hydrodynamical (SPH) or adaptive mesh hydrodynamical models (e.g. Katz et al. 1992, Navarro & Steinmetz 1997, Springel 2005, Davé et al. 2011, McCarthy et al. 2012) which are more computationally expensive Eulerian or Lagrangian-grid-based hydrodynamical simulations, which often adopt sub-resolution physics for e.g. star formation and gas cooling etc.

1.4 Observational Constraints and Updates to Models

1.4.1 Luminosity function

Perhaps one of the most fundamental observational probes of galaxy formation and evolution is the galaxy luminosity function, which quantifies the number of galaxies per unit volume as a function of luminosity. As early as the 1970s it was realised that the overall shape of the observed luminosity function for galaxies can be described by a power law with an exponential cut off at the bright end (Schechter 1976)

$$\Phi(L)dL = \Phi_* \left(\frac{L}{L_*}\right)^\alpha \exp\left[-\frac{L}{L_*}\right] \frac{dL}{L_*} \quad (1.1)$$

(where L_* and Φ_* are the characteristic luminosity and normalisation values, respectively and α describes the faint end slope), and that this functional form does not match the shape of the predicted dark-matter mass function from numerical simulations, as shown in Fig. 1.5.

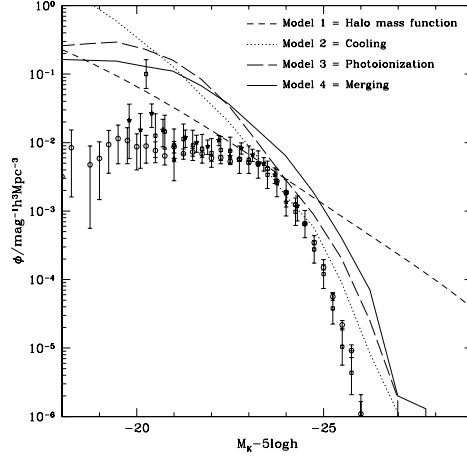


Figure 1.5 *The observed K-band luminosity functions from Cole et al. (2001), Kochanek et al. (2001) and Huang et al. (2003) over-plotted with the modelled dark matter halo mass function converted to a luminosity function assuming a fixed mass-to-light ratio (Model 1), along with a semi-analytic model of the galaxy luminosity function including no forms of feedback (Model 2). These are also compared to models where star formation has been suppressed via photo-ionisation (Model 3) and by gas stripping during merging (Model 4). Plot from Benson et al. (2003).*

In the first instance White & Rees (1978) realised that their models over-predicted the number of galaxies at the low-mass end, and they proposed that additional mechanisms must be taken into account to disrupt star formation in these low-mass haloes through processes of feedback. At this low-mass end star formation can be made inefficient by radiative and hydrodynamical supernova feedback as per Larson (1974), and by photoionisation heating (e.g. Efstathiou 1992).

However, with increasing advancements in imaging capabilities providing larger-area, multi-wavelength studies able to identify more massive systems at higher redshifts (e.g. Lilly et al. 1996, Ellis et al. 1996, Kauffmann & Charlot 1998, Steidel et al. 1999, Drory et al. 2005, Fontana et al. 2006, Cirasuolo et al. 2007) it was discovered that the galaxy luminosity function also requires star-formation suppression in the high-mass regime in order to reproduce both the number of massive galaxies observed locally and at high redshift, and the star-formation activity of already passive high-redshift massive galaxies (Cole et al. 2000, Somerville et al. 2001). At this higher mass end, where higher halo masses are no longer easily disrupted by supernova feedback, in order for feedback to remain an important process for quenching of star formation, it must be triggered instead by active galactic nuclei (AGN).

The exact processes of AGN feedback are still not fully understood but can be broadly split into two different categories: quasar and radio modes. The model for quasar-mode feedback (Hopkins et al. 2006) is motivated by the observations of cold-mode AGN which accrete material through a classical accretion disk. In this model it is suggested that energy radiated from the accretion disk couples thermally to the surrounding gas, heating and expelling it from the system until it cools down, at which point it may then fall back into the disk and resume star formation. As such, it is thought that quasar-mode feedback might trigger only a temporary halt in star formation within massive galaxies. The second case is that of radio-mode feedback (Best 2007), which proposes that feedback may be caused by hot-mode AGN, which are fuelled by gas directly from a spherical halo, not a classical accretion disk. In this case feedback is attributed to powerful radio jets injecting mechanical energy into the galaxy halo and blowing out hot bubbles, thereby sustaining star-formation suppression. There are also suggestions that AGN may provide radiative feedback in a scenario where, at the peak of accretion, in addition to a UV ionising background, the AGN itself provides strong ionisation to nearby surrounding regions, which alters the gas cooling rate. However, the detailed physics involved in coupling either radiative or mechanical energy to halo

gas remains one of the biggest challenges for current research. This is clearly highlighted by the latest studies shedding light on secondary processes, such as new evidence that jet-medium interactions may actually boost star formation (e.g. Feain et al. 2007, Tremblay et al. 2012), consistent with previous models from Elmegreen & Elmegreen (1978).

Nevertheless, ongoing studies such as those of Wise et al. (2007) and David et al. (2009), which directly image holes in gas in the radio and X-ray consistent with radio-mode feedback, and those of e.g. Feruglio et al. (2010), Ciccone et al. (2012), Cano-Díaz et al. (2012) which find evidence in line widths of molecular gas for massive outflows from winds driven by quasar feedback, give renewed hope that these complex feedback processes can be further understood with the next generation of instruments, such as ALMA, capable of exploring the gas reservoirs of galaxies out to higher redshifts. At present the prescriptions for various feedback processes have been somewhat successfully implemented in several generations of SPH and semi-analytic models (Granato et al. 2004, Baugh et al. 2005, Croton et al. 2006, Bower et al. 2006, De Lucia & Blaizot 2007, Naab et al. 2007). This has helped to reconcile the predicted luminosity function of high-mass galaxies with recent observations extending to higher redshifts, as is shown in Fig. 1.6, although see Bernardi et al. (2013) for a discussion of how luminosity measurement uncertainties affect the derived number densities of massive galaxies.

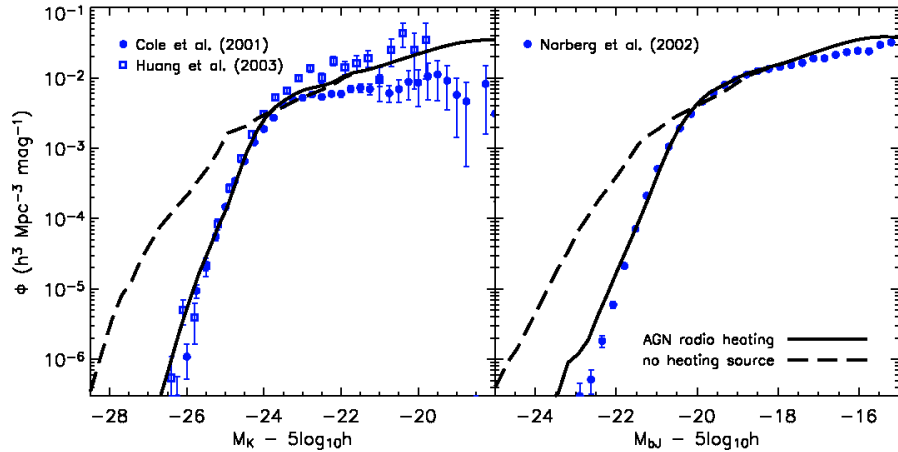


Figure 1.6 *The updated modelled galaxy luminosity functions of Croton et al. (2006) with and without AGN feedback, over-plotted in blue with observational data from Cole et al. (2001) (2dF survey), Huang et al. (2003) (Hawaii AAO survey) and Norberg et al. (2002) (2dF).*

1.4.2 The star-formation history of the Universe

Identifying the formation epoch of massive galaxies has also helped to constrain the baryonic physics in models of galaxy formation. As outlined above, the early monolithic models postulated a period of rapid, high-redshift, formation followed by secular evolution. This is in contradiction to the hierarchical theory, which advocates a bottom-up process where early star formation is followed by a prolonged phase of mergers, resulting in a gradual build up of mass in the most massive systems. The assembly of stellar mass is a clear tracer of galaxy evolution and can be further quantified by the evolution of star-formation rates with redshift. Star-formation rates can be derived from various broadband and emission-line fluxes, as summarised by Kennicutt (1998). However, early studies of the star-formation history of the Universe focussed on simply identifying rather than characterising star-forming galaxies at increasingly high redshifts, and provided the first indications that the star-formation rate density of the Universe peaked at $z \sim 1$ (Lilly et al. 1995, Madau et al. 1996; 1998), in reasonable agreement with the models of Cole et al. (1994).

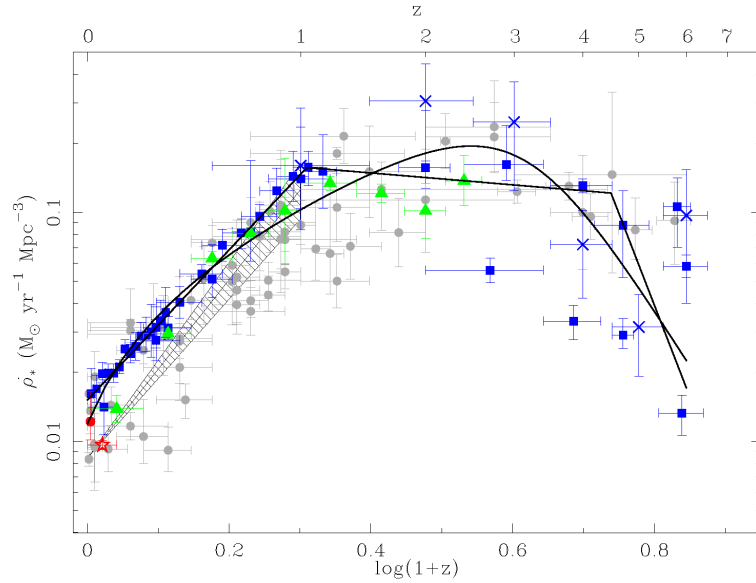


Figure 1.7 *An update to the Madau-Lilly plot of star-formation rate density evolution as a function of redshift provided by Hopkins & Beacom (2006) showing a peak consistent with $z \sim 2$.*

These observations have since been supported by an overwhelming number of studies (e.g. Hopkins & Beacom 2006, Daddi et al. 2007, Renzini 2009, Ilbert

et al. 2010, Nordon et al. 2010) which have extended this analysis out to much higher redshifts and longer wavelengths, and corroborate a peak in cosmic star formation at $1 < z < 3$, tantalizingly close the peak of AGN activity at $z \sim 2$ (Schmidt & Green 1983). The evolution in the star-formation rate density presented by Hopkins & Beacom (2006) is shown in Fig. 1.7.

Despite one of the most robust validations of the hierarchical scenario coming from the continued increase in stellar mass throughout cosmic time in spheroidal galaxies, indicative of a merger driven evolution (Brinchmann & Ellis 2000), the advancement in detailed star-formation studies of high-redshift galaxies has placed better constraints of the era of massive galaxy formation, pushing it back, increasingly close to the domain of reionisation (e.g. Bernardi et al. 1998, van Dokkum & Franx 1996, Kriek et al. 2006, Zirm et al. 2008). These advances have ultimately led to the observation of a significant population of massive and already passive galaxies in place at $z > 2$ (Fontana et al. 2004, Glazebrook et al. 2004, Drory et al. 2005). This may seem at odds with the idea of a bottom-up formation scenario from hierarchical models where the most massive galaxies would be expected to be young and star-forming, but Baugh et al. (1999) and later De Lucia et al. (2006) have demonstrated that star formation in over-dense regions such as galaxy clusters is shifted towards earlier times relative to less dense regions, as halos in denser environments will collapse faster. These claims were supported by observational studies such as those of Thomas et al. (2005), Clemens et al. (2006) and Cooper et al. (2010b) who found that field galaxies have delays in the onset of star formation of $1 - 2$ Gyrs compared to cluster members.

Coupling this idea with earlier studies, which suggested that a significant amount of a galaxy's mass is accreted through mergers rather than formed in situ (Baugh et al. 1996), it was realised that whilst the final mass assembly of massive galaxies is a more recent process, the stars which comprise the system may be significantly older. This realisation allows the hierarchical assembly of galaxy formation to be reconciled with these, otherwise challenging, observations. This has also led to the wide-spread adoption of a two-phase model of galaxy evolution, where galaxies undergo a rapid mode of early star formation from dissipative collapse of gas clouds at $z > 2$, followed by a second phase at $z < 2$, where galaxies accrete stars formed outside the galaxy (e.g Oser et al. 2010, Cooper et al. 2010a, Johansson et al. 2012). In fact the relative importance of these processes depends on galaxy mass, whereby in the most massive galaxies up to 80% of the final assembled

stellar mass can be from accretion (Oser et al. 2010).

However, despite the ability of current galaxy evolution models to more accurately reproduce the required star-formation histories and prevalence of massive, passive galaxies at high redshift, the detailed physics of star formation is not well understood, and the current shortcomings in our knowledge have resulted in other difficulties for galaxy evolution models. One of these main issues is the efficiency of star formation. In spite of some of the latest studies shedding new light on the trends of galaxy star-formation efficiency with both redshift and galaxy mass, revealing that even at the peak of activity (for $M \sim 5 \times 10^{11} M_{\odot}$ systems), star-formation efficiency is only $\sim 20\%$ (Behroozi et al. 2010; 2012), incorporating accurate prescriptions for star-formation efficiency in the latest models remains problematic.

One of these outstanding issues is the “bulge problem”, which refers to the relative ease with which models are able to reproduce bulge systems compared to disks. In terms of star-formation physics, current models are too effective at forming stars at high redshifts in disks, which are then more able to undergo merging events transforming them into spheroidals. This results in the predicted number of disks which survive to the present day being very low. If these stars do form at such high redshifts then one of the few mechanisms which would allow massive disk systems to survive is the process of “wet” mergers: where the merging galaxies have significant amounts of gas. This kind of merger will destroy the original disks, but the gas in the system will enable new disks to form after the merging event, thus increasing the number of disk galaxies surviving to lower redshifts. However, in order for the merging events to be “wet” there must still be a significant fraction of gas within the systems during the process, which requires the high-redshift star-formation process to be inefficient at converting the gas reservoir into stars.

At present, the question of how best to account for star-formation efficiency in the models and the observed number of disk galaxies, whilst still being able to reproduce other observable morphological features such as spiral arms and bars features within disks, is still ongoing but it is suggested that this scenario requires star formation to take place over an extended period rather than in a single burst at high redshift.

In addition to this, the newest generation of models are also refining how star formation within galaxies is best modelled spatially. In the past, models have used the overall distribution of gas within galaxies as tracers of star formation,

but it has been shown observationally that molecular gas is a better indicator (e.g. Kennicutt et al. 2007, Krumholz et al. 2011). Thus, current models are now adopting this approach. Unfortunately, the molecular gas content of galaxies is more concentrated (and thus bulge-like) and so acts to exacerbate the difficulty in modelling realistic, extended disks. Nevertheless, models such as Hopkins et al. (2011) claim to solve this issue by incorporating a mode of feedback from radiation pressure to smooth out star formation in models and sustain extended disks.

Despite the ongoing difficulties in star-formation modelling it is worth noting that whilst our current models are not able to reproduce all of the observational features of galaxies, there are still some marked successes, such as the predictions of morphologically clumpy star-forming features from the violent disk instability model of Dekel et al. (2009b), Ceverino et al. (2010) and Cacciato et al. (2012), which has been lent observational credence by the studies of high-redshift galaxies by Wuyts et al. (2012) and Mozena et al. (2013, in preparation). Thus, it is clear that although the detailed processes governing star formation are not yet fully understood, significant steps are being taken towards delivering more consistent models.

1.4.3 Downsizing

Another observational characteristic of galaxy formation which has led to the refinement of models is the effect of “downsizing”. The galaxy downsizing signature was first observed by Cowie et al. (1996), who coined the term to refer to the evolution of maximum star-formation efficiency from higher to lower mass systems with decreasing redshift. Cowie et al. observed that the maximum luminosity, and therefore maximum mass, of the most actively star-forming galaxies decreases with decreasing redshift, which indicates that massive galaxies have an accelerated star-formation history and cease activity first. This effect has also been supported by further observations of the stellar-mass function by Fontana et al. (2004), Drory et al. (2005) (see Fig.1.8), which demonstrate a stronger evolution in the number density of less massive galaxies with redshift than massive systems and provide evidence that star formation begins at higher redshifts and is limited to shorter timescales for the most massive galaxies.

Furthermore, detailed metallicity studies such as those of Tremonti et al. (2004), Savaglio et al. (2005) and Onodera et al. (2010) have provided additional evidence

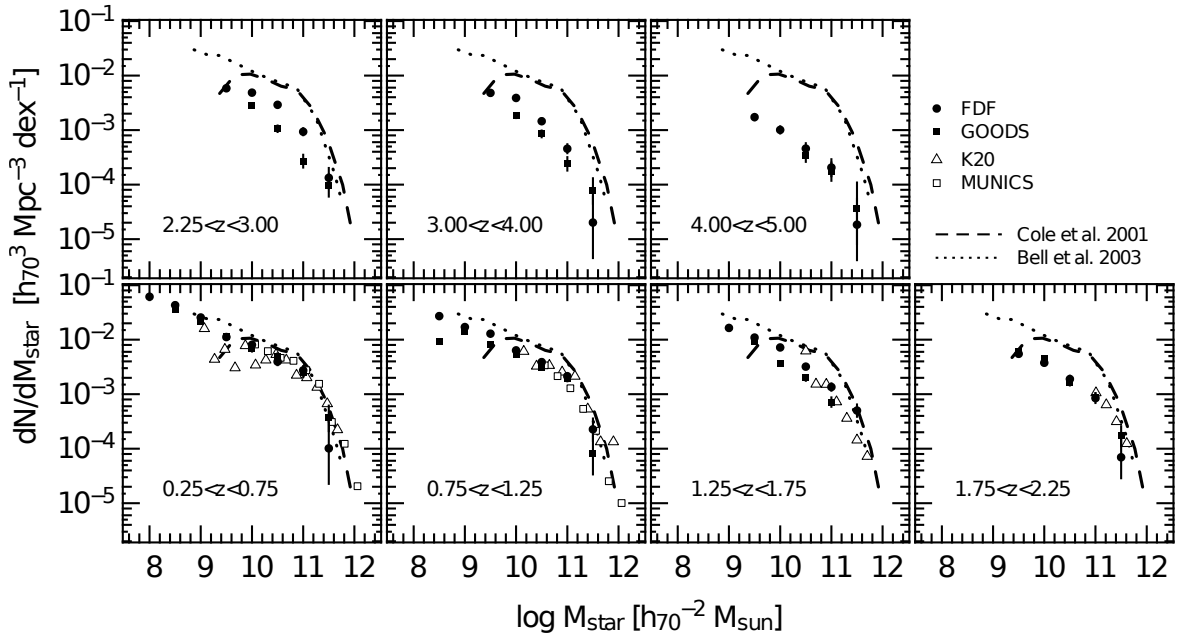


Figure 1.8 *Stellar-mass functions at $0.25 < z < 5$ from Drory et al. (2005), over-plotted with the local mass functions from Bell et al. (2003) and Cole et al. (2001). This illustrates the stronger evolution with redshift in the number density of less massive galaxies compared to more massive galaxies.*

that massive systems are already enriched to solar metallicity at much higher redshifts compared to lower-mass galaxies, substantiating the idea that massive galaxies have an accelerated star-formation history.

The incorporation of AGN feedback in the models of Bower et al. (2006), Croton et al. (2006) and De Lucia et al. (2006) went some way towards being able to reproduce the downsizing signature, by matching the decline in the star-formation rates of massive galaxies with redshift. However, even in the latest generation of galaxy evolution models star formation in present-day massive systems is still over-predicted, necessitating the need for further suppression in these systems, either by enhanced feedback from AGN or through additional secular quenching processes such as those proposed by the hydrodynamical simulations of Kereš et al. (2005) and Dekel et al. (2009a) and the analytic theories of Birnboim & Dekel (2003) and Dekel & Birnboim (2006). These authors hypothesise that above a given halo mass ($M > 10^{12} M_{\odot}$) and below $z \sim 2$ (where $M > 10^{12} M_{\odot}$ halos no longer only exist at the very peak of over-densities) shock heating in the halo can disrupt the cold filament inflows which feed star formation, observational evidence for which has been provided recently by Hartley et al. (2013). Additionally,

galaxies can also be potentially quenched through the violent disk instability (VDI) models of Dekel et al. (2009b), Ceverino et al. (2010) and Cacciato et al. (2012) which state that as massive disks evolve there is an inflow of mass to the centre of the system, which gradually builds to form a massive bulge. This inflow changes the density profile of the disk, making it no longer self-gravitating and thus quenches star formation by halting the collapse of molecular clouds in a process of morphological quenching (Martig et al. 2009). Hence it is clear that, even though the exact processes responsible have not yet been determined, the latest galaxy evolution models require additional quenching mechanisms, over and above the traditional major-merger scenario, which has previously been invoked to both transform morphologies in the hierarchical model and to halt star formation at late times.

1.4.4 Morphological and size evolution

Whilst the current generation of Λ CDM hierarchical galaxy-formation models which incorporate AGN feedback to quench star formation at early times have had some success reproducing the stellar population characteristics of previously observed galaxies out to high redshift, within the past few years the notable increase in the depth of photometric surveys has given rise to the widespread implementation of morphological analysis as a powerful diagnostic for theories of galaxy evolution.

Locally galaxies have traditionally been classified using the Hubble sequence to distinguish between bulge and disk dominated systems. Despite this classification system being developed in the 1920s, the latest detailed wide-area studies of the local Universe now available from SDSS (Sloan Digital Sky Survey, York et al. 2000) and GAMA (Galaxy And Mass Assembly, Driver et al. 2011) have revealed how well this local population is fitted overall by the Hubble scheme. In addition to galaxies being preferentially classified as bulge and disk dominated or irregular systems the multi-wavelength data available from these surveys has also provided colour information for these local objects which has provided observational evidence of the colour-morphology bimodality expected from a hierarchical formation scenario, whereby star-forming disks undergo major-merging which both quenches star formation and transforms their morphologies making them elliptical systems. Thus, red galaxies are dominated by bulge systems, making up the red sequence, and blue galaxies are predominantly disk-

dominated, comprising the blue cloud (Baldry et al. 2004, Driver et al. 2006, Drory & Fisher 2007), although there remains debate about how objects classified by colours which would place them in the “green valley” (Martin et al. 2007) evolve either off the blue cloud onto the red sequence or in fact vice versa.

Also in agreement with the current hierarchical models of galaxy evolution are observations at high redshift which show that, above $z = 2$, the most massive galaxies become increasingly disk-dominated (Buitrago et al. 2011) as expected if the main driver of galaxy evolution is the merging of high-redshift disk galaxies to build up massive “red-and-dead” ellipticals by the present day.

However, while the aforementioned studies deliver evidence for observational trends in line with the hierarchical model of galaxy evolution where major mergers are credited with both transforming the morphologies of galaxies and quenching their star formation, it is becoming increasingly clear that the exact processes responsible for both of these modes of evolution are more complicated. This has recently been highlighted by the identification of red disk galaxies and blue bulge systems at both low (Bamford et al. 2009, Masters et al. 2010) and high redshifts (van der Wel et al. 2011, McLure et al. 2013, Bell et al. 2012). In particular the presence of passive disk galaxies suggests that the physical processes responsible for morphological transformations and star-formation quenching are not simply connected and may occur via different channels. This picture is again more consistent with the models of morphological quenching and violent disk instability driven quenching posited by Martig et al. (2009) and Dekel et al. (2009b) than the traditional major-merging quenching scenarios. Furthermore, the exact nature of high-redshift disks provides further obstacles to correctly modelling the evolution and formation of these objects as they have recently been shown to display clumpier morphologies (Wuyts et al. 2012) with puffier dynamical structures (Förster Schreiber et al. 2009) and more disturbed visual morphologies (Mortlock et al. 2013) than their local counterparts. This introduces new questions about our understanding of the underlying physics shaping these systems.

In addition to the studies now capable of probing the underlying morphologies of both local and high-redshift galaxies, it is now possible to examine in detail further morphological properties such as size and axial ratios. In fact recent morphological observations (e.g. Daddi et al. 2005, Trujillo et al. 2006, Toft et al. 2007, Trujillo et al. 2007, Buitrago et al. 2008, Cimatti et al. 2008, Franx et al. 2008, van Dokkum et al. 2008, Stockton et al. 2008, McGrath et al. 2008, Damjanov et al. 2009, Cassata et al. 2010) have revealed a controversial

population of ultra-compact massive galaxies at $z > 2$ with $r_e < 1.5$ kpc, ranging from factors of 2–6 times smaller than similarly massive local galaxies, where the most compact systems are dominated by early-type morphologies. Examination of these high-redshift sources suggests that they comprise both star-forming and quiescent galaxies that lie significantly below the well-defined local size-mass relation (Shen et al. 2003) from SDSS (York et al. 2000) (shown in Fig. 1.9), with the most compact candidates showing little evidence for ongoing star formation (Toft et al. 2007, Kriek et al. 2009, McLure et al. 2013). A compilation of the size-mass results reported by these early studies is shown in Fig. 1.10, which is taken from Cimatti et al. (2008).

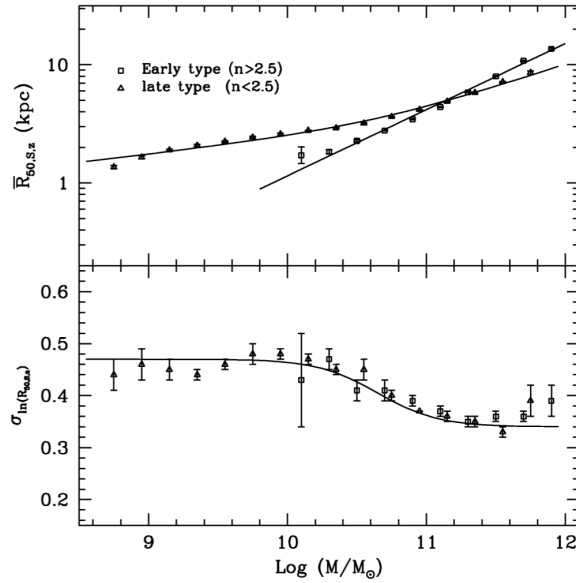


Figure 1.9 *The local size-mass relation of SDSS galaxies from Shen et al. (2003), using Sérsic half light radii from z-band imaging, effectively circularised due to the use of circular apertures. Masses are from Kauffmann et al. (2003b) which uses a Kroupa IMF with Bruzual & Charlot (2003) stellar population models. The relations have been split into late and early morphological types based on their Sérsic index fits, where $n < 2.5$ distinguishes late-type galaxies as commonly adopted in the literature.*

The compact sizes of these high-redshift objects were unexpected and remained a controversial measurement for some time. Accordingly, much scrutiny has been focused on the potential biases involved in these unanticipated measurements. In particular, the potential for size underestimates caused by selection effects (van der Wel et al. 2009) and the possibility of the existence of faint extended envelopes below current detection limits. Of further concern is the possibility of

mass over-estimates (Muzzin et al. 2009, Mancini et al. 2010) due to the well-known sensitivities and biases of stellar-mass estimates derived from photometric spectral energy density (SED) fitting on the initial mass function (IMF) (Rettura et al. 2006) and stellar population synthesis models (Magdis et al. 2010) employed in the fitting procedures.

However, Szomoru et al. (2010; 2012) and Trujillo et al. (2012) both obtained deep photometry for a small sample of these high-redshift compact objects and found no evidence for low surface brightness envelopes extending below the detection limits of shallower studies, while van der Wel et al. (2008), Newman et al. (2010), van de Sande et al. (2011), van de Sande et al. (2012) and McLure et al. (2013) conducted spectroscopic studies to determine dynamical mass estimates for compact high-redshift galaxies and verify that these objects do lie below the local size-mass relation. Furthermore, despite the effect of potential biases involved in the determination of both sizes and stellar masses, the latest generation of morphological studies now conducted in higher resolution with HST WFC3 (e.g. van Dokkum et al. 2010, Szomoru et al. 2012, Ryan et al. 2012) are providing even more robust evidence for the truly compact nature of this interesting population.

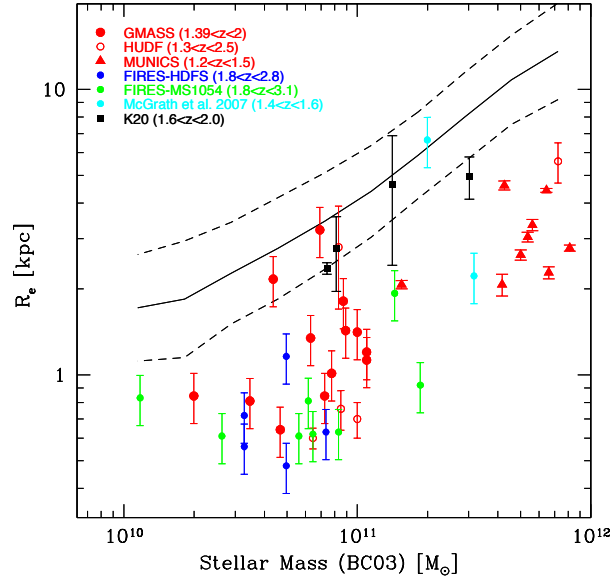


Figure 1.10 *Compilation of size-mass results for $1 < z < 3$ galaxies from Cimatti et al. (2008), over-plotted with the local early-type galaxy relation from Shen et al. (2003) (solid line) and its $1 - \sigma$ scatter (dashed line).*

While evidence is mounting for the presence of compact galaxies at high redshift,

it is now clear that not all high-redshift galaxies are compact (as initially pointed out by e.g. Mancini et al. 2010, Valentinuzzi et al. 2010b), and the question of whether or not similarly compact galaxies exist in the local Universe remains a highly contentious subject. Valentinuzzi et al. (2010a) and Poggianti et al. (2013) find that (when including both cluster and field environments) the number density of compact galaxies locally is comparable to that at high redshift; with roughly $\sim 20\%$ of local galaxies being compact. In contrast Trujillo et al. (2009) and Taylor et al. (2010) report that as little as $\sim 0.03\%$ of local galaxies are compact, where the study by Taylor et al. (2010) directly addresses suggestions that the local sample as studied by SDSS may be biased against bright compact objects so as to avoid saturation and cross-talk within their spectra, and reports no significant bias against massive compact objects in the local SDSS sample. Nevertheless, debate over the extent to which the size-mass relation evolves with redshift continues (with some authors suggesting an evolution as mild as a factor of 1.6 since $z = 2$ (Poggianti et al. 2013), with the other extreme being a factor ~ 4 (van Dokkum et al. 2010)), along with disagreement over whether or not a significant fraction of compact galaxies survive to the present day.

Part of the disagreement over the existence of local compact galaxies and the evolution of sizes may come from the dependence of galaxy size on environment and age. By including the effects of environment on galaxy sizes Rettura et al. (2010) find no correlation between galaxy size and environment, and interestingly report no offset in ages between field and cluster galaxies, but do find evidence for accelerated evolution in over-dense regions. In disagreement with this the latest study by Poggianti et al. (2013) shows that, for a given mass and size, cluster galaxies are older than field galaxies, and moreover, by using luminosity weighted ages Poggianti et al. find that for a fixed mass range, older galaxies are smaller in size. This age dependence is again extremely controversial with previous studies such as Saracco et al. (2009) and Valentinuzzi et al. (2010a) supporting these claims, in contrast to Trujillo et al. (2009), Kriek et al. (2009) and Trujillo et al. (2011) who claim that the compact galaxies observed at both high redshift and locally, have moderate ages of $\sim 1 - 2$ Gyr.

This continued debate over the dependence of galaxy size on properties such as age and environment further highlights issues for the proposed size evolution of galaxies, such as progenitor bias, where e.g. Poggianti et al. (2013) claim that in order to provide a consistent comparison for galaxy sizes across different redshift ranges the sizes of passive high-redshift galaxies should best be compared with old

cluster galaxies in the local Universe. This stems from the models of De Lucia et al. (2006), which demonstrate that 60% of $M > 10^{11} M_{\odot}$ galaxies at $z > 2$ will evolve into clusters. It is due to this assertion that Poggianti et al. (2013) find a much weaker size evolution than previous studies, although again see van Dokkum et al. (2010) for previous attempts to account for progenitor bias by matching populations based on co-moving number densities for given mass bins and assuming that the most massive local galaxies had a progenitor which was also among the most massive galaxies at higher redshifts.

This debate over the age dependence of galaxy sizes is also an issue when considering the processes responsible for size evolution, as evidence for the most compact galaxies being the oldest may provide further support for the suggestions by Cassata et al. (2011), Carollo et al. (2013) and Cassata et al. (2013), who propose that the evolution in the size-mass relation comes primarily from the addition of new, larger galaxies to the population with time (in line with the models of e.g. Khochfar & Silk 2006), rather than the growth of galaxies already in place. However, Trujillo et al. (2011), and the latest number density study by van der Wel et al. (2013, in preparation) disagree with this interpretation and claim that the evolution in the size-mass relation comes from the increase in size of individual galaxies. In reality the size growth of galaxies may be comprised of both of these modes.

Despite the conflicting results outlined above, it is now agreed that the previously unexpectedly compact sizes of high-redshift galaxies are robust and recent detailed photometric and spectroscopic studies have corroborated the idea that these compact systems have much higher central stellar-mass densities than the average densities of similarly massive local galaxies, although they are consistent with the central cores of present-day massive systems (e.g. Trujillo et al. 2012, Szomoru et al. 2010, van de Sande et al. 2011). In addition to this, there is increasing evidence that the evolution of the size-mass relation can be well represented by a constant offset in the slope of the relation that scales with redshift (e.g. Ryan et al. 2012, McLure et al. 2013, Damjanov et al. 2011 & van der Wel et al. 2013 in preparation). Moreover, there is also a growing consensus that the scatter in the relation does not evolve (e.g. Trujillo et al. 2011, McLure et al. 2013 & van der Wel et al. 2013 in preparation), which suggests that most of these compact galaxies follow the same evolutionary path.

In spite of the fact that the discovery of compact high-redshift galaxies was unexpected, the sizes of such objects are in fact a natural prediction of modern

galaxy-formation simulations (e.g. Khochfar & Silk 2006, Hopkins et al. 2010a, Wuyts et al. 2010). These models propose that the merging of two gas rich disks at high redshift would create remnant spheroidals whose size depends critically on the degree of dissipation allowed during the merging process. As shown by Erb et al. (2006), at redshifts greater than 2 galaxy gas fractions increase significantly, thereby lending support to the conjecture that these extremely compact objects could have been formed from a progenitor population of gas rich disks. However, the processes which govern the subsequent size growth of high-redshift galaxies are not only still greatly debated, but require additional evolutionary scenarios to be considered in our current paradigm of galaxy formation and evolution.

There are currently two major competing mechanisms which can arguably reproduce the required size growth; major or minor merging (Khochfar & Silk 2006, Naab et al. 2007, Hopkins et al. 2009, Shankar et al. 2011) and AGN feedback (Fan et al. 2008; 2010). The first scenario acts to increase the size of a galaxy through the virial theorem by transferring kinetic to potential energy, with minor mergers being more efficient at precipitating growth than major mergers. From simple virial estimates in the case of a major 1:1 merger, the size can increase by a factor of 2, whereas for a similar mass increase from minor mergers the size can grow by a factor of 4, although this growth factor increases for a more complex treatment of the systems (Naab 2012). The competing scenario describes an adiabatic expansion of the system due to slow mass loss from AGN feedback driving gas out from the galaxy, where now the size growth is inversely proportional to the mass loss from the system.

All of these scenarios can potentially induce sufficient size growth, but there are problems associated with some of the accompanying predictions of these growth mechanisms. For the major-merger scenario these include reconciling the number of major mergers required to facilitate the required size growth, with the number of major mergers expected since $z \sim 1$ from N-body simulations (Hopkins et al. 2010b, Naab et al. 2009). In addition to this the disparity between the inferred large mass growth of these (already massive) systems and the latest estimates of the local galaxy stellar-mass function (Baldry et al. 2012, McLure et al. 2013) also provides difficulty for this proposed growth process. These problems, coupled with results from numerical simulations, which show that AGN-driven expansion occurs when the galaxy is much younger than the typical ages of high-redshift compact objects (at > 0.5 Gyr) (Ragone-Figueroa & Granato 2011), have led current studies to conclude in favour of a picture in which most size growth since

$z \sim 2$ is driven by minor gas-poor mergers in the outer regions of galaxies. These act to build up extended stellar haloes around compact cores, leaving the centre of the system unchanged and resulting in (relatively) small overall mass growth (Bezanson et al. 2009, Naab et al. 2009, Hopkins et al. 2010a, van Dokkum et al. 2010, McLure et al. 2013, Trujillo et al. 2012). However, it should be noted that there remains some continued debate over whether minor mergers can fully account for the required size growth (Nipoti et al. 2012, Cimatti et al. 2012, Newman et al. 2012 and Naab et al. 2009, Oser et al. 2012, Oogi & Habe 2013).

One further key piece of evidence in favour of the minor-merger driven, rather than feedback based evolution, is the evolution in the velocity dispersion of these systems. Whereas the merger-driven scenario predicts very little evolution in velocity dispersion with size growth, at most 30% since $z \sim 3$ (Hopkins et al. 2009), the AGN driven adiabatic expansion mode requires that the velocity dispersion of the system decreases with increasing size, of order for the simplest case as $r^{-0.5}$, giving a much stronger evolution. Except for the controversial study by van Dokkum et al. (2009), which has since been re-addressed by van de Sande et al. (2012), the limited number of velocity dispersion studies conducted on $z \sim 1.5 - 2$ compact galaxies (Cappellari et al. 2009, Cenarro & Trujillo 2009, van de Sande et al. 2011; 2012, Onodera et al. 2012, Toft et al. 2012) return velocity dispersion estimates of order $200 - 400 \text{ kms}^{-1}$, which are most consistent with the mild evolution associated with the minor-merger driven growth model as similarly massive local galaxies have velocity dispersions of $\approx 200 \text{ kms}^{-1}$. Thus, the minor-merger driven growth model, where galaxies grow via an “inside-out” process by undergoing several merging events which add mass predominantly to the outer regions and leave the central galaxy relatively unchanged, is currently generally agreed to be the model most consistent with the observations of size growth and the idea that high-redshift compact galaxies accrete outer envelopes to become the central regions of larger local galaxies (van Dokkum et al. 2010, Patel et al. 2013b, Dullo & Graham 2013). The evolution of the central stellar-mass density profiles from van Dokkum et al. (2010), which shows support for the “inside-out” growth process is given in Fig. 1.11.

The latest models of galaxy evolution (e.g. Naab et al. 2009, Oser et al. 2012, Johansson et al. 2012) are also now able to reproduce this process, and it should be noted that the incorporation of a significant amount of evolution due to minor merging, necessitated here by the need to account for galaxy size growth, also reflects a more general departure in current galaxy modelling from a purely major-

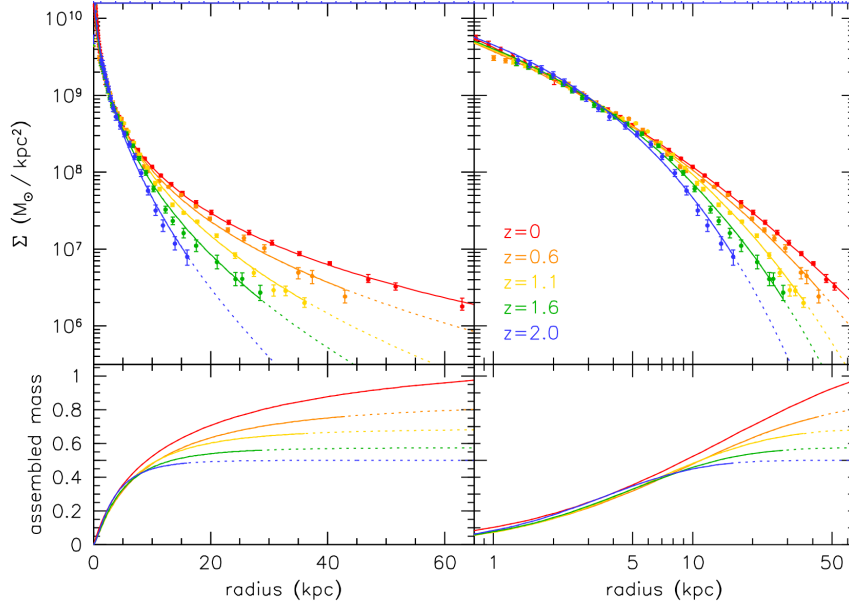


Figure 1.11 *Plots of the surface mass density profiles of stacks of galaxy populations in low and high-redshift bins from van Dokkum et al. (2010) providing evidence for the preferential addition of mass to the outer regions of galaxies, thus delivering support for the inside-out growth process of galaxy evolution. As mentioned previously, the sample of van Dokkum et al. (2010) was constructed by selecting massive galaxies across the $0.2 < z < 2.2$ redshift range at fixed co-moving number densities, so as to trace the same population as it evolves.*

merger induced evolution, as discussed in the context of galaxy quenching in Section 1.5. This issue has also been raised most recently by the studies of, for example, van Dokkum et al. (2013) and Patel et al. (2013a), which examine the central surface-density profiles of the progenitors of “normal” galaxies with masses corresponding to L_* , which dominate the stellar-mass budget of the Universe in terms of number. These studies conclude that the processes of evolution through which the central and outer regions of galaxies evolve concurrently through clump migration etc, are favourable over the traditional model of major mergers, which lead to the eventual relaxation and build-up of a younger massive disks at later times around the outskirts of previously assembled bulges.

1.5 Current State of Galaxy models: Progress and Outstanding Issues

In summary, the current paradigm of galaxy evolution is based on a Λ CDM cosmology where small perturbations in the density field of the Universe after the Big Bang grow to form the first sites of galaxy formation. Our current models describe how dark matter halos in the early Universe evolve through a process of hierarchical merging and the inclusion of prescriptions for gas cooling and star formation form the basis for reproducing the properties of galaxies observed, thus far, out to high redshifts. While many of the recent modifications outlined in the previous sections have managed to better reconcile model predictions with observations, there are still some outstanding discrepancies which must be addressed in order to achieve a fully-consistent model of galaxy evolution and formation.

1.5.1 *K*-band luminosity function and sub-mm populations

One of the longstanding issues with galaxy-formation models is the inability to accurately replicate both the luminosity function of galaxies observed in the *K*-band (in the near infra-red at $\lambda \sim 2.2\mu\text{m}$ where there is a smaller contribution from young stars which are more affected by dust, and is a better probe of the assembled stellar mass of the system) and the observed number density and redshift distribution of sub-mm galaxies (objects detected at wavelengths $\sim 450 - 850\mu\text{m}$), which are dominated by thermal emission from dust re-radiating the light from young stars. Some models (e.g. Baugh et al. 2005) have been able to reproduce the number counts and redshift distribution of sub-mm galaxies well by changing the IMF adopted, but have failed to reproduce the *K*-band luminosity function, finding too few massive galaxies at high redshift. In contrast, others (e.g. Bower et al. (2006)) have had the opposite problem, producing too few sub-mm galaxies and a redshift distribution peaked at too low a value. This problem is associated with our inability to fully understand star formation and the difficulties associated with modelling accurate stellar masses, although it has been suggested that reconciling these two observational constraints with the latest generation of models cannot be achieved by adjusting star-formation efficiency alone, but necessitates a change in the IMF which is adopted. By altering mass-to-light ratios with a top-heavy IMF it is possible for these models to better

reproduce both the observed K -band luminosity function and the number counts and redshift distribution of sub-mm galaxies as they are able to adopt a higher contribution from massive UV radiating stars, which give rise to the sub-mm properties, whilst retaining the observed luminosity function.

1.5.2 IMF

The IMF describes the distribution of mass in stars and is generally fit by a power law with different exponents for various models, or by a log-normal distribution. The nature of the IMF is in itself a major topic of current research, but a brief overview is given here within the context of the implications for the work carried out in this thesis. The functional form of the IMF is most often given by the number of stars within a given logarithmic mass bin: $\xi(\log M) = \frac{dN}{d\log M} \propto M^{-x}$, or by $\xi(M) = \frac{dN}{dM} \propto M^{-\alpha}$, where $\alpha = x + 1$. Currently in extragalactic studies the original Salpeter (1955) power-law IMF is most often replaced with the more bottom-light Kroupa (2001) or Chabrier (2003) IMFs (see Fig. 1.12), where there are more massive stars, or less low-mass stars, relative to other parameterisations of the IMF. The forms of these IMFs are given below.

$$\text{Salpeter} \quad \xi(\log M) \propto M^{-x}, \text{ for } 0.1 < M < 125 \text{ M}_{\odot}, \quad x = 1.35 \quad (1.2)$$

$$\text{Kroupa} \quad \xi(\log M) \propto M^{-x} \begin{cases} M < 0.08 \text{ M}_{\odot} & x = -0.7 \\ 0.08 < M < 0.5 \text{ M}_{\odot} & x = 0.3 \\ M > 0.5 \text{ M}_{\odot} & x = 1.3 \end{cases} \quad (1.3)$$

$$\text{Chabrier} \quad \begin{aligned} &\xi(\log M) \propto M^{-x}, \text{ for } M > 1 \text{ M}_{\odot}, \quad x = 1.3 \\ &\xi(\log M) = \frac{0.158}{\log M} \exp\left[\frac{-(\log M - \log 0.079)^2}{2 \times 0.69^2}\right] \text{ for } M < 1 \text{ M}_{\odot} \end{aligned} \quad (1.4)$$

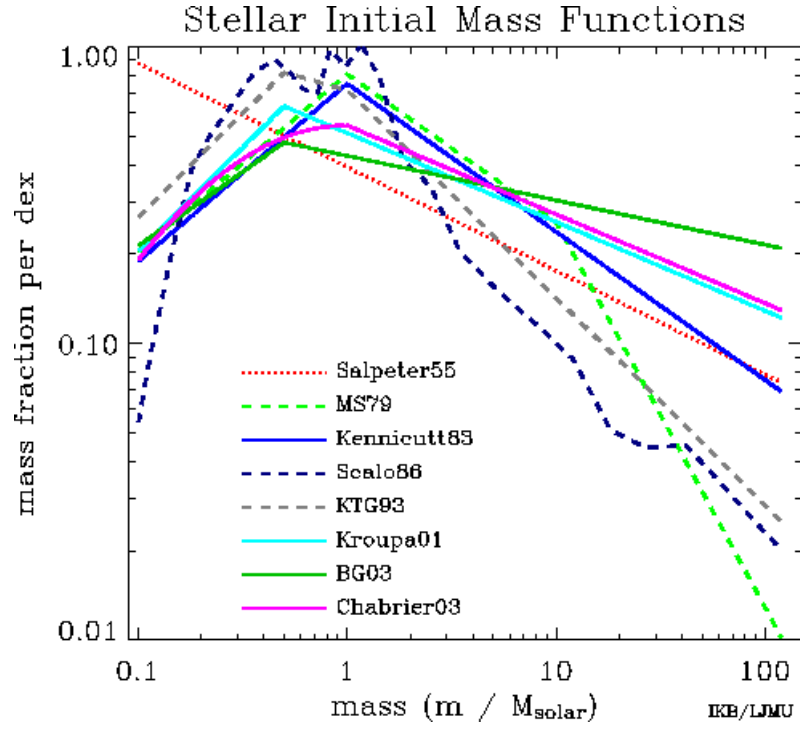


Figure 1.12 Comparisons of several of the widely-adopted initial mass functions. Image adapted from Baldry & Glazebrook (2003), credit: Ivan Baldry (<http://www.astro.ljmu.ac.uk/~ikb/research/imf-use-in-cosmology.html>).

Returning to the issues faced by the current generation of galaxy evolution models, Baugh et al. (2005) and Lacey et al. (2010) argue that by using a significantly more top-heavy IMF for merger triggered star-bursts they are able to reproduce both the observed properties of the K -band LF and the sub-mm population. There is also some motivation for adopting an IMF which is more top-heavy than Salpeter in order to reconcile the integrated cosmic star-formation history with the observed evolution in the stellar mass density (Hopkins & Beacom 2006). However, this modification remains controversial due to the debate over the nature of the IMF, both in terms of its form and its evolution with redshift. The contention over this issue has been fuelled by conflicting observations which have tried to address the universality of the IMF in other galaxies (in bulges and clusters in local galaxies) locally and at increasing redshifts, and have found evidence in favour of both top and bottom-heavy IMFs (e.g. Rieke et al. 1993, McCrady et al. 2003, Stolte et al. 2005, van Dokkum 2008, van Dokkum & Conroy 2012, Conroy & van Dokkum 2012, Spiniello et al. 2012, Ferreras et al. 2013, Smith & Lucey 2013).

Part of this speculation is due to the discovery of the dependence of certain IMF-sensitive absorption line strengths on velocity dispersion. For example the latest studies by van Dokkum & Conroy (2012), Conroy & van Dokkum (2012), Spiniello et al. (2012), Ferreras et al. (2013) and Conroy et al. (2013) reveal that the strength of the low-mass star sensitive lines (the NaI doublet and the FeH band) are proportional to the velocity dispersion of the systems, whereas the main high-mass star sensitive lines (the CaIII triplet) strengths are inversely proportional. This has led these studies to conclude that, overall, the IMF itself varies with velocity dispersion (although see Smith & Lucey 2013), becoming more bottom-heavy with increasing velocity dispersion and thus with increasing mass, which appears to be in disagreement with the requirements of some galaxy evolution models (e.g. Baugh et al. 2005). However, this new evidence for a potentially non-universal IMF when considered in light of previous studies such as those by van Dokkum (2008), which suggest the the IMF may become increasingly top-heavy with redshift, reveal how uncertain observational constraints on the IMF are. Therefore, it is easy to argue that they currently provide no definitive constraints for model requirements.

Moreover, the move towards a top-heavy IMF in galaxy models also helps to overcome another discrepancy with observations, the issue of the under-prediction of metal enrichment in the most massive systems, as observed by e.g. Tremonti et al. (2004). However, a top-heavy IMF still fails to reproduce the witnessed correlation between α -enhancement and velocity dispersion, leaving a further area for continued research.

1.5.3 Fundamental plane

Another underlying correlation which can not yet be fully reproduced by galaxy evolution models is the evolution in the zero-point of the Fundamental Plane. The Fundamental Plane (Djorgovski & Davis 1987) describes the correlation between a galaxy’s size, surface brightness and velocity dispersion. The models of Frenk et al. (1988) managed to deliver a realistic slope for this relation but reconciling the zero-point with observations, while still maintaining agreement with the galaxy luminosity function, can still not be achieved without introducing too high a star-formation efficiency (Guo et al. 2011a).

1.5.4 Galaxy sizes

Finally, both the size evolution of galaxies and the difficulty of models to predict enough disk galaxies surviving to present day have been addressed in previous sections, but as they represent serious challenges for current models they are worth noting again in brief. Not only does the “bulge problem” result in too efficient a formation of bulge over disk-dominated systems, but even the latest models (e.g. McCarthy et al. 2012, Marinacci et al. 2013) still struggle to produce realistic disk sizes for high-mass galaxies. This issue has become known as the “angular momentum problem” (e.g. Navarro & Steinmetz 2000), with models generally under-estimating disk sizes. Thus, it is clear that although the latest galaxy-formation models are able to describe observations in increasing detail, some key physical processes remain poorly understood and must be placed under further scrutiny if we are to further develop a fully consistent picture of galaxy formation and evolution.

To this end, the widespread employment of optical and, moreover, near infra-red studies since the early 1990s has revolutionised the study of galaxy evolutionary trends, extending them to previously unattainable redshifts. Not only has the capability to measure accurate photometric redshifts enabled the crucial study of number densities and luminosity functions throughout vital periods of cosmic time, but the simultaneous fitting parameters yielded through this technique have provided us with crucial estimates of galaxy masses, sizes, star-formation rates and even some insight into possible star-formation histories. It is the combination of these features that has enabled, and will continue to enable the comparison between observations and galaxy evolution models that drives the evolution of current theories. In order to achieve this, the progenitors of today’s most massive galaxies are ideally placed to further provide us with invaluable insight into these key evolutionary mechanisms, not only because it is at this high-mass end where models struggle most to reproduce observations, but these most massive galaxies also provide the brightest objects for study at any redshift.

1.6 Introduction to Photometric Techniques

In the previous sections I have presented a summary of the current state of galaxy evolution models, and have highlighted areas which are still subject to ongoing debate. However, the advancements in galaxy modelling over the past 20 years have unquestionably been driven by developments in photometric capabilities, which merit their own discussion.

While spectroscopic surveys provide the most secure estimates of galaxy redshifts, as they intrinsically measure the shift in well-defined spectral features, this process is traditionally time intensive as it requires long integration times. Moreover, spectroscopic redshift determinations rely heavily on the strength of the targeted spectral lines, thus they are heavily constrained by detection and resolution limits. Consequently, although current spectroscopic methods are the most accurate tools for redshift studies, providing not only secure redshift estimates, but also simultaneously offering additional spectral information helpful to determining the characteristics of target galaxies, they are limited as large area survey tools to low-redshift regimes ($z < 1.5$ e.g. zCOSMOS (PI Lilly) and VVDS (PI LeFèvre with VIMOS) where optical multi-object spectrographs are able to probe the rest-frame ultra-violet and optical. At higher redshifts ($1.5 < z < 3$) optical spectrographs begin to enter the redshift desert and near-infrared spectroscopy is required. However, multi-object near-infrared spectrographs are only just becoming available (e.g. KMOS, FMOS and MOSFIRE). Therefore, at present, near-infrared spectroscopy remains better suited to follow-up analysis.

In this respect photometry is key to providing both the depth and area required to best probe galaxy evolution out to high redshifts as photometric surveys are mainly hindered by a trade-off between survey depth and width, which can often be accounted for by making use of widely available complementary surveys. As such, photometry consistently produces large multi-wavelength libraries for the most complete samples of objects reaching far back in cosmic time and so forms an important basis for all current galaxy evolution studies.

The observation of high-redshift galaxies requires an *a priori* understanding of the stellar populations constituting galaxies that inhabit a much younger Universe than we see locally. It is the properties of these composite populations that govern the techniques that can be used to isolate galaxies at specific redshifts and underpin the main diagnostics used for both spectroscopic and photometric

surveys of galaxy populations at all redshifts.

Whereas, originally, local galaxies were classified by morphological type into the Hubble sequence, at high redshifts, where these characteristics are no longer easily identifiable and it becomes less clear how they evolve relative to other physical features, galaxies are classified by their photometric properties. Early on, these photometric classifications were predominantly based on colour distributions that preferentially select galaxies with distinctive features within the intermediate to high-redshift range (at $z > 1$), which includes the formation epoch of the bulk of stars that exist locally in massive galaxies (Hopkins & Beacom 2006). Initially, the most successful of these techniques was the detection of Lyman break galaxies (LBGs) (Steidel et al. 1996; 1999). LBGs represent a class of star-forming galaxies at $z > 3$, which are relatively unobscured by dust and emit a significant fraction of their rest frame light in the UV due to their abundance of young, massive photo-ionising stars. Very few stars, however, are hot enough to emit photons above the Lyman limit (at $\lambda \approx 912\text{\AA}$, the energy required to ionise a electron from the ground-state of Hydrogen), and any photons which are emitted at these short wavelengths will be readily absorbed by any neutral gas within the galaxy. This results in a decrement of flux blue-ward of the Lyman limit. In addition to this, the rest frame UV light corresponding to the wavelength of the *Lyman* $-\alpha$ line which is emitted by star-forming galaxies is then preferentially absorbed by interstellar neutral Hydrogen (Partridge & Peebles 1967) in intervening gas clouds along the line of sight. The range of redshifts of these intervening absorbers further results in a blanketing effect blue-ward of the *Lyman* $-\alpha$ ($\lambda \approx 1216\text{\AA}$) line in the galaxy’s spectrum. By $z = 3$ this flux “dropout” feature becomes visible in optical wavelengths and with the increasingly successful implementation of near-IR surveys, this technique has since be extended out to $z = 8 - 12$ (e.g. McLure et al. 2010, Oesch et al. 2010, Bouwens et al. 2011, Ellis et al. 2013), as can be seen in Fig. 1.13.

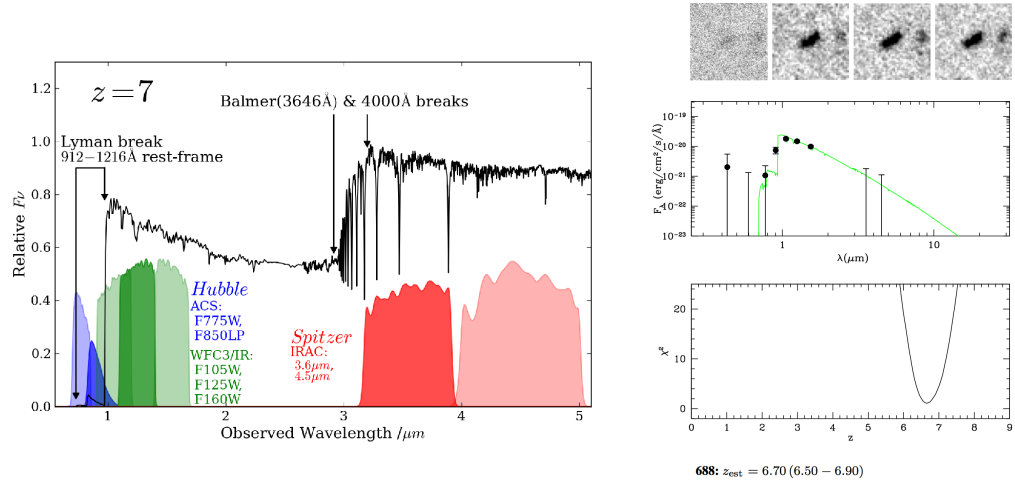


Figure 1.13 Representation of the SEDs of high-redshift Lyman Break Galaxies on the left. Image credit: A. B. Rogers & J. S. Dunlop taken from Dunlop (2013). The right hand panel shows image steps taken from McLure et al. (2010) for a $z \sim 6.7$ galaxy. The top row contains the 3×3 arcsec image stamps of the object in the HST ACS F850LP (z_{850}), WFC3 F105W (Y_{105}), F125W (J_{125}) and F160W (H_{160}) bands. The middle row shows the best-fit modelled SED for this object and the bottom panel is the corresponding plot of χ^2 versus redshift.

As a continuation of this photometric classification approach, galaxies at similar redshifts but with various other photometric characteristics have also been identified. These include:

- Distant red galaxies (DRGs) (Franx et al. 2003, van Dokkum et al. 2006). These galaxies were selected as having red colours in the near-IR ($J_s - K_s > 2.3[Vega]$), ensuring redshifts beyond $z = 2$. These galaxies can be either heavily obscured star-forming galaxies or passive galaxies at high redshift.
- Extremely red objects (EROs) (Elston et al. 1988, Thompson et al. 1999, Daddi et al. 2000) with $R - K_s > 5$, again containing populations of passive and obscured star-forming galaxies, but centred on lower redshifts of $z \sim 1$ (Cimatti et al. 2002).
- Luminous and ultra luminous infra-red galaxies :
 - LIRGS $10^{11} < L(8 - 1000\mu m) < 10^{12} L_{\odot}$
 - ULIRGS $L(8 - 1000\mu m) > 10^{12} L_{\odot}$

These have been shown to be galaxies with phases (Caputi et al. 2006) of

extremely intense star formation or AGN activity, which may or may not be triggered by merging.

- Sub-mm galaxies (SMGs) (Ivison et al. 1998, Smail et al. 1998) identified at $850\mu\text{m}$. These systems are heavily dust obscured with even higher intensity star-formation or AGN activity which is being re-radiating at much longer wavelengths.

These selection criteria allow otherwise blind photometric surveys to preferentially identify specific populations for follow-up. However, not only in some cases do these objects represent exclusively the extremes of activity, but the exact physics linking these galaxy populations is unclear and the prospect of significant selection bias in these samples must be taken into account before the properties of these objects can be confidently applied to observational relations.

As a result, the necessity for unbiased and uniform redshift samples is clear. This can be achieved by selecting galaxies with intermediate colour distributions using multiple colour cuts, for instance the “BzK” method employed by Daddi et al. (2004a) (Fig. 1.14), where $\text{BzK} \equiv (z - K)_{AB} - (B - z)_{AB}$. By establishing two colour regimes both passive and star-forming galaxies can simultaneously be targeted from within the same redshift regime, here at $1.4 < z < 2.5$. Daddi et al. used stellar population models coupled with spectroscopy to demonstrate that dust affects $B - z$ and $z - K$ colours equally within this redshift regime. Therefore, high-redshift dusty star-forming galaxies can be distinguished from lower redshift interlopers based on their blue $B - z$ colours ($\text{BzK} \geq -0.2$) and passive galaxies with old stellar populations can be separated from dusty star-forming galaxies based on their $z - K$ colours ($\text{BzK} < -0.2 \cap (z - K)_{AB} > 2.5$) which increase with age due to strengthening Balmer and 4000\AA breaks in the continuum. The Balmer break occurs at 3646\AA and is caused by the ionisation of electrons from the $n = 2$ energy state of neutral Hydrogen atoms in the photospheres of stars, but as a result of these two conditions the Balmer break does not increase simply monotonically with temperature but peaks around $\sim 10000\text{K}$ (A-type stars), corresponding to ages of $0.1 - 1\text{Gyr}$. Conversely, the 4000\AA break is caused by an accumulation of ionised metal absorption lines (e.g. Call H & K lines) in the photospheres of stars and increases as temperature decreases, thus the break is stronger for cooler, older, metal-rich stars.

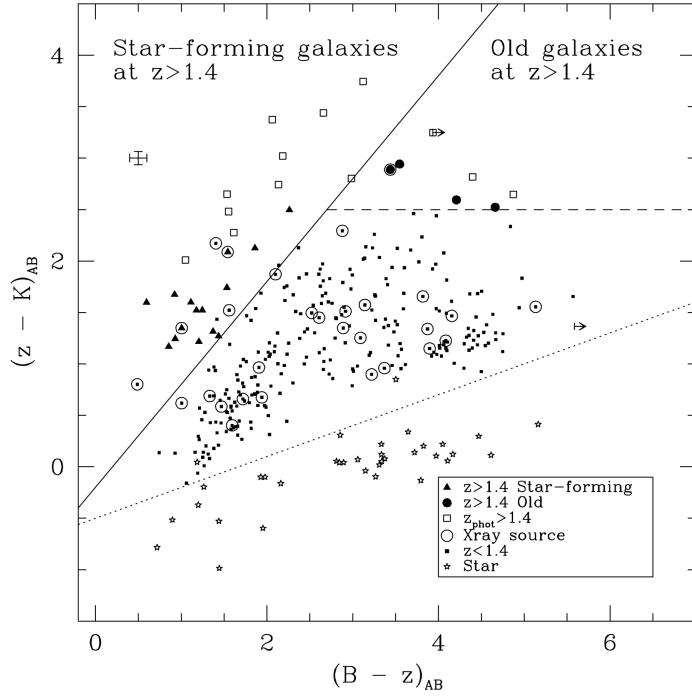


Figure 1.14 *Plot from Daddi et al. (2004b) illustrating the BzK diagram for distinguishing high-redshift passive from dusty star-forming galaxies. Plotted are the K20 data in GOODS, in addition to $z < 1.4$ galaxies from Cimatti et al. (2004) and x-ray sources from Giacconi et al. (2002).*

This technique has proved advantageous over previous colour cuts, such as those for selecting EROs by Roche et al. (2002) who use $R - K > 5$, or similar selections by Franx et al. (2003) who also make use of the 4000\AA break to identify $z > 2$ red galaxies. This is primarily due to the fact that it allows for the separation of dusty star-forming and passive red galaxies at high redshift. As a result, the BzK technique had powerful applications as it delivered a major step forward in constructing a complete census of the entire population of galaxies within this important redshift period, where massive galaxies are assembling the majority of their stellar mass, although it does also suffer from contamination from objects outwith the target $1.4 < z < 2.5$ redshift range.

The above techniques were usefully employed in generating catalogues of galaxies within fairly narrow redshift ranges from initial photometry, but for the instructive comparison with galaxy-formation models, not only is a definite redshift measurement required, but more informative galaxy properties such as the current and past star-formation rates, ages, dust content and stellar mass are crucial. These properties can be obtained from spectroscopic analysis,

as discussed above, but moreover, can also be determined from the further implementation of broad band photometry through the use of spectral energy distribution (SED) fitting (where in order to construct an SED a galaxy’s flux density is plotted against either wavelength or frequency over a wide baseline). Baum (1962) was the first to adopt this approach for optical data before it was later extended by Shapley et al. (2001) to encompass near-IR photometry after it was shown by Lilly & Longair (1984) and Kauffmann & Charlot (1998) that the rest frame K-band ($\sim 2\mu\text{m}$) provides the best probe of a galaxy’s stellar mass as it is insensitive to current star formation so represents the bulk of assembled stellar mass in any population. The addition of near-IR photometry is therefore crucial to the precision of galaxy mass estimation, and, by extension, to the determination of accurate photometric redshift measurements.

1.7 Introduction to SED fitting

In brief SED fitting can be conducted in two main ways:

1. Template fitting (e.g. Bolzonella et al. 2000), using low or high-redshift empirical templates or evolving model templates. These templates are then altered appropriately to reproduce the effects of observing them at higher redshifts, and are χ^2 fitted to the photometry to determine the best fitting redshift of observation, making use of strong spectral features such as the 4000Å break, Balmer break and Lyman decrement. This fitting procedure simultaneously yields estimates of the additional physical properties of the galaxies.
2. Neural Network fitting (e.g. Collister & Lahav 2004) where the fitting code is supplied with galaxy colours with known spectroscopic redshift. The code is then trained on this spectroscopic sample to correctly identify the redshift of the galaxy from the shape of the input SED. This provides accurate redshifts with fewer instances of catastrophic outliers from spectroscopic values but requires large training samples which are not available at high redshifts.

Due to their reliability at higher redshifts and the additional output parameters provided by the template fitting approach to SED fitting, it has become an increasingly popular and successful method for determining accurate redshifts

and extensive effort has been devoted to calibrating these photometric redshifts with those measured from spectroscopy. Three of the most widely-adopted SED fitting codes are: Hyperz (Bolzonella et al. 2000), LePHARE (Arnouts et al. 1999) and EAZY (Brammer et al. 2008), all of which are capable of providing photometric redshifts within a $1\text{-}\sigma$ scatter in $\Delta z/1 + z_{\text{spec}}$ of 0.1 of spectroscopic values (Abdalla et al. 2011, Brammer et al. 2008).

To give a brief overview, the general SED fitting procedure can be summarised by the following steps.

1. The stellar population synthesis technique (SPS) (e.g. Bruzual & Charlot 2003, Maraston et al. 2006) uses stellar evolutionary tracks which model how spectra evolve with time for stars of a given age.
2. These tracks are summed over an initial mass function to generate isochrones (curves on the Hertzsprung-Russell diagram for stellar populations of the same age) of a single coeval stellar population.
3. These contributions are then used to generate simple stellar population (SSP) models (Tinsley 1980) by summing the spectra of stars along the isochrones. An example SED of an SSP model from Bruzual & Charlot (2003) is given in Fig. 1.15. Next, the SSP models are integrated over an adopted star-formation history (e.g. burst models, continuous star formation, several exponentially decaying star-formation models, and in the latest cases exponentially increasing models are also included) to create composite stellar populations (CSPs).
4. The stellar evolutionary synthesis models are then subjected to the processes that would be involved in observing them at all potential redshifts. This includes extinction due to dust following an adopted extinction model, generally Calzetti et al. (2000), where the models are fitted over various amounts of reddening; the Lyman decrement due to absorption by the IGM along the line of sight as detailed by Madau (1995); and further reddening to incorporate additional extinction from being observed through galactic dust in the Milky Way.
5. Finally these models are integrated over the transmission functions of the filters used to observe the galaxies so that the models can be directly compared to the observed SED using a χ^2 test. The model SED is then

subject to certain sanity checks (e.g. that the age of the galaxy model does not exceed the age of the Universe at the predicted redshift).

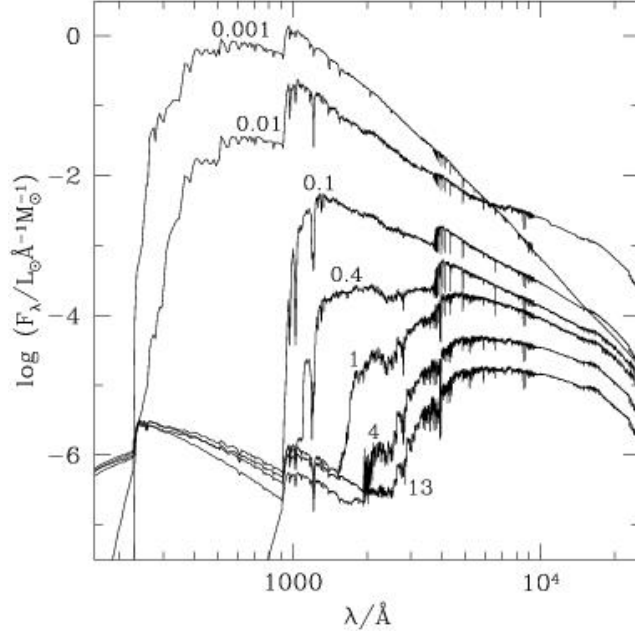


Figure 1.15 *An SED of a standard SSP model generated from the Padova 1994 evolutionary tracks with the STELIB/BaSeL 3.1 spectral library for solar metallicity using a Chabrier IMF limited between $0.1 M_{\odot}$ to $100 M_{\odot}$, where different ages in Gyr are plotted as denoted in the labels.*

As discussed previously (despite a small fraction of catastrophic outliers, of the order of a few percent) photometric and spectroscopic redshift estimates are generally in good agreement, especially at lower redshifts where extensive calibration has been conducted, although also see Fig.1.16 for the accuracy achieved for photometric redshifts at $0.2 < z < 4$ from the latest UltraVISTA survey (PIs Dunlop, LeFèvre, Franx and Fynbo) (McCracken et al. 2012). However, as is clear from the above synopsis of the fitting procedure, the accuracy of the photometric redshifts estimated from the template SED fitting approach depends critically on the use of physically meaningful input parameters.

For the estimation of accurate photometric redshifts the amount of reddening adopted and the reddening law which is used can significantly affect the fitted values. The Calzetti et al. (2000) reddening law provides a satisfactory estimation for photometric surveys limited to the optical and the near-IR, as any complications from less understood dust re-emission and PAH emission are

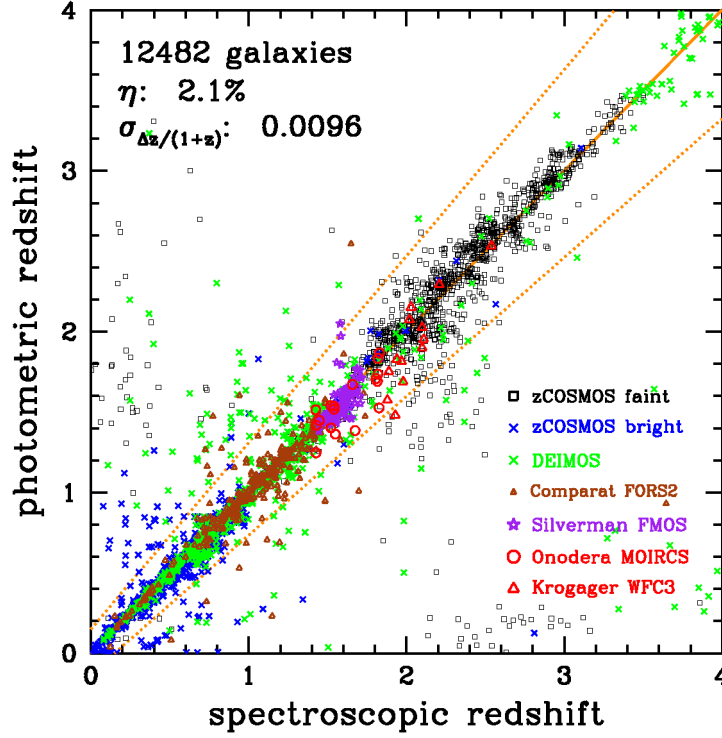


Figure 1.16 *Comparison between photometric and spectroscopic redshifts from Ilbert et al. (2013) from the UltraVISTA survey, using spectroscopic redshifts from the zCOSMOS bright and faint surveys. The photometric redshifts are highly precise with a 1- σ scatter in $\Delta z/(1+z_{\text{spec}})$ of 0.03 of spectroscopic values for the high-redshift sample at $1.4 < z < 4$.*

confined to longer wavelengths. Hence consideration of these effects is outwith the scope of the galaxy studies discussed here. Nevertheless, the amount of extinction allowed during the fitting can still substantially alter the derived redshift. As a consequence, the most complete estimations include higher levels of extinction than were previously required, in an attempt to avoid mis-classifying lower-redshift contaminants as high-redshift galaxy candidates (e.g. Dunlop et al. 2007).

Stellar-mass estimates are not only affected by the errors on the photometric redshift determinations, but can also be biased by the input parameters adopted in the SED fitting, including the metallicity of the synthetic population, the IMF and the SPS models implemented.

It is widely accepted that a single metallicity value is sufficient for these models as it has been shown that the majority of $1 < z < 3$ massive galaxies have metallicities very close to solar values (Shapley et al. 2004) and that even by

decreasing the metallicity to half solar values, derived masses decrease by only 10 – 20% (Papovich et al. 2001).

The most influential and contentious of the input parameters are the IMF, and the SPS models used, as both can significantly affect the associated SED stellar-mass estimates. As detailed above, one of the biggest ongoing debates in this research area is the universality of the IMF. Although the traditionally preferred Salpeter (1955) IMF is widely adopted in literature, it is generally agreed that more bottom light IMFs (Chabrier 2003) give a better fit to observed stellar populations and, moreover, reduce the derived masses and star-formation rates of these high-redshift galaxies by as much as 0.25 dex (Onodera et al. 2010). At present there is a slow migration towards the Chabrier IMF as a standard for the SED fitting of high-redshift galaxies, but Longhetti & Saracco (2009) present the following useful conversions: $M_{Chabrier} = 0.55M_{Salpeter}$, $M_{Kroupa} = 0.62M_{Salpeter}$.

Furthermore, the use of different SPS models has proved to introduce even higher levels of bias. This mainly arises from the introduction of increased effects from thermally pulsating asymptotic giant branch (TP-AGB) stars on the stellar tracks by Maraston (2005). The TP-AGB phase occurs for stars around 0.5 – 1 Gyr old, comprising a significant fraction of the population of $z > 2 - 3$ galaxies, and describes the evolutionary stage after a star has become a red giant and has exhausted both Hydrogen and then Helium burning in its core. At this point it then resumes shell burning and so moves along a track in the H-R diagram similar to its initial giant phase, as shown in Fig. 1.17. During this asymptotic giant branch phase the star will first burn Helium in a shell until it begins to become depleted, at which point the outer layers of the star contract and re-ignite Hydrogen burning in an outer thin shell. As this progresses Helium is produced from the fusion of Hydrogen and eventually replenishes Helium in a zone between the Helium and Hydrogen thin shells. At this point thermally unstable Helium burning will recommence and results in the “Helium flash”. This “flash” then heats the zone between the shells, causing it to expand and cool, turning off the Hydrogen shell burning. The inner Helium shell will continue to burn until the temperature becomes high enough to once again ignite Hydrogen burning in the outer shell, and the replenishment and Helium flash will repeat. This process causes the star to thermally pulsate and also results in a second, now asymptotic giant branch lifetime, during which the star will experience significant mass loss. As a result, even if only a few stars enter this additional phase, once on the TP-AGB they will contribute a significant component to the near-IR flux of the

integrated galaxy SED. Thus, adopting a Maraston (2005) SPS model reduces photometric masses by a factor of ~ 2 in comparison with the Bruzual & Charlot (2003) estimates. However, we do not yet have sufficient models of mass loss in stellar evolution to place reliable constraints on the level of mass loss experienced during such a phase and any such constraints currently employed come from empirical calibrations. Hence the time that star spends in the TP-AGB phase and the luminosity it can actually achieve is highly uncertain.

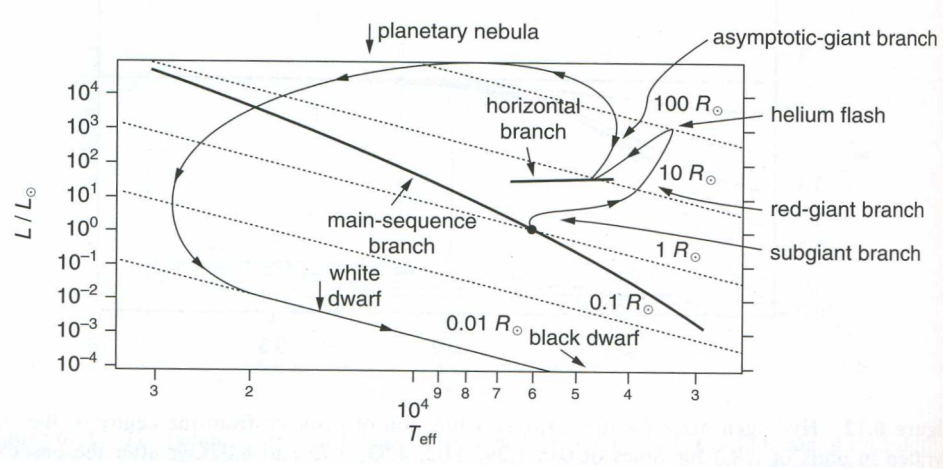


Figure 1.17 *The evolutionary track of the TP-AGB phase in the HR diagram from Leblanc (2010) Fig 6.13.*

The Maraston (2005) models controversially adopt lower levels of mass loss than the Bruzual & Charlot (2003) models, which allow stars to spend longer in the TP-AGB phase and contribute more near-IR flux. Along with the increased weight given to these stars, this gives rise to the discrepancies in stellar-mass estimates. However, the latest results from Kriek et al. (2010) and Zibetti et al. (2013) show that the level of contribution from TP-AGB stars in the Maraston (2005) models is an over-estimate, and they conclude that the Bruzual & Charlot (2003) SPS models are a better fit to data. Nevertheless, the models of both of these groups have been widely implemented and the ongoing disparity between the models is well acknowledged.

In addition to these issues, the majority of SED fitting procedures adopted include either single burst, or exponentially decaying star-formation histories, although it has been shown by Michałowski et al. (2012) and McLure et al. (2013), that including double-burst models in SED fitting often allow a more physical fit to the data. However, while Michałowski et al. (2012) show that two component models can produce significantly larger stellar masses than single-component models for

extreme star-bursting objects such as sub-mm galaxies, McLure et al. (2013) report that the mass difference is relatively small for more typical massive $z \sim 1-2$ galaxies. In this case the median difference in the stellar-mass estimates from the preferred Bruzual & Charlot (2003) exponentially decaying star-formation history (τ) models and the double-burst models is only ~ 0.17 dex, presumably because an exponentially decaying star-formation history provides a reasonable description for the most massive galaxies at these epochs.

When considered in the context of massive galaxy ($> 1 \times 10^{11} M_{\odot}$) studies, significant effort has been invested in quantifying such uncertainties by comparing photometric masses with those derived from dynamical and/or lensing surveys. The first concern to be addressed was the dependence of photometric masses on the SPS and IMF models adopted. Rettura et al. (2006) and Grillo et al. (2008) compared photometric masses with dynamical and a combination of dynamical and lensing estimates respectively. Grillo et al. (2008) implemented a technique for utilizing both strong lensing and high-resolution dynamical studies to resolve the stellar and dark matter components separately, as per Treu & Koopmans (2004). They found that the dynamical + lensing stellar-mass estimates agreed with photometric estimates to within an order of unity (1.1 ± 0.1), independent of the SPS models used. Furthermore, Rettura et al. (2006) showed that, more notably, the choice of IMF produces a significant deviation between photometric and dynamical masses. Adoption of a Kroupa IMF gives photometric masses with a consistent offset of 0.27 dex compared to dynamical masses, but using a bottom heavy Salpeter IMF uniformly increases the photometric estimates, resulting in an unphysical scenario where the photometric mass exceeds the dynamical value, a result in agreement with previous studies by Cappellari et al. (2005). Thus, it appeared from these studies that the choice of IMF may in fact be the predominant contribution to mass uncertainties. However these surveys were only limited to optical regimes. van der Wel et al. (2006) conducted the first work including near-IR photometry and concluded that by incorporating these critical wavelengths, where the Bruzual & Charlot (2003) and Maraston (2005) models differ considerably, the deviation between derived masses was found to be as substantial as a factor of 2.5. Thus, it is clear that there are significant offsets to be considered when reporting and comparing galaxy stellar-mass estimates obtained using different models. To this end, well-established mass conversion factors have been presented in the literature: $\log_{10} M_{*,M05} = \log_{10} M_{*,BC03} - 0.15$ (Cimatti et al. 2008); $\log_{10} M_{*,CB07} = \log_{10} M_{*,BC03} - 0.2$ (Salimbeni et al. 2009).

Notwithstanding these potential dependencies, SED fitting has proved to be a successful method of redshift fitting and cannot only be considered an ideal tool for widespread redshift analysis for photometric surveys but is also a crucial tool for generating the mass-selected samples of high-redshift galaxies necessary to deliver further constraints for the current generation galaxy evolution models.

1.8 Outline of Thesis and Impact

This introduction has focused on the current progress and the remaining challenges to our understanding of how galaxies form and subsequently evolve throughout cosmic time and has highlighted the role of the most massive galaxies in helping to constrain formation and evolutionary scenarios. Recent developments in the ability to conduct extremely deep photometric studies and the advancement in spectroscopic capabilities with new multi-object spectrometers and integral field instruments have been coupled with invigorated refinement of N-body hydrodynamical simulations and semi-analytical models, which has allowed us to analyse the properties of galaxies in the distant Universe with increasing resolution. This has provided renewed motivation for the unification of theoretical predictions with observational properties of high-redshift galaxies and has therefore driven significant advancements in our understanding.

Current Λ CDM hierarchical models are now capable of reproducing many observations out to high redshifts, including stellar-mass functions, global star-formation rates, luminosity functions and, to a lesser extent, downsizing. However, there are still some significant failures in model predictions, such as the sizes of disks, the size and morphological evolution of the population and the processes responsible for star-formation quenching. Thus the incentive for further study is clear and well recognised.

This thesis is laid out as follows. In Chapter 2 I present a full discussion of the sample selection procedure adopted, including the method for stellar-mass and star-formation rate estimates. I then discuss the development of a robust procedure for morphological model fitting of the HST WFC3 F160W imaging and present initial results from single-component Sérsic model fitting of the CANDELS-UDS sample, including the associated uncertainties on the best-fit model parameters. In Chapter 3 I present the multiple-component Sérsic model work and discuss the morphological trends displayed by the separate

bulge and disk components. In Chapter 4 I extend this multiple-component Sérsic model fitting to the CANDELS-COSMOS field and across the additional F125W, F814W and F606W-band imaging provided by CANDELS. I discuss how extension of this morphological analysis to the multiple bands enabled separate component photometry to be constructed, and detail how this photometry was utilised to conduct individual component SED fitting to provide stellar-mass and star-formation rate estimates for the decomposed bulge and disk components. The size evolution of the separate bulge and disk components is reported in Chapter 4, and in Chapter 5 I explore how the additional morphological properties evolve and correlate with decomposed star-formation rates in order to probe how the physical processes which govern morphological transformations are connected to those responsible for star-formation quenching. Finally, in Chapter 6 I present a summary of my conclusions and discuss how I intend to continue this work in the future.

Throughout this thesis magnitudes are quoted in the AB system (Oke 1974), and all physical quantities are calculated assuming a Λ CDM universe with $\Omega_m = 0.3$, $\Omega_\Lambda = 0.7$, and $H_0 = 70 \text{ km s}^{-1} \text{ Mpc}^{-1}$.

Chapter 2

The Sizes of Massive High-redshift Galaxies

2.1 Introduction

The study of the high-redshift progenitors of today's massive galaxies can provide us with invaluable insights into the key mechanisms that shape the evolution of galaxies in the high-mass regime, placing important constraints on current models of galaxy formation and evolution. In recent years the new generation of optical-infrared surveys have revealed that a substantial population of massive galaxies is already in place by $z \simeq 2$, and that the star-formation activity in a significant fraction of these objects largely ceases around this time, ~ 3 Gyr after the Big Bang (e.g. Fontana et al. 2004, Glazebrook et al. 2004, Drory et al. 2005). These results have driven the modification of models of galaxy formation to include additional mechanisms for the quenching of star-formation activity in massive galaxies at early times, such as AGN feedback (e.g. Granato et al. 2004, Bower et al. 2006, Croton et al. 2006, De Lucia & Blaizot 2007).

However, explaining the number densities and ages of massive galaxies at high redshift is only part of the challenge, as recent advances in imaging capabilities are now providing meaningful data on their sizes and morphologies during the crucial cosmological epoch $1 < z < 3$, when global star-formation activity in the Universe peaked. In particular, over the last $\simeq 5$ years, deep/high-resolution ground-based and space-based (i.e. HST) surveys have revealed that a significant

fraction of massive galaxies at $z > 1$ are surprisingly compact (e.g. Daddi et al. 2005, Trujillo et al. 2006; 2007, Cimatti et al. 2008, Franx et al. 2008, Damjanov et al. 2009, Targett et al. 2011), with derived effective radii and stellar-mass measurements which place these galaxies well below the local galaxy size-mass relation as derived from the Sloan Digital Sky Survey (SDSS) (Shen et al. 2003). Furthermore, it appears that the largest divergence from local values arises in galaxies which exhibit very little sign of ongoing star formation (e.g. Toft et al. 2007, Kriek et al. 2009, McLure et al. 2013).

As befits their potential importance, these studies have been carefully scrutinized to investigate possible sources of bias in the measurement of galaxy size and mass (Muzzin et al. 2009, Mancini et al. 2010). A particular concern has been the perceived potential for galaxy scale-lengths to be under-estimated due to low signal-to-noise imaging (which might be inadequate to reveal faint extended envelopes), morphological k-corrections, or selection effects related to surface-brightness bias (e.g. van der Wel et al. 2009). However, the latest generation of deeper rest-frame optical morphological studies have thus far provided mounting evidence for the truly compact nature of many high-redshift galaxies (e.g. van Dokkum et al. 2010, Cameron et al. 2011, Ryan et al. 2012, Szomoru et al. 2012). It should also be noted that the existence of such compact objects at early times, while perhaps initially unexpected, is in fact a natural prediction of modern galaxy-formation simulations (e.g. Khochfar & Silk 2006, Hopkins et al. 2010a, Wuyts et al. 2010). Moreover, several local studies have now clarified the relative dearth of comparably-compact systems surviving to the present day (Trujillo et al. 2009, Taylor et al. 2010), strengthening the argument that the compact high-redshift systems must undergo a period of significant size evolution with limited mass growth in order to reach the local galaxy size-mass relation by $z = 0$ (e.g. McLure et al. 2013).

Various physical mechanisms have been suggested as the primary drivers of this process, including major or minor mergers (Khochfar & Silk 2006, Naab et al. 2007, Hopkins et al. 2009, Shankar et al. 2011) or AGN feedback (Fan et al. 2008; 2010). However, constraints from observations of the stellar-mass function on the associated mass growth, coupled with conflict from AGN feedback timescale arguments have led to the adoption of the minor-merger mechanism as the preferred scenario. In this model, most size growth since $z \simeq 2$ is driven by minor gas-poor mergers in the outer regions of galaxies, building up stellar halos around compact cores, with relatively small overall mass growth (Bezanson et al.

2009, Naab et al. 2009, Hopkins et al. 2010b, van Dokkum et al. 2010, McLure et al. 2013, Trujillo et al. 2012).

In this chapter I attempt to provide significantly improved clarity on these issues by exploiting the new near-infrared HST WFC3/IR imaging provided by the CANDELS survey (Grogin et al. 2011, Koekemoer et al. 2011) of the central region of the UKIDSS UDS field. This provides the necessary combination of depth, angular resolution, and survey area to enable the most detailed and robust study to date of the rest-frame optical morphologies of massive galaxies at $1 < z < 3$. This chapter also properly explores a number of challenging technical issues in the field, investigating the extent to which my results are robust to the method and accuracy with which both the background and on-image PSF is determined. Unlike many previous studies in this area, I have placed special emphasis on obtaining a formally-acceptable model fit to the observed galaxy images, in order to enable meaningful errors to be placed on the key morphological parameters extracted from my analysis.

2.2 Data and Sample Selection

2.2.1 HST imaging and basic sample definition

The main aim of this chapter is to present a comprehensive and robust analysis of the morphological properties of a significant sample of the most massive galaxies in the redshift range $1 < z < 3$. In order to achieve this I have focussed this study on the UKIDSS Ultra Deep Survey (UDS; Lawrence et al. 2007), the central region of which has been imaged with HST WFC3/IR as part of the CANDELS multi-cycle treasury programme (Grogin et al. 2011, Koekemoer et al. 2011). The CANDELS near-infrared data comprise 4×11 WFC3/IR tiles covering a total area of 187 arcmin^2 in both the F125W and F160W filters (hereafter J_{125} and H_{160}). The integration times are $\frac{4}{3}$ -orbit per pointing in H_{160} and $\frac{2}{3}$ -orbit in J_{125} , giving $5\text{-}\sigma$ point-source depths of 27.1 and 27.0 (AB mag) respectively. For this study I have used the catalogue from Cirasuolo et al. (in preparation) as a master sample. This sample was constructed using SEXTRACTOR (Bertin & Arnouts 1996) version 2.8.6 run on the H_{160} mosaic and then cut at a limiting total magnitude of 24.5 (i.e. a factor of ten brighter than the $5\text{-}\sigma$ point-source detection limit) to ensure that a reliable morphological analysis was possible (see

Grogin et al. 2011); in practice the subsequent stellar-mass cuts described below result in a sample in which $>90\%$ of the objects under study have $H_{160} < 23$ (giving typically $>50\text{-}\sigma$ detections).

2.2.2 Supporting multi-wavelength data

In addition to the near-infrared imaging provided by HST, the data-sets I have used for sample selection (i.e. photometric redshifts, stellar-mass determination, and star-formation rates and histories) include: deep optical imaging in the B , V , R , i' , and z' -band filters from the Subaru XMM-Newton Deep Survey (SXDS; Sekiguchi et al. 2005; Furusawa et al. 2008); u' -band imaging obtained with MegaCam on CFHT; J , H , and K -band UKIRT WFCAM imaging from Data Release 8 (DR8) of the UKIDSS UDS; and *Spitzer* $3.6\text{ }\mu\text{m}$, $4.5\text{ }\mu\text{m}$ IRAC and $24\text{ }\mu\text{m}$ MIPS imaging from the SpUDS legacy programme (PI Dunlop).

2.2.3 Photometric redshifts

A multi-wavelength catalogue for photometric redshift fitting was constructed for the CANDELS master sample using the dual-image mode in SEXTRACTOR with the H_{160} mosaic smoothed to a FWHM of 0.8 arcsec to match ground-based PSFs as the detection image, and included u' , B , V , R , i' , z' , J , H , K , $3.6\text{ }\mu\text{m}$, $4.5\text{ }\mu\text{m}$, J_{125} and H_{160} , similarly PSF-matched and re-gridded to the WFC3 pixel scale (0.06 arcsec/pixel) imaging. Full details of the catalogue extraction, PSF matching and treatment of source de-blending are given in Cirasuolo et al. (in preparation). However, in brief, in order to de-confuse the IRAC photometry (which due to its large PSF of ~ 1.7 arcsec (Fazio et al. 2004) blends multiple sources) a model is created from the H_{160} data to which a kernel is applied to match the IRAC PSF, and this model is then scaled to match the flux in the IRAC imaging to produce a total magnitude brightness estimate for the selected sources in the IRAC bands.

Following Cirasuolo et al. (2007), photometric redshifts for this master sample were determined using a χ^2 fitting procedure based on the photometric redshift code HYPERZ from Bolzonella et al. (2000), which utilises both empirical and synthetic templates to characterise the SED of galaxies (Cirasuolo et al. in preparation). As has been discussed in Chapter 1 the basic procedure adopted

for template fitting SED codes is to construct a grid of model photometry based on the redshift parameter space searched, the reddening adopted due to dust obscuration, the input stellar population synthesis templates and the allowed galaxy ages. Once this model photometry has been generated it is then subjected to the effects which would manifest if it was observed at high redshift, such as the Lyman decrement due to absorption by the IGM along the line of sight and additional reddening from dust within the Milky Way, before it is finally multiplied by the transmission functions of the filters which have been used for the observations. The SED fitting code then reads in the observed photometry, converts this from magnitudes to fluxes if necessary, applies pre-determined criteria for any bands in which the object is not detected (here, for a non-detection in a given band, zero flux is adopted for that object and it is given an error equivalent to the $1 - \sigma$ depth of the image in that filter), normalises the models and then calculates a χ^2 fit to the observed photometry at that point in the model grid. The SED fitting code loops over the full parameter space and then returns the minimum χ^2 model as the best-fit.

The SED fitting conducted here utilised a range of synthetic templates generated with a Chabrier IMF, a fixed solar metallicity value, and a variety of single-component, exponentially decaying, star-formation histories with e-folding times in the range $0 \leq \tau(\text{Gyr}) \leq 5$, where the age of the galaxy at each redshift was not allowed to exceed the age of the Universe at that redshift. Absorption from the inter-galactic medium was accounted for using the prescriptions of Madau (1995), and the Calzetti et al. (2000) empirical star-burst galaxy obscuration law was used to account for reddening due to dust within the range $0 < A_V < 4$. In order to test the accuracy of the photometric redshifts they were compared with known spectroscopic estimates where possible. This comparison demonstrated remarkably good agreement, with a distribution of $(z_{\text{spec}} - z_{\text{phot}})/(1 + z_{\text{spec}})$ centred on zero, with a standard deviation $\sigma = 0.03$.

2.2.4 Stellar masses

Having fitted photometric redshifts to this sample, stellar-mass estimates were obtained (Cirasuolo et al. in preparation) from the best-fitting SED model effectively through comparing estimates of the model stellar template flux normalised to one solar mass with estimates of the absolute magnitude of each object. The absolute magnitude of each galaxy can be computed by coupling the

distance modulus equation with the luminosity distance from cosmology. Starting with:

$$m_1 - m_2 = -2.5 \log_{10} \left(\frac{f_1}{f_2} \right) \quad (2.1)$$

and defining the absolute magnitude as the observed magnitude of an object at a distance of 10 parsecs, where $f = \frac{L}{4\pi d^2}$ gives the distance modulus equation: $m - M = 5 \log_{10} \left(\frac{d}{10 \text{ pc}} \right)$, where m is the apparent magnitude and M is the absolute magnitude. Alternatively, this can be rearranged to give the distance in Mpc :

$$m - M = 5 \log_{10}(d) + 25 \quad (2.2)$$

Now when considering distances on cosmological scales, such as those involved when observing high-redshift galaxies, d , the distance between the observed and emitted reference frames, becomes D_L , the luminosity distance. To derive the luminosity distance some basic relations from cosmology need to be made use of: $D_L = D_A(1+z)^2$, where D_A is the angular diameter distance of the object and is equivalent to the object's transverse co-moving distance multiplied by the scale factor of the Universe at the time the light from the object was emitted ($\frac{R(z)}{R_0} = \frac{1}{(1+z)}$). This gives : $D_A = \frac{D_M}{(1+z)}$, where D_M is the transverse co-moving distance (the distance between 2 objects at the same redshift separated by some given angle on the sky).

It is also known that in a flat Universe the transverse co-moving distance is equal to the line of sight co-moving distance (the distance between 2 objects which remains constant with time if both objects are moving in the Hubble flow) : $D_M = D_C$, therefore,

$$D_L = D_C(1+z). \quad (2.3)$$

Now the line of sight comoving distance $D_C = R_0 r$ and from the equation of motion for a photon $Rdr = cdt$, which combined with the relations : $\frac{R_0}{R(z)} = 1+z$ and $\frac{dz}{dt} = -\frac{R_0}{R^2} \frac{dR}{dt} = -H(z) \times (1+z)$ gives :

$$D_C = \int_0^z \frac{cdz}{H(z)} \quad (2.4)$$

where $H(z)$ comes from the Friedmann equation and is given by : $H(z) = H_0[\Omega_\nu + \Omega_m(1+z)^3 + \Omega_r(1+z)^4 - (\Omega - 1)(1+z)^2]^{\frac{1}{2}}$. And, since we are in a flat Universe

$(\Omega - 1) = 0$ so the equation for D_C becomes :

$$D_C = \int_0^z \frac{c}{H_0} \frac{dz}{[\Omega_\nu + \Omega_m(1+z)^3 + \Omega_r(1+z)^4]^{\frac{1}{2}}} \quad (2.5)$$

This gives a relation for the absolute magnitude of the observed galaxy at an estimated photometric redshift to which the modelled magnitude from 1 solar mass can be compared. Thus, scaling up the modelled magnitude to the absolute magnitude of the galaxy within the observed band closest to the rest-frame K-band (which provides the best measure of the assembled stellar mass) will provide an estimate for the total stellar mass in the galaxy.

However, this is complicated by the fact that when observing in specific filters it is necessary to consider additional effects of cosmological redshift on the wavelength of light that is being observed. Namely, cosmological redshift causes a shift in the frequency of the galaxy's spectrum, which results in a dimming of the flux observed in a fixed filter with respect to the bolometric flux. This effect is accounted for by the K-correction giving:

$$m - M = 5 \log_{10}(D_L) + 25 + K(z) \quad (2.6)$$

where the K-correction depends on knowledge of the shape of the galaxy's spectrum with $K(z) = 2.5(\alpha - 1) \log_{10}(1 + z)$ for a galaxy with a spectral shape given by $\nu^{-\alpha}$ (Hogg et al. 2002). However, here no such analytical correction is necessary as from the best-fit SED model the photometry for a given filter for an object observed at both high redshift, and at its rest-frame ($z = 0$) can be generated. The ratio of these simulated fluxes then gives the K-correction which should be applied to that filter for a given object at its observed redshift:

$$K(z) = -2.5 \log_{10} \frac{\text{flux of model in filter at } z_{\text{best fit}}}{\text{flux of model in filter at } z=0} \quad (2.7)$$

So now the absolute magnitude of the SED model is known, which has been normalised in the stellar templates to a total mass of $1M_\odot$. Returning to equation 2.1, and assuming here flux is proportional to mass, equation 2.1 becomes : $m_1 - m_2 = -2.5 \log_{10}(\frac{M_1}{M_2})$, where M_1 is the total stellar mass of the galaxy and M_2 is

$1M_{\odot}$. Thus,

$$\log_{10}(\text{total stellar mass}) = \frac{\text{the normalised to } 1M_{\odot} \text{ magnitude from stellar templates} - \text{absolute magnitude of the best-fit model}}{2.5} \quad (2.8)$$

Finally, it is important to correct for the fact that the τ star-formation history model stellar templates are normalised to $1M_{\odot}$ based on their final mass so that, depending on the modelled galaxy age, the modelled total stellar masses must be further scaled by a factor of $(1 - \exp - \frac{\text{best-fit model age (in Gyrs)}}{\tau_{\text{best-fit}}})$. Estimates derived in this way provide a maximal estimate of the galaxy stellar-mass as opposed to methods which go on to further account for gas recycling, where mass which was previously locked-up in massive stars which have subsequently undergone a supernovae event is returned to the inter-stellar medium.

For the stellar-mass estimates presented here, the photometric redshifts were determined from the initial SED fitting run and were held fixed during a second fit to determine stellar-mass and star-formation rates.

There is currently much discussion in the literature over the dependence of stellar-mass estimates on the stellar population synthesis models employed during the fitting procedure, and more specifically on the treatment of thermally pulsating asymptotic giant branch (TP-AGB) stars. In particular it has been found that models including higher contributions from the TP-AGB population (Maraston 2005; M05, Charlot & Bruzual 2007, private communication) lead to stellar masses on average ~ 0.15 dex smaller (Pozzetti et al. 2007, Ilbert et al. 2010) than those derived using BC03 templates. However, the models with a strong contribution from the TP-AGB have now been essentially ruled out (Kriek et al. 2010, Zibetti et al. 2012), and it has also been shown that the TP-AGB contribution is only important in the specific age range $\simeq 0.5 - 1.0$ Gyr.

In this work I have therefore chosen to use the Bruzual & Charlot (2003)(BC03) models, and to define the most massive galaxies by the mass threshold $M_{*} > 10^{11} M_{\odot}$, as derived from single-component τ models. The effects of including “double-burst models” in the SED fitting have been explored by Michałowski et al. (2012) and by McLure et al. (2013) (where in order to avoid confusion in following chapters, in this case “double-burst models” are defined as combinations of two bursts of star formation with different ages and dust attenuation, which have no further constraints based on morphology or otherwise). However,

while Michałowski et al. (2012) show that two-component models can produce significantly larger stellar masses than single-component models for extreme star-bursting objects such as sub-millimetre galaxies, McLure et al. (2013) report that the mass difference is relatively small for more evolved $z \simeq 1 - 2$ galaxies ($\langle \Delta M_* \rangle \simeq 0.1$ dex), presumably because an exponentially-decaying star-formation history provides a reasonable description of reality for most massive galaxies at these epochs. Accordingly, for the study presented in this thesis it was decided to adopt the stellar-mass estimates obtained with the BC03 tau-models, in order to most easily facilitate direct comparison with previous studies.

In addition to inconsistencies in the stellar masses derived from various stellar population synthesis models, there is a further added offset in quoted stellar masses introduced by the IMF used in the fitting. To ease comparisons with previous studies, throughout this thesis I convert stellar masses quoted in the literature to those that would be obtained using the BC03 models with a Chabrier IMF using the following conversions: $\log_{10} M_{*,M05} = \log_{10} M_{*,BC03} - 0.15$ (Cimatti et al. 2008); $\log_{10} M_{*,CB07} = \log_{10} M_{*,BC03} - 0.2$ (Salimbeni et al. 2009); $\log_{10} M_{*,Chabrier} = \log_{10} M_{*,Salpeter} - 0.23$ (Cimatti et al. 2008); $\log_{10} M_{*,Chabrier} = \log_{10} M_{*,Kroupa} - 0.04$ (Cimatti et al. 2008).

Finally, in order to provide physically-meaningful and self-consistent fits for both stellar mass and the accompanying star-formation rate and age estimates the set of star-formation histories employed for the stellar-mass estimate generation were limited (Wuyts et al. 2011) to values in the range $0.3 \leq \tau(\text{Gyr}) \leq 5$, and a minimum model age of 50 Myr was imposed in the χ^2 fit of the model SED (Cirasuolo et al. in preparation).

2.2.5 Star-formation rates

Similarly to the stellar-mass estimates, star-formation rates were also determined in a second SED fit at fixed photometric redshift. I adopt the star-formation rate conversion of Kennicutt (1998):

$$SFR_{UV,dust\ corrected}[\text{M}_{\odot}\text{yr}^{-1}] = 1.4 \times 10^{-28} L_{\nu}(\text{ergs s}^{-1} \text{Hz}^{-1}) \quad (2.9)$$

in the approximation of continuous star formation using a Salpeter IMF and where L_{ν} is integrated over the wavelength range $1500 - 2800 \text{\AA}$. The dust corrected L_{ν} was calculated from the best-fit model integrated flux in the observed filter closest

to the middle of the required wavelength range at 2300\AA , shifted by $(1 + z_{\text{phot}})$, and for the best-fit dust model re-computed in the absence of any dust. This star-formation rate is then re-scaled to account for the differences between a Salpeter and Chabrier IMF.

Star-formation rates estimated in this way from a limited region of a galaxy's overall SED, where spectroscopic information is unavailable, are known to carry large uncertainties when compared to estimates obtained from large baseline SED fitting extending well into the far-IR. In order to account for this I additionally estimated star-formation rates from a combination of obscured and un-obscured indicators following Wuyts et al. (2011) who utilise the following prescription derived from Kennicutt (1998):

$$SFR_{UV+IR}[\text{M}_{\odot}\text{yr}^{-1}] = 1.09 \times 10^{-10} (L_{IR} + 3.3L_{2800})/L_{\odot} \quad (2.10)$$

where $L_{2800} = \nu L_{\nu}(2800\text{\AA})$ and L_{IR} is the contribution from radiation from hot young stars re-radiated by dust over the wavelength range $8 - 1000\mu\text{m}$. Obtaining full photometry from $8 - 1000\mu\text{m}$ for a large sample of high-redshift galaxies is unfeasible. However the latest results from Herschel PACS (Poglitsch et al. 2010) which is capable of imaging through the IR emission peak at 70, 100 and $160\mu\text{m}$ have revealed that the total IR luminosity L_{8-1000} can now be reliably derived from the luminosity within a single PACS band (Elbaz et al. 2010). By making use of these previous studies and combining Herschel PACS, IRAC MIPS, near-IR and optical data for SED fitting, Wuyts et al. (2011) produced a table of conversion factors from both PACS 70, 100 and $160\mu\text{m}$ and MIPS $24\mu\text{m}$ to L_{IR} . These new conversions use full SED galaxy templates to extrapolate the total luminosity over the $8 - 1000\mu\text{m}$ range and are an update on previous luminosity-dependent conversions by adopting a simple redshift dependence in agreement with other work by Elbaz et al. (2010) and Nordon et al. (2010). For the objects in my sample which have a match within a 2 arcsec radius aperture in the $24\mu\text{m}$ catalogues produced from SpUDS (PI Dunlop) ($\sim 36 \pm 5\%$) I adopt the conversions from Wuyts et al. (2011) for estimates of L_{IR} . These are used with the non dust-corrected luminosities of the best-fit SED models at 2800\AA and are input into equation 2.10 as a secondary SFR estimate.

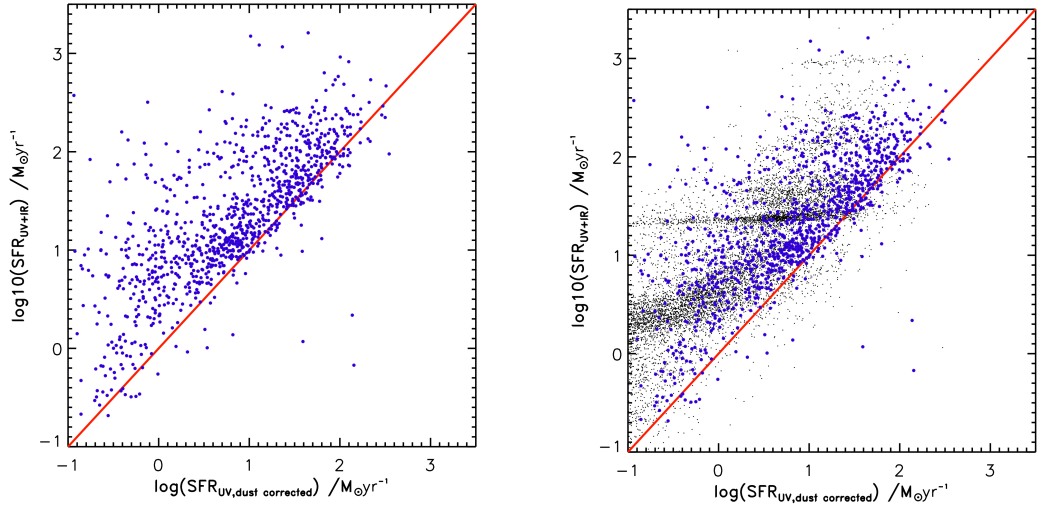


Figure 2.1 Comparison between $SFR_{UV,dust\ corrected}$ and SFR_{UV+IR} (where here the UV has not been dust-corrected). Left panel : All objects with $24\mu m$ counterparts, taken over the full mass range available for $0 < z < 3$ in the UDS to provide a significant sample. Similar to Wuyts et al. (2011) (Fig. 3), for objects with a $24\mu m$ counterpart, I find a reasonable correlation between these different star-formation rate indicators, with a significant amount of scatter in the direction of $SFR_{UV+IR} > SFR_{UV,dust\ corrected}$. As a result, in order to provide conservative estimates of quiescence, throughout this work I adopt the SFR_{UV+IR} where $24\mu m$ counterparts are available, and otherwise use $SFR_{UV,dust\ corrected}$. Right panel: All objects within the full mass range available for $0 < z < 3$ in the UDS. In this panel the objects which have $24\mu m$ counterparts ($\sim 36\%$ for the $M_* > 10^{11} M_\odot$, $1 < z < 3$, sample but $< 10\%$ for the full mass range taken across $0 < z < 3$) are shown in blue, whereas the objects without $24\mu m$ counterparts are given in black, and in these cases I have adopted the SpUDS $24\mu m$ limiting flux to compute an upper limit to the SFR_{UV+IR} . It is clear from the left panel that the scatter in this relation is preferentially in the direction of $SFR_{UV+IR} > SFR_{UV,dust\ corrected}$, whereas assuming the two star-formation rate indicators are comparable, the scatter would be expected to lie in both directions. By comparing the two star-formation rate indicators for the full sample, using the upper limits for SFR_{UV+IR} where necessary, there is an increase in the scatter below the one-to-one relation. However, there is still a dearth of objects whose star-formation rate estimates occupy this region. This is due to the flux limit of the SpUDS $24\mu m$ imaging, as it is too shallow to place meaningful upper estimates on the value of SFR_{UV+IR} .

As expected, comparison between these two estimates for the limited number of objects which have $24\mu\text{m}$ counterparts reveals a reasonable correlation, although with a significant amount of scatter preferentially towards SFR_{UV+IR} giving larger star-formation rates than $SFR_{UV,dust\ corrected}$ (Fig. 2.1). Thus, in order to be conservative when making any comments about quiescence, I adopt the maximum possible star-formation estimate for each object by utilising the SFR_{UV+IR} value for objects with $24\mu\text{m}$ counterparts and the $SFR_{UV,dust\ corrected}$ estimates otherwise. Examination of the $24\mu\text{m}$ SpUDS detection limit revealed that it was too shallow to provide meaningful upper limits on SFR_{UV+IR} estimates as the adoption of the SFR_{UV+IR} estimates derived from this $24\mu\text{m}$ flux limit resulted in $\sim 90\%$ of the objects in my sample being deemed as star-forming using the $sSFR < 10^{-10} \text{ yr}^{-1}$ discriminator.

2.2.6 Final sample selection

From the master catalogue described above I defined my sample as the most massive galaxies with $M_* > 10^{11} M_\odot$ in the redshift range $1 \leq z_{phot} \leq 3$. This gives a total of 215 galaxies identified from the H_{160} mosaic and provides a mass-complete sample where, for my cut at $H_{160} = 24.5$, the mass completeness limit is $M_* < 10^{11} M_\odot$ over the full redshift range of this study.

2.3 Morphologies: 2-D modelling

Previous studies of galaxy morphologies have implemented both parametric and non-parametric techniques for quantifying structure. Whereas parametric methods fit functional forms of the light profiles to data, non-parametric approaches use, e.g., CAS parameters (Conselice 2003) or Gini and M_{20} (Abraham et al. 2003, Lotz et al. 2004) coefficients to measure the relative distribution of flux within a galaxy via concentration and asymmetry etc. This approach is based upon the assertion that, at higher redshifts, galaxies appear to have more disturbed morphologies than local systems (Abraham et al. 2003), thus by allowing more flexibility for objects to deviate from symmetric functional fits the structure of high-redshift systems can be better studied. However, these non-parametric fits are sensitive to S/N such that they cannot be robustly used to extrapolate out to the fainter wings of objects, and as a result under-

estimate the overall flux and effective radii of high-redshift galaxies. As the robust determination of galaxy sizes and the modelling of multiple morphological components is the main aim of this work, I adopt a parametric light-profile fitting technique, and in fact later show that even at the level of the latest HST CANDELS data, the morphological properties of my high-redshift sample are extremely well represented by these symmetric light profiles.

I have employed the GALFIT (Peng et al. 2002) morphology fitting code to determine the morphological properties for all 215 objects in my sample. GALFIT is a two-dimensional fitting routine that can be used to model the surface-brightness profile of an observed galaxy with pre-defined functions such as a Sérsic light profile (de Vaucouleurs 1948, Sérsic 1968).

$$\Sigma(r) = \Sigma_e \exp[-\kappa((\frac{r}{r_e})^{\frac{1}{n}} - 1)] \quad (2.11)$$

where Σ_e is the surface brightness at the effective radius r_e , n (the Sérsic index) is a measure of the concentration of the light profile (where $n = 1$ describes a disk-dominated exponential profile and $n = 4$ describes a spheroidal de Vaucouleurs profile), and κ is a correction factor coupled to n such that half of the total flux of the object lies with r_e (obtained by using $\int_0^\kappa e^{-t} t^{2n-1} dt = \gamma(2n, \kappa)$, substituting $2\gamma(2n, \kappa) = \Gamma(2n)$ and solving numerically).

By re-fitting simulated galaxies, Häussler et al. (2007) present a thorough investigation of the relative biases and uncertainties associated with the adoption of the main light-profile fitting codes available: GALFIT (used with the GALAPAGOS wrap-around (Barden et al. 2012)) and GIM2D (Simard 1998). In brief GALFIT uses a set of initial parameters, convolves modelled light profiles with the point spread function (PSF) of the observed image and employs a Levenberg-Marquardt down-hill gradient algorithm for χ^2 fitting, whereas GIM2D uses a similar approach with a Metropolis algorithm for χ^2 fitting. This difference makes GIM2D more robust to local χ^2 minima but results in a much slower fitting process. Häussler et al. (2007) find that any advantages provided by the robustness of the GIM2D χ^2 minimisation are not significant over the GALFIT procedure and, moreover, that for faint objects GIM2D returns results biased towards higher Sérsic indices. As a result these authors conclude that GALFIT provides a better un-biased estimate of the simulated galaxies' morphological parameters.

However, it is well established that the robustness of the GALFIT output depends

heavily on the input files, such as the background-subtracted image, the σ map and the PSF. Häussler et al. (2007) also provide a discussion of the issues associated with background subtraction and report on the robustness of using background estimates based on mean values from sky annuli over the values determined internally by GALFIT or SEXTRACTOR.

As a result I have conducted rigorous tests of my fitting procedure to ensure that the morphological parameters that I have determined using the GALFIT code are not biased by the realistic uncertainties in these inputs. Specifically, in the next section I summarize and illustrate the results of thorough tests of the robustness of the derived morphological parameters with respect to the accuracy of the adopted PSF, and the implementation of various background-level determinations. These tests were carried out exclusively on the H_{160} mosaic, the reddest band accessible to HST, which thus best represents the majority of the assembled stellar mass in my objects at useful resolution.

I adopted a fixed set-up for the GALFIT fitting procedure. I first ran SEXTRACTOR on the H_{160} mosaic to determine initial estimates for the centroid x,y pixel positions, total magnitude, axis ratio and effective radius of each object, where the total magnitude is given by MAG_AUTO and the effective radius is taken as FLUX_RADIUS with the fraction of total flux within this radius set as 50%. SEXTRACTOR was also used to produce a segmentation map of the image.

In addition to the image and segmentation map, GALFIT also requires an input σ map in order to conduct the χ^2 fitting. To first-order this σ map can be given by the rms map generated for the CANDELS mosaic (see Koekemoer et al. 2011). This rms map contains noise from the sky, readnoise and dark current contributions from all the input exposures and is used as an initial input, but is adapted later in the procedure to include the Poisson noise contribution from the object itself, which proved to be a non-trivial contribution for the bright objects in my sample.

From the image, segmentation map and rms map I then generated 6×6 arcsec stamps for each object centred on the x,y pixel positions from SEXTRACTOR. These are the actual input files read into GALFIT and the code is allowed to use the full 6×6 arcsec area in the fit, with the exception of any pixels associated with companion objects in the image stamps (taken from the segmentation map), which are masked out by the bad-pixel map.

The method outlined here provides: a σ map, a bad-pixel mask and the best-

guess initial model parameters, which are read directly into GALFIT. This set-up procedure was implemented in a GALFIT wrap-around script and is consistent for all following tests of the PSF and background determinations used.

2.4 Single Sérsic models

As mentioned above, the two key elements which can significantly affect the best-fitting model parameters derived by GALFIT are, first, the accuracy of the adopted PSF and, second, the method used to establish the sky background. I have investigated both these issues, and their impact on derived parameter values and errors. For simplicity, the discussion of these issues is here restricted to the single Sérsic models.

2.4.1 PSF dependence

The precision of the PSF used in the fitting procedure, especially within a radius of $\simeq 0.6$ arcsec (corresponding to a physical scale of $\simeq 5$ kpc at the redshifts of interest here), is crucial for the accurate determination of the scale-lengths of the galaxies in my sample, as many of them transpire to have effective radii of comparable angular size. Previous morphological studies of massive galaxies at $z > 1$ have adopted both empirical and modelled PSFs in their fitting procedures, with modelled HST PSFs being generally determined using the Tiny Tim code (Krist 1995). I have explored the impact of using both empirical and Tiny Tim PSFs on the resulting morphological fits. Examination of the WFC3/IR H_{160} image revealed that the PSF did not vary across the field, thus a single PSF is sufficient to model all galaxies. As a consequence, the empirical PSF was constructed from a median stack of seven bright (but unsaturated) stars taken from across the CANDELS-UDS field, after centroiding and normalising each stellar image.

I show in Fig. 2.2 radial profile plots of the two PSFs tested here, the empirical stellar stack and the Tiny Tim model, along with the residuals between them and a magnified plot between 0.5 and 0.8 arcsec, the range encompassing a physical size comparable to the fitted sizes of the objects (which more clearly demonstrates the difference between the PSFs).

In the top-left plot I show the difference between the empirical stacked PSF and the Tiny Tim model. The other plots are included to emphasize the uniformity of the individual stars that were included in the stack as they compare the stack with three out of the seven stars that comprise the stack. This test also confirms that my empirical stacked PSF does an excellent job of reproducing the profile of individual stars in the CANDELS H_{160} image, providing reassurance that it has not been significantly broadened by any offsets in centroiding or otherwise damaged by the stacking process on the angular scales of interest.

This figure clearly highlights that the Tiny Tim model under-predicts the flux in the PSF at this critical radius. As a consequence I found that adoption of the Tiny Tim PSF returns fitted galaxy sizes that are on average systematically 5 – 10% larger than those determined using the empirical stacked PSF.

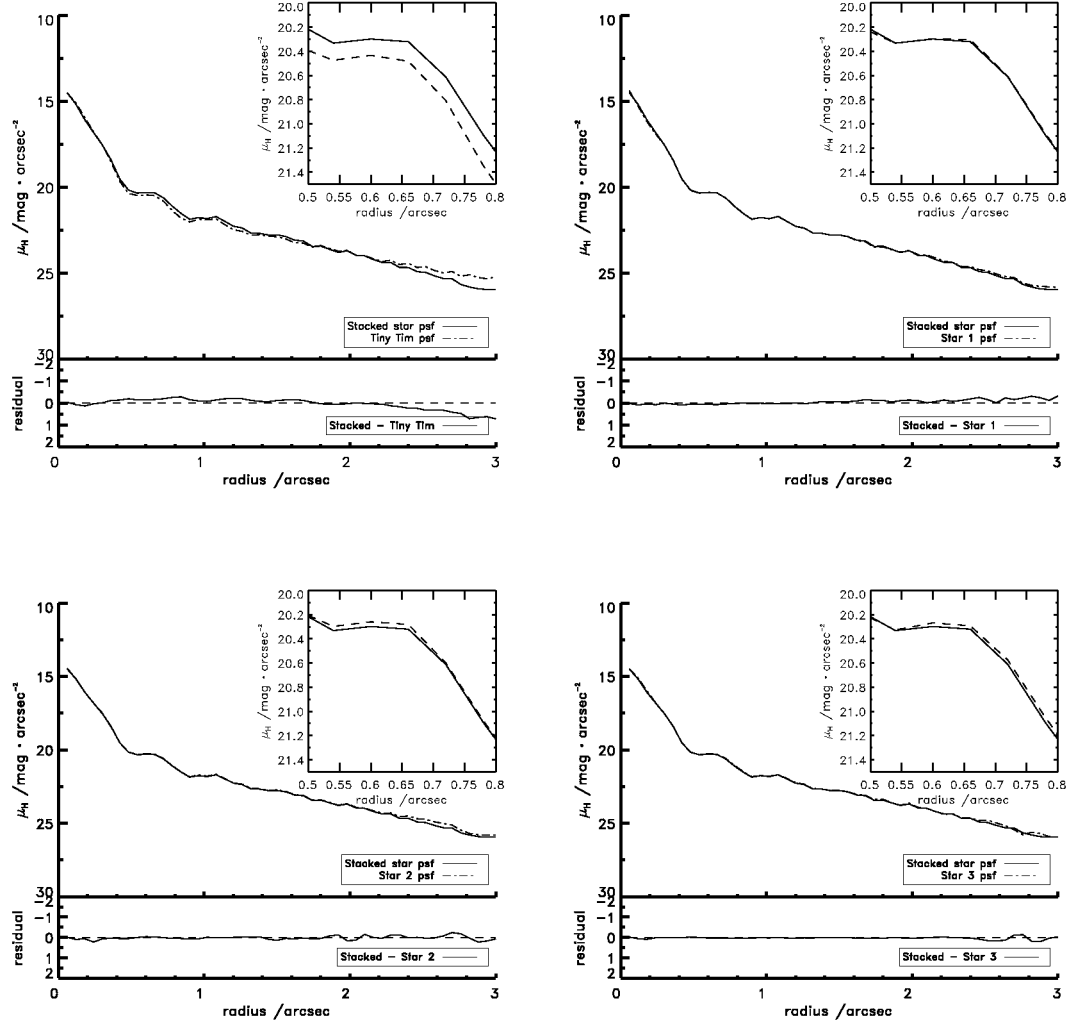


Figure 2.2 *Comparison of the radial surface-brightness profiles of alternative H_{160} PSFs. The top-left panel compares the empirical PSF I obtained from stacking stars taken from the real H_{160} CANDELS mosaic (solid-line) with the PSF produced by the Tiny Tim model (dashed line) (with the residuals given below). The inset shows a magnified view of the crucial region around $\simeq 6$ arcsec, which corresponds to a physical size of $\simeq 5$ kpc at $1 < z < 3$, comparable to the typical effective radii of the galaxies in my sample (the surface-brightness scale in the inset has been expanded to demonstrate more clearly the level of the offset between the Tiny Tim model and the empirical stack at these important scales). The remaining three panels simply show how well the empirical PSF matches the profiles of three of the seven individual stars which went into it, demonstrating that my empirical PSF has not been significantly broadened or otherwise damaged by the stacking process at any angular scales of interest.*

In order to ascertain the reason for this discrepancy between the modelled and empirical PSFs I constructed a difference image of the empirical stack - Tiny Tim PSF, shown in Fig. 2.3. The offsets at the very centre of the image are due to centroiding issues but it is clear that further out, beyond 0.5 arcsec, there is a distinct halo in the empirical PSF which is not present in the Tiny Tim model. This unequivocally shows that the empirical stacked PSF contains a much stronger contribution from the Airy rings, which is not properly modelled by the Tiny Tim PSF. In addition to this, the Tiny Tim model does not accurately reproduce the diffraction spikes.

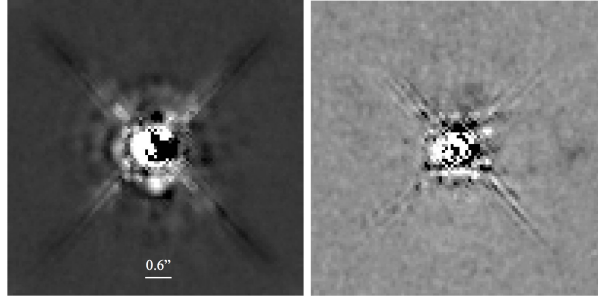


Figure 2.3 *Left: Difference image of the stacked empirical PSF – the Tiny Tim model. The image is 6×6 arcsec with a pixel scale of 0.06 arcsec (an illustrative 0.6 arcsec line has been added for clarity). The grey scale shows negative pixels as darker and positive pixels as whiter. The discrepancy between the two PSFs at the centre is due to minor mismatching during centroiding, but a real positive halo can be clearly seen at a radius of 0.5 arcsec and greater. This is due to the empirical PSF including a stronger Airy disk pattern than is modelled by the Tiny Tim PSF, and perhaps also containing additional scattered light. Inconsistencies in the contribution from diffraction spikes are also visible in the image. Right: A difference image of the stacked PSF – one of the component star PSFs is given for comparison, where the images have been constructed using the same cut in the brightness level.*

As a result of these tests, I have adopted the empirical stacked PSF for all the model fitting and testing undertaken in this work. Consequently I have generally derived fitted sizes which are systematically a factor of 5 – 10% smaller than those which would have been determined using a Tiny Tim PSF.

2.4.2 Background dependence

The HST mosaics provided in the CANDELS data release have already been background subtracted, and so initially I attempted to use GALFIT on image stamps extracted from the H_{160} mosaic without additional background corrections. However, upon inspection of the radial-profile plots of the fits, it became clear that additional object-by-object background corrections were required. Moreover, the impact of background determination on the best-fitting values of, and degeneracies between, the fitted values of Sérsic index and effective radius is non-trivial (Guo et al. 2009), and merits careful exploration.

To properly explore this issue, I constructed a grid of GALFIT runs sampling the full parameter space of Sérsic index, effective radius, and plausible background values.

This grid contains a set of additional background values to be subtracted from the image. This is done by determining two initial estimates of the additional background light. The first is done by masking out an aperture of radius 1 arcsec around the object centroid position and calculating the median background value in the remaining 6×6 arcsec image stamp. This method provides a reliable estimate of the median background light in most cases, with the exception of those for the largest objects in my sample. These largest objects are particularly susceptible to biased size estimates as careful consideration must be given to their extended wings. For these cases it is clear that the masking of a 1 arcsec radius aperture may not be sufficient to mask out the full extent of the wings, therefore for every object I adopt a second median background estimator. This secondary method expands the image stamp of each object to 12×12 arcsec, generates an annular aperture centred on each source with an inner radius of 3 arcsec and an outer radius of 5 arcsec, and measures the median background light within this aperture. By adopting this second technique, although my median background estimate is conducted further from the source, it ensures I have not biased my median background estimate too high by failing to account properly for the extended wings of the largest objects.

For each object I therefore have two estimates of the local median background, where comparison of these estimates gives me an indication of the error associated with determining median background estimates from the CANDELS images. I found that the offset between these two estimates for each object is well

described by a Gaussian distribution centred on zero with a $2 \times \text{FWHM}$ value of 0.001 electrons/s (for comparison the typical sky level has a mean value of 2.12×10^{-4} electrons/s with a standard deviation of 3.33×10^{-4}), as shown in Fig. 2.4. I subsequently used this $2 \times \text{FWHM}$ as the error associated with any median background estimate, where the factor of two was chosen to minimise the parameter space searched while ensuring that all possible best-fit backgrounds for each object were still included in the parameter space.

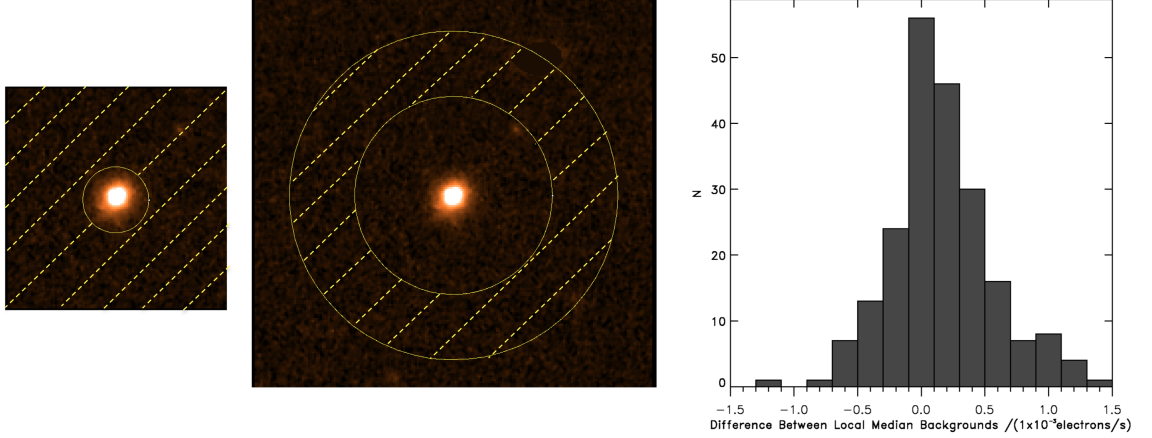


Figure 2.4 *Comparison of the two different median background estimations discussed in the text. The left panel is an illustration of a 6×6 arcsec image stamp with the central 1 arcsec around the object given by the yellow aperture. The filled region represents the area included in the background estimation. The middle panel is an illustration of the 12×12 arcsec image stamp of the same object, where the background is now estimated within an aperture centred on the source with an inner radius of 3 arcsec and an outer radius of 5 arcsec. The right panel shows the distribution of the difference in the backgrounds estimated with the two techniques for every object in my sample. I use $2 \times \text{FWHM}$ of this distribution as the error associated with a given background estimate and adopt this as the range for the full grid search.*

From my inspection of the individual sources I became aware that sources can be equally subject to background over-subtraction from the first order analysis performed on the images, as well as under-subtraction. Thus, for each object, I generated a grid of additional background subtraction values to be used in the fitting procedure, which was taken to be in the range -0.001 to $+0.001$ electrons/s (where -0.001 is the upper limit of background light added back into the image,

accounting for original over-subtraction, and +0.001 is the upper limit to the amount of background light additionally subtracted off the images, accounting for original under-subtraction).

For each of the points in additional background subtraction space I then constructed a loop over Sérsic index and effective radius parameters allowed in the fit. I ran an initial fit on every object using the median additional background subtraction value determined above using a 1 arcsec masking aperture. The Sérsic index and effective radius parameters returned for these fits were used as the centroid points for the Sérsic index and effective radius loops. For Sérsic index I constructed a loop of steps of 0.1 in size, and for effective radius I chose steps of size 0.025 arcsec. These step sizes were determined to incorporate the full range of generally-accepted realistic Sérsic index and effective radius values (i.e. 0.1–10 in Sérsic index and 0.025 – 2 arcsec in angular effective radius).

For each point in the effective radius and Sérsic index grid I locked these values during the GALFIT fit and stepped through a range of different additional background subtraction values to find the best-fit background subtraction value at that grid point, using the χ^2 values of each background fit.

Such an analysis is computationally expensive, but allowed me to explicitly examine the impact of uncertainties in the background on the GALFIT results. This problem is, of course, well known, and previous studies have attempted similar tests using different approaches (e.g. Häussler et al. 2007, van Dokkum et al. 2010). However, by marginalising over the additional background subtraction value which gives the best χ^2 fit for each combination of Sérsic index and effective radius I was able to properly expose the impact of background determination by constructing the χ^2 surface in the Sérsic-index/effective-radius plane for each object.

In Fig. 2.5 I show the resulting $\Delta\chi^2$ contours in the $n-R_e$ plane for three examples of galaxies in my sample. The upper panels show the contours which result from adopting the median background from the 6×6 arcsec image stamp centred on the object in question. The lower panels show the corresponding contours from fitting to the same three galaxies marginalising over the varying background from my full background-grid search. From these examples it can be seen that allowing the background to vary during the fitting process can significantly open up the contours for some galaxies, increasing the errors on the fitted parameters to arguably more realistic values. Moreover, the third example (far right) shows

a clear case where using the 6×6 arcsec median background can clip the wings of the galaxy and lead to an under-estimate of effective radius. Note that the contours from the full background-grid fitting do not in fact include the best-fit solution achieved with the fixed median background, and vice versa. This is a potential for bias in the fits for the largest galaxies in my sample. However, as discussed further below, it transpires that the number of such objects (i.e. objects whose scale-length is substantially boosted by the full background-grid search) within my sample is relatively small.

However, it should also be noted that, even with allowance for a variable background, there are a considerable number of objects within my sample for which the derived $1\text{-}\sigma$ error-bars for the Sérsic index and effective radius parameters fell below the size of the grid steps used in the full parameter search (0.025 in arcsec, 0.1 in Sérsic index). Such accuracy testifies to the power of the deep, high-resolution imaging provided by WFC3/IR for these (relatively) bright objects. However, it does mean that it is difficult to establish a robust error for the parameter values in these tightly-constrained fits; to be conservative, for such objects I have simply adopted the smallest grid steps as the $1\text{-}\sigma$ errors on R_e and n .

This analysis has thus enabled me to produce more realistic errors on the Sérsic index and effective radius parameters for all the objects in my sample than would be inferred from the errors provided directly by GALFIT. The error-bars produced by GALFIT are purely statistical and are determined from the covariance matrix used in the fitting. It is well known that this often results in unrealistically-small uncertainties in the derived galaxy parameters. This issue is well documented in Häussler et al. (2007), where they used GEMS data (Rix et al. 2004) to test how well GALFIT can recover the input parameters of simulated $n = 1$ (disk) and $n = 4$ (bulge) galaxies. They found that GALFIT returns errors which are significantly smaller than the offset between the fitted and simulated input parameters, and so concluded that the dominant contribution to the real errors in the fitting procedure arises not from statistical shot noise or read noise (as is calculated by GALFIT), but from contamination of the fitting region by companion objects, underlying sub-structure in the sky, correlated pixels or potentially profile mismatching.

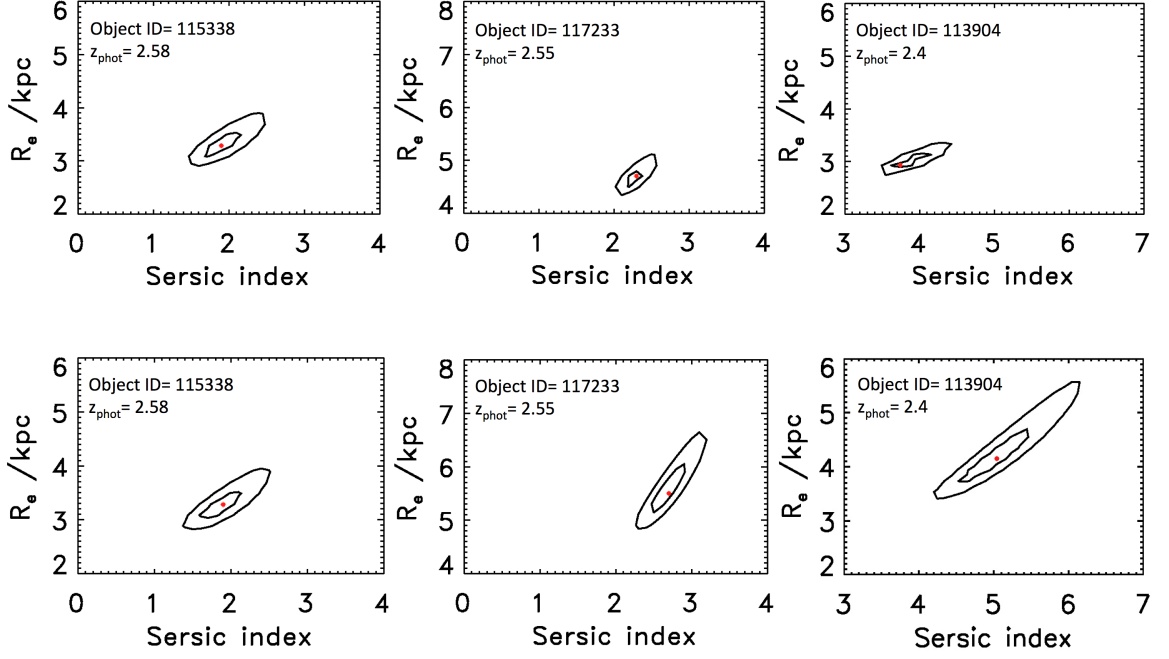


Figure 2.5 *An illustration of the errors in, and degeneracies between, fitted effective radius R_e and Sérsic index n , also showing the effect of allowing the background to vary during the fitting process. Results are shown for three example objects, with contours plotted in the $n - R_e$ plane at $\Delta\chi^2 = 4$ ($\equiv 2\text{-}\sigma$ for 1 degree of freedom) and $\Delta\chi^2 = 9$ ($\equiv 3\text{-}\sigma$ for 1 degree of freedom) above the the minimum χ^2 value achieved by the best-fitting model (marginalising over all other fitted parameters). The location of the best-fitting model is indicated by the red dot in each case. The upper panels show the contours which result from adopting a single fixed background for each source, in this case the median background from the 6×6 arcsec image stamp centred on the object in question, but excluding the central region of radius 1 arcsec (in addition to excluding pixels masked out via the segmentation map). The lower panels show the corresponding contours which result from fitting to the same three galaxies, but in addition marginalising over a varying background (from the full background-grid search described in the text). As can be seen from these examples, allowing the background to vary during the fitting process can significantly open up the contours for some galaxies, increasing the errors on the fitted parameters to arguably more realistic values. Moreover, from inspection of the third example (far right) it is clear that, for some of the largest objects in my sample, use of the 6×6 arcsec median background can clip the wings of the galaxy and lead to an under-estimate of effective radius (note that the contours from the full background grid fitting do not in fact include the best-fitting solution achieved with the fixed median background, and vice versa).*

From my full background grid search I find that the distribution of errors is centred on $\simeq 5\%$ for Sérsic index and $\simeq 10\%$ for effective radius. This can be compared with the errors returned by GALFIT (which are often simply adopted in the literature) where I find that, for the deep, high-quality imaging used here, the error distributions are centred on $\simeq 2\%$ for Sérsic index and $\simeq 1\%$ for effective radius.

To complete my analysis of the impact of background determination on derived morphological parameters I have considered not only the best-fitting background from the grid and the original 6×6 median background, but also an alternative median background determination involving exclusion of all pixels within a larger central aperture (i.e. the median of those pixels lying within an annulus between 3 and 5 arcsec radius), and finally also zero background correction (i.e. just adopting the CANDELS mosaics as supplied, as I initially attempted).

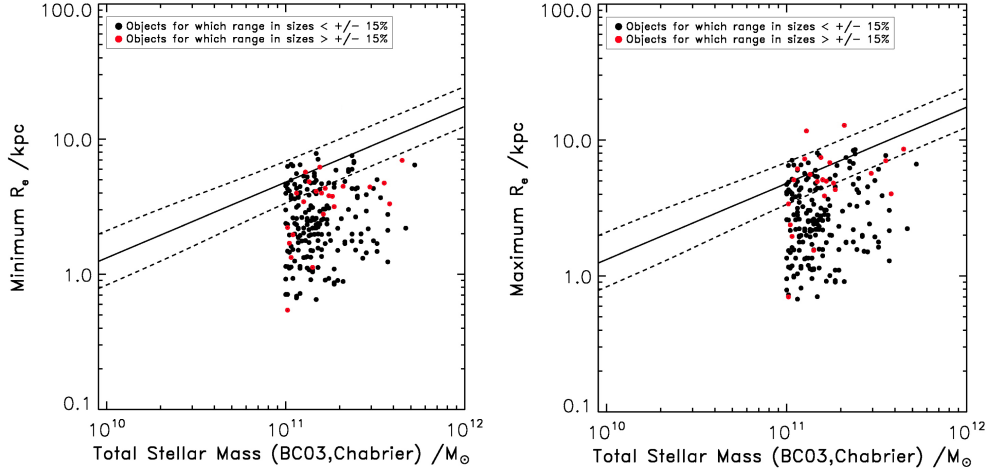


Figure 2.6 *The size–stellar-mass ($R_e - M_*$, using semi-major axis R_e values) relation displayed by my $M_* > 10^{11} M_\odot$, $1 < z < 3$ galaxy sample utilising the minimum (left-hand panel) and maximum (right-hand panel) derived values of scale-length, R_e , as determined utilising the full range of background estimators. The objects marked in red ($\simeq 15\%$ of the sample) are those for which the maximum value of R_e is $> 15\%$ larger than the minimum, although it should be noted that the adopted range of plausible values of R_e has here been chosen to be unrealistically pessimistic. Also plotted (solid line) is the local relation for early-type galaxies (ETGs) from Shen et al (2003), with its $1\text{-}\sigma$ scatter indicated by the dashed lines. Despite my efforts to here exaggerate the uncertainty in R_e , it is clear that the size-mass relation for this sample as a whole, as derived from the high-quality CANDELS WFC3/IR imaging, is remarkably robust.*

All four of these background values typically lie within the range searched within the background grid, but it is nevertheless instructive to consider these four specific alternatives because they represent choices frequently adopted in the literature.

Since my aim was to establish how robust my derived morphological parameters are to such choices, I used each of these four background estimates to establish a minimum and maximum scale-length that could plausibly be derived for each object. The resulting extremes are almost certainly pessimistically large representations of the uncertainty in scale-length, but nevertheless, as I show in Fig. 2.6, the impact on the typical sizes of the galaxies in my sample is still reassuringly small. Fig. 2.6 shows the two alternative versions of the size-mass relation for the galaxies in my sample which result from adopting the minimum (left-hand panel) or maximum (right-hand panel) scale-lengths as explained above. Those objects where the maximum value of R_e is $> 15\%$ larger than the minimum value have been highlighted in red, but it is clear that such objects are in a small minority ($< 15\%$), and the overall impact on the size-mass distribution exhibited by the sample as a whole can be seen to be small.

In Fig. 2.7 I provide an additional representation of the robustness of my scale-length measurements, and also show that the determination of Sérsic index is extremely reliable, little affected by the alternative background determinations, except for the very small number of objects with unusually large values of n .

In conclusion, therefore, my full background-grid search has enabled me to place realistic errors on the values of the derived parameter values such as R_e and n , but has also shown that, *for the quality of data utilised here*, my results for the sample as a whole are reassuringly robust to sensible alternative choices of the background level for each object.

I stress the point that the problems of systematic bias I have explored here could be much more serious for alternative datasets, especially for ground-based observations with broader PSFs and higher backgrounds (or alternatively when pushing HST data closer to the detection limit).

Given the results presented in Figs 2.6 and 2.7, I did not invoke the full background search again for the multiple component modelling described in Chapters 3 and 4. In Chapter 3, for those objects which yielded robust values of R_e in the single Sérsic fitting described in this section, I have continued to simply adopt the 6×6 arcsec (excluding the central aperture of 1 arcsec radius)

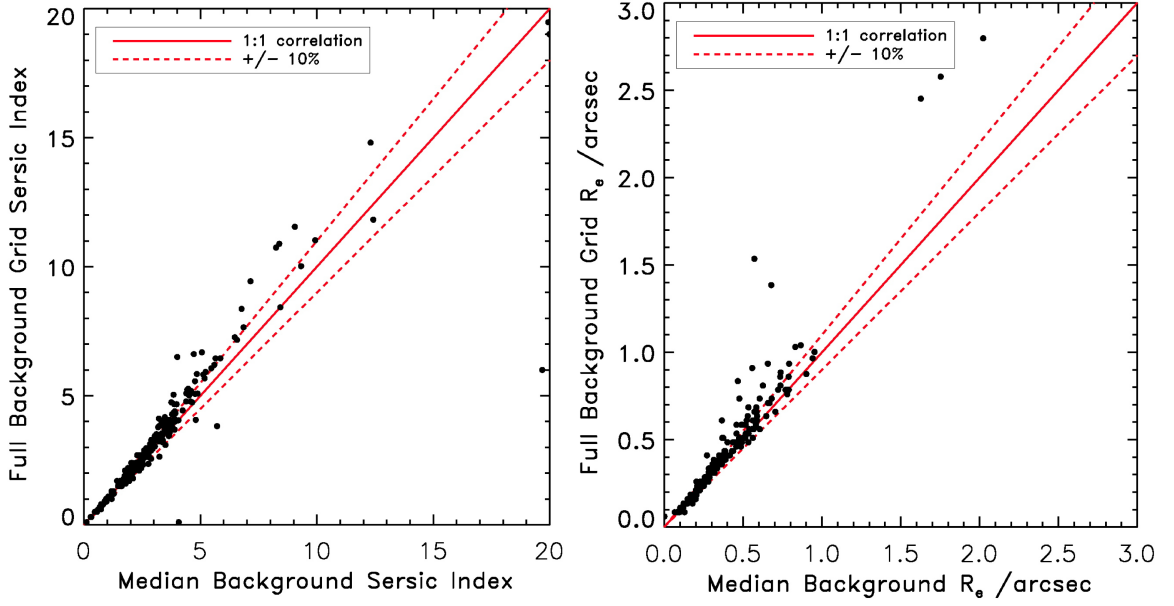


Figure 2.7 *A comparison of the Sérsic indices and effective radii R_e of the galaxies in my sample as derived using the background determined from the median value within a 6×6 arcsec square image stamp (excluding pixels within 1 arcsec of the object centroid), and as obtained allowing the background level to float as part of the fitting process. For $\simeq 90\%$ of the objects in the sample the results are in excellent agreement; the full background-grid search yields significantly larger values of Sérsic index and R_e for $\simeq 5\%$ of the galaxies in my sample.*

median background determination. For the subset of $\simeq 15\%$ of objects whose sizes varied by more than 15% (i.e. those marked in red in Fig. 2.6) I found that the median background as determined in the 3 – 5 arcsec annulus returned a size centred close to the middle of the derived range in R_e , and so adopted this larger annular median as the appropriate background level for this subset of (generally larger) objects hereafter. I adopted the median background as determined in the 3 – 5 arcsec annulus for all objects in the COSMOS field in Chapter 4.

2.5 Conclusions

I now use my modelling results to explore the size-mass ($R_e - M_*$) relation for massive galaxies in the redshift range $1 < z < 3$, considering the results from my full background grid search technique.

The best-fit results from my single-Sérsic analysis detailed above are shown in Fig. 2.8, over-plotted with the local relation from Shen et al. (2003). The galaxy sizes determined by Shen et al. were determined by fitting 1-D surface-brightness profiles within circular apertures, therefore I have converted their results to reflect estimated semi-major axis sizes by dividing the circularised Shen et al. sizes by the square root of the median axis ratio (b/a) for the $1 \times 10^{11} M_{\odot} < M_{*} < 1 \times 10^{12} M_{\odot}$ SDSS sample. This median axis ratio value was taken to be 0.75, following the results from Holden et al. (2012). Alongside my single-Sérsic analysis in Fig. 2.8 is a compilation of results from some of the previous literature at $1 < z < 3$. Unsurprisingly, previous studies have adopted a variety of different techniques for stellar-mass determinations and morphological modelling. However, the results plotted in the left-hand panel of Fig. 2.8 have been adapted to provide the fairest comparison with my results by ensuring that all stellar-mass estimates have been converted to those that would have been determined using a Chabrier IMF with a Bruzual & Charlot (2003) stellar population synthesis model. Nevertheless, the comparison remains imperfect both because the literature results are taken from imaging at a range of different rest-frame wavelengths, and because they comprise a mixture of both circularised and semi-major axis effective radii (although, as the literature results come predominantly from studies of early-type galaxies, the correction from circularised to semi-major axis values is generally small). An additional complication arises from the fact that the studies in the literature have utilised a variety of different selection criteria, with most previous studies deliberately biased towards passive and/or early-type galaxies. By contrast my own sample is based on a relatively straightforward mass limit; while this inevitably limits the dynamic range of my study, it can be seen from Fig. 2.8 that this work represents a significant contribution towards populating the high-mass regime of the size-mass plane at these redshifts.

Armed with my modelling results for this first substantial, complete, high-mass-limited sample, I find that the majority ($68 \pm 7\%$) of these galaxies have effective radii which place them well below the local relation and its $1\text{-}\sigma$ scatter (where in this high-mass regime the local early and late-type relations are essentially the same). However, there is also a significant subset of $32 \pm 4\%$ of my objects which, within the error-bars, are consistent with the sizes of similarly-massive local galaxies. Within the limited redshift range spanned by my study, I see no dramatic trend in these statistics with redshift; splitting the sample at $z = 2$, in the redshift range $1 < z < 2$ I find $70 \pm 10\%$ of objects lie below the local relation,

with $30 \pm 5\%$ essentially on it, while at $2 < z < 3$ the corresponding figures are $62 \pm 11\%$ and $38 \pm 8\%$ respectively.

One consequence of the majority of the galaxies lying significantly below the local relation is that the median size of these most massive galaxies at $1 < z < 3$ is a factor 2.3 ± 0.1 times smaller (2.6 ± 0.2 kpc) than comparably-massive local galaxies. Again I see no significant redshift trend in this global statistic within my limited redshift range. There is potentially a gradual trend to smaller sizes with increasing redshift, although this is within the uncertainties; splitting my sample below and above $z = 2$, the median size becomes 2.7 ± 0.3 kpc and 2.5 ± 0.3 kpc respectively, corresponding to 2.2 ± 0.2 and 2.3 ± 0.2 times smaller than the local relation.

These figures are somewhat ($\simeq 20\%$) smaller than the results reported for a comparable mass-selected sample of galaxies at comparable redshifts by van Dokkum et al. (2010) ($R_e \simeq 4 \pm 0.3$ at $z \simeq 1.6$, $R_e \simeq 3 \pm 0.3$ at $z \simeq 2.0$), but their results were based on stacks of ground-based images taken in 1.1 arcsec seeing, and are thus superseded by the results presented here.

However, these basic statistics conceal a number of potentially important details. First, the scatter in size is large, spanning $\simeq 1$ dex (see Fig. 2.8) and, due to my relatively small errors on R_e ($< 10\%$; e.g. Fig. 2.5) and my exploration of systematic effects (e.g. Fig. 2.6), I can say with confidence that this scatter is real. My analysis reveals that massive galaxies display half-light radii which range from $R_e \simeq 8$ kpc, fully consistent with comparably massive local galaxies, to $R_e \simeq 1$ kpc, consistent with the very small sizes previously reported for the most extreme examples of compact galaxies at these redshifts (e.g. Kriek et al. 2009).

A full discussion of the scientific implications of these results is presented in Chapter 3 where these first results from my technical analysis are coupled with a more detailed morphological bulge-disk decomposition of the CANDELS-UDS sample and the observed trends are placed in the context of current galaxy evolution paradigms.

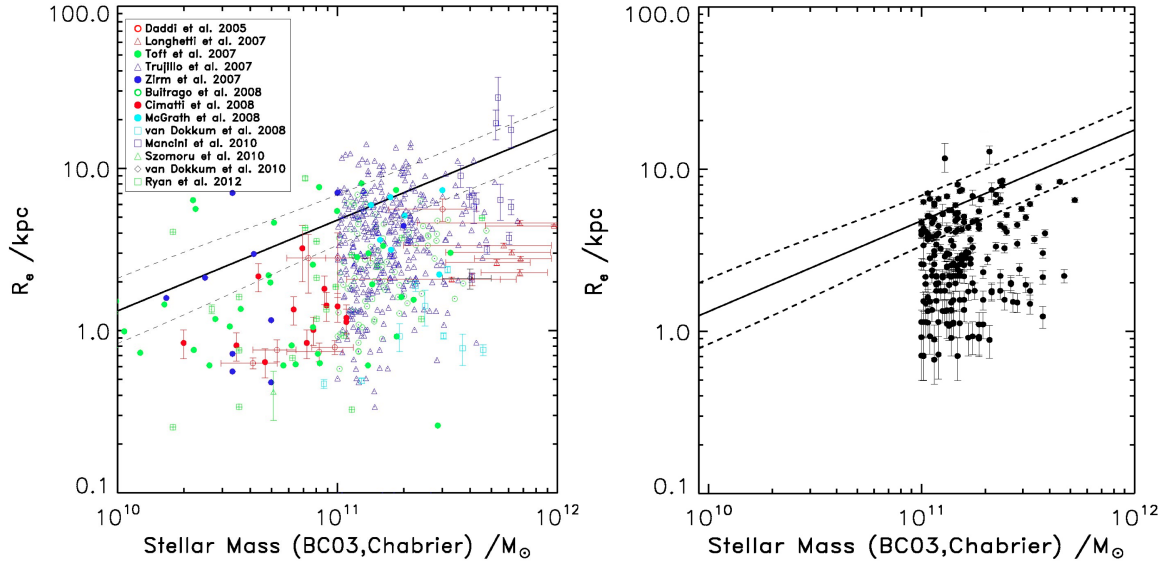


Figure 2.8 Various determinations of galaxy-size versus stellar mass at $1 < z < 3$ from the literature are shown in the left-hand panel, for comparison with my new results for $M_* > 10^{11} M_\odot$ galaxies over the same redshift range as shown in the right-hand panel. In order to facilitate comparison of the semi-major axis scale-lengths determined here with an appropriate low-redshift baseline I have plotted a solid line on both panels to indicate the local early-type galaxy relation from Shen et al. (2003) (with the scatter in this relation indicated by the dashed lines). Because the galaxy sizes determined by Shen et al. were determined by fitting 1-D surface-brightness profiles within circular apertures, I have converted their results to reflect estimated semi-major axis sizes by dividing the circularised Shen et al. sizes by the square root of the median axis ratio (b/a) for the $1 \times 10^{11} M_\odot < M_* < 1 \times 10^{12} M_\odot$ SDSS sample. This median axis ratio value was taken to be 0.75, following the results from Holden et al. (2012). The results from the literature shown in the left-hand panel have all been converted to the masses that would have been derived using the Bruzual & Charlot (2003) models with a Chabrier IMF (see text for details). Unfortunately the scale-lengths plotted in the left-hand panel contain a mix of both circularised and semi-major axis values, but since they come mainly from studies of early-type galaxies the correction from circularised back to semi-major axis values is generally small. My own points shown in the right-hand panel are all based on Chabrier BC03 masses, and semi-major axis effective radii derived from my single-Sérsic modelling of the H_{160} images. This figure serves to demonstrate the extent to which my study has advanced knowledge of the size-mass relation for galaxies in this crucial redshift range in this high-mass regime. It can be seen that, while the majority of the objects in my sample lie below the local relation, a significant subset ($32 \pm 4\%$) are consistent with it within the plotted $1\text{-}\sigma$ errors.

Chapter 3

The Evolution of Galaxy Morphologies

3.1 Introduction

The morphological properties of galaxies provide us with some of their fundamental characteristics, such as size and shape. As a result, detailed morphological studies of galaxies have been conducted since the very birth of extragalactic astrophysics with Slipher and Hubble in the 1920's. However, in spite of this, the underlying physical processes responsible for the formation and subsequent evolution of these morphological properties remains to be fully understood.

Since the first extragalactic classification system presented by Hubble in 1926, galaxies have preferentially been separated into at least two broad classes: bulge-dominated (e.g. elliptical) and disk-dominated (e.g. spiral) systems. This segregation was originally based on the visual distinction between galaxies which had visible disk or spiral-arm structures and those which were dominated by a central spheroidal component. Nevertheless, as the field of extragalactic astronomy has developed, more advanced studies have supported the basis for this distinction by revealing further differences between both the stellar populations in terms of ages, colours, metallicities and star-formation rates, and the dynamics of these two populations. It has been observed that bulge-dominated galaxies generally have older, redder, more passive stellar populations which are dynamically pressure supported, in contrast to disks which have bluer

colours with evidence of on-going star formation and are rotationally supported.

In reality, as imaging studies have increased in resolution and depth they have revealed a more complicated scenario in the local Universe with disk-dominated galaxies often possessing additional structure such as bars, and centrally more disk than bulge-like cores, classified as pseudo-bulges (Kormendy & Kennicutt 2004), which are proposed to originate through secular processes. In addition to this, the pioneering local population morphological studies conducted using SDSS data, while having revealed a strong colour bimodality comprising a prominent red-sequence of bulge-dominated galaxies and blue-cloud of disk-dominated galaxies (Baldry et al. 2004, Driver et al. 2006, Drory & Fisher 2007) consistent with the merger driven hierarchical evolution paradigm, have in more recent years also led to the discovery of a more puzzling population of blue bulges and red disks (Bamford et al. 2009, Masters et al. 2010). These blue bulges and red disks appear to be at odds with the idea of major mergers transforming morphologies from disk to bulge-dominated systems while simultaneously quenching star formation.

In fact such detailed morphological studies are now able to push further back in cosmic time, into the key cosmic epoch at $1 < z < 3$ where the star-formation rate density of the Universe peaks. These studies have found evidence that, while the Hubble sequence is observed to already be in place at these high redshifts, a larger fraction of galaxies are disk-dominated or composite systems (Buitrago et al. 2011, van der Wel et al. 2011, McLure et al. 2013) and there is an increase in the fraction of visually disturbed morphologies (Mortlock et al. 2013). In addition, disk structures are also observed to be “clumpier” (Mozena et al. 2013, Wuyts et al. 2012) and “puffier” (Förster Schreiber et al. 2009). Intriguingly, the presence of passive disks has also been observed at higher redshifts ($z > 1$) (e.g. McGrath et al. 2008, Stockton et al. 2008, Cameron et al. 2011, van der Wel et al. 2011, McLure et al. 2013), providing further evidence that the physical processes which quench star formation may be distinct from those that drive morphological transformations. Thus, further study of this informative regime is crucial for improving our understanding of the main drivers of galaxy morphology evolution and the processes responsible for star-formation quenching.

In order to best conduct studies of the morphological evolution of galaxies at high redshift it is vital to trace both the bulge and disk components separately by decomposing galaxy morphologies into these two fundamental components, rather than fitting a single profile which will be a sum of the bulge and disk structures. Previously, similar bulge-disk decompositions have been conducted

in the local Universe (e.g. de Jong 1996, Allen et al. 2006, Cameron et al. 2009, Simard et al. 2011, Lackner & Gunn 2012), where higher resolution imaging is more readily available. However, decompositions at high redshifts have been limited to very low sample numbers (van der Wel et al. 2011).

Here I present the largest galaxy bulge-disk decomposition conducted to date fitting multiple Sérsic models in the redshift range $1 < z < 3$. This decomposition has allowed me to further explore the size evolution of individual bulge and disk components, in addition to better studying the overall morphological evolution of these systems in terms of the dominance of their bulge and disk fractions. Furthermore, the trends displayed by the individual bulge and disk components can be coupled with star-formation rate information to allow a new exploration of the extent to which morphological transformations may or may not be linked to star-formation quenching.

3.2 Data Overview

The work presented in this chapter is based on the same $M_* > 10^{11} M_\odot$ $1 \leq z_{phot} \leq 3$ sample as described in Chapter 2, taken from the CANDELS HST WFC3/IR H_{160} imaging (Grogin et al. 2011, Koekemoer et al. 2011) of the central 187 arcmin^2 of the UKIDSS Ultra Deep Survey (UDS; Lawrence et al. 2007). Full details of the SED fitting procedure for photometric redshifts, stellar masses and star-formation rates have been presented in Chapter 2.

3.3 Morphology Fitting Procedure

The basic morphology fitting procedure established in Chapter 2 is further developed for the work presented here. I adopted the same wrap-around script for the implementation of the GALFIT fitting code, where, as discussed extensively in Chapter 2, an empirical stacked PSF is used with an additional level of background subtraction estimated on an object-by-object basis. For the majority of objects in my sample I used a background determined as the median value within a $6 \times 6 \text{ arcsec}$ image stamp, excluding a 1 arcsec radius aperture centred on the object. However, from my previous analysis I find that for a subset of $\simeq 15\%$ of my objects that are the most extended it is necessary to adopt a

background determined in a $3 - 5$ arcsec annulus, which despite being measured further from the source ensures the estimate is not biased too high by failing to account properly for the extended wings of these largest objects. The full background search analysis conducted in the previous chapter also provided me with an estimate of the biases and degeneracies associated with the single component Sérsic fits, which have been taken into consideration for the following multiple-component analysis.

3.4 Multiple-Component Models

Encouraged by the robustness of the single-component Sérsic fits carried out in the previous chapter, I decided to attempt to decompose the H_{160} images of all the galaxies in my sample into separate bulge ($n = 4$) and disk ($n = 1$) sub-components. For each object I adopted the median background measurements as described above, and locked all sub-components at the galaxy centroid as determined from the single Sérsic fits.

To determine whether multiple components were actually merited to describe the data, I first fitted three models to each galaxy, namely i) a bulge-only model with $n = 4$ (i.e. a de Vaucouleurs spheroid), ii) an exponential disk-only model with $n = 1$, and iii) a double-component bulge+disk model, with again the Sérsic indices locked to $n = 4$ and $n = 1$, but the relative amplitudes of the components, their scale-lengths, axial ratios and position angles all allowed to vary independently.

I note here that I have deliberately limited this analysis by fixing the Sérsic index of both components as opposed to allowing the spheroid component to have a variable index value during the fitting (as has been adopted for some lower-redshift studies). Decomposition of the CANDELS data at these redshifts is already a challenge, and the addition of the spheroid Sérsic index as a free parameter could potentially introduce additional significant degeneracies in my fits. Moreover, as described below, it transpires that $n = 1$ and $n = 4$ models are able to adequately reproduce the vast majority of CANDELS images.

It might seem that the first two of these models are simply a subset of the third (i.e. the bulge+disk model). However, my aim was to see if the second component was actually required (i.e. whether the more sophisticated model was statistically

justified). In addition, inspection of the results from the double-component fits revealed that whenever the fainter component contributed less than $\simeq 10\%$ of the H_{160} -band light, the parameter values for the fainter component were often unphysical and could not be trusted for scientific interpretation (e.g., left to its own devices, GALFIT will still often choose a secondary component with, for example, a completely unphysical scale-length in order to fix some unevenness in the background, even when such a component is not really required to achieve a formally-acceptable fit). Thus, as explained further below, whenever a secondary component contributed less than 10% of the flux, I simply reverted to the appropriate single-component model, designating the object as disk-only or bulge-only as appropriate.

Finally, I also explored the effect of introducing a further additional component in the form of a point-source at the galaxy centre. This was to allow for the possibility of an AGN or central star cluster, both to quantify the evidence for such components, and to check whether any point sources were distorting the galaxy fits. I explored adding an additional point-source contribution to the single variable Sérsic, bulge-only, disk-only, and disk+bulge models. Consequently, in total I eventually fitted eight alternative models to each galaxy.

The exact fitting procedures implemented are detailed in the following subsections, while the process by which I decided which model to adopt for a given galaxy is described in Section 3.5.

3.4.1 Bulge-only and disk-only models

The bulge-only and disk-only models are the simplest I attempted to fit to each galaxy. I constructed a GALFIT parameter file for each object using the best-fitting single-Sérsic parameter values as a starting point, locking the centroid position (to ensure that I avoid generating physically unrealistic offset models where the centroids of the individual components have been biased by any underlying variations in the background or by close companion objects which have not been fully masked out), and locking the Sérsic parameter at $n=4$ or $n=1$. Thus GALFIT was free to vary only the total magnitude, the effective radius, the axial ratio, and the position angle of the forced disk or de Vaucouleurs bulge model. As with all the model fitting, great care was taken (via image masking) to exclude pixels which contained any significant flux from companion objects, so as not to distort the best fitting value of χ^2 .

3.4.2 Double-component bulge+disk models

For the bulge+disk models I again locked the centroid (of both components) at the x, y position returned from the single-Sérsic fitting, and locked the Sérsic indices of the two components to $n=4$ and $n=1$. The other parameters of both components were allowed to vary independently (i.e. allowing the bulge and disk to have very different fluxes, sizes, axial ratios and position angles if required).

When using GALFIT for this simultaneous double-component fitting, with the consequent increase in the number of degrees of freedom, there is an increased danger of the fit becoming trapped in a local χ^2 minimum during the minimisation routine. To tackle this issue, and ensure that any double-component fits do indeed reflect the global minimum in χ^2 , I constructed a grid of different starting values for the total magnitudes and effective radii of the two components, and repeatedly restarted GALFIT from different positions on this grid. The grids were constructed with 11 steps in starting magnitudes for the two components, for each of which there were then 21 steps in initial effective radii. The grid initial magnitudes were set at 99% of the SEXTRACTOR MAG_AUTO for each object in the bulge (and hence 1% in the disk), then 90% bulge and 10% disk, 80% bulge and 20% disk, continuing similarly to 10% bulge and 90% disk and finally 1% bulge and 99% disk. Meanwhile the grid of effective radius values were stepped from 99% of twice the SEXTRACTOR r_{50} value for each object in the bulge and 1% in the disk, to 95% bulge and 5% disk, 90% bulge and 10% disk, and again continuing similarly to 5% bulge and 95% disk and finally 1% bulge and 99% disk. I restarted GALFIT from each of these 231 alternative starting points in order to ensure I found the global minimum in χ^2 , and then adopted the corresponding parameter values as the best-fitting double-component model. After this extensive additional fitting, I found that the models fitted for the individual components are actually relatively robust to the initial starting conditions to an accuracy of $\simeq 20\%$ in the fitted effective radii and magnitudes.

3.4.3 Introduction of an additional point-source

When conducting the single-Sérsic model fits (as described in Chapter 2) I allowed the Sérsic index, which is a measure of the central concentration of the light profile, to range across the full $n = 0 - 20$ parameter space allowed by GALFIT, as opposed to capping it at more physical values limited to $n < 8$. This allowed

me to fully explore how n and R_e are traded off against each other by GALFIT when attempting to deliver model fits to some of the more unusual objects in the sample.

I found that 28 out of my full sample of 215 objects yielded Sérsic indices in the range $5 < n < 20$. Upon inspection it appeared that these objects did indeed often have strongly-peaked central components. I therefore introduced the option of an additional point-source to the single-Sérsic fits, allowing GALFIT to vary the relative amplitude of the point-source and the single-Sérsic component.

This additional option of a point-source yielded significantly improved fits for 10 of these 28 objects, at the same time also yielding new, arguably more realistic, values of $n < 5$. Of the remaining 18 “high-Sérsic index objects”, 13 had $5 < n < 8$, and remained essentially unchanged (rejecting the additional option of a point-source) while the remaining five yielded only slightly-reduced values of n , and thus remained outside of the generally-accepted Sérsic index range.

Finally, in order to maintain a fully consistent approach across my entire sample, I decided to revisit the single-Sérsic, disk-only, bulge-only and disk+bulge models of every object to allow the option of an additional point source in every case. This was done by again locking the centroid of all components at the single-Sérsic centroid, and initially setting the brightness of the point-source at 1% of the SEXTRACTOR MAG_AUTO value. For the bulge+disk+point-source models I again generated a grid of initial starting parameters as detailed above.

Out of the complete sample of 215 objects, 59 preferred to accept the contribution of a point-source comprising $> 10\%$ of the overall light of the galaxy (as before, I deemed unreliable/insignificant any contribution of $< 10\%$ by any individual model sub-component). In no case did the contribution of the point-source ever exceed 43% of the total brightness of the object, indicating that none of my objects are “stellar” or AGN dominated. Out of curiosity I checked whether those fits which preferred to accept a significant contribution from a point source showed any enhanced probability of yielding a $24\mu\text{m}$ detection in the SpUDS *Spitzer* MIPS imaging, but I did not find any significant correlation. However, clearly a point-source contribution might arise from a central starburst rather than an AGN. I also note that a preference for a point-source contribution does not necessarily mean that it is statistically required, an issue which I discuss further below in the general context of choosing between the array of alternative models I ultimately generated for each object.

3.5 Final Galaxy Models

With the inclusion of the point-source option in all models, I was left with eight alternative model fits, of varying complexity, for every object in the sample. In deciding which “best-fit” model to adopt for each source for future science analysis, I chose to split the models into two categories within which the models are formally nested, and thus χ^2 statistics can be used to determine the “best” model given the appropriate number of model parameters. The first category consists of the single Sérsic models and the single Sérsic plus point-source models. The second category comprises the bulge-only and disk-only models, the bulge+point-source and disk+point-source models, the bulge+disk models, and the bulge+disk+point-source models. Comparison between these two categories is more problematic, except in those cases where no satisfactory fit was achieved with a category-1 model, while a satisfactory fit was achieved with a category-2 model.

3.5.1 Selection of the best model

For each object I recorded the best-fitting parameters from each of the eight (2 single Sérsic and 6 multiple component) models fitted to the data. However, before undertaking a statistical comparison of the alternative model options, I applied a series of criteria to reject unreasonable or physically-unrealistic models.

The first criterion imposed is the one already mentioned above, namely that I decided to throw away any model in which any sub-component contributed $< 10\%$ of the total H_{160} -band light. Accordingly, any model with a very weak point-source was rejected as unnecessary, as was any model with a very weak bulge or disk component. As discussed above, this decision was made after intensive inspection of the alternative model results revealed that such low-level components were often, in effect, artefacts of an unjustifiably complex fit (and even when physically plausible, their derived parameter values were too uncertain to be trusted in further analysis).

The second criterion again directly addresses how meaningful the fitted parameters are, as I decided to exclude any model with a sub-component whose effective radius exceeded 50 pixels (i.e. 3 arcsec), the fitting radius of my image stamps. This criterion did not in fact lead to the rejection of many models, but those

that were rejected on this basis had clearly unphysical effective radii (i.e. they substantially exceeded the 3 arcsec angular diameter threshold).

The third criterion, again aimed at confining my best-fitting models to those which are physically realistic, involved the rejection of any model which contained a bulge component with an extreme axial ratio $b/a < 0.1$. This additionally served to exclude any bulge models where the fitted effective radii were less than one pixel in size.

Having applied these criteria, it remained to consider, for each object, the relative merits of the surviving model alternatives within each category. First, I rejected any of the remaining models which did not deliver formally acceptable fits at the $3\text{-}\sigma$ level, as judged from the absolute value of χ^2 achieved, and the number of degrees of freedom, ν (where here, the number of degrees of freedom means the number of pixels minus the number of fitted parameters minus 1, and is typically 7000 – 10000 for the images and models fitted here, the precise value for each object depending on the degree of image masking; see Fig 3.4).

A model fit was thus deemed formally acceptable if the minimum value of χ^2 satisfied:

$$\chi^2 \leq \nu + 3\sqrt{(2\nu)} \quad (3.1)$$

and if any model failed this test it was no longer considered (although see below for model refinement).

Finally, if more than one model within each category survived all of the above tests, I chose between the acceptable fits of varying complexity by adopting the simplest acceptable model, unless a model of higher complexity satisfied:

$$\chi_{complex}^2 < \chi_{simple}^2 - \Delta\chi^2(\nu_{complex} - \nu_{simple}) \quad (3.2)$$

where now ν represents the number of degrees of freedom in the model (in effect the number of parameters), and $\Delta\chi^2(\nu_{complex} - \nu_{simple})$ is the $3\text{-}\sigma$ value for the given difference in the degrees of freedom between the two competing fits.

In this way I narrowed down the alternative models to a single, final, best-fitting model within each category. In the relatively small number of cases where no

formally acceptable model survived the first of the χ^2 tests described above, I have still applied the final *relative* quality-of-fit test, so as to retain parameter values for every galaxy in case this is required (note that very few other studies in this area have actually been concerned with assessing whether the best-fitting models are genuinely formally acceptable, even though a failure to achieve this renders the assessment of errors in parameter values problematic). These unacceptable fits, and my efforts to minimize the number of such cases, are discussed further in the next sub-section.

3.5.2 Model fit refinement

As a final comment on the technical aspects of the model-fitting described in this chapter, I briefly consider the problems I encountered in achieving formally-acceptable fits to a subset of my objects, and the steps I took to minimize the number of objects for which the modelling still proved formally inadequate.

Upon completion of my initial model fitting, I found that 70 out of my full sample of 215 objects had no formally-acceptable model fits as judged by the first of the two χ^2 tests described above (i.e. equation 3.1). To establish the cause of the excessively-high values of χ^2 , I visually inspected the images of all 70 objects. I found that there were several obvious, but different, reasons for these high χ^2 values, with the problematic objects including i) $z < 2$ spiral galaxies with very prominent spiral arms, ii) interacting/asymmetric systems, iii) objects in very crowded fields, and iv) objects with extremely close companions which had not been separately identified by SEXTRACTOR despite the high level of de-blending employed in my catalogue generation (DEBLEND_MINCONT=0.0008). Examples of these systems are shown in Fig. 3.1, and they contain some of the best examples of prominent spiral structure.

I therefore included an additional round of modelling for these objects, refitting after masking out the problematic non-axisymmetric structures (such as spiral arms or close companions) on the basis of χ^2 maps produced from the original attempted fits. Using this approach I re-ran all the model fits as described above, and re-selected the best-fitting models. Doing this delivered acceptable fits for all but 14 objects in my entire catalogue. The quality of the final fits achieved in this work is demonstrated by the final distribution of minimum χ^2 for the full sample, which is shown in Fig. 3.4.

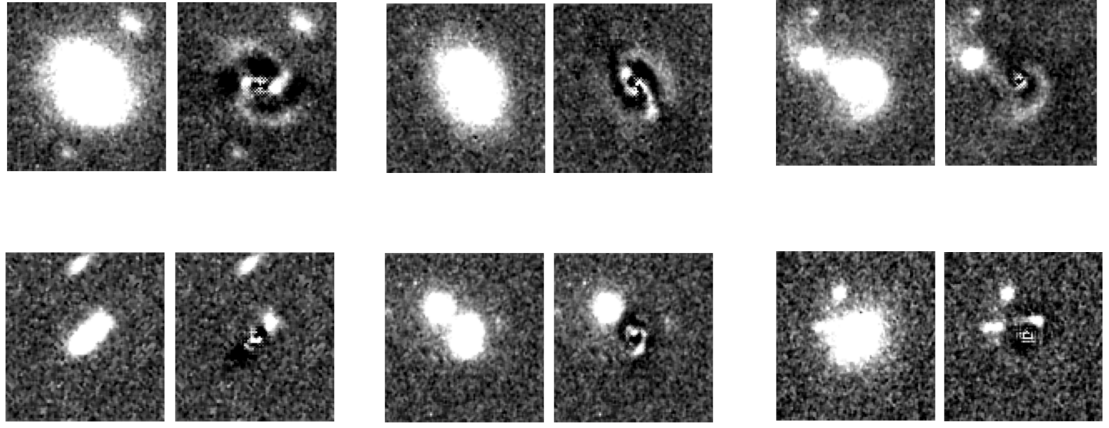


Figure 3.1 *Six examples of objects where the initial modelling failed my χ^2 acceptability test due to additional structure which could not be properly accounted for by the smooth models. For each object I show the 6×6 arcsec image stamp on the left, and the data-model residual image on the right at the same grey-scale (as produced by the best-fitting double-component model). The top row shows some clear examples of spiral structures and interacting systems, whereas the bottom row shows objects where the fits have been influenced by close companions the light from which has not been adequately masked out.*

The details of my refined fitting include incorporating masking of pixels for which the model fit to my data exceeds a certain χ^2 threshold. This serves to mask out any additional structure, which is not modelled by my symmetric Sérsic profiles, by ensuring that such pixels are not considered during the fitting process, and so do not contribute to the χ^2 returned for the overall fit.

My first refinement involved setting the χ^2 threshold for each pixel at 9, the point at which secondary structure became clearly visible in the χ^2 maps of these objects, and the point in the χ^2 distribution for all pixels for these objects where the distribution has peaked and begins to fall into the tail. Applying the refinement with this threshold improved the fits of 32 objects to within statistically acceptable levels, but I was still left with a further 37 objects which still failed to meet the acceptability criterion.

Accordingly, I re-ran my modelling with a lower χ^2 threshold for a second refinement in the fitting. This second pass used a χ^2 threshold of 5, a value cutting further into the main distribution of the χ^2 values for each pixel (from inspection of the χ^2 maps of these complex objects it became apparent that spiral

structure could be present and significant enough to influence the fits even at this low level). Examples of the χ^2 masks used in both levels of refinement are shown in Fig. 3.2 for three representative objects.

This second level of refinement resulted in formally acceptable model fits for all but 14 objects. Residual image stamps of these 14 objects are shown in Fig. 3.3. These objects comprise only $\sim 6\%$ of the overall sample and have a range of single-Sérsic index and effective radius structural parameters, which do not place them preferentially within any e.g. bulge or disk-dominated, compact or extended sub-populations. Thus, these 14 unacceptable models have been removed from all further results presented hereafter so as not to potentially bias any science results.

Throughout the analyses presented in this thesis it is the parameters derived from the best-fit refined models which have been utilised.

The statistical quality of my final model fits is illustrated in Fig. 3.4, which shows the distribution of minimum χ^2 achieved from the modelling of the 69 “troublesome” galaxies in my sample both before and after the refinement in the model fitting as described above. The figure also shows the distribution of degrees of freedom for all objects, which is typically $\simeq 10,000$ but varies on an object-by-object basis depending on the degree of object masking employed. As can be seen, my model fits have reduced χ^2 values centred exceptionally close to unity with very little spread (as detailed in the caption to Fig. 3.4, in practice equation 3.1 dictates that an acceptable model has to have typically $\chi^2 < 1.05 \times 10^4$ given the number of degrees of freedom involved in the fit).

Finally, it is important to stress that, while this re-fitting was sometimes required to achieve formally-acceptable values of χ^2 , the initial attempt to model these objects did in fact successfully recover their key morphological parameters (even if errors on these quantities would have been under-estimated on the basis of $\Delta\chi^2$) despite the presence of additional high-surface brightness features which cannot be reproduced by my smooth models. This is clearly illustrated in Fig. 3.5, which shows the tight correlation between the underlying physical properties determined from the initial general fitting procedure and the first stage of additional modelling refinement. It should also be noted that the re-fitting conducted for these objects followed the same procedure as the initial fits, whereby GALFIT was run on a grid of different initial starting conditions for effective radius and the magnitudes of each component, thus allowing any new minima to

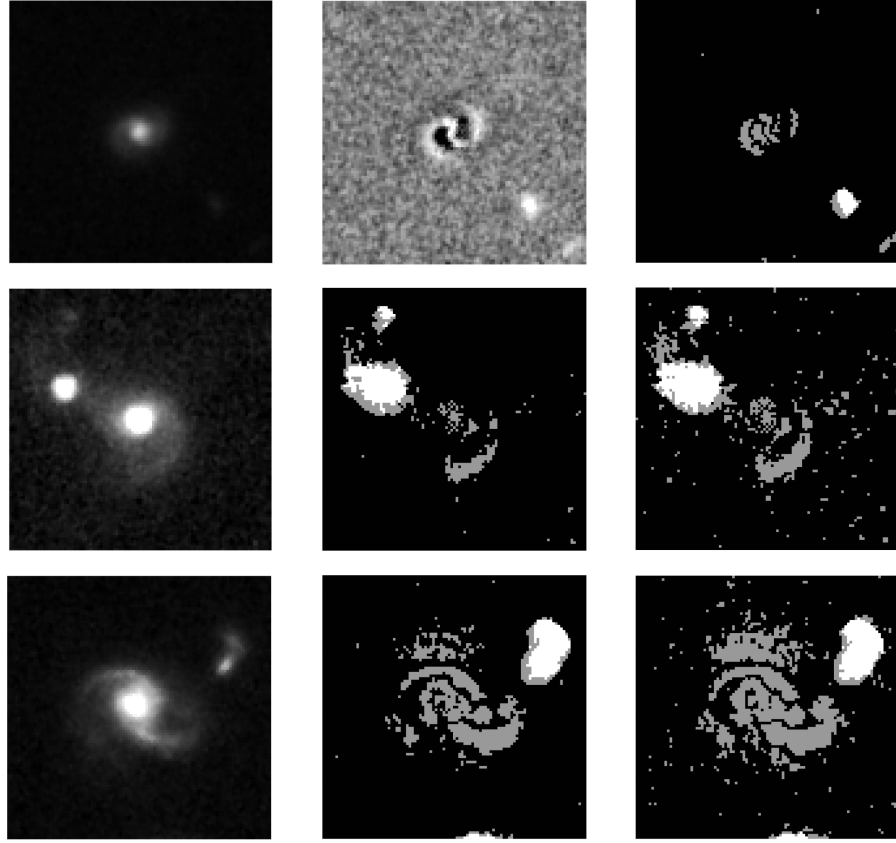


Figure 3.2 *Examples of three objects where my initial modelling failed the χ^2 acceptability test (due to additional structure), which were then re-fitted with masking of pixels for which the model fit to my data exceeded a certain χ^2 threshold. The top row is an example of an object for which I was able to achieve a statistically acceptable model fit after only one level of re-fitting, with masking based on my highest χ^2 threshold. The middle row shows an object where the additional lower χ^2 threshold masking was needed to achieve an acceptable fit, and the bottom row is one of the 14 objects which continued to fail the formal model-fitting acceptability criteria, even after both degrees of additional masking. The images displayed for the top row are the 6×6 arcsec image stamp on the left, the residual of my initial (non- χ^2 masked) fit in the middle and the χ^2 mask for the first degree of masking on the right. Whereas, for the middle and bottom rows the images displayed are the 6×6 arcsec image stamp on the left, the χ^2 mask for the first degree of masking in the middle and the χ^2 mask for the second degree of masking on the right. The brightness levels of the χ^2 masks make the distinction between pixels which were masked out in all initial fits as being associated to companion objects identified by the segmentation maps (brighter pixels), and the additional levels of χ^2 masking in both cases of χ^2 thresholds (darker pixels).*

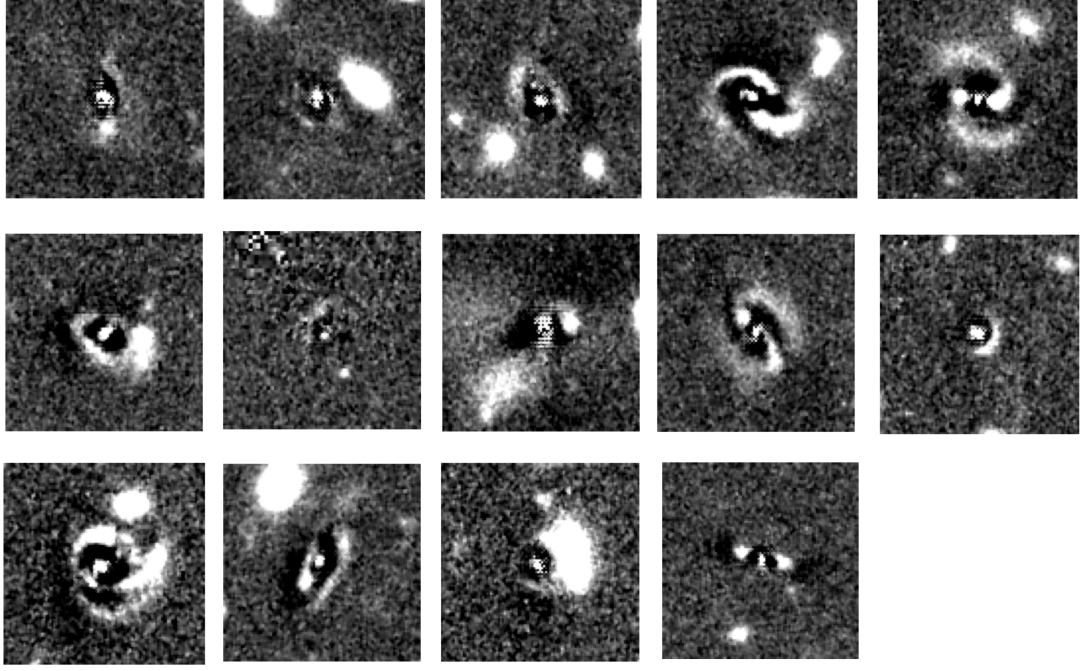


Figure 3.3 *Residual map image stamps for the 14 objects which continued to fail the formal model-fitting acceptability criteria, even after additional masking. These image stamps have been constructed in the same way as in Fig. 3.1, with the same brightness level and pixel scale. However, it should be noted that the brightness levels adopted for the image stamps in these figures is deeper than those adopted subsequently. This is to allow faint sub-structure to be clearly visible but should be taken into account when comparing with subsequent image stamps presented in this thesis. As noted in the text, these 14 objects have a range of both Sérsic indices and effective radii, and are not confined to e.g. the most extended or disk-dominated objects in this sample.*

be properly explored.

The reason for this is simply that while high surface-brightness features which cannot be represented via axisymmetric modelling can contribute significantly to χ^2 , they rarely actually dominate a sufficiently-large fraction of my object image stamps (which each contain $\simeq 10,000$ pixels) to significantly distort the morphological properties of the underlying mass-dominant galaxy as established via my modelling.

For all multiple-component science results presented I use a final sample of 192 objects, where from our original sample of 215 objects I have removed the 14 objects which still had formally unacceptable multiple-component model χ^2

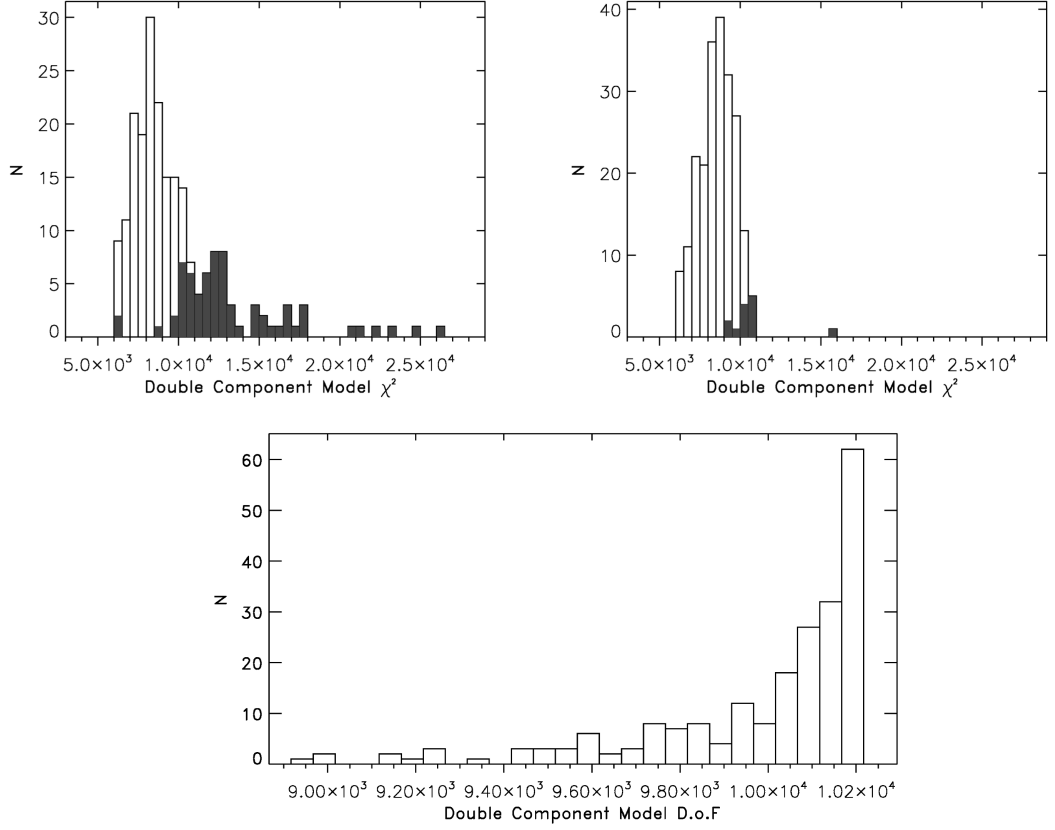


Figure 3.4 *Distributions of minimum χ^2 achieved by the modelling of all objects in the sample. The upper-left panel shows this distribution as it resulted from the first pass of modelling, with the shaded region indicating those objects which failed to pass the acceptability criterion as defined in equation 3.1, given the number of degrees of freedom (which is typically $\simeq 10,000$, but varies on an object-by-object basis depending on the level of local pixel masking, as illustrated in the lower panel). The upper-right panel shows the final distribution achieved after the model refinement including additional pixel masking of high surface-brightness features as described in the text. Here the remaining shaded region indicates the 14 objects for which I still failed to achieve an acceptable model fit (and whose residual images are shown in Fig. 3.3). In practice, equation 3.1 means that a formally acceptable model has to typically have $\chi^2 < 1.05 \times 10^4$. As a result of the careful treatment given to modelling of all the objects in my sample, this have been achieved for 94% of the galaxies studied here.*

values even after the χ^2 masking described in the text, as well as seven objects which have unrealistically-large single Sérsic indices ($n > 10$), and two unresolved objects which may be stars. For completeness the percentages of the final sample

of 192 objects with multiple-component best-fits corresponding to each of the six fitted models is given in Table 3.1.

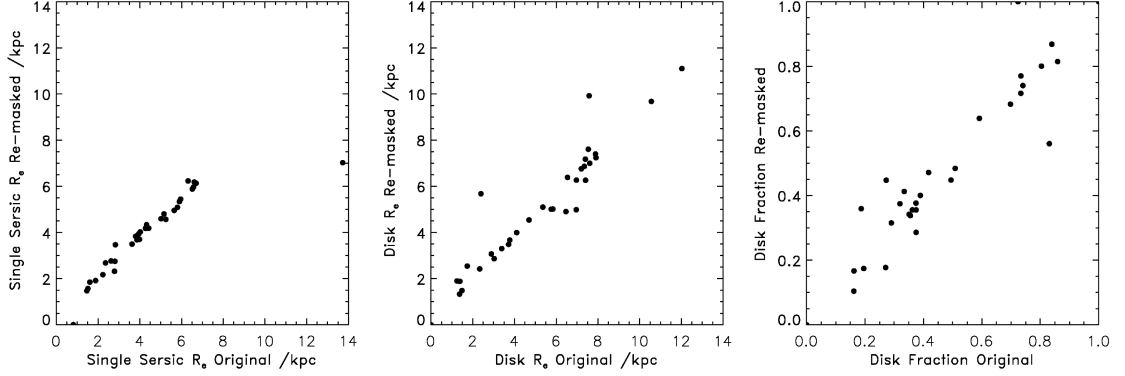


Figure 3.5 *Demonstration of the excellent agreement between the key derived galaxy physical parameter values obtained with the original model-fitting and with the first set of re-masked/refined fits. Left: comparison between single Sérsic model effective radii, middle: comparison between disk effective radii, right: comparison between disk fractions. These plots clearly illustrate that the underlying structure of these more complicated systems has in fact been accurately fitted by my procedure and has not been significantly influenced by the high surface brightness features, such as spiral arms, etc.*

bulge	bulge +psf	disk	disk +psf	bulge +disk	bulge+disk +psf
$10 \pm 2\%$	$1 \pm 1\%$	$18 \pm 3\%$	$8 \pm 2\%$	$58 \pm 7\%$	$5 \pm 2\%$

Table 3.1 *Percentages of the final sample of 192 objects with multiple-component best-fits corresponding to each of the six fitted models.*

3.6 Science Results

Having determined both accurate and acceptable single-Sérsic models and bulge+disk decompositions for the vast majority of the objects within my sample, I am now able to proceed to explore the scientific implications of my results. First, however, it is interesting to consider the correlation between single Sérsic index and B/T flux-ratio delivered by my modelling of these massive galaxies at $1 < z < 3$, a relation which has been extensively studied and debated at lower redshifts (e.g. Ravindranath et al. 2006, Cameron et al. 2009, Simard et al. 2011, Lackner & Gunn 2012). This is plotted in Fig. 3.6, where it can be seen that, in contrast to some previous studies at lower redshift ($z < 1$), I find that Sérsic index and B/T flux-ratio are generally in remarkably good agreement; from Fig. 3.6 it can be seen that disk-dominated systems with $B/T < 0.5$ are almost completely confined to the Sérsic-index range $0 < n < 2$, and that virtually all bulge-dominated galaxies with $B/T > 0.5$ have $n > 2$. These results provide further confidence in the reliability of my morphological analysis, and suggest that my attempt to separate the galaxies into bulge and disk components is meaningful and, moreover, justified by the quality of the WFC3/IR data.

3.6.1 The size-mass relation

In Chapter 2, Fig. 2.8 included all objects, of whatever morphology, and shows that while $68 \pm 3\%$ of my objects have effective radii which place them well below the local relation and its $1\text{-}\sigma$ scatter, a significant subset of $32 \pm 3\%$ of my objects which, within the error-bars, are consistent with the sizes of similarly-massive local galaxies. This results in the median size of the most massive galaxies at $1 < z < 3$ being a factor 2.3 ± 0.1 times smaller than comparably-massive local galaxies. As discussed in that chapter, splitting these objects into two different redshift bins, above and below $z = 2$, does not reveal a strong size evolution with redshift, but there is gradual trend to smaller sizes with increasing redshift; the median sizes become 2.7 ± 0.3 kpc at $z < 2$ and 2.5 ± 0.3 kpc at $z > 2$, corresponding to 2.2 ± 0.2 and 2.3 ± 0.2 times smaller than the local relation. This can also be seen in the results that at $1 < z < 2$ I find $70 \pm 4\%$ of objects lie below the local relation, with $30 \pm 4\%$ essentially on it, while at $2 < z < 3$ the corresponding figures are $62 \pm 5\%$ and $38 \pm 5\%$ respectively.

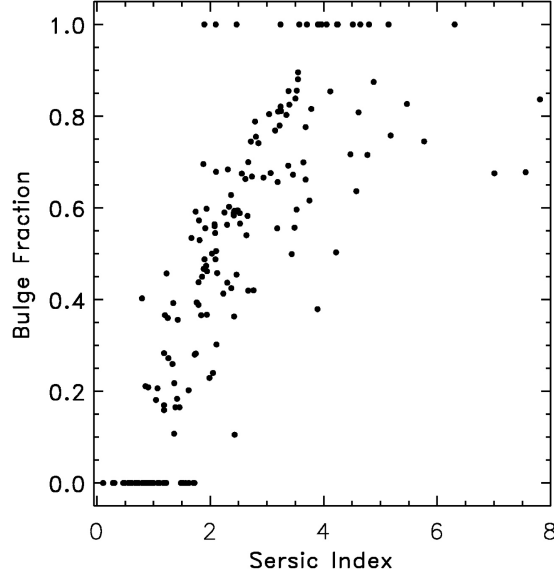


Figure 3.6 *Sérsic index from the single-Sérsic fits, versus bulge to total (B/T) fractional contribution to the H_{160} -band light (as determined from the multi-component modelling) for the final sample of 192 objects used in all subsequent double-component science plots and analysis. I have removed the 14 objects which still had formally unacceptable χ^2 values even after the χ^2 masking described in the text, as well as seven objects which have unrealistically-large single Sérsic indices ($n > 10$), and two unresolved objects which may be stars. It can be seen that there is a good correlation between the two estimators of bulge dominance, with $n \simeq 2$ corresponding to roughly equal bulge and disk contributions. Note that the objects at the top and bottom of the plot are located at $B/T = 1.0$ or $B/T = 0.0$ due to my insistence (based on intensive inspection of the modelling results) that any sub-component contributing less than 10% of total flux is discarded as insignificant and unreliable. This of course also leads to two artificial gaps in the distribution of bulge fraction. Reassuringly, the group of objects with B/T rounded down to zero is centred on $n = 1$, while the “pure-bulge” objects with B/T equal to unity is centred on $n = 4$.*

I next use the results from my bulge+disk modelling to check for any significant trends with morphological type, or indeed for trends with redshift within a given morphological sub-class. Since I have attempted bulge+disk decomposition for all galaxies in the sample, I can now plot the relevant size-mass relations not just for pure bulge or disk galaxies, or bulge- or disk-dominated galaxies, but for *all* bulges and disks (i.e. including the bulges from the disk-dominated objects and vice versa).

The size-mass relations for the separate bulge and disk components from the

best-fit multiple component model are plotted in Fig. 3.7, shown both for the full redshift range, and subdivided for $z < 2$ and $z > 2$. Because I am plotting sub-components, these plots contain some objects with stellar masses M_* substantially smaller than my original mass limit. This provides additional dynamic range, but I note that the stellar-mass subdivision has been performed here solely on the basis of the fractional contribution of each sub-component to the H_{160} -band light. This is clearly not quite correct, but a full SED-based mass determination for each sub-component is deferred to Chapter 4, involving fitting of the bulge+disk models to multi-band optical-infrared imaging. It also does not mean that my study is in any sense mass-complete at masses substantially smaller than $M_* \simeq 10^{11} M_\odot$. Nonetheless, it is instructive to see whether the minor components (e.g. the bulges in disk-dominated galaxies) follow the same trends as the dominant components (although to avoid pushing the data too far, I do not plot any sub-components with estimated masses $M_* < 2 \times 10^{10} M_\odot$). In Fig. 3.7 I also over-plot the local early and late-type size-mass relations as described in the figure caption.

These plots reveal a number of interesting features. First, consistent with previous studies, it can be seen that the size evolution is more dramatic in the bulges than in the disks, but nevertheless most disks are also smaller than in the local Universe; over the full redshift range $81 \pm 3\%$ of the bulges lie significantly below their relevant local relation, while for the disks the corresponding figure is $58 \pm 4\%$ (conversely this means that only $19 \pm 3\%$ of bulges are consistent with the local relation, but this figure rises to $42 \pm 4\%$ for the disks).

An interesting aspect of the more dramatic size evolution displayed by the bulges is that their size-mass distribution, especially at the highest redshifts, appears bi-modal (although the statistics are weak), with the dominant population of compact bulges becoming increasingly separated from the minority of objects which appear still consistent with the local relation (see the top-right panel of Fig. 3.7). Interestingly these trends also seem to apply to the lower-mass bulges embedded in the disk-dominated galaxies, which display the smaller sizes as “expected” from a simple offset of the size-mass relation as determined from the more-massive bulge-dominated galaxies. (I note that it is at least plausible that some low-mass bulges at these redshifts become the cores of local disks; Graham 2011.)

The trends with redshift shown in Fig. 3.7 can be quantified in terms of the fractions of bulges and disks on or significantly below their respective local relations at $1 < z < 2$ and $2 < z < 3$. For the bulges the relevant figures are

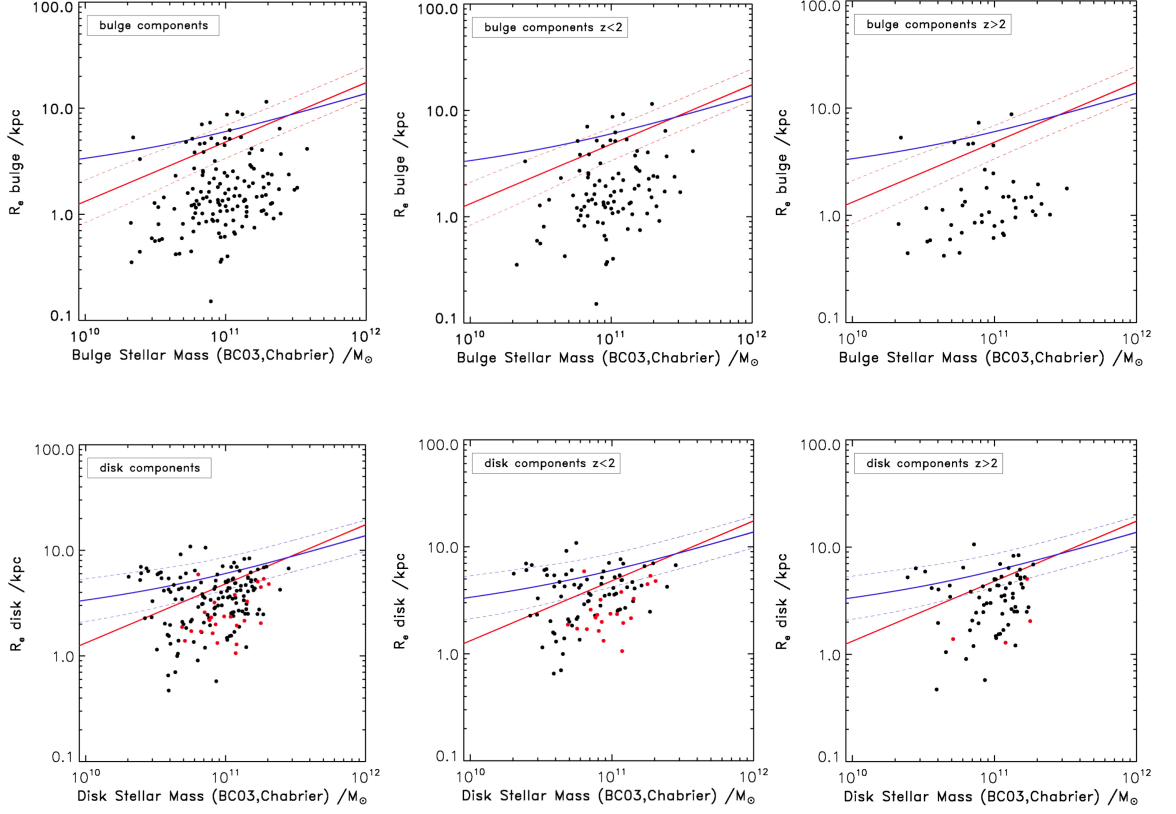


Figure 3.7 *The size-mass relations displayed by the separate bulge components (upper row) and disk components (lower row) as produced from the bulge+disk modelling analysis of my massive galaxy sample (shown both for $1 < z < 3$ and then subdivided into two redshift bins). The masses plotted here for the individual sub-components simply reflect the total mass of the “parent” galaxy sub-divided in proportion to the contribution of each component to the H_{160} -band light. For consistency, and to avoid over-interpreting the location of the weakest sub-components, I have excluded nine objects whose component masses fall below $2 \times 10^{10} M_{\odot}$. In the lower row of plots, the disk components from the passive disk-dominated galaxies discussed in Section 3.6.3 (i.e. objects with $sSFR < 10^{-10} \text{ yr}^{-1}$, no $24 \mu\text{m}$ counterparts and $B/T < 0.5$) are over-plotted in red. In order to provide a comparison with the sizes of comparably-massive low-redshift bulge and disk counterparts, I have taken the local early-type, and late-type galaxy relations from Shen et al. (2003) and converted them to non-circularised sizes (as described in the caption to Fig. 2.8, where the median axis ratio values were taken to be 0.75 for bulges (Holden et al. 2012) and 0.62 for disks (Padilla & Strauss 2008)). These non-circularised relations are plotted as a solid red line for the local early-type relation, and a solid blue line for the local late-type galaxy relation; the dashed lines indicate the typical $1\text{-}\sigma$ scatter in these relations. These plots reveal the more dramatic size evolution displayed by the bulges which, by $z > 2$ are on average a factor of > 4 smaller than their local counterparts. Nevertheless some bulges, and a rather large fraction of disks are still found to lie on the local relation throughout the redshift range.*

$20 \pm 4\%$ on and $80 \pm 4\%$ below in the lower redshift bin, and $15 \pm 5\%$ on, $85 \pm 5\%$ below on the upper redshift bin. For the disks there really is no evidence for any evolution in the relevant fractions within my redshift range; the percentages are $41 \pm 5\%$ on and $59 \pm 5\%$ of disk components below the local relation at $1 < z < 2$, and $43 \pm 6\%$ on and $57 \pm 6\%$ below at $2 < z < 3$.

These trends are also reflected in the evolution of the median sizes of the bulge and disk components. Even within my limited redshift range the (apparent) evolution in size of the bulges is evident (although at only the $\sim 2 - \sigma$ level), where taking the median sizes of bulges which lie below the local early-type relation gives an offset from the local early-type relation already a factor of 3.5 ± 0.5 at $1 < z < 2$ rising to a factor 4.4 ± 0.3 at $2 < z < 3$. By contrast, the offset for the disks from the local late-type relation is more modest and apparently unchanging; a factor of 2.4 ± 0.4 at $1 < z < 2$, and 2.5 ± 0.2 at $2 < z < 3$.

Finally, marked in red on the lower panels of Fig. 3.7 are the locations of the “passive” disks in my sample, a population discussed further below. Interestingly, the vast majority of the passive disks lie below the local late-type size-mass relation.

3.6.2 Evolution of morphological fractions

I next consider how the relative number density of galaxies of different morphological type changes over the redshift range probed by my sample. In Fig. 3.8 I illustrate this by binning my sample into four redshift bins of width $\Delta z = 0.5$, and consider three alternative cuts in morphological classification as measured by B/T from my disk-bulge decompositions. I present the data in this way both to try to provide a complete picture, and to facilitate comparison with different categorisations in the literature. In the left-hand panel of Fig. 3.8 I have simply split the sample into two categories: bulge-dominated ($B/T > 0.5$) and disk-dominated ($B/T < 0.5$). In the central panel I have separated the sample into three categories, with any object for which $0.3 < B/T < 0.7$ classed as “Intermediate”. Finally, in the right-hand panel I have expanded this Intermediate category to encompass all objects for which $0.1 < B/T < 0.9$.

From the first panel it can be seen that disks dominate at $z > 2$ and that this situation is reversed at $z < 2$. However, the other two panels help to emphasize that, at $z < 2$, pure bulges and disks are rare, and that the vast majority of

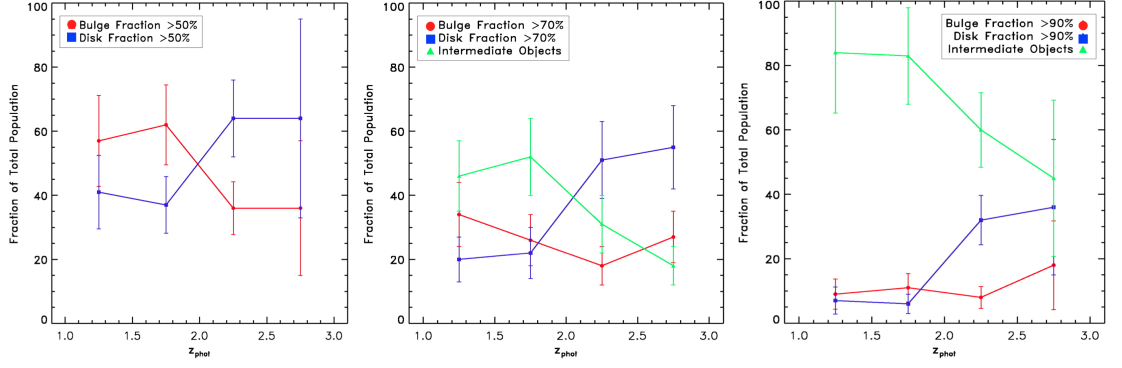


Figure 3.8 *The redshift evolution of the morphological fractions in my galaxy sample, after binning into redshift bins of width $\Delta z = 0.5$. I show three alternative cuts in morphological classification, both to try to provide a complete picture, and to facilitate comparison with different categorisations in the literature. In the left-hand panel I have simply split the sample into two categories: bulge-dominated ($B/T > 0.5$) and disk-dominated ($B/T < 0.5$). In the central panel I have separated the sample into three categories, with any object for which $0.3 < B/T < 0.7$ classed as “Intermediate”. Finally, in the right-hand panel I have expanded this Intermediate category to encompass all objects for which $0.1 < B/T < 0.9$ (see Section 3.6.2 for discussion).*

lower-redshift objects are, to a varying degree, disk+bulge systems. Interestingly, however, it is clear that, however the cuts are made, at $z > 2$ the population is disk-dominated, and a substantial fraction of the sample are “pure” disks, which have largely disappeared by $z < 2$. Since the number density of galaxies in this high-mass regime falls dramatically with increasing redshift at $z > 3$, these plots illustrate that the redshift range $2 < z < 3$ is the *era of massive disks*.

Conversely, at the lowest redshifts probed by this study ($z \simeq 1$) it is seen that, while bulge-dominated objects are on the rise, pure-bulge galaxies (i.e. objects comparable to present-day giant ellipticals) have yet to emerge in significant numbers, with $> 90\%$ of these high-mass galaxies still retaining a significant disk component. This is compared with 64% of the local $M_* > 10^{11} M_\odot$ galaxy population, which would be classified as pure-bulges by my definition ($B/T > 0.9$, corresponding to $n > 3.5$ from Fig. 3.6) from the sample of Buitrago et al. (2011).

3.6.3 Star-forming and passive disks.

The primary aim of this chapter is to focus on the morphological analysis of the H_{160} images, with a full treatment of the SEDs, including dependence of morphology on wavelength, deferred to Chapter 4. Nevertheless, in Fig. 3.9 I make use of the single component SED fitting already employed in the sample selection to explore the relationship between star-formation activity and morphological type.

Fig 3.9 shows specific star-formation rate ($sSFR$) versus morphological type for the massive galaxies in my sample, where morphology is quantified by single Sérsic index in the left-hand panel, and by bulge-to-total H_{160} -band flux ratio (B/T) in the right-hand panel.

The values of $sSFR$ plotted are derived from the procedure outlined in Chapter 2, where the SFR is determined from the $24\mu\text{m}$ and non dust-corrected SED model UV flux (SFR_{UV+IR}) for objects with a $24\mu\text{m}$ counterpart within a 2 arcsec matching radius from the *Spitzer* SpUDS MIPS imaging of the UDS, and otherwise are calculated from the UV dust-corrected SED fit ($SFR_{UV,dust\ corrected}$). To explicitly show the robustness of this SFR_{UV+IR} and $SFR_{UV,dust\ corrected}$ estimation approach to correctly identify reddened dusty star-forming galaxies, I have highlighted in blue those objects which yielded a MIPS counterpart within the 2 arcsec search radius.

Reassuringly, relatively few $24\mu\text{m}$ detections have been uncovered for the objects in the lower regions of the panels shown in Fig. 3.9, while the vast majority of star-forming objects are confirmed via MIPS counterparts. This shows that the determination of $sSFR$ as deduced from my approach has been good at cleanly separating the star-forming galaxies from the more quiescent objects.

It is clear from these plots that the majority of disk-dominated galaxies are star-forming, whereas the majority of bulge-dominated galaxies are not (as judged by $sSFR < 10^{-10} \text{ yr}^{-1}$). Nonetheless, the sample also undoubtedly contains star-forming bulge-dominated galaxies and, perhaps more interestingly, a significant population of apparently quiescent disk-dominated objects, which I quantify and discuss further below.

First, though, I note that the most obvious feature of Fig. 3.9 is the prominent group of pure-disk galaxies which dominate the star-forming population. Since I

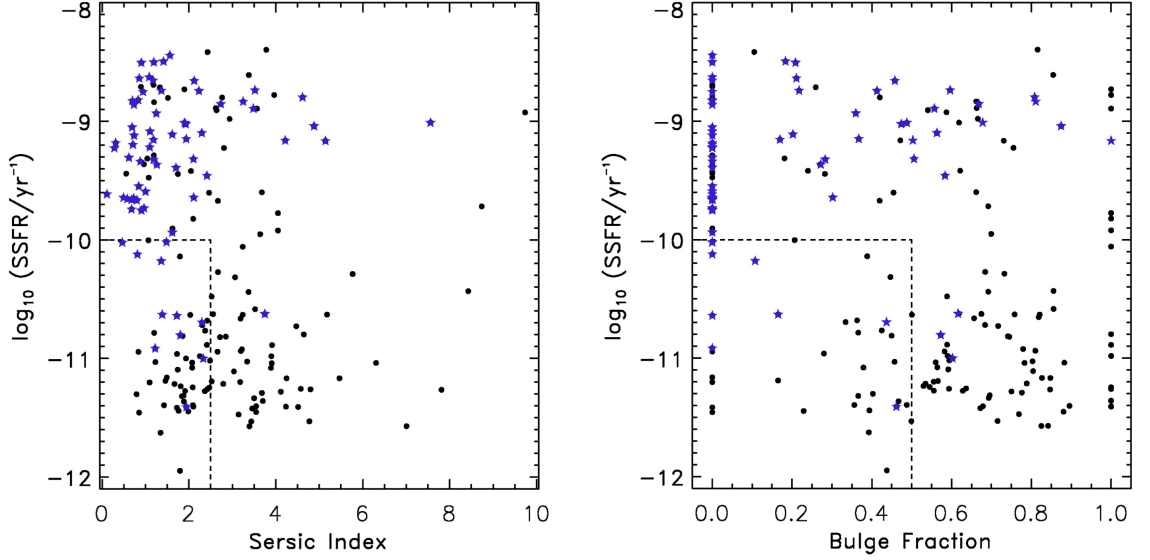


Figure 3.9 *Plots of specific star-formation rate ($sSFR$) versus morphological type as judged by single Sérsic index (left-hand panel) and bulge-to-total H_{160} -band flux ratio (B/T) (right-hand panel). The values of $sSFR$ plotted are derived from the procedure outlined in Chapter 2, where the SFR is determined from the $24\mu m$ and non dust-corrected SED model UV flux for objects with a $24\mu m$ counterpart within a 2 arcsec matching radius from the Spitzer SpUDS MIPS imaging of the UDS, and otherwise are calculated from the UV dust-corrected SED fit. As a secondary check I have highlighted by blue stars those galaxies which have a $24\mu m$ counterpart, indicative of some dust enshrouded star-formation and/or AGN activity. It is clear from these plots that the vast majority of disk-dominated galaxies are star-forming, and the majority of bulge-dominated galaxies are not (as judged by $sSFR < 10^{-10} \text{ yr}^{-1}$). However, I have indicated by a box on both the panels the region occupied by a potentially interesting population of passive disk-dominated objects; in the left-hand panel disk-dominated is defined as $n < 2.5$, and $52 \pm 9\%$ of the quiescent galaxies lie within this box, while in the right-hand panel disk-dominated is defined by $B/T < 0.5$, in which case $34 \pm 7\%$ of the quiescent objects lie within this region.*

already emphasized in Fig. 3.8 that the pure-disk population is largely confined to $2 < z < 3$, it becomes clear that, at $z > 2$, my massive galaxy sample is dominated by disk-dominated/pure-disk star-forming galaxies. As is discussed in a related CANDELS paper, this population of massive star-forming disks at $2 < z < 3$ is, to first-order, the same as the population of sub-millimetre galaxies revealed by continuum sub-millimetre and millimetre wavelength surveys over the last decade (Targett et al. 2013).

Equally interesting, however, is the apparently significant population of quiescent disks revealed on these plots. To highlight and quantify this population I have indicated by a box on both the panels the region occupied by objects with disk-dominated morphologies and $sSFR < 10^{-10} \text{ yr}^{-1}$. In the left-hand panel, disk-dominated is defined as $n < 2.5$, and $52 \pm 9\%$ of the quiescent galaxies lie within this box ($40 \pm 7\%$ if I also exclude all $24 \mu\text{m}$ detections to take the maximal approach to remove *any* obscured star-formation activity), while in the right-hand panel, disk-dominated is defined by $B/T < 0.5$, in which case $34 \pm 7\%$ of the quiescent objects lie within this region ($25 \pm 6\%$ if I exclude the $24 \mu\text{m}$ detections).

As discussed further in later sections, quiescent disk galaxies are of particular interest because they suggest that the quenching or exhaustion of star-formation activity need not be simply linked to a process (e.g. major merging) which is also directly associated with inducing morphological transformations. I re-emphasize that it is clear the majority of disk-dominated galaxies in my sample are star-forming, and that this is true for an even clearer majority of the pure disks. However, my sample does appear to include a significant population of quiescent disk-dominated objects, including $\simeq 5$ pure disks. In fact ten pure disks lie in the box, but the upper five of these possess $24 \mu\text{m}$ detections indicating that they may be reddened star-forming disks, or contain obscured AGN.

Note that I now use an additional $24 \mu\text{m}$ to SFR conversion, over and above the Wuyts et al. (2011) corrections implemented already, as a secondary check. For this I have adopted the conversion from Rieke et al. (2009) given by: $\log(SFR) = A(z) + B(z)\{\log(4\pi D_L^2 \times f_{24}) - 53\}$, where $A(z)$ and $B(z)$ are tabulated values. At the depth of the *Spitzer* SpUDS MIPS imaging, and the redshifts and masses of interest here, a significant detection at $24 \mu\text{m}$ always corresponds to a $sSFR$ above my adopted threshold of $sSFR = 10^{-10} \text{ yr}^{-1}$, if the mid-infrared emission is interpreted as due to star-formation activity. This supports the removal of any objects with a $24 \mu\text{m}$ detection from the passive fraction statistics.

I have double-checked that none of the quiescent disk-dominated objects not already marked by the blue stars in Fig. 3.9 (indicating a counterpart in the MIPS catalogue) have even marginal detections in the $24 \mu\text{m}$ imaging. I have also checked that this population is not biased towards higher redshift, which might make MIPS detections more challenging. I thus conclude that this population really is quiescent as judged by $sSFR$, and needs to be explained in any viable model of galaxy formation and evolution.

3.6.4 Axial ratio distributions

Some additional (and independent) information on the morphologies of the galaxies in my sample can potentially be gained from examining the distribution of their axial ratios. In Fig. 3.10 I have split my sample into disk-dominated ($B/T < 0.5$) and bulge-dominated ($B/T > 0.5$) galaxies, and then plotted the axial-ratio distributions of the disk components in the disk-dominated galaxies (left-hand panel), and of the bulge components in the bulge-dominated galaxies (right-hand panel) (I do this to avoid potential contamination of these plots by poorly-constrained axial ratios from weak sub-components; Fig. 3.10 thus displays the axial ratio distributions of my more robustly measured disks and bulges). In addition, in each panel I split the sub-samples further into star-forming (black outlined histogram) or quiescent (shaded grey histogram) objects, as again defined by whether a given galaxy lies above or below a specific star-formation threshold $sSFR = 10^{-10} \text{ yr}^{-1}$.

From the right-hand panel of Fig. 3.10 it can be seen that the axial-ratio distributions of the star-forming and quiescent bulges are indistinguishable, both peaking around $b/a \simeq 0.7$ (the K-S test yields $p = 0.71$ for the null hypothesis that they are drawn from the same distribution). This result is consistent with previous studies of bulge-dominated objects, both at low (Padilla & Strauss 2008) and high redshifts (Ravindranath et al. 2006).

Perhaps of more interest are the axial distributions of the disk components as plotted in the left-hand panel of Fig. 3.10. Here the two distributions look markedly different (although the statistical significance of the difference is marginal; $p = 0.09$). Specifically, it appears that the passive disks display a fairly flat distribution (as expected for a set of randomly-oriented thin disks) whereas the star-forming disks display a significantly more peaked distribution, in fact indistinguishable from the axial-ratio distributions displayed by the bulges.

The flat axial-ratio distribution found for the passive disk-dominated galaxies lends some additional support to my conclusion that I have uncovered a genuine population of passive disk-dominated galaxies, but the peaked distribution of the star-forming disks might be viewed as surprising. However, these results agree well with other recent studies of star-forming disk-dominated galaxies at comparable redshifts, as I illustrate in Fig. 3.11. The left-hand panel of Fig. 3.11 shows again the axial-ratio distribution of my star-forming disks (simply taken

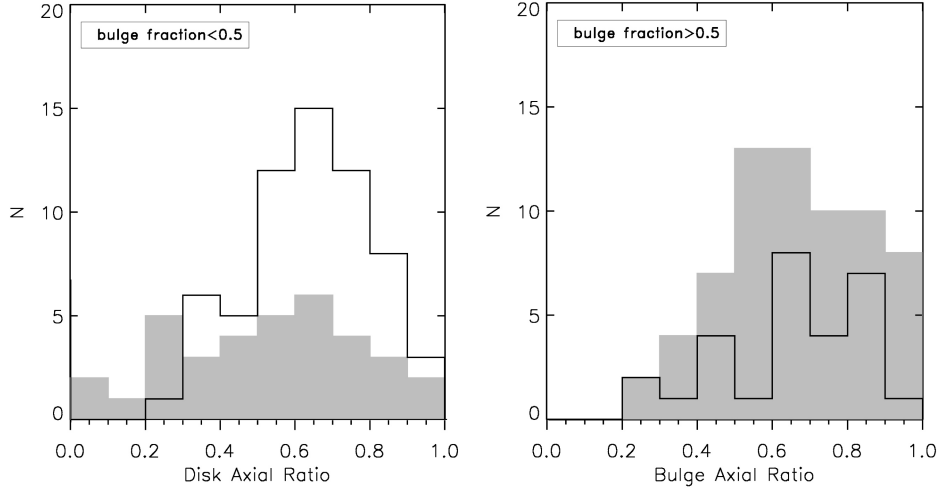


Figure 3.10 *Axial-ratio distributions displayed by the dominant disk components in the disk-dominated galaxies ($B/T < 0.5$; left-hand panel) and by the dominant bulge components in the bulge-dominated galaxies ($B/T > 0.5$; right-hand panel). These sub-samples have been further split into star-forming objects ($sSFR > 10^{-10} \text{ yr}^{-1}$; black outlined histograms) and quiescent objects ($sSFR < 10^{-10} \text{ yr}^{-1}$; grey shaded histograms). Both the star-forming and quiescent bulge populations show similar distributions peaked, as broadly expected, at $b/a \simeq 0.7$. However, the active and passive disk populations are marginally different, with the passive disks showing a relatively flat distribution as seen for low-redshift disks (see also Fig 3.11), while the star-forming disks display a peaked distribution more comparable to that displayed by the bulges (see text for details and K-S statistics).*

from the left-hand panel of Fig. 3.10), but this time over-plotted with results from Law et al. (2012), who utilised a larger sample of galaxies at $z \sim 1.5 - 3.6$, but plot only the single-Sérsic model axis ratios of $n \simeq 1$ galaxies. It can be seen that the two distributions are in good agreement, both peaked around $b/a \simeq 0.6 - 0.7$, and displaying a deficit of objects with $b/a < 0.3$; these results are also consistent with those obtained by Ravindranath et al. (2006) who used HST ACS optical data to model the rest-frame UV morphologies of galaxies at $z \sim 3 - 4$, and with Yuma et al. (2011) who conduct a similar analysis at $z \simeq 2$. The implications of these peaked axial-ratio distributions are discussed further in Section 3.7.3.

Finally, in the right-hand panel of Fig. 3.11 I confirm that the axial-ratio distribution displayed by my *passive* disks at $1 < z < 3$ is indeed consistent with that displayed by the disk-galaxy population at low redshift as deduced from

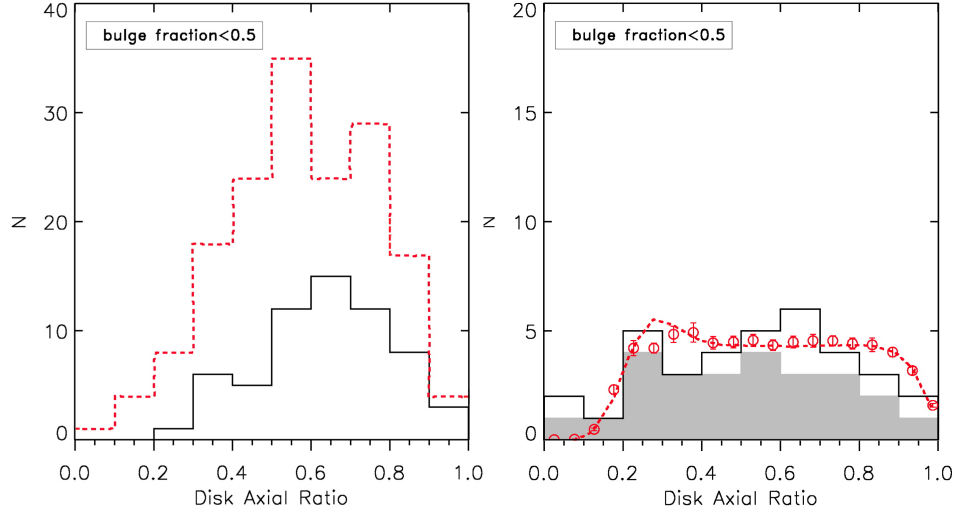


Figure 3.11 *Comparison of my disk-dominated galaxy axial-ratio distributions with other relevant recent results from the literature. In the left-hand panel I again plot the axial-ratio distribution of my star-forming disks (in black solid outline), but also over-plot (in the red/dashed histogram) the axial-ratio distribution of $n \simeq 1$, $z \simeq 1.5 - 3.6$ star-forming disk-galaxies from Law et al. (2012); the two distributions are indistinguishable. In the right-hand panel I plot (in black solid outline) the axial-ratio distribution of my passive disks as judged by $sSFR = 10^{-10} \text{ yr}^{-1}$ from SED fitting and over-plot (in grey shaded regions) the corresponding distribution after excluding the apparently passive disks which appear to have $24 \mu\text{m}$ counterparts. These are compared with local results in the form of the best-fit model axial-ratio distribution (red dashed line) and the actual measured distribution of axial ratios from a fitted single-component model (red points with corresponding error-bars) of local SDSS spiral galaxies from Padilla & Strauss (2008) (where here I plot their normalised frequency scaled appropriately for direct comparison with my results). This comparison illustrates that the relatively flat axial-ratio distribution displayed by my sample of passive disks at $1 < z < 3$ is consistent with results from local disks, whilst the peaked distribution of star-forming galaxies is in good agreement with previous studies of similar galaxies conducted at $z \simeq 2$.*

the SDSS. The axial-ratio distribution for my passive disks is shown here both with and without inclusion of the $24\,\mu\text{m}$ -detected objects, to demonstrate that its shape is unchanged by this extra level of caution in excluding potential star-forming objects. These histograms have been over-plotted with the data points and best-fit model from Padilla & Strauss (2008); their normalised frequencies have simply been re-scaled here by the area under my solid histogram to ease direct comparison with my results. As can be seen, my distribution agrees well with the relatively flat distribution displayed by present-day disk-dominated galaxies. I also compared my results with the axial-ratio distribution presented by van der Wel et al. (2011) for a sample of 14 $z \simeq 2$ disk-dominated passive galaxies, and found them to be consistent, although the statistics are weak given the limited size of both samples ($p = 0.15$).

3.7 Conclusions

I now discuss the implications of my results in the context of other recent studies of massive galaxies at comparable redshifts, and current models of galaxy formation and evolution.

3.7.1 Galaxy growth

Based on a complete, mass-selected sample of $\simeq 200$ galaxies with $M_* > 10^{11} M_\odot$, my HST WFC3/IR study provides the most detailed information to date on the sizes of the most massive galaxies at $1 < z < 3$.

First considering the single component analysis presented in Chapter 2, my most basic statistical measurement is that the median size of these galaxies is 2.6 ± 0.2 kpc, a factor 2.3 ± 0.1 smaller than the size of comparably-massive galaxies today. Splitting the sample at $z < 2$ and $z > 2$ yields a gentle trend with redshift (at $\sim 2 - \sigma$ level), with the median descending from 2.7 ± 0.3 kpc at $1 < z < 2$, to 2.5 ± 0.3 kpc at $2 < z < 3$, corresponding to factors of 2.2 ± 0.2 and 2.3 ± 0.2 below the local size-mass relation.

These results are $\simeq 20\%$ smaller than the results reported for a comparable mass-selected sample of galaxies at comparable redshifts by van Dokkum et al. (2010), but potential reasons for this disparity are discussed in Chapter 2. Moreover, this

detailed single-component analysis reveals that the scatter in size for the most massive galaxies within this redshift regime is large, with $32 \pm 3\%$ of my objects lying on the local size-mass relation, within its $1\text{-}\sigma$ scatter, and $68 \pm 3\%$ lying below it.

In comparison with the work presented in this chapter, when my galaxies are split into their bulge and disk components, it is clear that the bulges display more rapid evolution to small sizes, both in terms of median size, and in terms of the relative numbers of objects which lie on and below the present-day size-mass relation. For the disks, I find that, throughout my redshift range, $\simeq 40\%$ lie on the local relation, with $\simeq 60\%$ below, while for the bulges the percentage of objects which lie significantly below the local relation is significantly higher: $80 \pm 4\%$ at $1 < z < 2$ and $85 \pm 5\%$ at $2 < z < 3$. Clearly bulges consistent with the local size-mass relation are rare at these redshifts and, moreover, the compact bulge population appears to become increasingly compact with increasing lookback time, lying a factor 3.5 ± 0.5 below the local relation at $1 < z < 2$ but a factor 4.4 ± 0.3 below at $2 < z < 3$ (the corresponding figures for the subset of compact disks are more modest, 2.4 ± 0.4 and 2.5 ± 0.2 respectively). Here, my results for bulges match very well those recently reported by Szomoru et al. (2012), who used the CANDELS imaging in GOODS-South to deduce that quiescent galaxies at $1.5 < z < 2.5$ with median Sérsic indices $n \simeq 3.7$ lie a factor of $\simeq 4$ in size below the local size-mass relation. A related issue is the morphological mix of the objects selected as compact. For example, it has recently been suggested by van der Wel et al. (2011) (albeit based on a sample of only 14 objects) that the “majority” of compact galaxies at $z \simeq 2$ are disk-dominated. Fig. 3.7 illustrates that such a statement is not straightforward, as it depends on what one defines as compact and what mass range is to be considered. Certainly it is clear from Fig. 3.7 that the most massive and compact objects (i.e. the galaxies with $M_* > 2 \times 10^{11} M_\odot$, and $R_e < 3 \text{ kpc}$) are *all* bulge-dominated, but at more moderate masses the situation is certainly more mixed. A direct comparison is limited by the somewhat complex mix of criteria used by van der Wel et al. (2011) to classify an object as disk-dominated (as compared to my straightforward use of $B/T < 0.5$) but clearly Fig. 3.7 does reveal a substantial population of compact disks as quantified above, and I confirm that essentially all the *passive* disks are comparably compact to their spheroidal counterparts.

Third, while my sample is clearly somewhat limited in terms of dynamic range in stellar mass, I find evidence for a lower envelope in size which tracks the slope

of the present-day size-mass relation. This trend is strengthened by the results of my bulge+disk decomposition, which extends the size mass relation down to estimated sub-component masses $M_* \simeq 2 \times 10^{10} M_\odot$. Thus, for $M_* > 2 \times 10^{11} M_\odot$ I find no objects significantly smaller than $R_e \simeq 1$ kpc, while at $M_* < 1 \times 10^{11} M_\odot$ I start to see examples of even smaller bulges and disks, with some bulges as small as $R_e \simeq 0.4$ kpc. These details, including the trend of minimum size with stellar mass are important when comparing with previous studies; for example, Szomoru et al. (2010) have reported a very small scale-length of $R_e = 0.42 \pm 0.14$ kpc from WFC3/IR imaging of a compact bulge-dominated galaxy at $z = 1.91$, but with an estimated stellar mass of $M_* \simeq 5 \times 10^{10} M_\odot$ (Wuyts et al. 2008), it is clear that this object lands perfectly on the lower envelope of the size-mass relation displayed by the bulge components in Fig. 3.7. The single object studied by Szomoru et al. (2010) was the most massive, quiescent $z \simeq 2$ galaxy available for study in the Hubble Ultra Deep Field. A comparably-detailed study of the brightest galaxy at $z > 1.5$ in the ten-times-larger ERS field by van Dokkum & Brammer (2010) again yielded a Sérsic index $n \simeq 4$, but this time an effective radius $R_e \simeq 2.1 \pm 0.3$ kpc and a much larger galaxy mass $M_* \simeq 4 \times 10^{11} M_\odot$; again, comparison with the results shown in Fig. 3.7 shows that this is perfectly consistent with the size-mass locus for bulges uncovered here. I also note that within Fig. 3.7 I see no real evidence in support of the claim advanced by Ryan et al. (2012) that the required size growth of galaxies from $z \simeq 1.5$ to the present is a strong function of stellar mass. A direct comparison is difficult because my extension to lower masses is primarily based on bulge+disk decomposition, but I note here that Cimatti et al. (2012) also find no evidence for any stellar-mass dependence in the redshift growth-rate of early-type galaxies.

Fourth, it is also clear that the objects which remain on the local relation, even out to the highest redshifts, are star-forming disks, with the passive galaxies, including the passive disk components, confined to the more compact population. This result mirrors that recently reported by McLure et al. (2013) who found, for spectroscopically-confirmed galaxies of comparably high mass at $z \simeq 1.4$, that all objects with low $sSFR$ (i.e. $sSFR < 10^{-10} \text{ yr}^{-1}$) lie below the present-day size-mass relation, irrespective of morphological classification. At $z \simeq 2.3$ a comparable trend for star-forming objects to be 2 – 3 times larger than their quiescent counterparts has been reported by Kriek et al. (2009) for a sample of 28 galaxies with $M_* \simeq 3 \times 10^{10} M_\odot$, a result confirmed as extending to even lower masses by Szomoru et al. (2011), who also found star-forming galaxies at $z \simeq 2$ to be larger than their quiescent counterparts in the mass range $M_* \simeq$

$1 - 10 \times 10^{10} M_{\odot}$.

In summary, my results confirm and clarify a number of trends in the galaxy size-mass relation previously reported from detailed studies of small numbers of objects with HST, or larger samples studied via ground-based imaging. Within the high-mass regime my study provides significantly improved statistics on the scatter in size, and how the size-mass relation evolves differently for bulges and disks in the redshift range $1 < z < 3$. My bulge+disk decomposition is the most extensive attempted to date, and suggests that these trends extend to the bulge components of disk-dominated galaxies, and to the disk components of bulge-dominated galaxies. I also provide the first clear evidence for a lower envelope in size which my bulge+disk decomposition suggests extends from my high-mass sample down to lower masses ($M_* \simeq 2 \times 10^{10} M_{\odot}$), tracking the slope of the present-day size-mass relation.

Many authors have discussed the theoretical challenge of explaining the growth in the size of massive galaxies from $z \simeq 2$ to the present. Various arguments, based on Λ CDM simulations, clustering analyses (e.g. Quadri et al. 2007, Hartley et al. 2010) and simple comoving number density comparisons (e.g. van Dokkum et al. 2010) indicate that the $M_* \simeq 10^{11} M_{\odot}$ galaxies studied here at $1 < z < 3$ must evolve into galaxies with stellar masses $M_* \simeq 3 \times 10^{11} M_{\odot}$ which are essentially all giant elliptical galaxies on the high-mass end of the local early-type size-mass relation plotted in red in Fig. 3.7. The issue of what happens to the disk components so evident in the high-redshift population (but essentially absent in the present-day descendants) is discussed further below. But in terms of size evolution, the challenge is to explain how such compact massive galaxies (especially the extremely compact bulges at $z > 2$ which lie a factor $\simeq 4$ below the present-day relation) can evolve onto the present-day size-mass relation without simultaneously attaining excessively high masses which violate constraints imposed by the measured present-day mass function (Baldry et al. 2012).

As pointed out by various authors (e.g. McLure et al. 2013), major mergers do not provide a sufficiently vertical evolutionary track on the size-mass plane to lift the compact high-redshift galaxies onto the present-day relation without yielding excessively high masses. In any case, size growth driven primarily by major mergers would require many more major mergers since $z \simeq 2$ than appears plausible from N-body simulations (which suggest < 2 per massive galaxy by the present day; e.g. Hopkins et al. 2010b), or indeed from observed merger rates

(e.g. Robaina et al. 2010).

Thus while the rare major mergers may be responsible for the relaxation process which at some stage destroys the disk component (although a series of minor mergers may also achieve this; Naab et al. 1999, Bournaud et al. 2007b) it appears that the bulk of the size growth must be attributed to minor mergers which are much more effective at adding stars and dark matter in the outer regions of galaxies, increasing observed size with relatively limited increase in stellar mass. It is also worth noting that minor mergers are more effective than major mergers at raising the dark-matter to stellar-mass ratio to the levels observed for the most massive galaxies today, are better able to add mass while leaving the age and metallicity gradients in the central regions of massive galaxies unscrambled, and may provide a natural explanation for the kinematically decoupled cores frequently observed in present-day ellipticals (e.g. van den Bosch et al. 2008)

As illustrated by McLure et al. (2013), a combination of five minor (mass ratio 1:10) mergers and a single major merger (mass ratio 1:3) appears sufficient to achieve the required evolution since $z \simeq 1.4$. Recent simulations analysed by Oser et al. (2012) also support the idea that minor mergers can produce the required size evolution at $z < 2$. However, whether this sort of evolutionary path can also solve the problem for the most compact spheroids at $z > 2$ is still a matter of some debate (Newman et al. 2012, Cimatti et al. 2012).

Finally, it is worth emphasizing that despite the ongoing debate of how such compact high-redshift galaxies can climb onto the present-day size-mass relation, the existence of such compact objects at early times, while perhaps initially unexpected, is in fact a natural prediction of modern galaxy-formation simulations (e.g. Khochfar & Silk 2006, Obreschkow & Rawlings 2009, Hopkins et al. 2010a, Wuyts et al. 2010).

3.7.2 Morphological evolution

As the bulge components decline in size with increasing redshift, I also find a clear trend for the massive galaxies in my sample to become increasingly disk-dominated. As shown in Fig.3.8, $z \simeq 2$ appears to mark a morphological transition epoch, at least for my chosen galaxy mass range; crudely speaking, the majority of my galaxies are bulge-dominated ($B/T > 0.5$) at $z < 2$, while the situation is reversed at $z > 2$. Moreover, at the highest redshifts ($z \simeq 2.5$),

over half the galaxies have $B/T < 0.3$ and over half of these (i.e. $\simeq 35\%$ of all objects in the relevant redshift range) are “pure disks” as judged by $B/T < 0.1$ (which I cannot distinguish from $B/T = 0$). Such highly disk-dominated objects are virtually absent in my high-mass sample by $z \simeq 1.5$, although it is still true that the vast majority of objects contain some detectable disk component, with “pure de Vaucouleurs bulges” (i.e. $B/T > 0.9$) still largely absent until $z < 1$.

The relative lack of pure de Vaucouleurs bulges at $z > 1$ appears broadly consistent with the findings of Buitrago et al. (2011) who reported that ellipticals have been the dominant morphological class for massive galaxies only since $z \sim 1$, although a direct comparison of my results is difficult as Buitrago et al. (2011) did not attempt bulge+disk decomposition and relied on a combination of single Sérsic fitting and visual classification.

The presence of a significant fraction of disk-dominated objects, even among the apparently passive subsample, has already been reported at $z \simeq 1.5$ for masses $M_* > 10^{11} M_\odot$ by McLure et al. (2013) ($44 \pm 12\%$) and at $z \simeq 2$ for masses $M_* > 6 \times 10^{10} M_\odot$ by van der Wel et al. (2011) ($40 - 65\%$). However, these studies do not extend to high enough redshift to capture the full extent to which disk-dominated galaxies, primarily star-forming, come to dominate the massive galaxy population at $z > 2$ as illustrated in Figs. 3.8 and 3.9.

Given the axial ratio distributions plotted in Figs. 3.10 and 3.11, it might be argued that, while the more passive disks may indeed be disks, the star-forming disk-like objects might be more tri-axial in nature, given their more peaked (i.e. typical rounder) axial ratios. However, as discussed further in the next subsection, visual inspection of both the active and passive disk dominated objects supports the view that they are indeed disks; the only mystery is the lack of any very thin edge-on disks in the star-forming population which I return to at the end.

It is worth again bearing in mind that virtually all the objects in this study are destined to evolve into today’s very massive $M_* > 3 \times 10^{11} M_\odot$ giant elliptical galaxies which display, at most, very low-level disk components. This alone means it may be naive to expect the properties of many of these disks to correspond closely to those of $M_* \simeq 1 \times 10^{11} M_\odot$ disk galaxies in the present-day Universe. Indeed it has been argued that the stellar densities of these high-redshift massive disks are comparable to those found in the cores of massive present-day bulges (Bezanson et al. 2009, van Dokkum et al. 2010), consistent with the inside-out model of massive galaxy growth discussed above.

3.7.3 Star-forming and quiescent galaxies

Chapters 2 and 3 have deliberately focussed on H_{160} morphologies, with a detailed analysis of the colours of the bulge and disk components deferred to Chapter 4. Nevertheless, as explained in Chapter 2, the SED fitting undertaken to deduce the photometric redshifts also yielded dust-corrected ($SFR_{UV,dust\ corrected}$) and $24\mu\text{m} + \text{non dust-corrected}$ (SFR_{UV+IR}) star-formation rates and stellar masses, from which I can derive an estimate of $sSFR$ for each galaxy in my sample. As illustrated in Fig. 3.9, I have then followed Bell et al. (2012) by also highlighting *all* $24\mu\text{m}$ detections to try to ensure against misinterpreting dust-reddened star-forming galaxies as quiescent objects. In general the results of this latter test are reassuring, with the vast majority of star-forming objects (defined as $sSFR > 10^{-10} \text{ yr}^{-1}$) yielding $24\mu\text{m}$ detections, as compared to relatively few of the objects with $sSFR < 10^{-10} \text{ yr}^{-1}$ being detected by the SpUDS MIPS imaging. As already summarized in Section 3.6.3, the vast majority of the disk-dominated galaxies are star-forming, while the majority of the bulge-dominated objects are quiescent, but yet my sample contains a significant number of star-forming bulges and a significant number of “quiescent” disks; 25 – 50% of the passive subsample are disk-dominated, depending on whether one splits by Sérsic index or B/T , and on whether the few $24\mu\text{m}$ detections of the supposedly passive objects are deemed symptomatic of star-formation or buried AGN.

Thus, to first order, my results show that the well-documented bimodality in the colour-morphology plane seen at low redshift, where spheroidal galaxies inhabit the red sequence, while disk galaxies occupy the blue cloud (Baldry et al. 2004, Driver et al. 2006, Drory & Fisher 2007) is at least partly already in place by $z \simeq 2$. However, the colour-morphology division is undoubtedly much less clean than in the nearby Universe, and a key challenge is to determine the prevalence and physical significance of the passive disks and the active bulges.

Recent studies have produced apparently conflicting results over the prevalence or otherwise of massive passive disks at these redshifts. Specifically, while van der Wel et al. (2011) and McLure et al. (2013) both conclude that $\simeq 50\%$ of passive objects at these redshifts are disk dominated, Bell et al. (2012) find that the key parameter which correlates best with quiescence at these redshifts is still Sérsic index, with the presence of a substantial bulge a necessary (but not necessarily sufficient) condition for the termination of star-formation activity. This confusion may be partly a matter of definition; it is not clear what a “substantial” bulge

component means, or how comparable the morphological criteria applied in these studies really are. Nevertheless, given the controversy over this issue, and its potential importance, I have carefully revisited the passive disk-dominated objects in my sample, motivated in part by the fact that five of the ten apparently passive “pure disks” (i.e. $B/T < 0.1$) originally isolated on the basis of the $SFR_{UV,dust\ corrected}$ or SFR_{UV+IR} in Fig. 3.9 transpired to have $24\mu\text{m}$ detections.

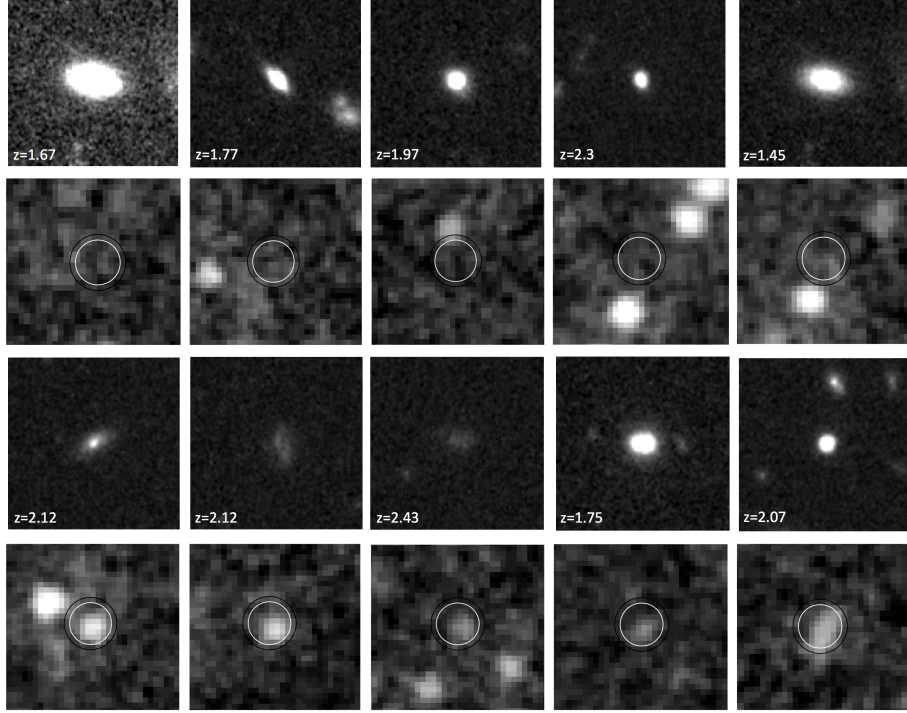


Figure 3.12 *The WFC3/IR H_{160} and Spitzer $24\mu\text{m}$ images of the ten apparently bulgeless pure-disk objects in my sample which the optical-near-infrared SED fitting suggests are passive (i.e. $sSFR < 10^{-10}\text{ yr}^{-1}$). The top row shows 6×6 arcsec images of the five objects which have no significant $24\mu\text{m}$ counterpart, as shown in the 20×20 arcsec MIPS image stamps in the second row (the circle indicates a 5 arcsec radius aperture, which is a very generous search radius). The third and fourth rows show the same information for the five objects which do have $24\mu\text{m}$ counterparts.*

In Fig. 3.12 I show the H_{160} image stamps for these ten interesting objects, along with their $24\mu\text{m}$ MIPS imaging. The $24\mu\text{m}$ detections of the five MIPS catalogue-matched objects (shown in the bottom row) are clear, but equally clear is the fact the top five objects do not possess even marginal mid-infrared detections at the depth of the SpUDS imaging. I note that adopting my secondary check from the $24\mu\text{m}$ to SFR conversion from Rieke et al. (2009), the $24\mu\text{m}$ -detected objects in

the bottom row of Fig. 3.12 have fluxes which, if interpreted as arising from star formation, imply typical values of $sSFR \simeq 10^{-9} \text{ yr}^{-1}$, and that the SpUDS MIPS detection limit (Rieke et al. 2009) conveniently corresponds rather closely to the adopted passive/active $sSFR$ threshold of $sSFR \simeq 10^{-10} \text{ yr}^{-1}$ (for galaxies in this redshift and mass range).

Thus, since I have no real reason to assign the MIPS detections to AGN activity (other than the fact that several of these objects prefer a small contribution from a point-source rather than a resolved bulge in the multi-component H_{160} modelling) I have taken an *even more conservative* approach, and have classified the lower five objects in Fig. 3.12 as star-forming, which reduces the number of passive “pure” disks by half, to five. This represents less than 15% of the “pure disk” sample, and so clearly the vast majority of *apparently bulgeless* disks are actively star-forming galaxies on the main-sequence. Nevertheless, this still means that a substantial fraction of the passive galaxy subsample (25 – 40%) is disk-dominated, and it is as yet unclear whether the relative rarity of completely bulgeless quiescent disks reflects an important causal link between bulge growth and passivity at these redshifts, or is simply an inevitable symptom of the dimming of star-forming disks as star-formation activity dries up (for whatever reason). These issues, and the prospects for further progress, are discussed further in Section 3.7.4.

Moving now to consider the active disks, I attempt to investigate a little further the apparent contradiction between the results of my Sérsic fitting and the axial-ratio distribution displayed by these supposedly disk-like star-forming objects. As already mention in Section 3.6.4 (and see Figs. 3.10 and 3.11) while the axial distribution for the passive disk components is as flat as that displayed by low-redshift disk galaxies, that displayed by the star-forming “disks” does not extend to such low values, and peaks at $b/a \simeq 0.7$. This is essentially identical to the distribution found by Law et al. (2012), who also commented that such an axial-ratio distribution was more in line with that expected from a population of tri-axial objects.

I have therefore tried to check whether my active disk-dominated objects do indeed look like star-forming disks. This is somewhat against the spirit of my analysis which seeks to deliberately avoid the pitfalls of visual classification. Nevertheless, image inspection can still offer an interesting sanity check on the interpretation of modelling results. In Fig. 3.13, I therefore show, for illustrative purposes, the images, model-fits, and residual data-model images of the five star-forming galaxies which I find to have Sérsic indices closest to unity (in practice,

$n \simeq 0.9 - 1.1$). By (possible) coincidence all five of these objects are in fact fairly round, but it is visually obvious that they are not spheroidal galaxies, but rather face-on disks with spiral arms and/or star-forming clumps. I am thus left to conclude that I have no reason to really doubt the disk-like nature of these objects just because of their axial ratio distribution. Perhaps it is simply the case that very few of the (violently) star-forming disks at these epochs are genuinely thin enough to display low axial ratios, or alternatively such disks may be so dusty that near edge-on examples have in fact evaded my detection limit (this might seem unlikely, but see Targett et al. 2013).

A full review of the already extensive observational and theoretical literature on the nature and importance of clumps in star-forming disk galaxies at $z \simeq 2$ is beyond the scope of this work. Suffice to say that, given the above-mentioned lack of evidence for major mergers being the primary driver of elliptical galaxy evolution, it has now been suggested that the progenitors of today's giant ellipticals are these high velocity dispersion, clumpy disks, in which star formation is fed by cold streams and minor mergers (e.g. Dekel et al. 2009b, Ceverino et al. 2010; 2012) with the clumps eventually coalescing to form a spheroid. However this view of the potential importance of the observed clumps in building bulges (e.g. Guo et al. 2011b) has been challenged observationally (e.g. Wuyts et al. 2012) and theoretically (e.g. Genel et al. 2012). Nevertheless, whether or not the clumps are the direct ancestors of bulges, what is clear from my study is that the majority of progenitors of today's most massive elliptical galaxies are indeed, at least at $2 < z < 3$, clumpy, and fairly extended, star-forming disk galaxies (a result reinforced by the properties of the extreme star-forming galaxies as deduced from the CANDELS imaging of sub-millimetre galaxies by Targett et al. 2013).

Finally, I note that the presence of at least some star-forming spheroids in my $1 < z < 3$ sample is unsurprising. Various authors have observed this before at comparable redshifts, including Bell et al. (2012) who, while arguing that bulge formation was a potentially necessary condition for the quenching of star formation, also concluded that it was not sufficient to ensure this, given the presence of star-forming galaxies in their sample with $n > 2.5$ (although see also Wang et al. 2012).

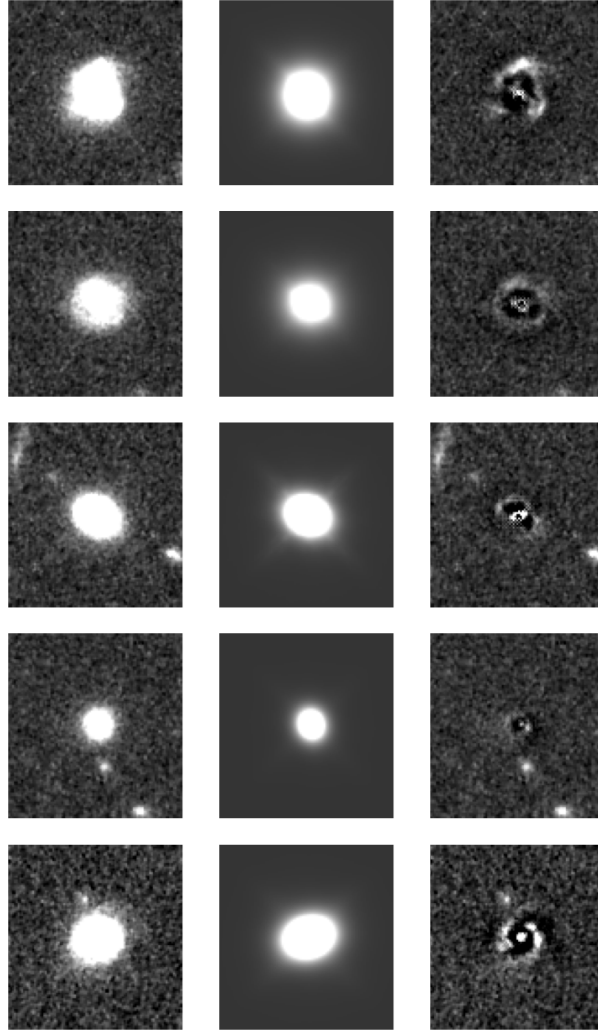


Figure 3.13 H_{160} images (left), models (centre) and model-data residual (right) (all 6×6 arcsec) for a subset of five of my star-forming ($sSFR > 10^{-10} \text{ yr}^{-1}$) disk-dominated ($B/T < 0.5$) galaxies. The five galaxies shown here have been chosen to have single Sérsic indices in the range $\simeq 0.9 - 1.1$ thus demonstrating that, despite the bulge-like axial ratio distributions for my sample of star-forming galaxies (as discussed in Section 3.6.4), the galaxies with single Sérsic index consistent with traditional disk-like ($n = 1$) values show clear face-on disk morphologies, and are not especially disturbed systems. In addition my residual image stamps highlight the clumpy structure within these disks, as expected for violently star-forming disks at high redshift (see Section 3.7.3).

3.7.4 Passive disks and quenching

I conclude this discussion by exploring further the nature of the apparently passive disk-dominated objects in my sample, and considering briefly the potential implications for the the connection, if any, between termination of star-formation activity and morphological transformation.

As already noted, the axial-ratio distributions presented in Figs. 3.10 and 3.11 suggest that the passive disks in my sample have similar intrinsic shapes to low-redshift disks, while, on average, the star-forming disks do not. As a final check on the nature of the passive disks I show, in Fig. 3.14, images of the model disks fitted to all 25 of the confirmed passive disk-dominated galaxies in my sample (i.e. those with $B/T < 0.5$ and $sSFR < 10^{-10} \text{ yr}^{-1}$ which also have no $24 \mu\text{m}$ detection). In this plot the disks are shown at high resolution (i.e. FWHM 0.05 arcsec) and scaled to comparable surface brightness levels, making it easier to see the full range of axial ratios found. This figure demonstrates that the flat axial-ratio distribution of passive disks is not a result of strange, excessively-elongated or otherwise unphysical disks which GALFIT has attempted to fit to deal with other peculiarities in the data. In addition, the full range of fitted sizes can be seen at a wide range of axial ratios (i.e. viewing angles).

I thus have no reason to doubt that these are, as suggested by the Sérsic and double-component fits, genuine passive disks.

The presence of a significant population of passive disks among the massive galaxy population at these redshifts indicates that star-formation activity can cease without a disk galaxy being turned directly into a disk-free spheroid, as generally previously expected if the process that quenches star formation is a major merger. Thus, while some fraction of the substantial population of star-forming disks may indeed suffer a major merger (possibly transforming rapidly into a compact passive spheroid, although see also Kaviraj et al. 2012) my results argue that another process must exist which is capable of terminating star-formation activity while leaving a substantial disk intact.

One possibility arises from the latest generation of hydrodynamical simulations (Kereš et al. 2005, Dekel et al. 2009a) and analytic theories (Birnboim & Dekel 2003, Dekel & Birnboim 2006), which suggest a formation scenario whereby at high redshift star formation in massive disks takes place through inflows of cold gas until the dark-matter halos in which the galaxies reside reach a critical mass

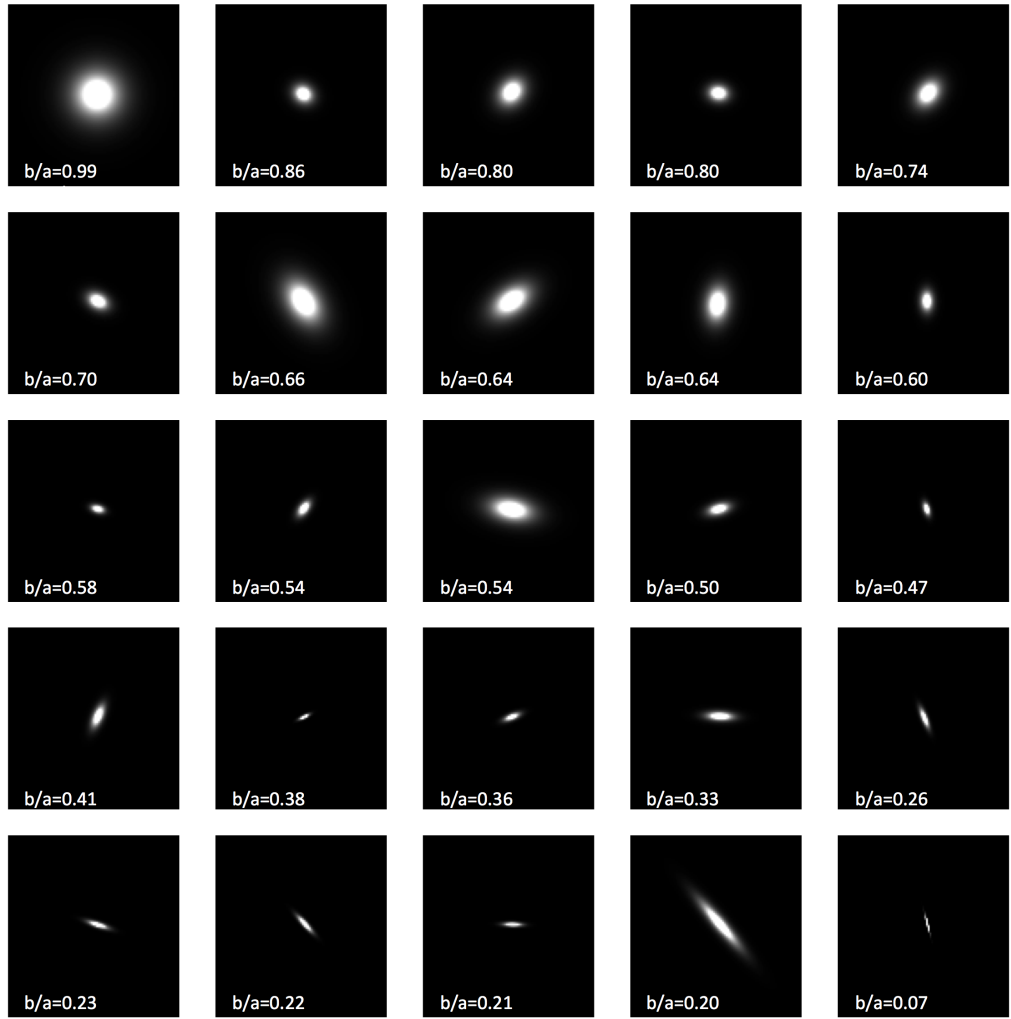


Figure 3.14 *The model disk components of the 25 disk-dominated ($B/T < 0.5$) galaxies within my sample which show no evidence for star formation from either SED fitting ($sSFR < 10^{-10} \text{ yr}^{-1}$) or $24 \mu\text{m}$ counterparts. The models have been constructed from the best-fit disk parameters from my double-component analysis and have been convolved with a model PSF generated from a Gaussian of $FWHM=0.05 \text{ arcsec}$, providing artificial imaging comparable to that achievable by HST at the bluest optical wavelengths. Each stamp is again $6 \times 6 \text{ arcsec}$ in size, and the grey-scale for these images is set at black=0 and white= $1/3$ of the maximum pixel value of each image, so as to provide consistent brightness cuts for each stamp at an appropriate level. The models have been ranked by descending axial ratio from the top left to the bottom right. These are the 25 models which were used to produce the axial-ratio distribution of passive disks shown in Fig. 3.11 (in the grey histogram of Fig. 3.10b), and this illustration shows that there is no reason to doubt that they are genuine disks (i.e. no disk displays an unreasonable scale-length, and disks covering the full range of fitted sizes are apparently visible over the full range of inclination angles). This provides further evidence of the genuine disk-like morphologies of these passive systems, the implications of which are discussed in Section 3.7.4.*

($> 10^{12} M_{\odot}$) below $z = 2$. At this point the virial temperature of the halos is high enough to prevent efficient cooling such that pressure can be built to support a stable extended virial shock, which can be triggered by minor mergers. This results in the galaxy residing in a hot medium and below $z = 2$ a stable shock can also be sustained in the cold streams, which stops cold gas inflowing and quenches star formation, but does not cause any accompanying change in underlying morphology.

The idea that star-formation quenching and morphological transformation are distinct processes is also consistent with the empirical description of Peng et al. (2010), who suggest that, in this high-mass regime, the star-formation quenching of galaxies is driven by a process governed by “mass-quenching”, where the rate of star-formation suppression is proportional to the star-formation rate of the galaxy.

Another scenario which can account for star-formation quenching, whilst still being consistent with the existence of passive disks, is the model of violent disk instabilities (Dekel et al. 2009b, Ceverino et al. 2010, Cacciato et al. 2012). This model suggests that, as the disk evolves, there is an inflow of mass to the centre of the disk, which gradually builds to form a massive bulge. This mass inflow can quench star formation whilst still retaining a massive disk in a process known as “morphology quenching” (Martig et al. 2009). In addition to this, it also agrees with the observed trend in morphologies with redshift observed in this study, i.e. the transition from predominantly bulge systems in the local Universe, to the increase in mixed bulge+disk morphologies between $1 < z < 2$, and then the dominance of disk-dominated objects beyond $z = 2$.

Finally, returning to the data, in considering the possible evolutionary links between the active and passive disks in my sample, it must be remembered that there are important observational differences between these populations. First, while the passive disks are not especially compact (median disk-component $r_e = 2.6 \pm 0.7$ kpc), they are, on average, significantly smaller than the active disks (median disk-component $r_e = 4.0 \pm 0.5$ kpc). However, it is not clear that this is a serious problem; Fig. 3.7 shows a significant fraction of the active disks are also reasonably compact and, in any case, some scenarios (e.g. the model of morphology quenching described above) might naturally lead to a disk reducing in size somewhat as star-formation activity turns off. Second, of course, how the relatively thin disks in the passive population emerge from a star-forming population which apparently lacks objects with low axial ratios still needs to be

explained. Again, it is hard to know if this is a real problem. It seems entirely plausible that a maximally-unstable, violently star-forming disk will settle down into a significantly flatter configuration once the fuelling source of, and violent feedback from star-formation activity ceases, but (to my knowledge) this has yet to be convincingly and quantitatively demonstrated by simulations. There are also still potential issues of selection effects which might mean that edge-on star-forming disks are unrepresented in flux-limited optical-UV selected samples (due, possibly, to dust obscuration). Interestingly, the axial-ratio distribution presented by Targett et al. (2013) for the extreme population of star-forming disks selected via sub-millimetre emission is relatively flat, and statistically indistinguishable from the axial-ratio distribution displayed by the passive disks in the current study.

Chapter 4

Multiple-Component SED Fitting

4.1 Introduction

Following on from Chapter 3, I have further utilised the bulge-disk morphological decomposition approach to extend my analysis to the additional three photometric bands covered by CANDELS in order to conduct separate-component SED fitting. This analysis has allowed separate stellar masses and star-formation rates to be estimated for the individual bulge and disk components. This new information has provided new insights into the size evolution of the bulge and disk components, which can now be separated into star-forming and passive sub-populations based on their specific star-formation rates.

4.2 Data

In Chapters 2 and 3, I have discussed the morphological analysis carried out on the high resolution near-IR H_{160} WFC3 imaging provided by CANDELS in the central 187 arcmin^2 of the UKIDSS UDS field. In order to provide improved statistics and to combat the issues of cosmic variance, for the following work I have extended my multiple component morphological analysis to the CANDELS COSMOS field. And have proceeded to conduct multiple-component SED fitting on both datasets.

As before, I have used the HST WFC3/IR data from the CANDELS multi-cycle

treasury programme (Grogin et al. 2011, Koekemoer et al. 2011) centred on the UKIDSS Ultra Deep Survey (UDS; Lawrence et al. 2007) field, and now also make use of the CANDELS imaging in the COSMOS (Scoville et al. 2007) field. Both the CANDELS UDS and COSMOS near-infrared data comprise of 4×11 WFC3/IR tiles covering a total area of 187 arcmin^2 in each field, in both the F125W and F160W filters. The integration times are $\frac{4}{3}$ -orbit per pointing in H_{160} and $\frac{2}{3}$ -orbit in J_{125} , giving $5\text{-}\sigma$ point-source depths of 27.1 and 27.0 (AB mag) respectively for both fields. In addition to the near-infrared data used in the previous chapters, for this extended analysis I have also made use of the accompanying CANDELS HST ACS parallels in the F814W and F606W filters (hereafter i_{814} and v_{606}). The WFC3 and ACS cameras are offset by 6 arcmin in the HST focal plane and during the CANDELS observations were oriented to provide the maximum area of contiguous WFC3+ACS coverage. A schematic of the WFC3 and ACS coverage of both the UDS and COSMOS fields is shown in Fig. 4.1 and illustrates that $\sim 80\%$ of the area of both fields are covered by ACS and WFC3 pointings.

Whereas the WFC3 data has a depth of 2 orbits split between J_{125} and H_{160} , the larger field of view of ACS results in an effective 4 orbit depth, which has been split similarly to WFC3 to give $\frac{8}{3}$ -orbit per pointing in i_{814} and $\frac{4}{3}$ -orbit in v_{606} . This corresponds to $5\text{-}\sigma$ point-source depths of 28.4 for both the i_{814} and v_{606} bands in UDS and 28.5 in COSMOS, due to the inclusion of existing ACS legacy data in COSMOS (Grogin et al. 2011).

4.2.1 Supporting multi-wavelength data

In addition to the near-infrared imaging provided by HST, I have also utilised the multi-wavelength data-sets available in each field to constrain the SED fitting and determine the physical properties for the galaxies. For the UDS these include: u' -band imaging obtained with MegaCam on CFHT; deep optical imaging in the B , V , R , i' and z' -band filters from the Subaru XMM-Newton Deep Survey (SXDS; Sekiguchi et al. 2005; Furusawa et al. 2008); J , H and K -band UKIRT WFCAM imaging from Data Release 8 (DR8) of the UKIDSS UDS; and *Spitzer* $3.6 \mu\text{m}$, $4.5 \mu\text{m}$ IRAC and $24 \mu\text{m}$ MIPS imaging from the SpUDS legacy programme (PI Dunlop). For COSMOS they include: optical imaging in u' , g' , r' , i' and z' -bands from MegaCam CFHTLS-D2; z' -band from Subaru; Y, J, H & K_s from Ultra-VISTA (PI Dunlop); and *Spitzer* $3.6 \mu\text{m}$, $4.5 \mu\text{m}$ IRAC and $24 \mu\text{m}$ MIPS imaging

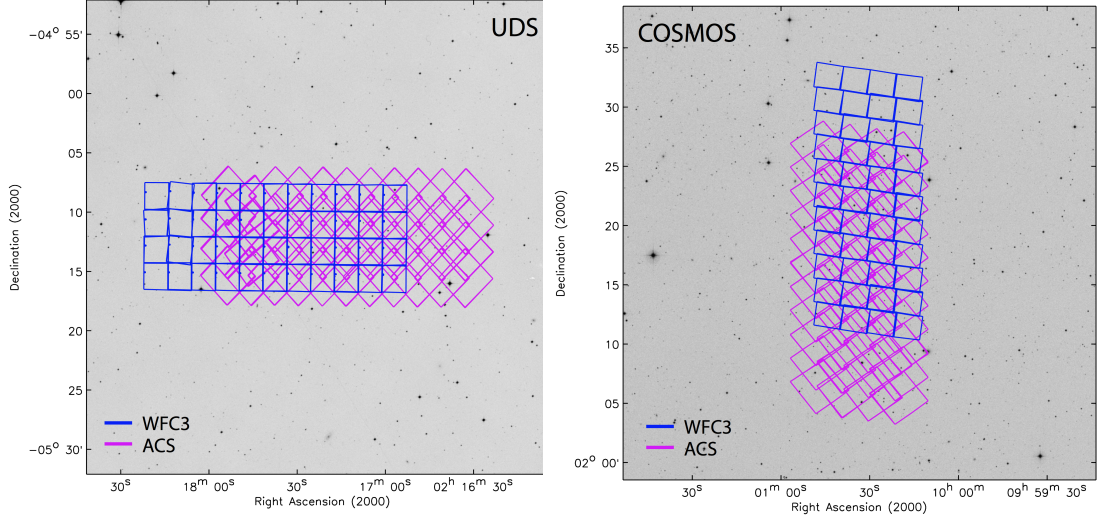


Figure 4.1 *Schematic of the WFC3 and ACS coverage in the UDS and COSMOS fields, taken from Grogin et al. (2011). The WFC3 pointings are outlined in blue, with the accompanying ACS parallels in purple.*

from the S-COSMOS survey (PI Sanders).

4.2.2 Sample selection

Following the sample selection procedure detailed in Chapter 2, the COSMOS sample was constructed using SEXTRACTOR (Bertin & Arnouts 1996) version 2.8.6 run on the H_{160} mosaic, smoothed to match ground-based resolution, and then cut at a limiting total magnitude of $H_{160} = 24.5$ to ensure that a reliable morphological analysis was possible. A multi-wavelength catalogue for SED fitting was then produced by Bowler et al. (2013, in preparation) by running SEXTRACTOR in dual-image mode on PSF-matched and re-gridded supporting photometry, with the CANDELS H_{160} mosaic adopted as the detection image. It should be noted that for both the UDS and COSMOS fields the photometry used in these catalogues, and employed in the subsequent SED fitting, is effectively taken from the iso-magnitude apertures generated by SEXTRACTOR on the H_{160} photometry, which provides the best estimate of the total magnitude of the objects in my samples. The only notable difference in the generation of the COSMOS catalogue compared to that for the UDS is the adoption of an updated IRAC de-confusion technique. GALFIT is first used to produce model fits to the high-resolution H_{160} imaging of the source. Subsequently, using the IRAC PSF,

GALFIT is used to generate a model of the IRAC data based on the structural parameters measured in the H_{160} data. By fitting the flux of each galaxy in the model to best reproduce the IRAC image, it is possible to extract accurate photometry from the confused $3.6\,\mu\text{m}$, $4.5\,\mu\text{m}$ data. Comparisons between this treatment of the IRAC imaging and the previous approach adopted in the UDS (Cirasuolo et al., in preparation) have been conducted to ensure that both techniques are robust and not prone to bias.

As detailed in Chapter 2, photometric redshifts for the COSMOS master sample were also determined using a χ^2 fitting procedure based on the photometric redshift code HYPERZ from Bolzonella et al. (2000), following Cirasuolo et al. (2007). These photometric redshifts were then used to conduct a secondary SED fitting in order to determine stellar mass estimates. As before, these estimates were based on the Bruzual & Charlot (2003) models with single-component exponentially decaying star-formation histories with e-folding times in the range $0.3 \leq \tau(\text{Gyr}) \leq 5$. However, in order to be fully consistent between both samples from UDS and COSMOS, the minimum model age limit of 50 Myr and the limited star-formation history templates adopted in the stellar mass and star-formation rate SED fitting (to ensure physically meaningful and self-consistent estimates, as discussed in Chapter 2), have been implemented in an updated manner and applied to both the COSMOS and UDS samples. Overall, this update has very little effect on the mass estimates of the UDS sample used in Chapter 2, however in a few cases it does act to lower the stellar mass of the best-fit model. As a result, I have redefined the UDS sample using the previous $1 < z < 3$ redshift and $M_* > 10^{11} M_\odot$ mass criteria and have applied the same selection to the COSMOS sample.

This results in a sample of 205 objects in the UDS (originally 215) and 191 objects in COSMOS. A comparison between the UDS and COSMOS samples is presented in Fig. 4.2, where it can be seen that the two fields show similar distributions of galaxy stellar mass as a function of redshift.

The co-moving number densities of both fields, and the combined sample, are shown in Fig. 4.3. These have been over-plotted with the co-moving number densities determined from the latest stellar mass function study at $0.2 < z < 4$ by Muzzin et al. (2013), which was conducted over the full $1.62\,\text{deg}^2$ of COSMOS covered by UltraVISTA. These plots show the co-moving number densities for galaxies with derived stellar masses of $M_* > 1 \times 10^{10} M_\odot$ (in asterisks) and $M_* > 1 \times 10^{11} M_\odot$ (in crosses), illustrating how the steepness of the mass function

at this high-mass end affects the number densities of objects. As can be seen, the number densities for $M_* > 1 \times 10^{11} M_\odot$ galaxies from Muzzin et al. (2013) are a factor of ≈ 1.6 lower than the values for my combined sample. However, given the mass functions fitted by Muzzin et al. (2013), the factor of 1.6 can be accounted for by a $\sim 35\%$ decrease in the mass estimates derived by Muzzin et al. at $M_* \simeq 1 \times 10^{11} M_\odot$ which, given the non-standard star-formation histories and stellar population age ranges adopted by Muzzin et al., is consistent with the expected level of systematic uncertainty associated with stellar masses derived from SED fitting.

As the sample sizes and areas in the UDS and COSMOS fields are comparable and there is good agreement between the co-moving number densities of the two fields, in the following sections the science results are based on the combined UDS and COSMOS sample, except for a few cases where the results are presented individually for each field specifically to facilitate comparison with the work described in Chapter 3.

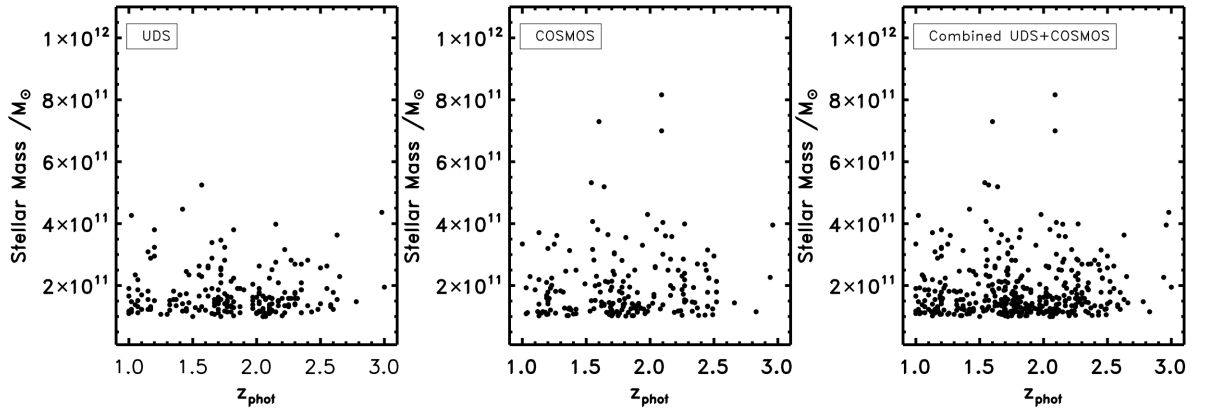


Figure 4.2 *Stellar mass versus redshift for the UDS, COSMOS and the combined fields. The similarity between the fields and the lack of obvious structures support the decision to combine the fields for the proceeding analysis.*

Finally, as discussed in detail in Chapter 2, the star-formation rate estimates for the COSMOS sample were determined in the same way as the UDS. I have adopted a value from SFR_{UV+IR} , as per Wuyts et al. (2011), if any of the objects in the sample have a $24\mu\text{m}$ counterpart within a 2 arcsecond radius in the catalogue of Roseboom et al. (2012), or a value from $SFR_{UV,dust\ corrected}$ if they do not have a $24\mu\text{m}$ counterpart.

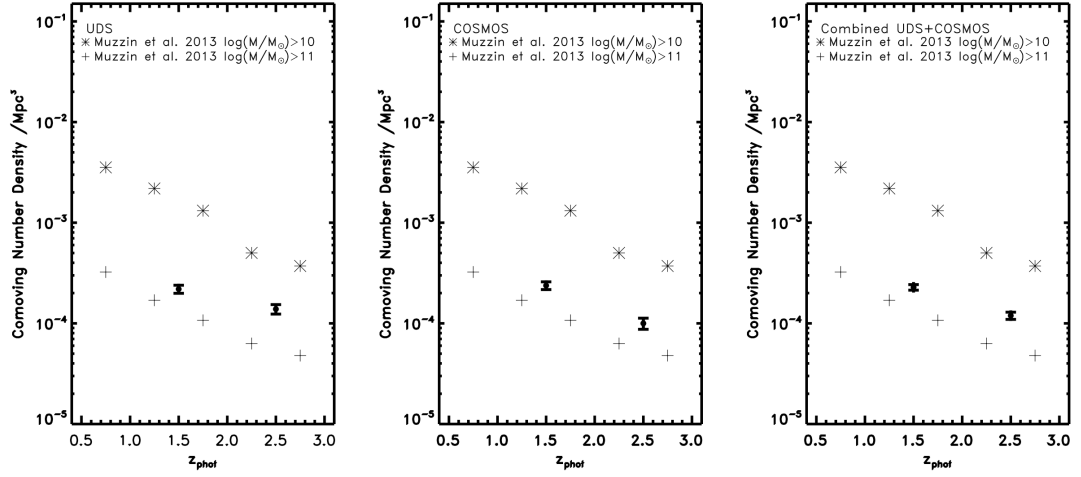


Figure 4.3 *Co-moving number densities of the UDS (left), COSMOS (middle) and combined fields (right) at $M_* > 10^{11} M_\odot$. These number densities have been over-plotted with the values from Muzzin et al. (2013) for their $M_* > 1 \times 10^{10} M_\odot$ and $M_* > 1 \times 10^{11} M_\odot$ mass bins, given by asterisks and crosses respectively. As has been discussed in the text, the lower values reported by Muzzin et al. for galaxies within a similar mass range to my study can be understood within the uncertainties associated with stellar mass estimates from SED fitting, especially given the steepness of the stellar mass function in this high-mass regime.*

4.3 Multiple-Component Morphology Fitting

The morphologies of the 396 objects in my combined UDS and COSMOS sample have been fitted with both single and multiple-Sérsic light profiles using GALFIT (Peng et al. 2002). The explicit procedures adopted for this analysis have been presented in Chapter 2 and Chapter 3, but are now outlined again in brief for completeness. For both the fitting procedures I have used an empirical PSF generated from a median stack of the brightest (unsaturated) stars in the individual fields. As detailed in Chapter 2, this provides the best measure of the on-image PSF, particularly in the 0.5 to 0.8 arcsec radius region of interest around the centre of each object (which corresponds to a physical size of $\simeq 5$ kpc at $1 < z < 3$), and has been tested in comparison to a modelled PSF from Tiny Tim (Krist 1995).

In addition to this, I have also adopted a consistent object-by-object background determination by calculating the median value within an annular aperture centred

on each source with an inner radius of 3 arcsec and an outer radius of 5 arcsec. This technique has been tested extensively in Chapter 2, and the background from the 3 – 5 arcsec annulus was determined to provide a robust estimate of the background for the massive, bright, galaxies in my sample. Once the background estimates were calculated for each object they were then subtracted from the 6×6 arcsec image stamp which is used as the input to GALFIT. This image stamp is used in conjunction with the corresponding sigma and bad-pixel maps constructed from the CANDELS mosaic rms maps and the SEXTRACTOR segmentation maps respectively.

In addition to more basic single-Sérsic light-profile fits, I have also extended the multiple-component Sérsic light-profile fitting technique established in Chapter 3 to the objects in my COSMOS sample. As before, this was done by fitting two sets of nested models to each object: 2 single-Sérsic models; $n=\text{free}$ and $n=\text{free} + \text{PSF}$; and 6 multiple-component models; $n=4$ bulge, $n=1$ disk, $n=4 + \text{PSF}$, $n=1 + \text{PSF}$, $n=4 + n=1$ and $n=4 + n=1 + \text{PSF}$.

The initial conditions for this fitting were adopted from the fits of the initial single-Sérsic light profiles and the same grid search of different starting magnitudes and radii for each component were used as outlined in Section 4 of Chapter 3. The best-fit multiple-component models within each of these nested sets were then determined as per the χ^2 comparison given by equation 3.2 in Chapter 3, where the minimum acceptability criteria were again applied (equation 3.1) and objects which failed this cut were re-masked from their χ^2 -maps. As also detailed in Chapter 3, $\sim 10\%$ of objects from both the UDS and COSMOS samples have been removed from the final sample due to unacceptable χ^2 fits, $n > 10$ Sérsic indices, unresolved sizes or due to controversially large and un-robust size estimates. This analysis provides acceptable multiple component model fits for 163 objects in the COSMOS sample, and is combined with the further 184 objects with acceptable model fits and re-evaluated masses with $M_* > 10^{11} M_\odot$ in the UDS field.

4.3.1 Extension to additional bands

Having established H_{160} bulge-disk decomposed morphological fits for all the objects in my UDS and COSMOS samples I was then able to extend this analysis to the other bands available within CANDELS. During the WFC3 H_{160} and J_{125} pointings, ACS i_{814} and v_{606} parallels were also taken, providing me with a total of 4 bands available for my morphological decomposition analysis. For this study

I used the H_{160} -band fits as the master fits as they parameterise the morphology of the high-redshift objects in my sample in the reddest band, which represents the majority of the assembled stellar population. In accordance with this, and in order to extend my bulge-disk decomposition to the bluer bands, I have fixed all model parameters at the values determined for the H_{160} -band fits and in the fitting procedure have allowed only the magnitude of each component to vary as a free parameter. This required keeping the centroids of the objects fixed, along with the effective radius, axis ratio and position angle. During the fitting across the additional J_{125} , i_{814} and v_{606} bands the background subtraction value for each object was calculated using the same procedure developed for the H_{160} contribution, by taking the median value within an annulus between $3 - 5$ arcsec in radius. The sigma maps and PSFs used were also taken from the corresponding mosaics of the individual bands, while a single bad-pixel map was applied. This map was constructed from the segmentation map of the H_{160} image, rather than from each of the individual mosaics, as this was deemed to be the best way to ensure consistent masking of companions in relation to the master model fits across all bands. By fixing the rest of the model parameters I was able to scale the contributions of the separate bulge and disk (and PSF) components across all 4 of the bands and provide magnitudes for these components. This was used to generate 4-band photometry allowing separate-component SED fitting to be conducted.

In $\sim 10 - 15\%$ of the sample, fixing the other model parameters and allowing only the magnitude of each component to vary resulted in GALFIT crashing, and returning no output model fits for those objects. For these cases, I determined that this failure is due to the fact that GALFIT performs the fitting procedure in magnitude rather than flux parameter space. Thus, where the magnitude of one component during a multiple-component fit becomes very faint, in the preferred parameter space, GALFIT is not able to return a zero contribution and becomes confined to a non-physical fitting region (e.g. magnitudes of > 50), which when limited by the other model parameters, crashes the fit. In order to account for this, for those objects which crashed in the GALFIT fitting, I constructed a grid of different component magnitudes ranging from 20 to 35 (well below the $5 - \sigma$ depths of the 4 bands) AB magnitudes (in steps of 0.1 mags). From these fits I then determined the best-fit by adopting the model with the lowest χ^2 fit. Where the fitted magnitude of a component in one of the three accompanying bands fell below the $1 - \sigma$ detection limit of the corresponding band I disregarded the model fitted to that component and set it as a non-detection in the subsequent

SED fitting, where in that case the flux of that object will be set to zero and the error given to it will be equal to the depth of the image in that band.

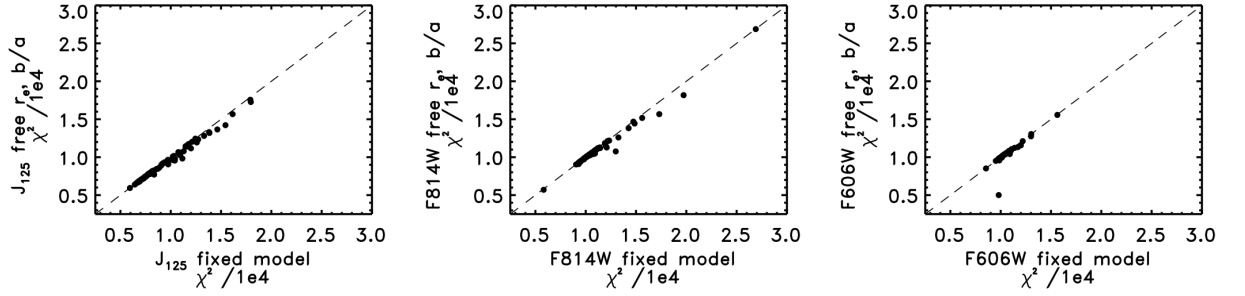


Figure 4.4 *Comparison of the χ^2 statistics between the fixed r_e and b/a , and the free r_e and b/a model fits. Left: comparison in the J_{125} -band, middle: for the i_{814} -band, right: for the v_{606} -band. These comparisons illustrate that the additional degrees of freedom introduced by allowing the r_e and b/a parameters to be freely fitted significantly improve the fits for only a small subset of the galaxies in my sample.*

As a check of the validity of this approach of fixing the model parameters to the H_{160} -band fit and allowing only the magnitudes of the individual component to vary across the multi-wavelength fitting, I have conducted several tests of the effects of also allowing both the effective radius and the effective radius plus the axis ratio to float as free parameters. Despite the naive expectation that in bluer bands the disk component of a galaxy will become both more prominent and more extended in size as extended faint envelopes become brighter, I found from examining the χ^2 statistics and effective radii parameters of the different fits for each object that in the majority of cases this is not the case, as can be seen in Fig. 4.4.

While allowing the effective radii (r_e) and axis ratios (b/a) parameters to be freely fitted in the modelling did, unsurprisingly, provide appreciable improvement in the χ^2 fits for a few of the objects in the sample, there is the potential for significant biases to be introduced as a consequence of adopting the increased degrees of freedom. Moreover, when comparing the bulge and disk component magnitudes in all bands it is clear that in both cases, where r_e and b/a are held fixed (Fig. 4.5) and allowed to fit freely (Fig. 4.6), the overall trend for the magnitude of both components to become fainter than the H_{160} estimates remains, with the introduction of only additional scatter to this relation for the case where the r_e and b/a parameters are fitted freely.

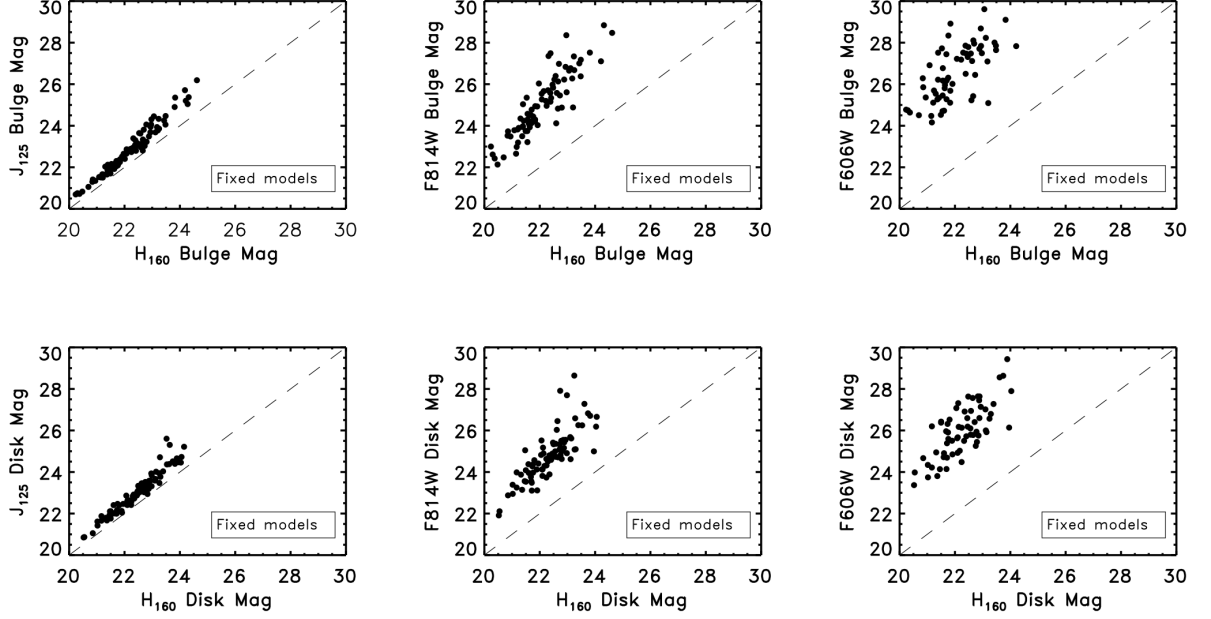


Figure 4.5 *Comparison of the fitted magnitudes of the fixed-parameter multi-wavelength models for the separate bulge and disk components in relation to the H_{160} model fits. The top panels show the comparison between the magnitudes of the bulge components across the additional three bands and the original H_{160} model fits, and the bottom panels illustrate this comparison for the disk components.*

Furthermore, from examining the total multiple-component (bulge+disk and bulge+disk+PSF) magnitudes of each component from both the fixed and free r_e and b/a parameter models, I found that towards the bluer wavelengths, the scatter in the relation between this integrated measure of the total magnitude of the object and the iso-magnitude estimate, measured directly from the image, increases in the case of the free r_e and b/a fits. This is demonstrated in Fig. 4.7, where it can also be seen that this increase in scatter is preferentially in the direction of the total multiple-component magnitude being brighter than the measured iso-magnitude.

In addition to this, a comparison of the bulge and disk sizes of each component in the 4 different bands revealed that by allowing the effective radius and axis ratio to be free parameters, the scatter in the relation between the effective radius of each component in the given bands compared to the master fit from the H_{160} -band (Fig. 4.8) also increases, and highlights clear cases where in the v_{606} -band, the bluest available, the bulge component becomes significantly larger than in the H_{160} -band. These trends suggest that introducing the effective radius and

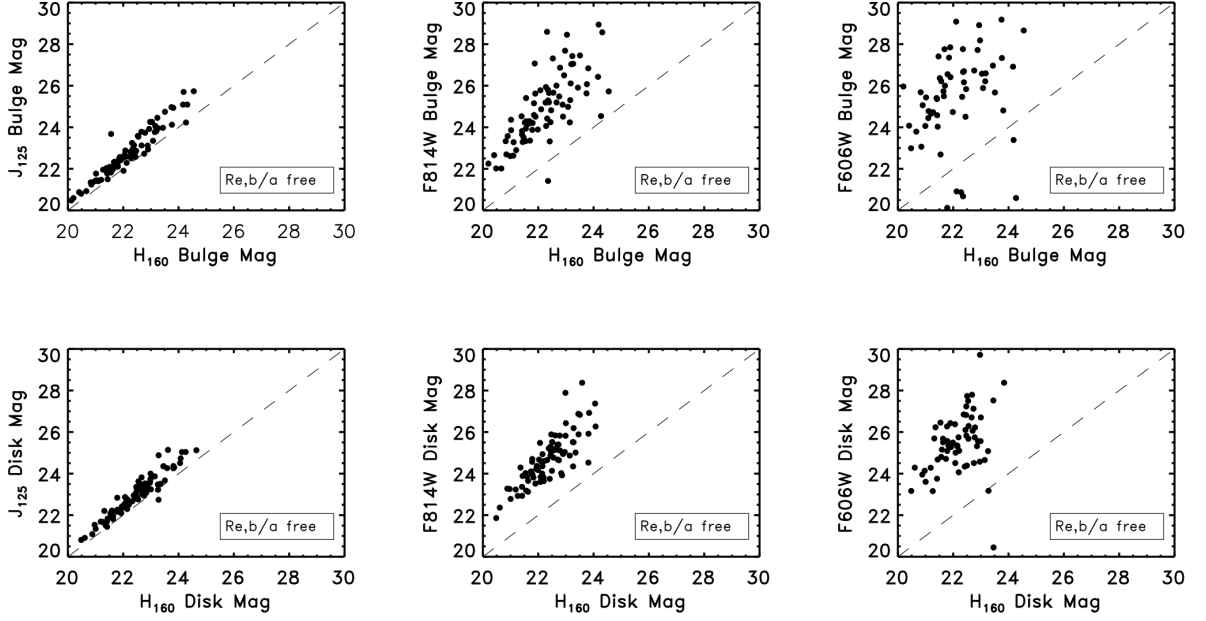


Figure 4.6 *The fitted magnitudes of the free-parameter multi-wavelength models for the separate bulge and disk components in relation to the H_{160} model fits. The panels follow the same configuration as in Fig. 4.5, with the comparison for the bulge components in the top panels and the disks in the bottom panels.*

axis ratio as free parameters, and removing the H_{160} -band constraints on these parameters, introduces new biases in the fitting procedure which, while hard to correctly interpret, do not significantly improve the ability of the models to reproduce the underlying morphologies of the galaxies in my sample. Moreover, this also holds true for the case of objects which were modelled as pure bulges in the H_{160} -band, and where I have added an additional $n=1$ disk component in the bluer bands (where for this additional disk model all other parameters except for the centroid position and Sérsic index were allowed to vary).

For these objects, the addition of the second component to account for any faint disks becoming dominant in bluer bands still did not provide a significant improvement in the ability of the model to fit the data, and due to low number statistics, it is hard to argue from examining the fraction of light which becomes attributed to the disk in the v_{606} -band compared to the H_{160} -band that the addition of such a disk component is motivated. Thus, I have chosen to adopt fixed r_e and b/a parameter models for this multi-wavelength morphological analysis in order to avoid additional degrees of freedom, which are not required and may introduce an additional degree of bias (where much effort was invested

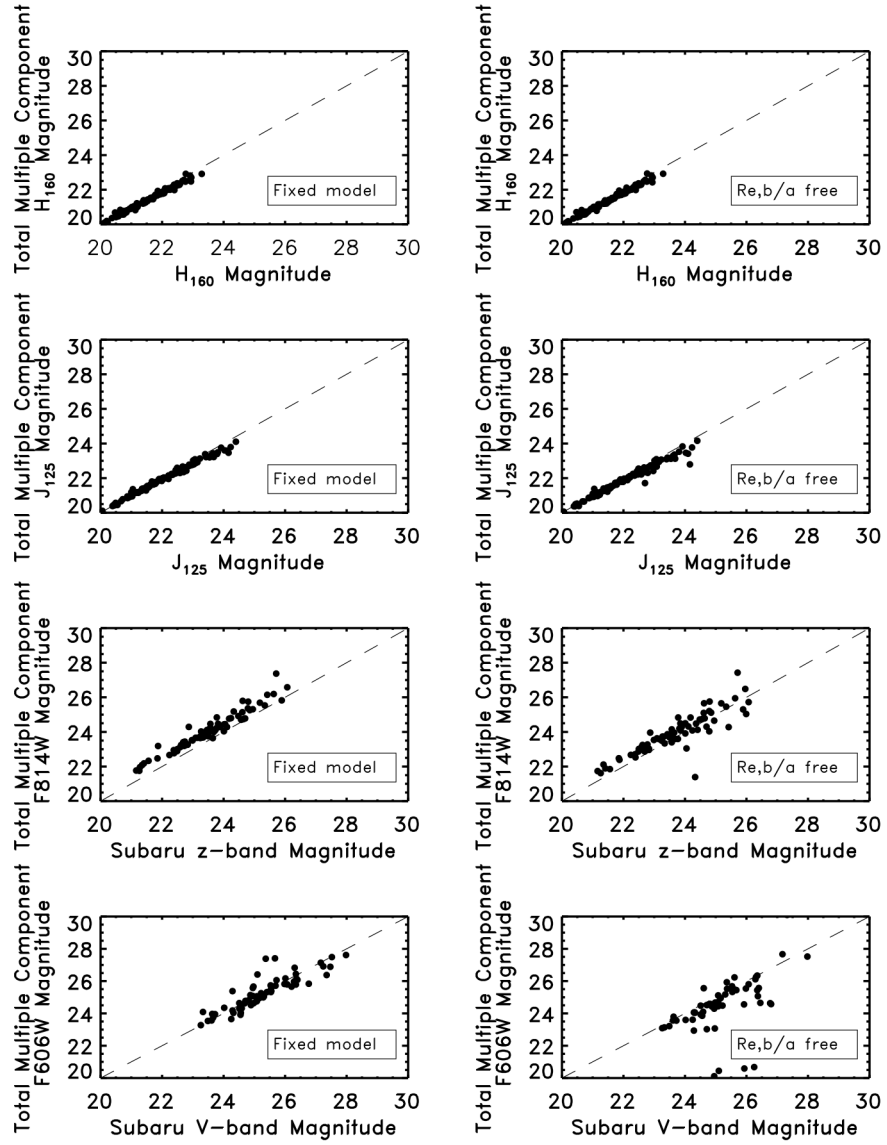


Figure 4.7 *Relation between the sum of the best-fit multiple-component model magnitudes and the measured iso-magnitude of each object for the fixed and free r_e and b/a parameter models. The fixed parameter models are shown on the left, with the free parameter models on the right, and the plots are ranked from top to bottom by decreasing wavelength. The constant offset between the best-fit modelled z_{814} -band magnitudes and the measured Subaru z -band magnitudes is due to the mis-match in the central wavelengths of these filters.*

to fully understand any such issues, as presented in the work in Chapters 2 and 3). It should also be noted that the adoption of the fixed morphological parameter approach delivered magnitudes for each component over the 4 band wavelength

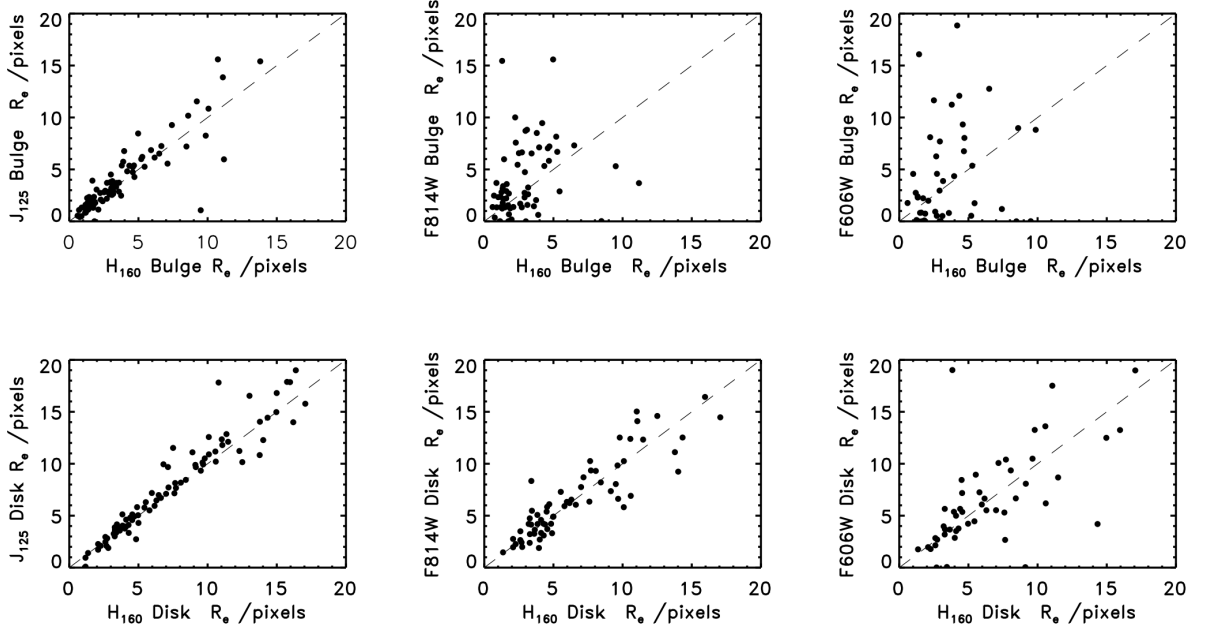


Figure 4.8 *Comparison of the fitted sizes of the individual components between the fixed and free-parameter models for the four bands. These plots illustrate that the allowing the r_e and b/a parameters to be fitted freely, even in the bluest band (v_{606}), results in cases where the disk component becomes both larger and smaller compared to the master H_{160} -band fit, and, moreover, highlights cases where in the v_{606} -band the bulge size exceeds the fitted sizes in the redder bands.*

range available in this study, which naturally reproduced realistic colours for the bulges and disks. This feature of my fits verifies the validity of this approach and further demonstrates the power in applying this simplified and well-constrained procedure.

Finally, due to the difference in area coverage between the WFC3 pointings and the accompanying ACS parallels taken as part of CANDELS, as demonstrated in Figure 4.1, the sample of objects which have the required photometry across all 4 of the CANDELS HST bands, and are best-fit by a multiple-component model, is 89 objects in COSMOS and another 89 objects in the UDS field. It is this final sample of 178 objects which is utilised for the double component SED fitting discussed in the next section.

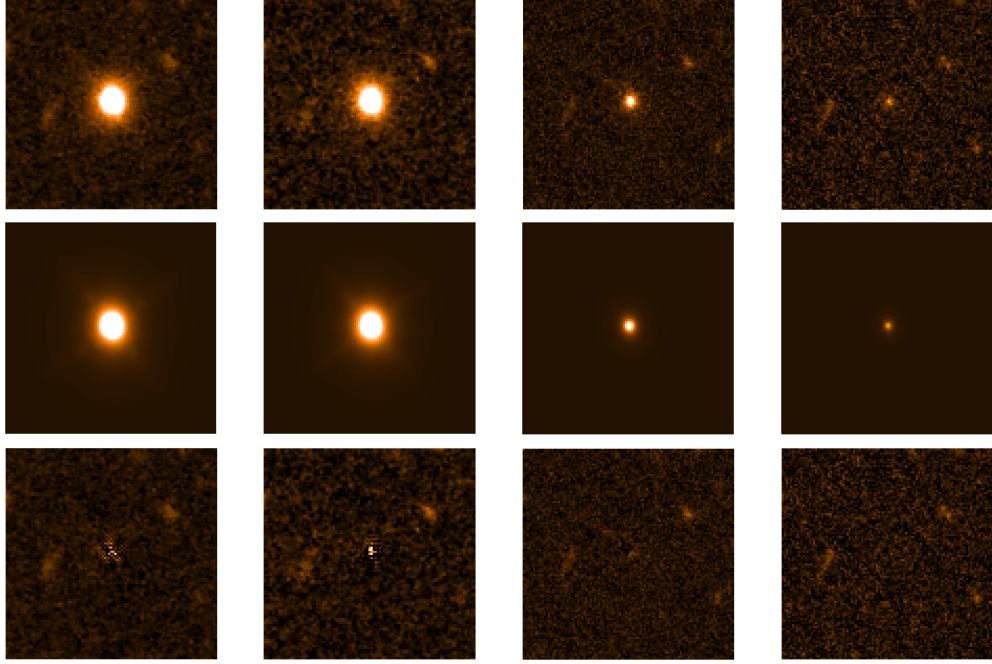


Figure 4.9 *Image stamps of an example fit for a pure-bulge object. The images displayed are 6×6 arcsec stamps with the images in the top panels, the best-fit models in the middle panels and the residual stamps in the bottom panels. The columns are ranked from left to right by decreasing wavelength, with the H_{160} -band stamps on the far-left, then the J_{125} -band stamps, the i_{814} -band stamps and the v_{606} -band stamps on the far-right. This is a representative fit for an object which is best fit with a pure bulge model, and illustrates the level of fits achieved across the full wavelength range adopted in my study by fixing all model parameters, except magnitudes, to the H_{160} -band fits.*

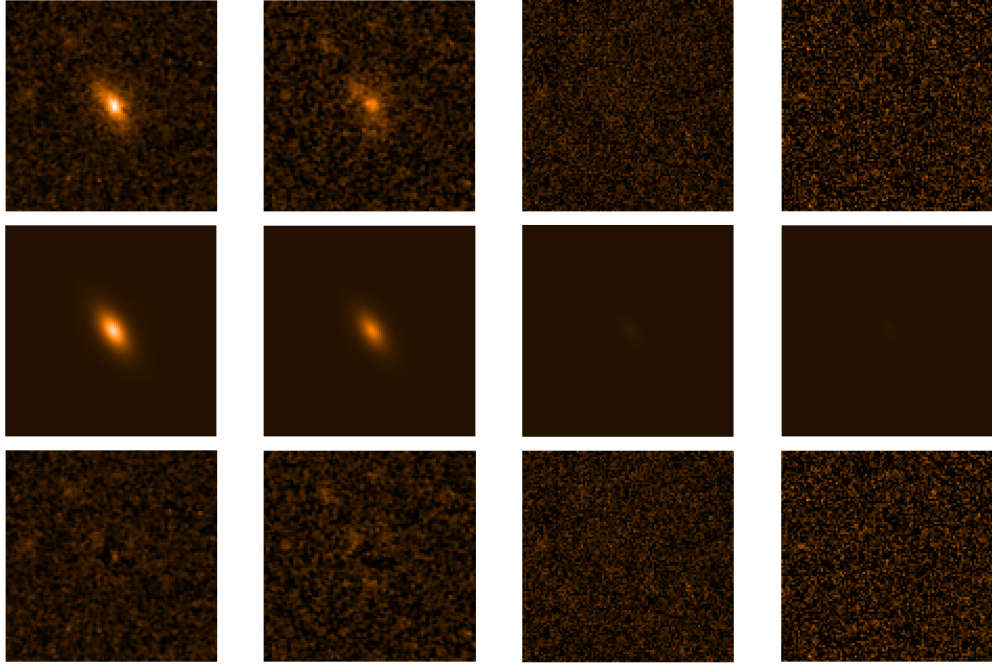


Figure 4.10 *Image stamps of an example fit for a pure-disk object. As in Fig. 4.9, displayed are 6×6 arcsec image, model and residual stamps, ranked from left to right by decreasing wavelength. In this case, the image and model stamps from this fitting clearly illustrate that, despite being best fit by a pure-disk morphology, this component becomes fainter in the bluer bands. The residuals show that no additional structure becomes prominent at the bluer wavelengths which has failed to be accurately modelled by my fixed parameter, symmetric models.*

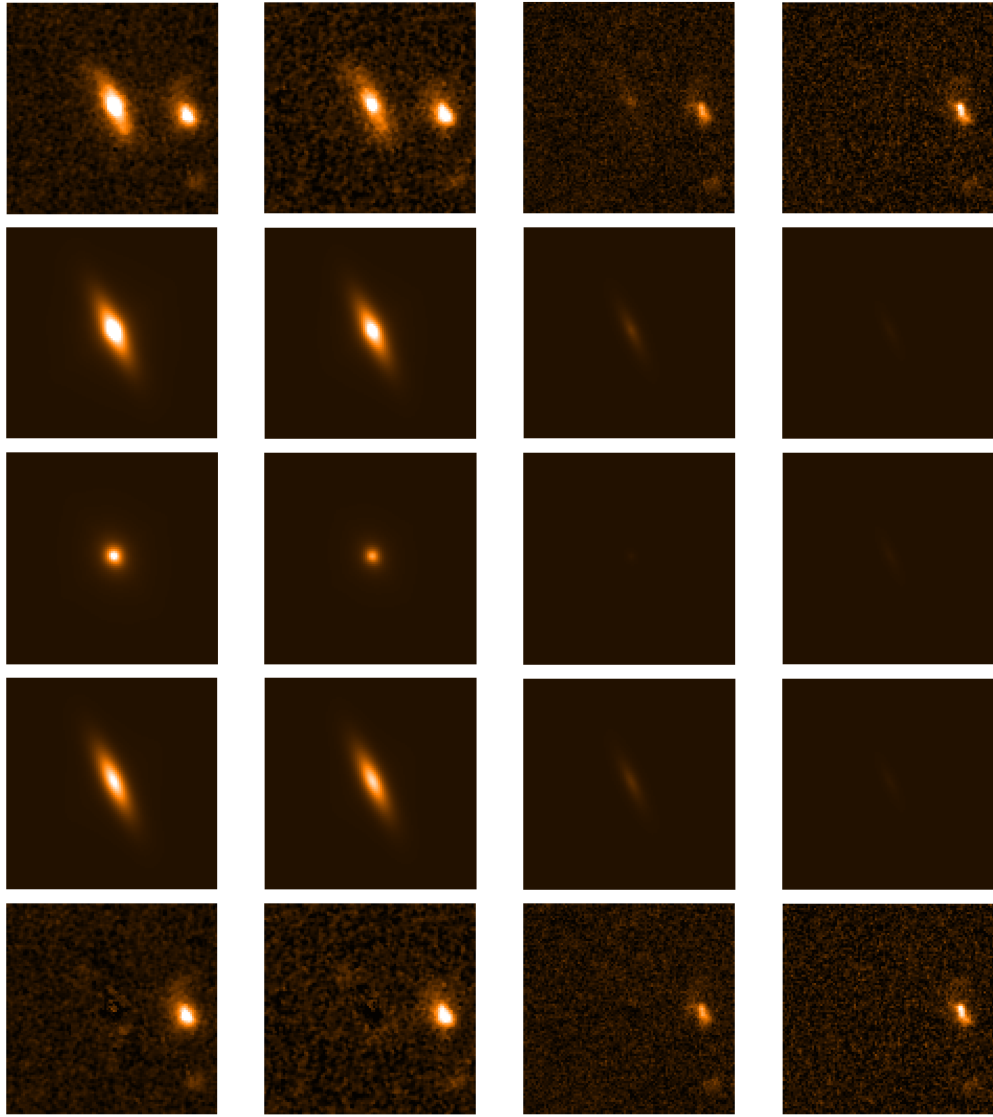


Figure 4.11 *Image stamps for an example fit for a bulge+disk object with $B/T < 0.5$. Here the stamps are again ranked from left to right by decreasing wavelength, but now I have also included the best-fit individual bulge and disk models. Thus, the vertical placement is as follows, from top to bottom: images, best-fit combined bulge+disk models, individual best-fit bulge components, individual best-fit disk components, combined model residuals. This fits illustrates how the contribution from the bulge component decreases at shorter wavelengths, while the disk-component remains more prominent in the blue bands, but is well fitted by the fixed-parameter model.*

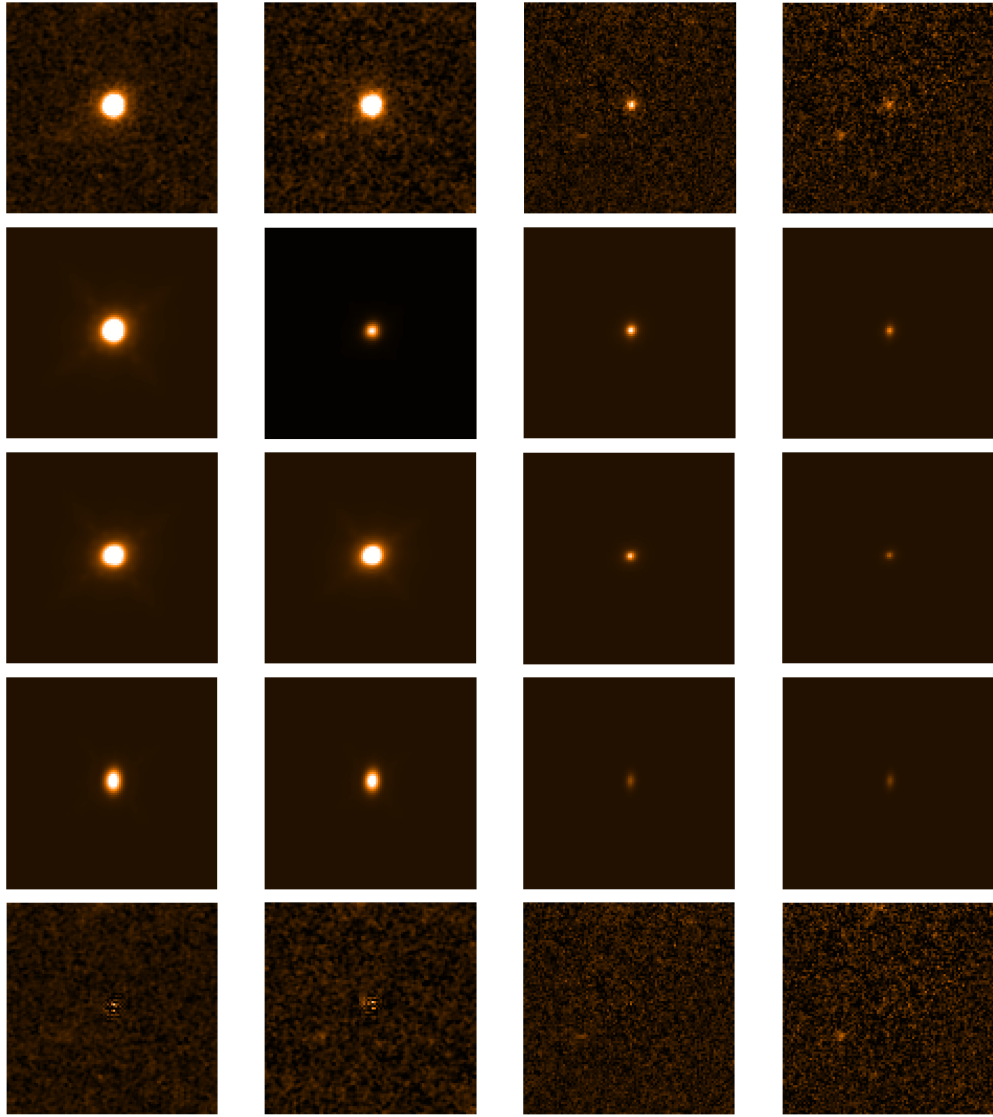


Figure 4.12 *Image stamps of an example fit for a bulge+disk object with $D/T < 0.5$. The configuration of these stamps follows Fig. 4.11, but in this case the disk is the dominant component, although it can also be seen that the bulge component remains prominent even in the v_{606} -band.*

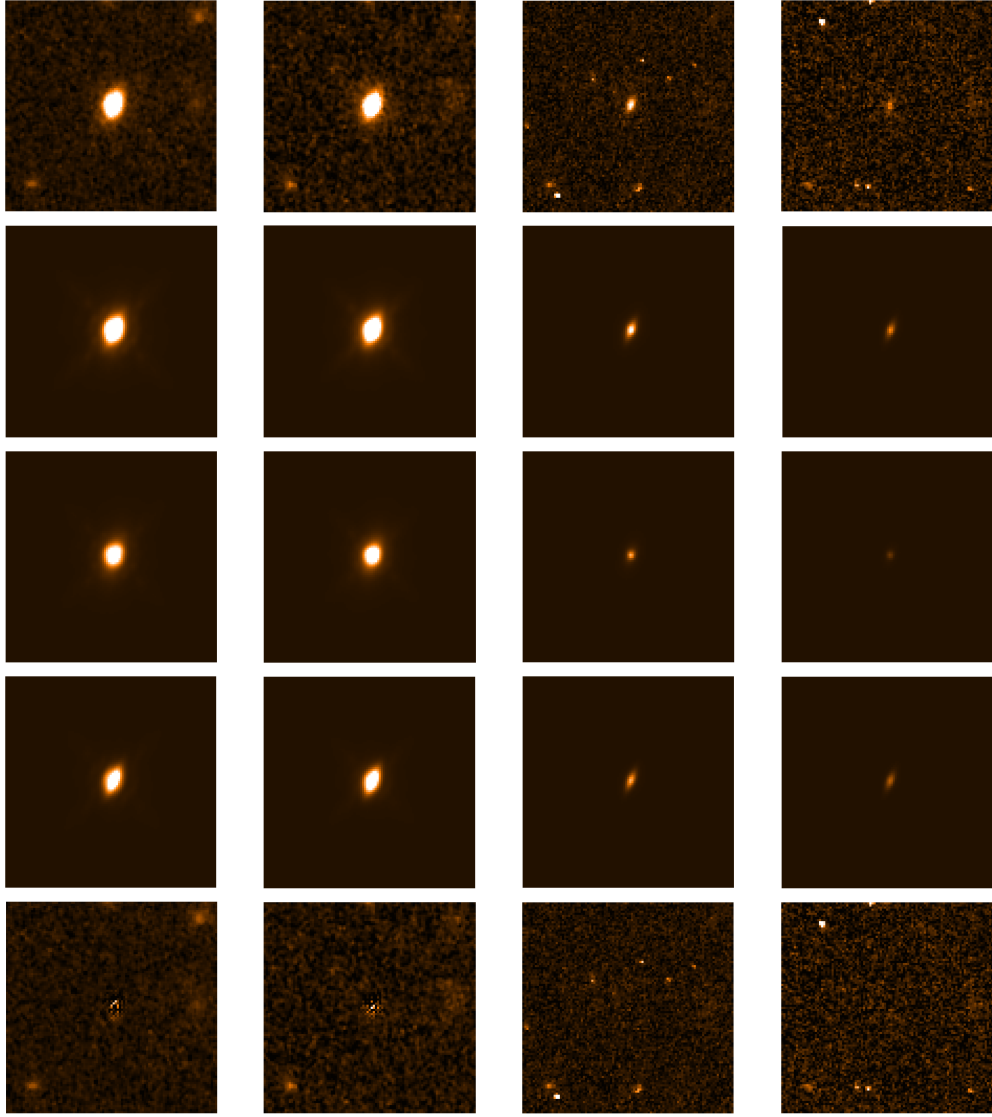


Figure 4.13 *Image stamps of an example fit for a bulge+disk object with $B/T = 0.5$, again following the placement of stamps described in the caption of Fig. 4.11. This object has a more equal contribution from the bulge and disk components. As with the previous examples, examination of the residual stamps for all 4 bands illustrates the good quality of the fits achieved by the adopted modelling technique, with no evidence of any additional structure in the bluer bands which has failed to be reproduced by the best-fitting models.*

4.4 Double-Component SED Fitting

The photometry generated from the above multi-wavelength morphology fitting was then used to conduct separate bulge and disk SED fitting in order to provide more accurate masses for the two components. For this analysis I used only the 178 objects in my combined UDS and COSMOS sample which require both bulge and disk components. As detailed in Chapter 3 one of the conditions of my morphological decomposition is the criteria that each component in an acceptable model fit must contain $\geq 10\%$ of the total flux of the object. This safeguards against selecting models which have a spurious additional component. However, for the purposes of individual component SED fitting, those objects from the original fits which chose to incorporate a ($\geq 10\%$) PSF component in their best-fit model were modelled with only a bulge and disk component to provide photometry. The removal of the PSF component was deemed necessary for the SED fitting as, having conducted several tests into the origin of a centrally concentrated additional component by searching for correlations between the presence and strength of a PSF component with X-ray, $24\mu\text{m}$ and radio counterparts from SXDS (Ueda et al. 2008), C-COSMOS (PI Elvis), SpUDS (PI Dunlop), S-COSMOS (PI Sanders), VLA in SXDF (PIs Simpson & Ivison) and VLA-COSMOS Deep and Large (PI Schinnerer), I found no definitive evidence to suggest that the inclusion of this component is due to the presence of either an AGN or a nuclear starburst. Given that it is not clear how any such PSF component should be correctly physically modelled in a SED fit, they are omitted and the flux of these objects is given by the next best-fit bulge+disk component model.

It is well known that the physical properties, most importantly the stellar masses, fitted by the template fitting SED approach can be strongly influenced by how well constrained the SEDs are by data across a broad wavelength range, particularly at the red end, where Spitzer IRAC data are important. In light of this, and given the limitations of using only the 4-band H_{160} , J_{125} , i_{814} and v_{606} decomposed photometry available from my CANDELS analysis, I have adapted the SED fitting code of Cirasuolo et al. (2007) to additionally constrain the model fits to my 4-band decomposed photometry at the extreme blue and red ends. This is done by fitting the sum of the bulge and disk photometry to the single-band photometry available at $\lambda < 0.6\mu\text{m}$ and $\lambda > 1.6\mu\text{m}$ which was used previously in the full single-component SED fitting.

In brief, the SED fitting code of Cirasuolo et al. (2007) is itself adapted from the Hyperz code from Bolzonella et al. (2000) and generates a grid of different SED models from the input stellar population synthesis templates, dust correction steps, allowed ages, redshifts and star-formation histories. At each point in this grid a χ^2 fit is performed between the data and the SED model using the uncertainty on each photometric data point. In order to allow the additional constraints to be applied at the red and blue ends, I have adapted the SED fitting code to allow simultaneous fitting to both the bulge and disk component photometry separately. At every step of this model SED grid, I then imposed the condition that the χ^2 of that fit must not only include the fit of the model bulge and disk SEDs to their respective photometry, but also that the sum of the bulge and disk components in the u' (and B-band for UDS), K/K_s, 3.6 μ m and 4.5 μ m bands are fitted to the overall photometry measured for the entire object in those bands.

The errors on the input decomposed photometry data points were determined for each component by: constructing a grid of different component magnitudes ranging from -10 to $+10$ magnitudes (in steps of 0.1 mags) from the component magnitude in the best-fit H_{160} model (fixing all parameters) and re-running GALFIT to generate χ^2 values for each of these different magnitude grid steps. This allowed the error on e.g. the bulge component magnitude to be estimated including also the uncertainty on the disk component magnitude by exploring the two dimensional parameter space. The error on each component magnitude was then taken to be the $1 - \sigma$ level of the bulge-disk χ^2 -contour for each object, unless this value fell below the minimum error limit imposed from the error associated with the direct measurement of the object magnitudes from the image, where this value is taken to be 0.1 magnitudes, in which case this 0.1 magnitude error was adopted.

4.4.1 Refinement of photometry

Upon conducting tests of this approach and comparing the final SED fits of the separate and combined bulge and disk components to the single-component original SED fit it was discovered that in the u' and B-bands often the flux of the total object measured from the SEXTRACTOR iso-magnitude was significantly brighter than the sum of the modelled bulge and disk components. This was determined to be due to the effect of close companions in the H_{160} -band image

which, in that band, contribute a negligible amount to the total flux of the object and have not been de-blended by SEXTRACTOR. However, as the H_{160} SEXTRACTOR segmentation map has been used in dual mode to measure the iso-magnitude fluxes of each of the objects in the accompanying bands, the flux of these close companions can begin to dominate the total flux at the shorter wavelengths (where the high-redshift galaxy is faint).

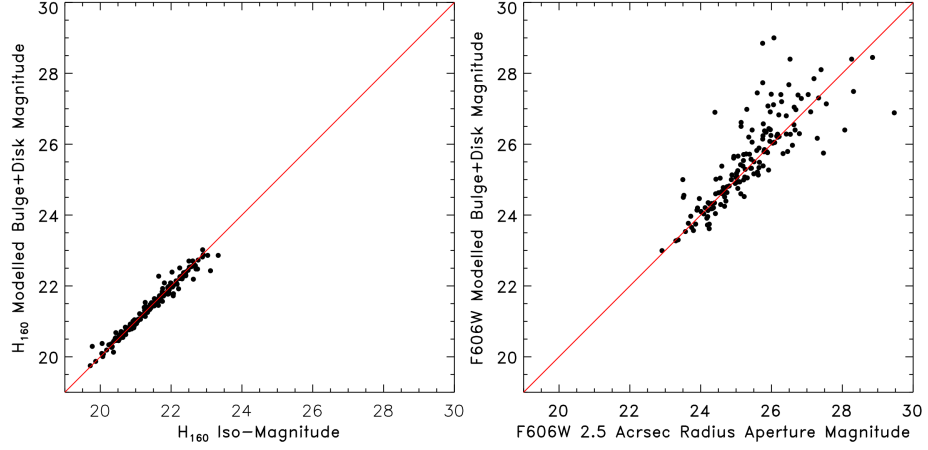


Figure 4.14 *Iso-magnitude (left) and 2.5arcsec radius aperture photometry (right) comparisons to the sum of the integrated model-fit photometry in the H_{160} and v_{606} -bands, respectively. This plot illustrates the good correlation between the iso-magnitude and 2.5arcsec radius aperture magnitude estimates to the integrated model magnitudes at both ends of the wavelength range fitted in my analysis. Although the scatter is higher for the comparison in the v_{606} -band, it should be noted that overall there is a one-to-one correlation, which was not the case when the iso-magnitude estimates were adopted at the blue end.*

From visual examination of the H_{160} SEXTRACTOR segmentation maps it was determined that a circular aperture of radius 2.5 arcsec was sufficient to include the full extent of the flux from the object, whilst minimising the contamination from the close companions, as illustrated in Fig. 4.14. Accordingly, in the blue bands where this problem becomes prevalent, I have re-measured the object fluxes in 2.5 arcsec radius apertures, and it is these values which are used to constrain the SED fits in the u' and B -bands. Close visual inspection of these cases also revealed that this excess in flux at the bluer wavelengths may also arise from additional structure in my objects becoming prominent, such as clumps. However, as the main exercise of this study is to trace the assembled mass, as observed in the reddest available H_{160} -band where my original decompositions were conducted, and as the mass in such blue clumps has been shown to comprise a small fraction ($< 7\%$) of the overall mass of the galaxy (Wuyts et al. 2012), this effect was noted but not accounted for.

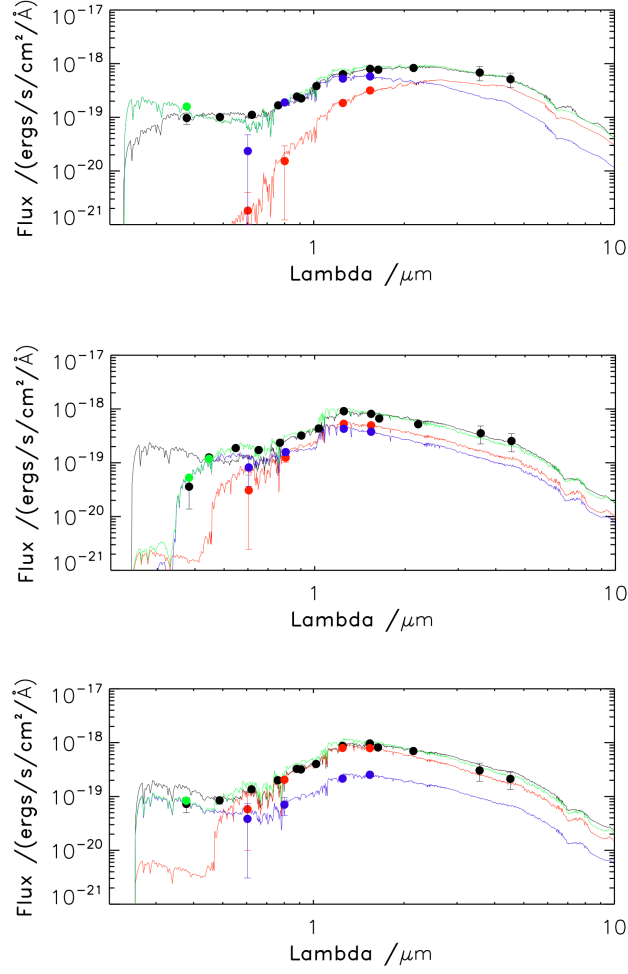


Figure 4.15 *SED fits for the example objects shown in Figs. 4.11, 4.13 and 4.12, respectively. Top panel for the $B/T < 0.5$ object, middle panel for the $B/T \sim 0.5$ fit, bottom panel for the $B/T > 0.5$ object. Plotted as black data-points and the solid black line is the total, overall galaxy photometry (with its associated error-bars) and the corresponding best-fit single-component SED. In blue is the modelled disk component photometry and the corresponding best-fit decomposed disk SED model, and in red is the modelled bulge photometry and the best-fit decomposed bulge SED model. Over-plotted in green is the sum of the best-fit bulge and disk SED models, which can be directly compared to the single-component fit in black and can be seen (in the bottom panels) to be in better agreement with the overall galaxy photometry. Finally, the green points, and their error-bars, are the re-measured 2.5 arcsec radius photometry for the blue bands. The top and bottom panels show objects from the UDS field, therefore they have re-measured photometry for both the u' and B bands, whereas the middle panel shows the fits to an object from the COSMOS field, where only u' photometry is available.*

4.4.2 The effect of stellar template choice on stellar-mass estimates and ages

During the simultaneous SED fitting of the separate bulge and disk components the dust attenuation, ages and star-formation histories of each component were allowed to vary freely and independently. This provides a clear distinction between my approach for multiple-component SED fitting, based purely on morphological decompositions, and the “double-burst model” fits of e.g. Michałowski et al. (2012), who fit one set of photometry points with a composite of constrained old and young stellar components.

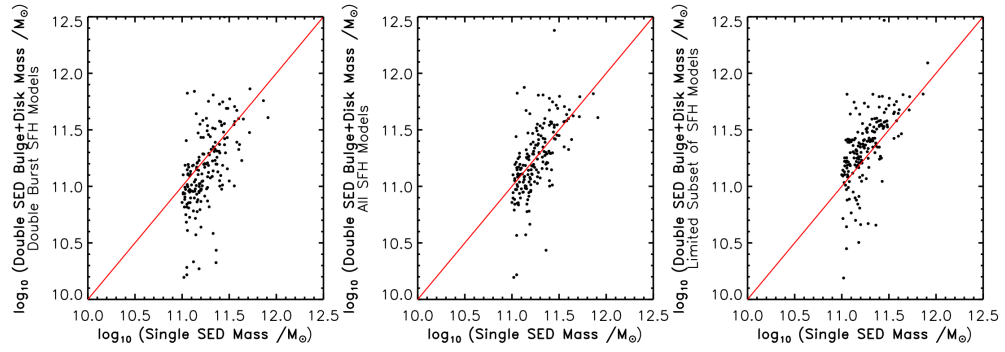


Figure 4.16 *Stellar mass estimates from double-burst models (left), double $0 \leq \tau(\text{Gyr}) \leq 5$ models (middle) and double $0.3 \leq \tau(\text{Gyr}) \leq 5$ models plotted against the mass estimates from the single-component SED fits. These panels clearly demonstrate that the double $0 \leq \tau(\text{Gyr}) \leq 5$ models provide stellar-mass estimates which are more comparable to the single-component masses.*

The adoption of multiple stellar population components can significantly influence the best-fit SED models so I have examined the impact of adopting different constraints and limitations on the input model parameters during my multiple-component fitting. For the single-component SED fitting, a minimum age limit of 50 Myr was necessary to ensure that, when fitting old objects with some on-going star-formation, the χ^2 minimisation model parameter space did not become restricted to un-physically young ages (i.e. galaxies with ages < 50 Myr at $1 < z < 3$) with large amounts of dust extinction. By adding the extra degrees of freedom to the models associated with the second component no such age restriction was needed for the multiple-component fitting. I have also experimented with limiting the star-formation histories implemented in the models which are fitted (always adopting BC03 models). By running fits with

both components limited to: pure burst histories ($\tau=0$); with the components limited to $0.3 \leq \tau(\text{Gyr}) \leq 5$; and with the full set of models ($0 \leq \tau(\text{Gyr}) \leq 5$), I have explored the effect on the mass determinations and the accompanying fitted ages of each component.

Having conducted this comparison I find that the full $0 \leq \tau(\text{Gyr}) \leq 5$ set of star-formation history models produce total bulge+disk component masses which are most comparable to the single-component SED fit masses (central panel of Fig. 4.16). Reassuringly, these models also represent the scenario in which I have applied the least constraints to the physical models fitted. By including the additional degrees of freedom from the second component there is no longer any physically motivated reason to restrict either component in age or star-formation history, as a second younger burst, or exponentially decaying star-forming population can reasonably account for any continued or recent star-formation superimposed on an older, redder population.

In fact, in the 56 cases where the best-fit two-component models are double-burst models, 53 galaxies have at least one component with an age of > 50 Myr and 49 galaxies have at least one component with an age of > 500 Myr, which I use as a more robust measure of passivity. This trend also extends to the double- τ and burst+ τ models, where none of the fits have both components with ages < 500 Myr. Moreover, for the double-burst models there are only 21/56 objects overall where both components are older than > 500 Myr and the SED fits to the photometry find no evidence for ongoing star-formation. The agreement between the ages of the old component from the full $0 \leq \tau(\text{Gyr}) \leq 5$ double-component models and the ages of the single populations from the original single-component, limited $0.3 \leq \tau(\text{Gyr}) \leq 5$ and age capped, SED fitting is shown in Fig. 4.17.

As a secondary check, the ages of these double-burst fits for objects which have $24\mu\text{m}$ counterparts from SpUDS and S-COSMOS have also been examined and are consistent with the fitting in that for these double-burst models there is always a young component which can account for star-formation and none of the galaxies with $24\mu\text{m}$ counterparts have both components with ages > 500 Myr, as can be seen in Fig. 4.18.

Furthermore, the ability of the multi-wavelength photometry for the bulge and disk components, which has been decomposed purely based on their H_{160} -band morphologies, to reproduce colours which are fitted well by physically motivated SED templates demonstrates the validity of this technique, as it is

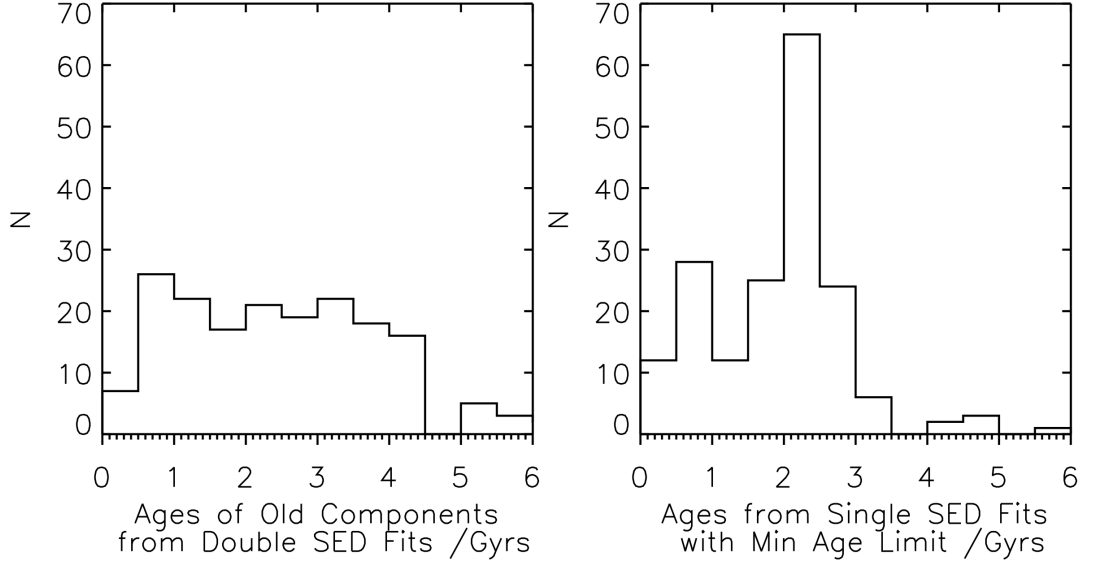


Figure 4.17 *Comparison between the age distributions of the single-component models and the older components of the double-component models. Left: the age distribution of the old component of double $0 \leq \tau(\text{Gyr}) \leq 5$ models. Right: distribution of the ages from single, limited $0.3 \leq \tau(\text{Gyr}) \leq 5$ and age-capped SED fits. The broad agreement between these distributions verifies that the additional degrees of freedom given to the double $0 \leq \tau(\text{Gyr}) \leq 5$ models naturally resolve the problem encountered with single SED fits sometimes becoming restricted to un-physically young ages.*

clear that no fixed correlation or pre-determined trends with colour (such as the polynomial wavelength dependencies implemented in the single-Sérsic and multiple-component multi-wavelength fitting package of MegaMorph Häußler et al. (2013) and Vika et al. (2013)) are required.

4.4.3 Separate component star-formation rates

Following the adopted stellar-mass estimates, the specific star-formation rates of the individual components have also been determined from SED fitting of the individual-component photometry using models which include bursts and exponentially declining star-formation histories in the range $0.1 \leq \tau(\text{Gyr}) \leq 5$. Previous single component SED fitting studies by Wuyts et al. (2011) found, when comparing star-formation rates determined from dust-corrected SED fitting with those from combinations of non dust-corrected UV and infra-red contributions

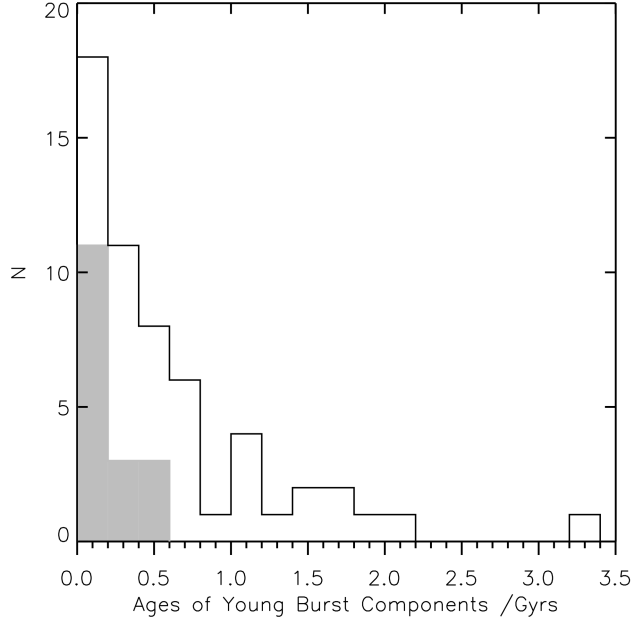


Figure 4.18 *Age distribution of the young components of the double-burst fits, over-plotted by the shaded region with the objects which were found to have a $24\mu\text{m}$ counterpart. The lack of objects with $24\mu\text{m}$ counterparts and ages > 500 Myr confirms that the 500 Myr criterion for passivity is physically motivated, and that the double-burst models do a good job of reproducing realistic ages and star-formation properties for the massive galaxies in my sample.*

(SFR_{UV+IR}) calibrated on PACS imaging, that the adoption of very sharply declining star-formation e-folding timescales, $\tau < 0.3$ Gyr, provided statistically improved SED fits, but that these fits had stellar population ages which were unrealistically young and had star-formation rates that were systematically lower than the estimates derived from SFR_{UV+IR} . As a result, they suggested removing such short e-folding timescales for SED fitting and it is this approach which I have adopted in the previous chapters for the SED fitting of the single components (although it should be noted that this problem could also be exacerbated by the fact that the Kennicutt (1998) star-formation rate conversions assume constant star-formation rates).

However, from the careful SED fitting comparisons conducted for the double-component models I have found that the extra degrees of freedom incorporated with the addition of the second component remove the bias of including these sharply declining star-formation histories in the SED fits. This has been found from examination of the ages of the old stellar component, which show that

they are no longer biased towards implausibly young values and show an age distribution comparable to the ages of the single component fits which were limited to the $0.3 \leq \tau(\text{Gyr}) \leq 5$ subset (Fig. 4.17). Furthermore, by adding a second component I have also allowed the model fits to include the case of burst star-formation histories. The removal of such objects from single-component SED fitting was observationally motivated at these redshifts by e.g. Wuyts et al. (2011) and Genzel et al. (2010), whose studies revealed evidence for stable extended star-formation timescales, but the inclusion of a second component allows for the superposition of an old population, which experienced a burst of star-formation in the past, with an additional population exhibiting on-going or slowly-declining star-formation. However, while the incorporation of burst models in the double-component SED fitting has been validated by the above exploration, burst models obviously do not provide any estimates for even low levels of on-going star-formation in young components.

In this respect the star-formation rates derived for the separate-component modelling may be under-estimated in comparison with the star-formation rates derived from the single-component SED fitting, which was forced to have some level of on-going star-formation activity by adopting $0.3 \leq \tau(\text{Gyr}) \leq 5$. Thus, in order to better reconcile these two approaches, for the double-component model results I adopt different sSFR estimates for the several possible modelled scenarios.

1. For fits with double- τ ($0.1 \leq \tau(\text{Gyr}) \leq 5$) models, I use the UV dust-corrected star-formation rates from the SED models of each component and divide through by the corresponding modelled mass of those components to provide the sSFR for each component separately.
2. For fits with double-burst models where both components are older than 500 Myr, I deem them both to be passive and allocate them a $sSFR = 10^{-12}\text{yr}^{-1}$. Where one burst component is young (< 500 Myr) I attribute the entire star-formation rate derived from the limited single-component SED fitting to that young component and calculate the sSFR by dividing through by the mass of that component modelled from the decomposed photometry, and assume the old component is passive and adopt a $sSFR = 10^{-12}\text{yr}^{-1}$.
3. For a single burst + τ model I generate a sSFR for the τ model based on the UV dust-corrected SED fitted star-formation rate and mass of that

component from the decomposed photometry and for the burst model I adopt the passive limit of $sSFR = 10^{-12} \text{yr}^{-1}$.

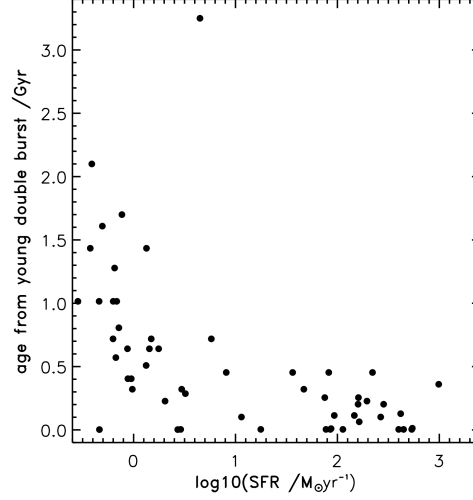


Figure 4.19 *of the young component of the double-burst models with the star-formation rates from the single-component SED fit, illustrating good overall agreement between the ages of the components to which all star-formation activity in the galaxy has been attributed, and the overall star-formation rates for the galaxies.*

In this way I have best accounted for the mass decomposition of the objects, by adopting a model which can incorporate both a burst and steeply declining star-formation rate for one or both of the components, and have provided an indication of the star-formation rates in each component, which otherwise would not have been achievable for model fits of burst star-formation histories. In fact, Fig. 4.19 demonstrates the general correlation between the ages of the young components from the double-burst models and the star-formation rates estimated from the single-component SED fitting. As an additional check of this approach, it can also be seen from Fig. 4.18 that my adoption of the 500 Myr age boundary (above which I attribute none of the entire galaxy's star-formation to the component) is justified as there is no additional evidence from 24 μm of on-going star formation in these components with older ages.

4.5 Correlation Between Single and Multiple-Component Model Morphologies

Having conducted the detailed morphological decomposition described above, and extended this analysis across the 4-band wavelength range available from CANDELS, I was then able to compare the overall morphologies fitted by the single-component and the multiple-component fitting techniques. This comparison is shown in Fig 4.20, which demonstrates the good correlation between the Sérsic indices fitted from the single-component models and the bulge/total (B/T) light fraction ratios from the H_{160} -band multiple-component decompositions. As was discussed in Chapter 3 for the UDS sample alone, overall there is a reasonable one-to-one correlation between the B/T light fractions from the multiple-component decompositions and the fitted single-Sérsic indices (although there is significant scatter), and the Sérsic index cut at $n = 2$ to distinguish between bulge and disk-dominated galaxies closely corresponds to a cut at $B/T = 0.5$, with only a few cases where galaxies have $n < 2$ and $B/T > 0.5$. These trends also extend to the COSMOS decompositions and, as a result, to the combination of both fields. However, there is an increase in scatter at high Sérsic indices, which is more pronounced in the COSMOS field analysis, with some galaxies now having $n > 4$ but $B/T < 0.5$.

In fact, part of this scatter can be explained by the fact that the light fractions are plotted as the bulge/total fraction, where the total light can contain contributions from a PSF. In this case $\text{total} = (\text{bulge} + \text{disk} + \text{PSF})$, which is not the same as the ratio of the bulge/bulge+disk light. For comparison, bulge/bulge+disk fractions are plotted in Fig 4.21, where objects which have a best-fit multiple-component model with a PSF component are highlighted in blue. Adopting this bulge/bulge+disk ratio helps to remove some of the scatter towards high Sérsic indices but low bulge fractions. In the cases where best-fits contained a PSF, the bulge/total ratios fall as the PSF component has replaced some of the contribution which would otherwise be modelled by the bulge, and the Sérsic indices are higher because a simple de Vaucouleurs profile no longer provides an adequate fit to these centrally concentrated objects. Thus, for these systems plotting bulge/bulge+disk light ratios arguably provides a characterisation of bulge dominance which is easier to interpret. By highlighting those objects with a significant PSF component ($> 10\%$), Fig 4.21 also reconciles the single and multiple-component fits for the 2 objects which have $B/T = 0$ with $n > 2.5$ as it

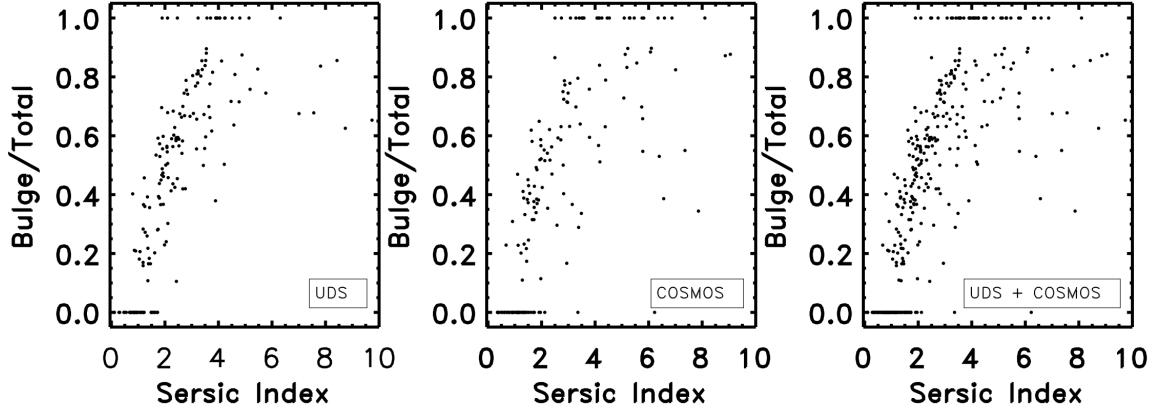


Figure 4.20 *Bulge/Total light fractions against single-Sérsic index fits, split by field. The plot for the UDS field can be directly compared with Fig. 3.6, where now the 10 objects with re-estimated masses $M_* < 10^{11} M_\odot$ have been removed. These plots illustrate that the same trends witnessed in the UDS analysis extend to the COSMOS field.*

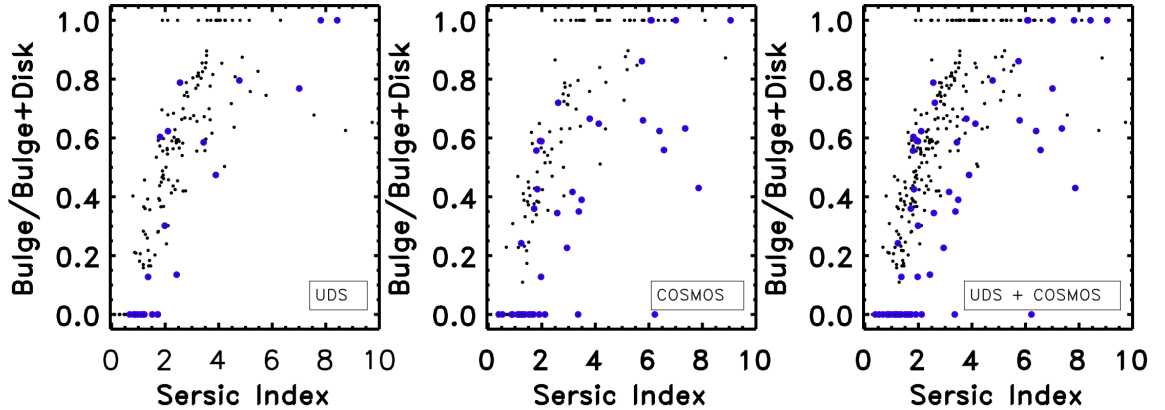


Figure 4.21 *Bulge/Bulge+Disk light fractions from the H_{160} -band modelling against single-Sérsic index fits, with objects which have best-fit models which contain a PSF component highlighted in blue. This demonstrates the same overall trends as in Fig. 4.20, but here some of the scatter has been reduced and specific cases have been highlighted where the inclusion of a PSF component helps to resolve low $B/B + D$ and high Sérsic index fits.*

can now be easily seen that these fits have a PSF component. Hence, whilst they have no bulge component these are not “pure” disk systems, but have a centrally concentrated light component modelled in the multiple-component analysis by a

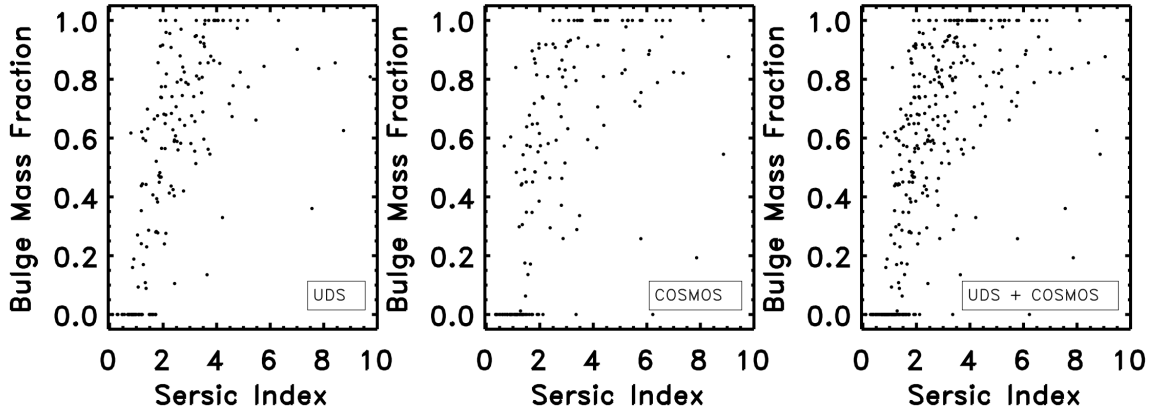


Figure 4.22 *Bulge/Total mass fractions against single-Sérsic index fits. These panels show the same overall trends as with the B/T light fractions but also demonstrate how adopting mass fractions increases the bulge contribution to most galaxies, as would be expected due to the higher M/L fractions of the stellar populations of bulge components compared to disks.*

PSF and in the single-component fits by a high Sérsic index.

Finally, for completeness I have also included the correlation between the bulge/total mass fractions from the full SED decompositions and the single-component fit Sérsic indices in Fig 4.22. For the SED decomposition it should again be noted that I did not include any PSF components in the model photometry, so objects which had a best-fit with a PSF were modelled across the 4-bands with the next-best bulge+disk only models. Overall, it can be seen that adopting fractions based on stellar-mass estimates generally increases the contribution from the bulge component, as expected given the different stellar populations comprising the bulge and disk components, but otherwise does not lessen the agreement between the Sérsic index light-based morphological indicator and the decomposed mass-based discriminator.

4.6 Size-Mass Relations

The results from the multiple-component decomposition have allowed me to explore how the size-mass relations for the separate bulge and disk components evolve with redshift by accurately decomposing their masses from the multiple-component SED fitting. However, before this is discussed, it is first interesting

to explore how the size-mass relations constructed by splitting the mass of each galaxy into each of its separate components according to their contributions to the H_{160} -band light compare to the results presented in Chapter 3, now using the re-defined UDS sample and the new COSMOS sample. The new UDS size-mass relations are given in Fig. 4.23, along with the similarly-constructed relations for the COSMOS field in Fig. 4.24 and the combination of these results from both fields in Fig. 4.25. As described in Chapter 3, these plots show the size-mass relations for all bulge components in the top panels and disk components in the bottom panels. They are further split by redshift, where the full redshift range ($1 < z < 3$) is displayed in the far left panels, $1 < z < 2$ in the middle and $2 < z < 3$ in the right-hand panels. As before, the bulge relations have been over-plotted with the local Shen et al. (2003) ETG relation in red, with its $1-\sigma$ scatter, and the disk components by the local LTG relation and its scatter, where these relations have been corrected to un-circularised values following the prescriptions outlined in Chapter 3, Fig. 3.7. In these plots I only display components with $M_* > 2 \times 10^{10} M_\odot$, as below this mass the components become sufficiently faint that they may introduce potential biases to the morphological properties fitted, therefore they have been removed from these plots to avoid over-interpretation of sub-components. This convention for the decomposed size-mass relations has been adopted for all of the following plots.

It is clear from Fig. 4.23 that, re-assuringly, adopting the re-defined sample for the UDS analysis has not revealed any bias in the results presented in Chapter 3, which contain 10 objects with masses which were unstable to my re-fitting and have been determined to have $M_* < 10^{11} M_\odot$. Furthermore, it can also be seen that the trends reported for the UDS sample are also in place in the COSMOS field, where again I find that the bulge components of massive galaxies display a stronger size evolution with redshift than the disk components. The majority of bulge components have sizes which place them well-below their corresponding local relation, whereas the disk components show a smaller scatter in size with an increased fraction of disks displaying sizes consistent with similarly massive local systems. These results also support the claim of a lower envelope of sizes which scales with mass broadly parallel to the local relation.

Interestingly, the scatter in the size-mass relation of the bulge and disk components is arguably higher than would be expected from the uncertainties associated with my size and mass estimates, thus instead of displaying a tight intrinsic relation with scatter due to measurement uncertainty, these plots suggest

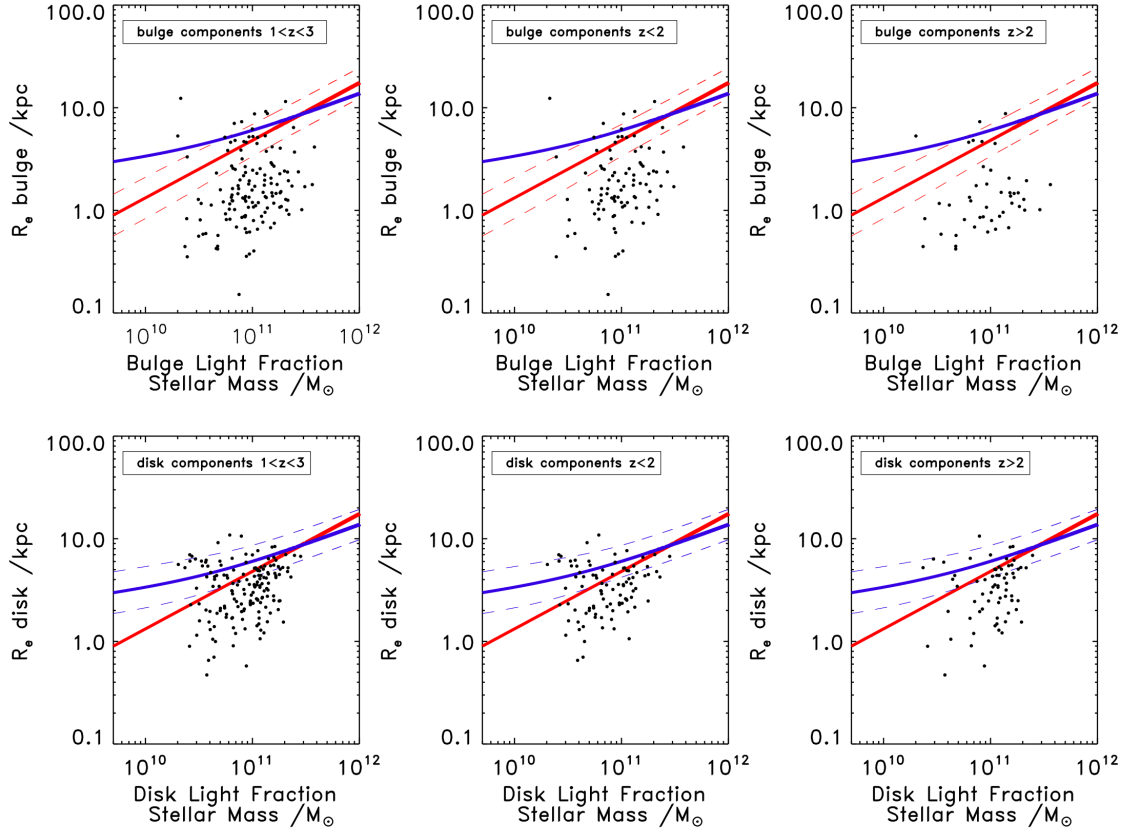


Figure 4.23 *UDS size-mass relations for each component, where component masses are determined based on the H_{160} -band light fractions. As in Fig. 3.7 the relations have been split into different redshift intervals: left $1 < z < 3$, middle $1 < z < 2$, right $2 < z < 3$. The bulge components are displayed in the top panels over-plotted with the Shen et al. (2003) local ETG relation in red, with its corresponding $1 - \sigma$ scatter, and the local LTG relation in blue. The disk components are displayed in the bottom panels and have been over-plotted with the local LTG relation in blue, with its corresponding $1 - \sigma$ scatter, and the local ETG relation in red where, as per Fig. 3.7, these relations have been re-scaled to uncircularised sizes. This configuration is adopted for all following size-mass relation plots. This plot can be directly compared to Fig. 3.7 as it uses the re-evaluated UDS stellar-mass sample.*

that the scatter in the size-mass relations of the bulge and disk components of massive $1 < z < 3$ galaxies is intrinsic. As a result, I do not find any stronger evidence for the growing bimodality of bulge sizes with increasing redshift, and given the uncertainties, cannot say anything definitive about how the form of the relations evolve but in the following sections discuss the evolution of the median

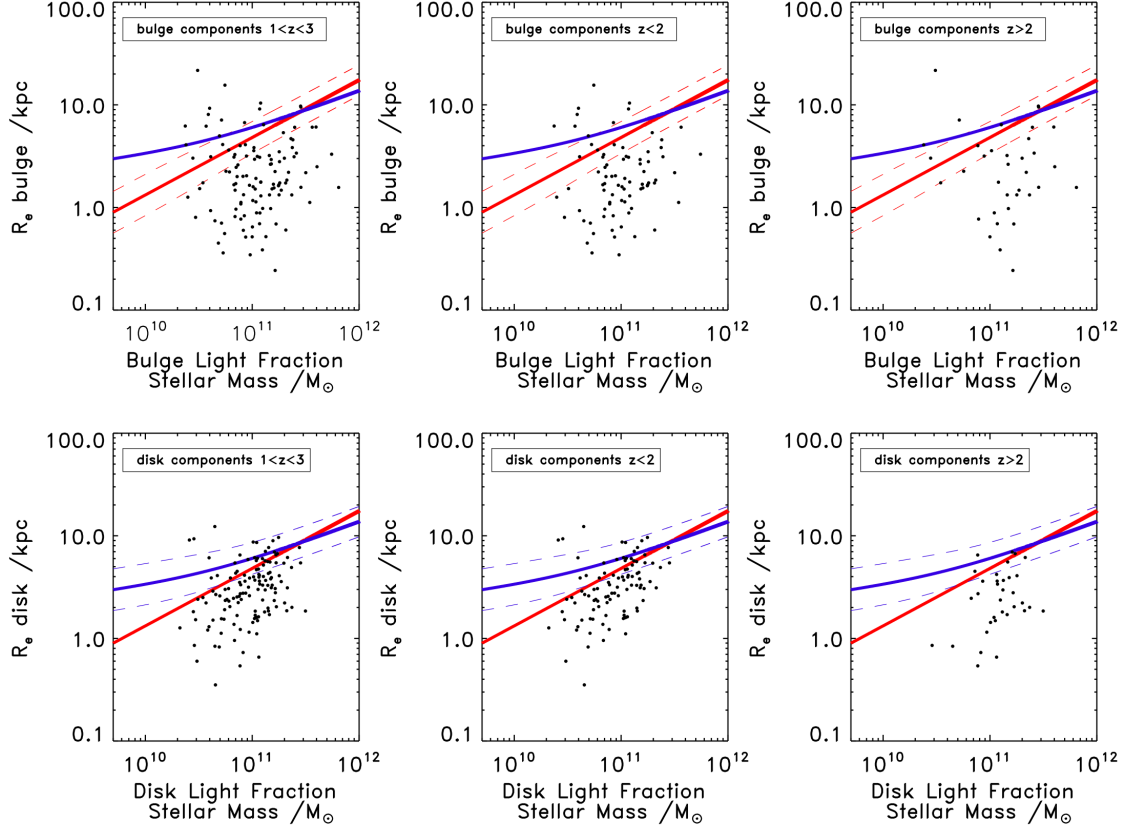


Figure 4.24 *COSMOS size-mass relations for each component, where component masses are determined based on the H_{160} -band light fractions.*

sizes with redshift.

In addition to applying this analysis to the CANDELS-COSMOS field, considerable effort has been dedicated to extending the morphological bulge-disk decompositions across multiple bands in order to allow separate-component SED fitting, which has delivered individual stellar masses and star-formation rates for the decomposed bulge and disk components. One of the main motivations of this work was to utilise these accurate component masses to further explore the evolution in the size-mass relations. The bulge and disk relations constructed using these separate component masses estimated from SED fitting are given in Fig. 4.26 for the combined UDS and COSMOS fields. Comparison between these size-mass relations and those plotted in e.g. Fig. 4.25, using component masses estimated from simply splitting the galaxy mass based on the component H_{160} -band light fractions, reveals no significant change in the reported relations for either the bulge or disk components. This suggests that the simplified

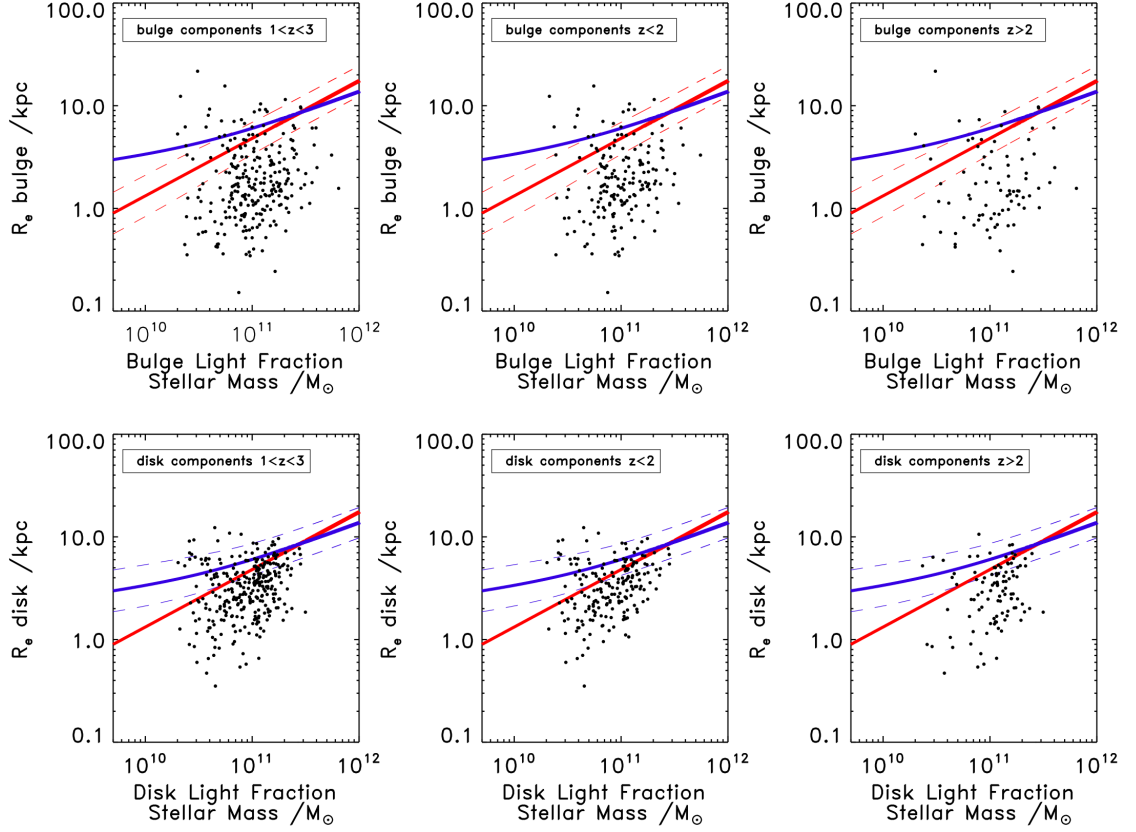


Figure 4.25 *Combined UDS + COSMOS size-mass relations for each component, where component masses are determined based on the H_{160} -band light fractions.*

approach of attributing masses to each component based on their contributions to the H_{160} -band light fractions provides a good proxy for SED fitted stellar-mass decompositions, as was also displayed in the previous comparison of the correlation between Sérsic indices and bulge/total light and mass fractions.

This stellar mass decomposition confirms all of the morphological trends revealed by the previous light-fraction decomposed size-mass relations, including the stronger evolution witnessed for bulge components over disks, both in terms of the number of bulges which fall below their respective local relations, and in the median sizes of the populations in both the $z < 2$ and $z > 2$ redshift bins. These results are summarised in Table 4.6, which shows that, within the errors, these trends are consistent across both fields, and are in agreement with the statistics quoted in Chapter 3 from the size-mass relations from masses based on H_{160} -band light fractions for the UDS field alone. Again, the uncertainties on these values do

not allow me to draw any robust conclusions about the change in these fractions with redshift, although I do note that the CANDELS-COSMOS sample contains a larger number of bulge-dominated objects at $z > 2$ which is responsible for the rise of bulges with sizes comparable to local ETGs within this redshift bin. This could be produced by a systematic error (focussing) in the determination of the photometric redshifts. However, the effects of redshift focussing have been studied in both fields with the, albeit low numbers of, spectroscopic redshifts available, but I find no strong evidence for this effect amongst the bulges and conclude that this larger abundance of high-redshift bulges in the CANDELS-COSMOS field may be due to an interception of genuine structure in the COSMOS field, although no obvious spatial clustering of these objects was observed.

One other additional feature in the refined size-mass relations which should be discussed is the apparent structure in the $z > 2$ disk-component relation at high masses (perhaps better illustrated in Fig. 4.27 by the blue colour-coded star-forming disks). The disk component sizes at $z > 2$ seem to be more concentrated in terms of the mass range that they span, compared to the relations plotted using component masses determined from the H_{160} -band light fractions, and appear as a “clump” in the relation. Having explored the potential causes of this concentration I find no evidence for potential biases manifesting as this result, but attribute this effect to a consequence of my mass selection. As has been shown in Chapter 3, these most massive systems become increasingly disk-dominated above $z = 2$, and the total galaxy mass must be $M_* > 10^{11} M_\odot$ in order to be retained by the mass-selection cut. Thus, it follows that these disk-dominated systems must have very large disk-component masses. Moreover, the sharp truncation of disks in the size-mass relation can be accounted for by the steepness of the mass function in this high-mass regime.

From this discussion it is evident that the adoption of the more rigorous SED decomposed component masses, over the H_{160} -band light fraction mass decompositions, has not significantly influenced the positions of components in their respective size-mass relations, nor altered the basic trends reported. However, the full SED stellar-mass decomposition not only provides robust individual component masses, but also delivers estimates of the star-formation activity of each object.

Early size-mass studies (e.g. Kriek et al. 2006, Toft et al. 2007) reported a correlation between compactness and passivity which has since gained substantial support in the literature, but these studies are not only limited to morphological

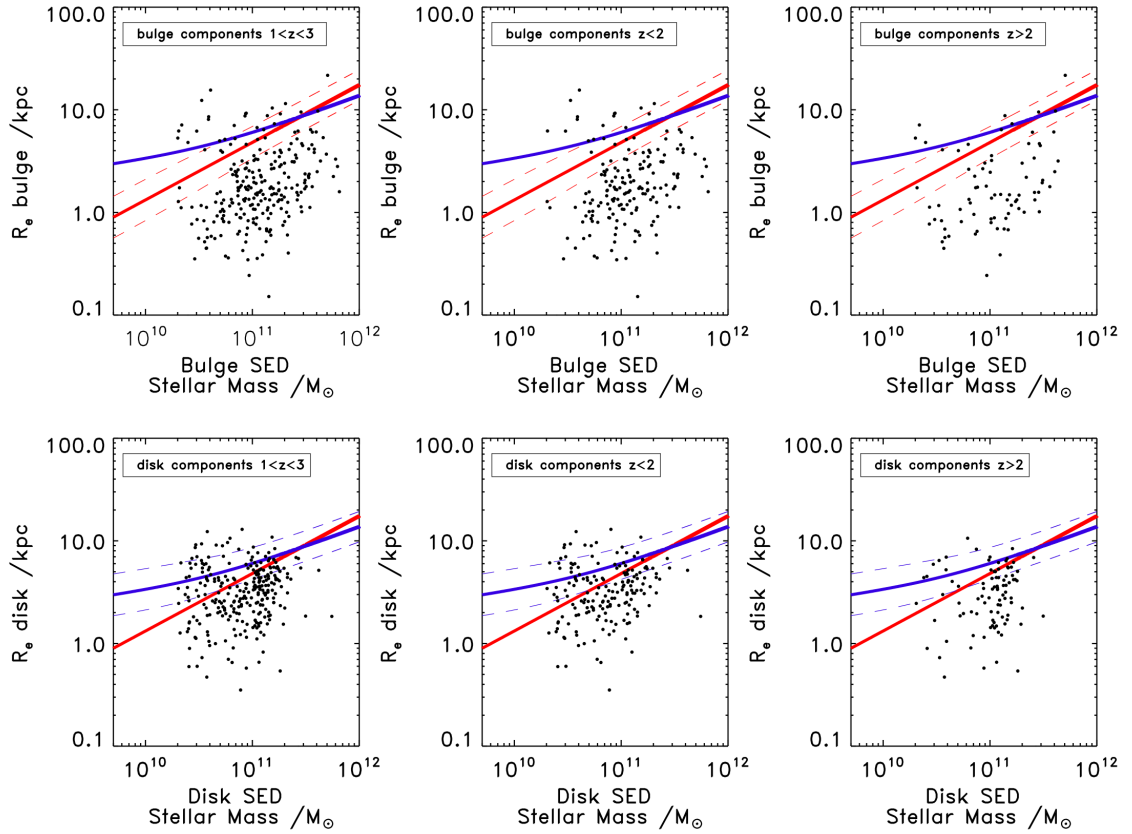


Figure 4.26 *Combined UDS + COSMOS size-mass relations for each component, where now component masses are estimated from the multiple-component SED fitting. The same trends in the sizes of the components witnessed for the relations constructed using masses split according to the H_{160} -band light fractions are also displayed by these relations, which adopt the more robust decomposed SED-fitted component masses. This includes the larger fraction of bulges components which lie below the local relation and the smaller median sizes compared to the disk components, in addition to the lower envelope of sizes displayed. However, I find no stronger evidence for the growing bimodality of bulge sizes with increasing redshift.*

classifications based on single-Sérsic index fits but also (with the exception of IFU spectroscopic studies) global star-formation rates. In this respect, the advantage of my full SED multi-band decomposition technique becomes clear, as it has allowed me to explicitly decompose star-formation rates for bulge and disk components photometrically for the first time, and to better probe the underlying drivers of size evolution by separating out morphological and star-formation trends.

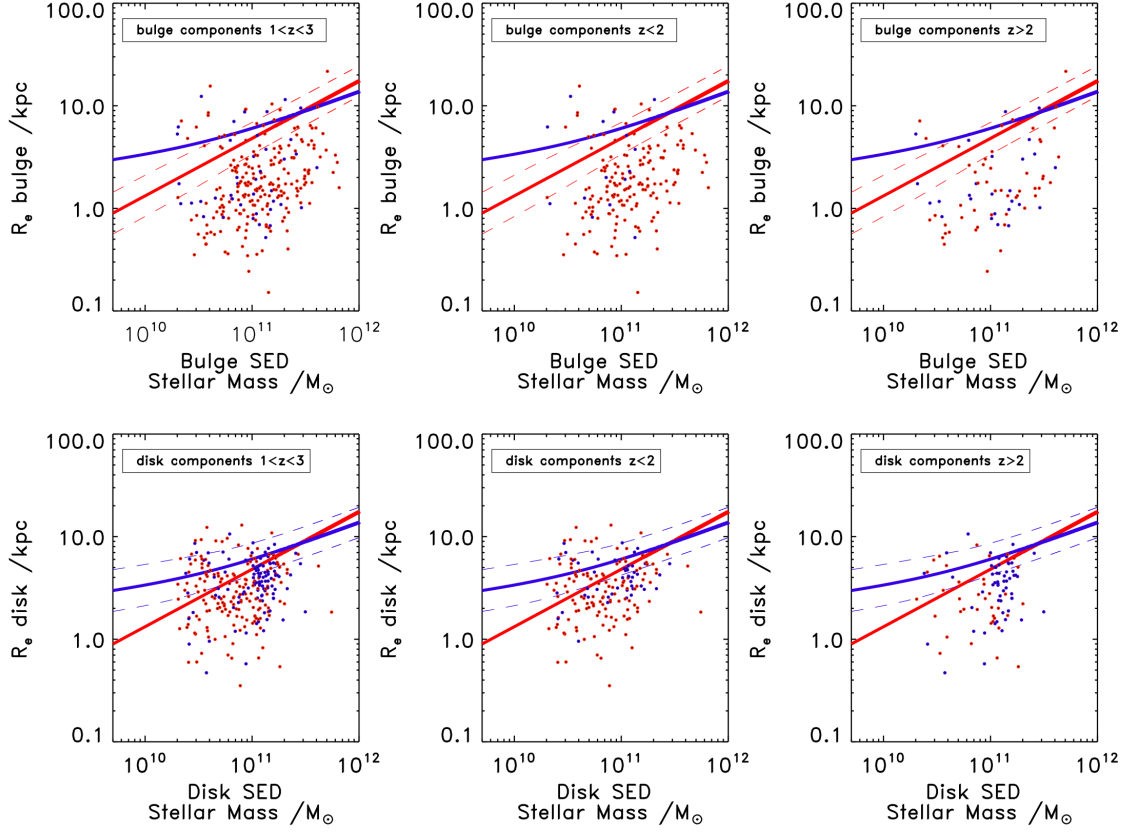


Figure 4.27 *Combined UDS + COSMOS size-mass relations for each component, where component masses are estimated from the multiple-component SED fitting and components are coloured by their star-formation activity using the $sSFR < 10^{-10} \text{ yr}^{-1}$ limit for passivity (blue is used for star-forming and red for passive), and based on the separate component $sSFR$ s from the multiple-component SED fitting. These coloured relations do not reveal a clear division in the sizes of passive and star-forming components, but instead show that the star-forming and passive bulges have comparable sizes with some of the largest bulges being passive and some of the most compact bulges displaying evidence of on-going star formation.*

		$1 < z < 3$	$1 < z < 2$	$2 < z < 3$
COSMOS	bulges on	$21 \pm 4\%$	$14 \pm 4\%$	$36 \pm 8\%$
	bulges below	$79 \pm 4\%$	$86 \pm 4\%$	$64 \pm 8\%$
	disks on	$35 \pm 4\%$	$39 \pm 5\%$	$25 \pm 8\%$
	disks below	$65 \pm 4\%$	$61 \pm 5\%$	$75 \pm 8\%$
UDS	bulges on	$15 \pm 3\%$	$16 \pm 4\%$	$12 \pm 5\%$
	bulges below	$85 \pm 3\%$	$84 \pm 4\%$	$88 \pm 5\%$
	disks on	$56 \pm 4\%$	$59 \pm 5\%$	$52 \pm 6\%$
	disks below	$44 \pm 4\%$	$41 \pm 5\%$	$48 \pm 6\%$
Combined	bulges on	$18 \pm 2\%$	$15 \pm 3\%$	$23 \pm 5\%$
	bulges below	$82 \pm 2\%$	$85 \pm 3\%$	$77 \pm 5\%$
	disks on	$47 \pm 3\%$	$49 \pm 4\%$	$43 \pm 5\%$
	disks below	$53 \pm 3\%$	$51 \pm 4\%$	$57 \pm 5\%$

Table 4.1 *The fractions of components which lie on (or above) their respective local relations within the $1 - \sigma$ scatter and below the $1 - \sigma$ scatter of their relations, where masses for each component have been estimated separately from the multiple-component SED fitting.*

The size-mass relations plotted with the SED-fitted decomposed stellar masses are now coloured by their individual component star-formation rates, where for simplicity I have adopted the $sSFR = 10^{-10} \text{ yr}^{-1}$ discrimination between star-forming and passive components and plot the passive components in red and the star-forming components in blue. These size-mass plots, containing separate component star-formation information, are shown in Fig. 4.27. These plots do not immediately display a clear division between the sizes of passive and star-forming components, but instead reveal that a fraction of the most compact bulges and disks display signs of continued star-formation, while some of the largest bulges and disks are classified as passive. In order to better explore the evolution of bulge and disk components split into their star-forming and passive populations, the fractions of each population which display sizes consistent with or below their respective local relations are given in Table 4.6, along with the offsets of the median sizes of these populations from their local relations in Table 4.6. For clarity all bulges have been compared with the local ETG relation, and disks with the local LTG relation (Shen et al. 2003).

These results reveal that the sizes of passive and star-forming bulges are consistently compact, within the errors, and that star-forming disks are significantly larger. However, they also show that passive disks have intermediate sizes, larger than their passive bulge counterparts, but smaller than the disks which remain active. To better explore these results I have calculated the sizes of these sub-

		$1 < z < 3$	$1 < z < 2$	$2 < z < 3$
COSMOS	sf bulges on	$25 \pm 11\%$	$17 \pm 15\%$	$30 \pm 14\%$
	sf bulges below	$75 \pm 11\%$	$83 \pm 15\%$	$70 \pm 14\%$
	sf disks on	$31 \pm 7\%$	$37 \pm 9\%$	$20 \pm 10\%$
	sf disks below	$69 \pm 7\%$	$63 \pm 9\%$	$80 \pm 10\%$
	passive bulges on	$20 \pm 4\%$	$14 \pm 4\%$	$38 \pm 10\%$
	passive bulges below	$80 \pm 4\%$	$86 \pm 4\%$	$62 \pm 10\%$
	passive disks on	$38 \pm 5\%$	$40 \pm 6\%$	$29 \pm 11\%$
	passive disks below	$62 \pm 5\%$	$60 \pm 6\%$	$71 \pm 11\%$
UDS	sf bulges on	$32 \pm 9\%$	$56 \pm 17\%$	$19 \pm 10\%$
	sf bulges below	$68 \pm 9\%$	$44 \pm 17\%$	$81 \pm 10\%$
	sf disks on	$59 \pm 6\%$	$76 \pm 9\%$	$50 \pm 8\%$
	sf disks below	$41 \pm 6\%$	$24 \pm 9\%$	$50 \pm 8\%$
	passive bulges on	$11 \pm 3\%$	$12 \pm 4\%$	$8 \pm 5\%$
	passive bulges below	$89 \pm 3\%$	$88 \pm 4\%$	$92 \pm 5\%$
	passive disks on	$54 \pm 5\%$	$53 \pm 6\%$	$57 \pm 11\%$
	passive disks below	$46 \pm 5\%$	$47 \pm 6\%$	$43 \pm 11\%$
Combined	sf bulges on	$29 \pm 7\%$	$40 \pm 13\%$	$23 \pm 8\%$
	sf bulges below	$71 \pm 7\%$	$60 \pm 13\%$	$77 \pm 8\%$
	sf disks on	$48 \pm 5\%$	$54 \pm 7\%$	$42 \pm 7\%$
	sf disks below	$52 \pm 5\%$	$46 \pm 7\%$	$58 \pm 7\%$
	passive bulges on	$15 \pm 2\%$	$13 \pm 3\%$	$23 \pm 6\%$
	passive bulges below	$85 \pm 2\%$	$87 \pm 3\%$	$77 \pm 6\%$
	passive disks on	$46 \pm 4\%$	$46 \pm 4\%$	$45 \pm 8\%$
	passive disks below	$54 \pm 4\%$	$54 \pm 4\%$	$55 \pm 8\%$

Table 4.2 *The fractions of components which lie on or below their respective local relations, where masses for each component have been estimated separately from the multiple-component SED fitting, split further into their star-forming and passive populations using the individual component sSFRs.*

divided populations as a fraction of the present-day sizes of similarly massive galaxies, using both the fraction of the median sizes and the median fractional sizes of all objects. As I did not find any difference between these two different estimators I only show the results for the median fractional sizes of all objects. These fractional sizes for the bulge and disk components from the full SED-fitting decomposition are shown in Fig. 4.29. This interpretation of the data confirms the trends determined from the size-mass relation plots, but also allows for a more direct and intuitive comparison of component sizes split into star-forming and passive populations at different redshifts. In Fig. 4.28 I have also included the fractional size evolution as determined from the single-Sérsic fitting, as all previous $1 < z < 3$ light-profile fitting size-mass studies have relied on this parameter to distinguish between bulge and disk-dominated systems. Thus, it allows not only a direct comparison with previous literature, but also with the multiple-component SED-fitting decomposition results and so serves to highlight the additional insight which can be gained from adopting the decomposition method for galaxy size measurements.

Starting with Fig. 4.28 for the single-Sérsic fitting technique, where disk-dominated galaxies are classified as $n < 2.5$ following the convention of Shen et al. (2003) and bulges as $n > 2.5$, I found that the size of passive bulges, passive disks and active bulges are all consistent within their errors and are similarly compact, but that star-forming disks are significantly larger. This can clearly be seen in Fig. 4.28, where I have over-plotted as the dotted line the size evolution for ETGs as fitted by van der Wel et al. (2008), given by $R_e(z)/R_0 \propto (1+z)^{-1}$, and as the dashed line the fitted size-evolution of the decomposed star-forming disks (top-right panel of Fig. 4.29), as given by $R_e(z)/R_0 \propto (1+z)^{-0.5}$.

These trends are consistent with previous studies such as McLure et al. (2013), but raise questions over the mechanisms by which star-forming galaxies quench and also significantly reduce in size to form the passive-disk population. One possible reason for this apparent discrepancy may be that the passive-disk galaxies are more bulge-dominated than the star-forming disks, and are therefore biased to smaller sizes in this comparison.

In order to test this I have explored the Sérsic index distributions of both the passive and star-forming disks and do find that using a cut at $n = 2.5$, the passive disks are centred on a higher n values than the star-forming disks. As a result, I have experimented with decreasing the Sérsic index value used as the discriminator between bulges and disks, in an attempt to ensure that in

	$1 < z < 3$	$1 < z < 2$	$2 < z < 3$
bulge components	3.09 ± 0.20	2.93 ± 0.32	3.41 ± 0.58
star-forming bulges	2.81 ± 0.64	1.83 ± 0.30	3.81 ± 1.0
passive bulges	3.01 ± 0.19	3.00 ± 0.14	3.24 ± 0.44
disk components	1.77 ± 0.10	1.65 ± 0.14	1.99 ± 0.25
star-forming disks	1.62 ± 0.15	1.50 ± 0.13	1.78 ± 0.20
passive disks	1.94 ± 0.25	1.72 ± 0.27	2.35 ± 0.41

Table 4.3 *The offsets of the median sizes of each population from their respective local relations.*

order to be classified as passive disks these galaxies are as disk-dominated as possible. By decreasing the Sérsic index cut to $n = 2$ and $n = 1.5$ I find a better agreement between the Sérsic index distributions for the passive and star-forming disks (although the passive disks are still centred on slightly higher values of n), but this does not affect the derived fractional sizes of this population. Thus, from the single-Sérsic fitting technique one would always find that the star-forming disks are substantially larger than the passive disks, and in fact that the passive disks have sizes comparable to the star-forming and passive bulges.

However, by adopting the multiple-component SED-fitting decompositions I was able to construct the fractional size evolutions displayed in Fig. 4.29, which have again been over-plotted with the van der Wel et al. (2008) ETG ($R_e(z)/R_0 \propto (1+z)^{-1}$) and the fitted star-forming disk ($R_e(z)/R_0 \propto (1+z)^{-0.5}$) relations. Inspecting these new results, I found similar size evolution for the bulge components and star-forming disks, but that the passive disks now have an intermediate size, between the passive and star-forming bulges and the star-forming disks.

It is possible that the adoption of all passive disk components introduces some effects associated with the lower masses that are being probed, as for the single-Sérsic index fits all bulges or disks have stellar masses $M_* > 10^{11} M_\odot$, but the decomposed component masses can range as low as $M_* = 2 \times 10^{10} M_\odot$. For these low mass components I then compared their sizes to similarly massive local galaxies via the Shen et al. (2003) LTG relation, but in this case I am comparing

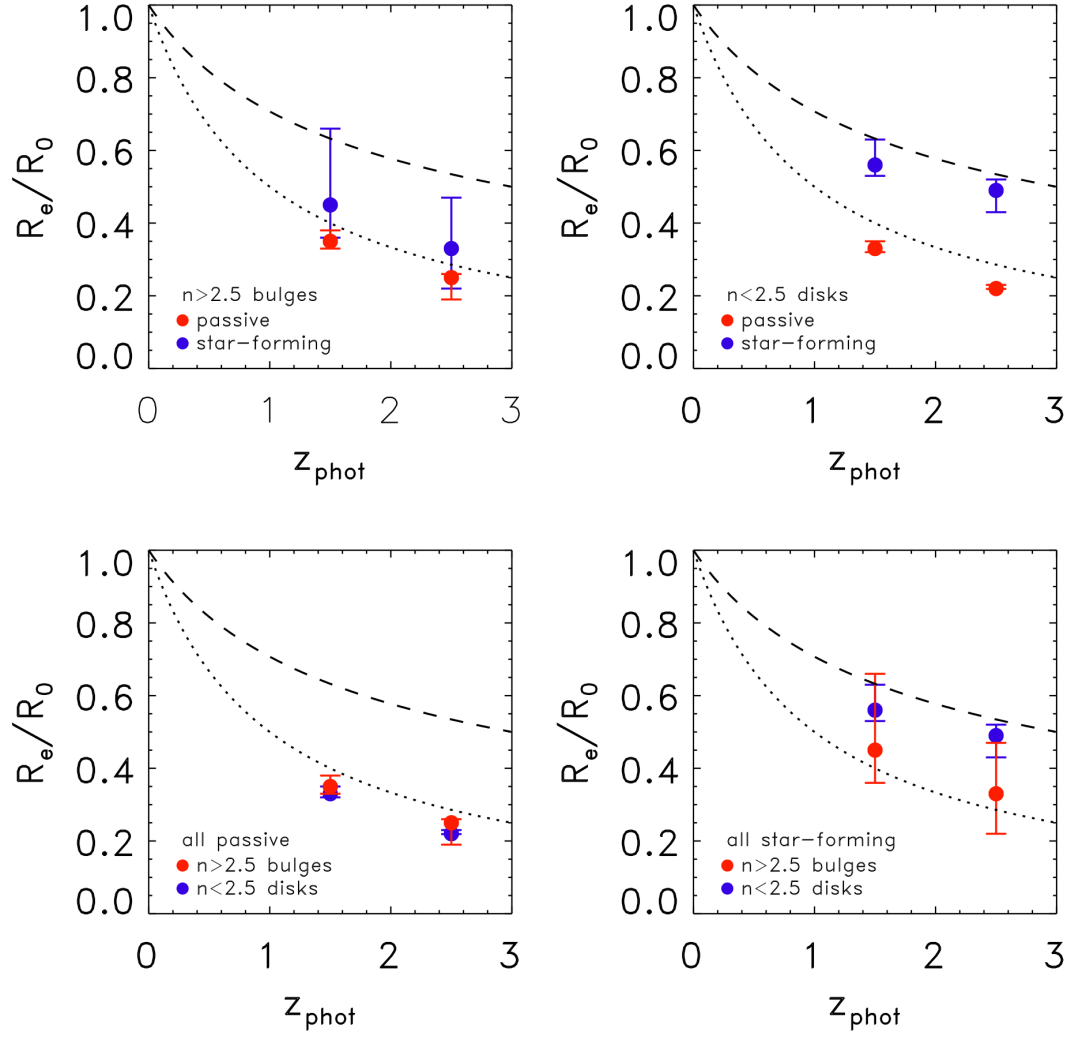


Figure 4.28 *The fractional size evolution of galaxies classified as ETGs and LTGs based on a cut at $n = 2.5$ for my single-Sérsic index fits. The top panels are split into all ETGs (left) and all LTGs (right), whereas the bottom panels show all passive galaxies (left) and all star-forming galaxies (right) to allow an easier comparison of the same data depending on the morphological or star-formation activity distinctions. Over-plotted as the dotted line is the fitted $R_e(z)/R_0 \propto (1+z)^{-1}$ ETG size evolution from van der Wel et al. (2008), and the dashed line is the relation fitted to my decomposed star-forming disk sample (top-right panel of Fig. 4.29) given by $R_e(z)/R_0 \propto (1+z)^{-0.5}$. Using the single-Sérsic fits, the sizes of passive disks are as compact as star-forming and passive bulges, and are significantly smaller than the sizes of star-forming disks. The sizes of the passive and star-forming bulges are equally compact within the errors, and despite the larger uncertainties, this trend remains for the multiple-component SED decompositions represented in Figs. 4.29 and 4.30.*

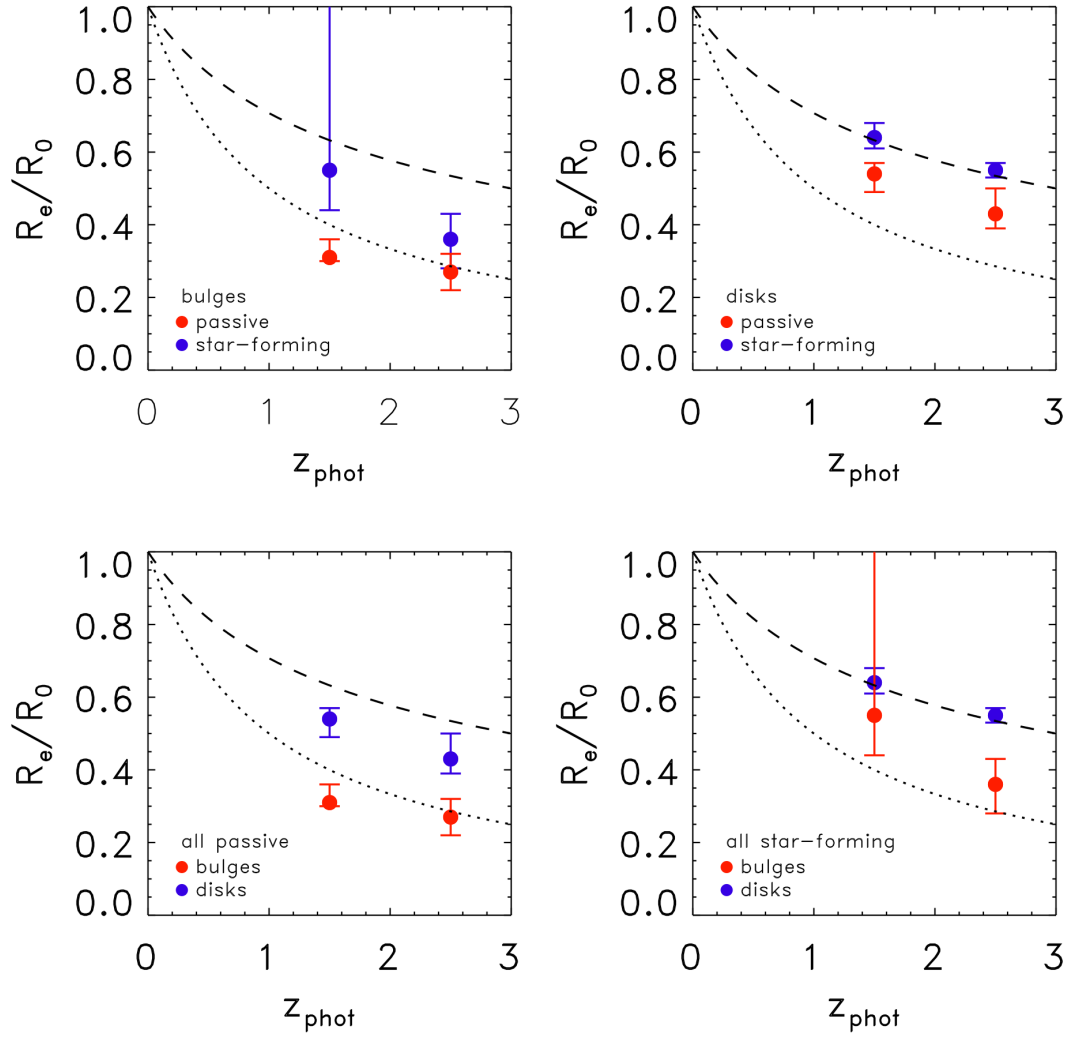


Figure 4.29 *The fractional size evolution of all the bulge and disk components with respect to their local relations in the top-left and right panels, respectively, and for all passive and star-forming components in the bottom-left and right panels. In this case star-forming and passive disks have been compared to the local LTG relation and star-forming and passive bulges have been compared to the local ETG relation. Over-plotted as the dotted line is the fitted $R_e(z)/R_0 \propto (1+z)^{-1}$ ETG size evolution from van der Wel et al. (2008), and the dashed line is the relation fitted to my decomposed star-forming disk sample (top-right panel) given by $R_e(z)/R_0 \propto (1+z)^{-0.5}$. Using the multiple-component SED decompositions, the sizes of passive and star-forming bulges arguably remain equally compact within the large errors, but passive disks display an intermediate size as they are larger than their bulge counterparts but smaller than the star-forming disks.*

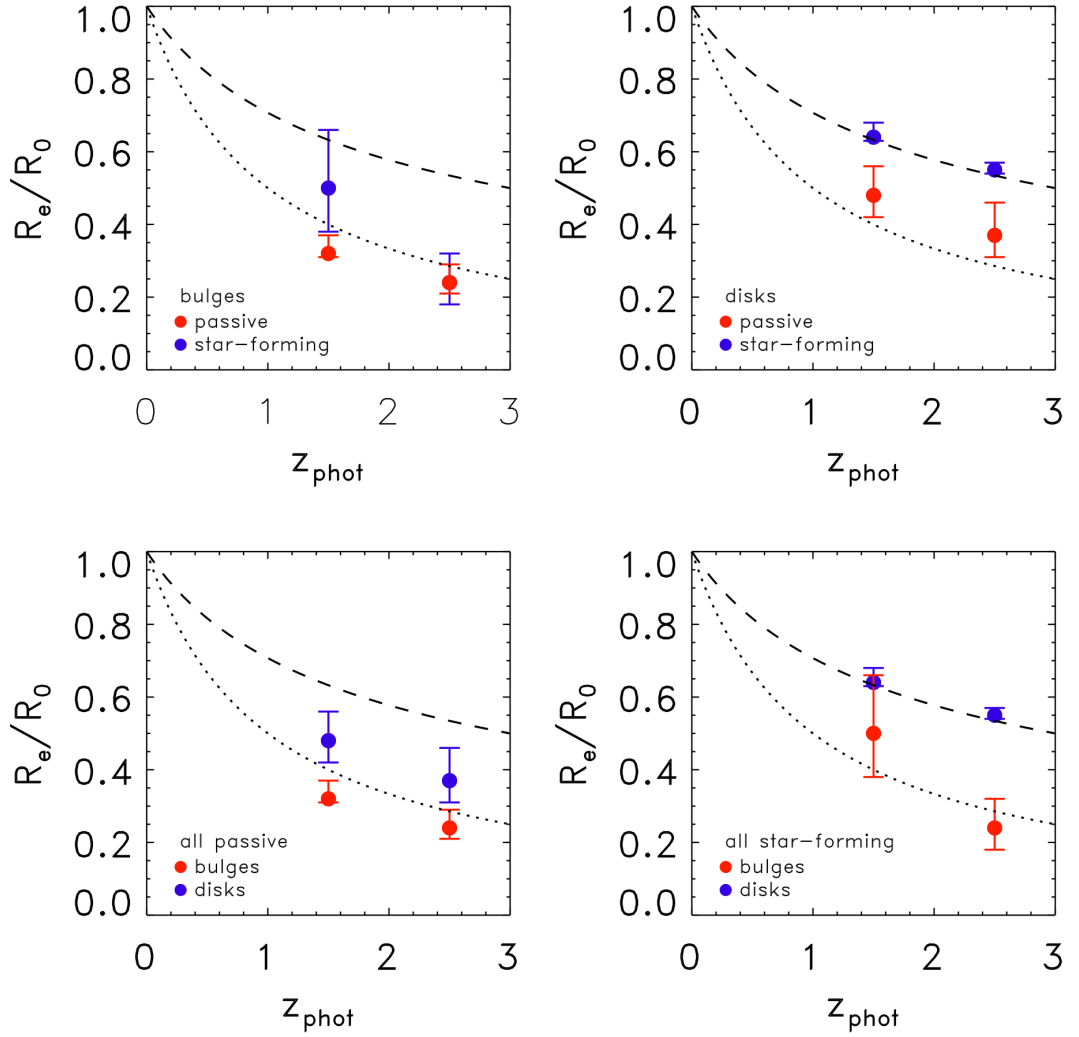


Figure 4.30 *The fractional size evolution of only the dominant components from the multiple-component SED decompositions. The dominant bulge and disk components with respect to their local relations in the top-left and right panels, respectively, and for all passive and star-forming components in the bottom-left and right panels. As above, star-forming and passive disks have been compared to the local LTG relation and star-forming and passive bulges have been compared to the local ETG relation. Over-plotted in the dotted line is the fitted $R_e(z)/R_0 \propto (1+z)^{-1}$ ETG size evolution from van der Wel et al. (2008), and in the dashed line is the relation fitted to my star-forming disk sample given by $R_e(z)/R_0 \propto (1+z)^{-0.5}$. Using only the dominant components from the multiple-component SED decompositions, reveals that the sizes of passive disks from disk-dominated galaxies are still significantly smaller than the size of star-forming disks from disk-dominated galaxies, and are significantly larger than the bulge components of all bulge-dominated galaxies.*

the size of a low-mass disk component of a much more massive bulge-dominated galaxy to a low-mass disk-dominated system at low redshift, which may bias the fractional size measurements of these galaxies to higher values. However, to account for this I have re-plotted these relations using only the bulge component of bulge-dominated galaxies and the disk component of disk-dominated galaxies, and show the resulting relations in Fig. 4.30. Whilst the adoption of this subset does not significantly affect the fractional sizes of the bulges or star-forming disks, it does reduce the size of the passive disks, although not by an amount which makes them consistent with the $n < 2.5$ single-Sérsic index passive galaxies. Hence, even though there may be some effect from low-mass sub-components which drives the passive disks to larger sizes, it is not the dominant reason for the increase in passive disk sizes from the multiple-component SED-fitting decomposition, and I am left to conclude that the more accurate decomposition of both individual component stellar masses and star-formation rates reveals a potential bias in the results from the single-Sérsic index fitting technique, with passive disk components genuinely having an intermediate size.

4.7 Comparison to Literature

Over the past 5-10 years there has been a profusion of morphological studies for massive $z > 1$ galaxies, which have shed light on the size-evolution of the progenitors of today's massive elliptical systems. However, these studies have adopted a number of different selection criteria, and given the discovery that the most compact galaxies are also the most passive (Toft et al. 2007), are often biased towards selecting passive or early-type systems. In spite of the different selection criteria of previous studies, there is general agreement in the literature that galaxies with early-type (ETG) morphologies are more compact than late-type (LTG) systems, and that passive galaxies are more compact than those which display on-going star-formation. However, it has thus far been difficult to disentangle these trends as it is often also expected that ETGs are passive and LTGs are observed to be more star-forming. Thus, in order to conduct a robust and direct comparison between the size evolution of bulge and disk-dominated galaxies, sub-divided further into their passive and star-forming populations, it is important to adopt an unbiased, mass-selected sample, as has been done for this work. A complete comparison with all previous works is difficult due to the selection biases in different samples, so here I limit comparison of my results to

several of the most notable studies which have well-defined samples and stellar-mass and size determination procedures most directly comparable with my own.

In the first case, I draw a comparison between my single-Sérsic fits and the study of Buitrago et al. (2008) conducted at $2 < z < 3$ for $82 M_* > 10^{11} M_\odot$ galaxies with NICMOS HST imaging. In this study, Buitrago et al. split their sample into bulge and disk-dominated systems using a Sérsic index cut at $n = 2$ and find that, on average, the $n < 2$ disks have a fractional size compared to similarly massive local galaxies of $R_e/R_0 = 0.38 \pm 0.05$, and bulge systems with $n > 2$ have $R_e/R_0 = 0.23 \pm 0.04$. Within the errors, these results are consistent with my $z > 2$ sample using the similarly modelled single-Sérsic fits, where as discussed previously, cutting my sample at the lower $n = 2$ limit does not affect the median fractional sizes that I determine.

Following this, I also compare to the study of McLure et al. (2013) for $M_* > 6 \times 10^{10} M_\odot$, $z = 1.4$ galaxies in the UDS covered in the K-band by UKIDSS UDS, and with spectra from FORS2. McLure et al. (2013) split their mass-selected sample by both morphology, above and below $n = 2.5$, and in terms of the overall galaxy star-formation activity. They report that, at this redshift, $n < 2.5$ disks have a median $R_e/R_0 = 0.465 \pm 0.032$ and $n > 2.5$ bulges have $R_e/R_0 = 0.42 \pm 0.05$, whereas splitting by star-formation activity, their passive galaxies have a median $R_e/R_0 = 0.42 \pm 0.035$ and the star-forming sample have a median $R_e/R_0 = 0.625 \pm 0.078$. McLure et al. (2013) comment that the apparent difference in size between their star-forming and $n < 2.5$ disk samples may be due to the contribution of a significant fraction of passive disks to the median size offsets. In comparison, both my $z < 2$ single-Sérsic and multiple-component fits are roughly consistent with the results from this study, although I note that the fractional sizes of the McLure et al. (2013) star-forming and passive samples are more consistent with my multiple-component fits than my single-Sérsic results. However although McLure et al. adopt the same $sSFR < 10^{-10} \text{yr}^{-1}$ passivity criterion, the FORS2 spectroscopic data allowed them to perform simultaneous photometric and spectroscopic fitting to determine stellar-mass and star-formation rates, which in addition to their adoption of “double-burst” star-formation histories during SED fitting, may account for the better agreement between their passive and star-forming fractional size measurements and my decomposed fits (which have also allowed multiple star-formation history components for each galaxy).

I next compare my results to the study of Toft et al. (2007), which was among

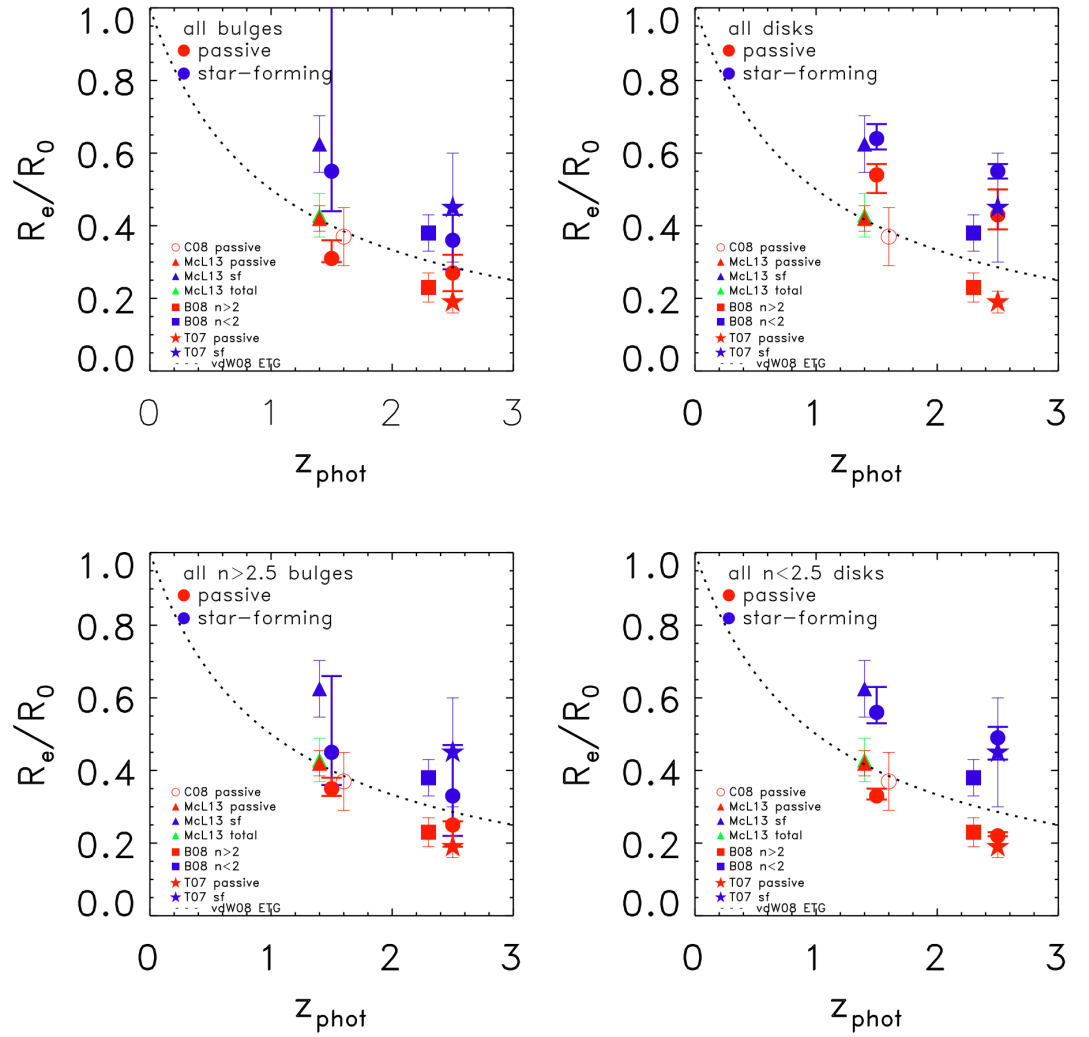


Figure 4.31 *Upper panels: the fractional size evolution of all bulge and disk components from my multiple-component SED decomposition fitting, lower panels: the evolution in the sizes of the ETGs and LTGs from my single-Sérsic index fitting. The samples have again been split into their star-forming and passive populations and are now compared to results from previous studies, as discussed in the text. The additional data have been taken from Cimatti et al. (2008), McLure et al. (2013), Buitrago et al. (2008), Toft et al. (2007) and van der Wel et al. (2008).*

the first to note the correlation between galaxy passivity and compactness. The Toft et al. (2007) study was conducted at $z \approx 2.5$ using HST NICMOS and ACS imaging, and classified galaxies as active or passive depending on whether or not the SED fits to the galaxies were better modelled by constant or burst star-formation histories, and were then cross-checked with $24\mu\text{m}$ data. Toft et al. (2007) report that at $z = 2.5$ passive galaxies have $R_e/R_0 = 0.19 \pm 0.03$ and star-forming galaxies have $R_e/R_0 = 0.45 \pm 0.15$. Again, these results are broadly consistent with the passive and star-forming fractional size estimates from both my single-Sérsic and decomposed fits within the errors, especially given the different classifications adopted for star-forming and passive galaxies and that the Toft et al. (2007) sample spans a much wider, and lower mass range ($0.4 \times 10^{10} < M_* < 5.5 \times 10^{11} M_\odot$) given their purely $z > 2$ and positional selection criteria for HST follow-up. It should also be noted that the Toft et al. (2007) passive sample has a Sérsic index distribution centred on $n < 4$, with $\approx 80\%$ of objects being better fit with $n = 1$ rather than $n = 4$ light profiles.

Finally, in order to complete the literature comparison with previous morphological and star-formation selected samples in both my low and high-redshift bins, I consider the study of Cimatti et al. (2008) at $1.4 < z < 2$ for a spectroscopically confirmed passive GMASS sample imaged with HST NICMOS and ACS. Cimatti et al. (2008) split their sample into two redshift bins and report that at $z = 1.6$ their passive galaxies have a median $R_e/R_0 = 0.37 \pm 0.08$ and at $z = 2.5$ $R_e/R_0 = 0.29 \pm 0.14$. Again, these results are in general agreement with my single-Sérsic fits, but it in this case, as to some extent with the study of Toft et al. (2007), a departure between the size of passive disks and those of the passive bulges begins to become more apparent.

The large sizes of passive disks have been discussed above, but it can be seen from this review of previous studies that this trend only becomes clear when the full morphological decompositions are conducted to accurately model both the sizes and star-formation rates of the individual components, otherwise this trend becomes washed out by the larger contribution of bulges to the passive population, and the considerable scatter in sizes at these redshifts. As a consequence, the majority of single-Sérsic model studies (with the exception of McLure et al. 2013) have concluded that for bulge-dominated systems, morphology is the main indicator of compactness, whereas for disks the main indicator is star-formation, and that passive disks have the same median size as bulges. However, from this study it is clear that the scenario is actually more complex as, although within

bulges passive and active populations appear to be equally compact in size and within disks there is a distinction between the sizes of passive and star-forming components, there is also a difference in the sizes of passive disks and bulges. This suggests that compactness may correlate with some combination of passivity and the presence of a significant bulge component in the galaxy.

4.8 Discussion

By extending my multiple-component light-profile fitting to multi-band photometry and SED fitting to provide individual component masses and star-formation rates, I have directly shown that the median sizes of passive disks are smaller than those of star-forming disks, which raises questions of how these star-forming disks evolve into the passive population. In order to better understand this evolution, it is important to note that it is not necessarily physically meaningful to compare the sizes of passive and star-forming disks at the same redshifts. In a secular evolution scenario we expect the star-forming disks to evolve into the passive population, therefore it is more meaningful to compare the star-forming disks at higher redshifts to passive disks at lower redshifts. In order to conduct this comparison I have used the SED fits of the passive disks to evolve their fitted star-formation histories back to the point at which they would last be classified as star-forming, given my $sSFR > 10^{-10}\text{yr}^{-1}$ criterion, and determine the time that the component has been quenched as the difference between the age of the galaxy at the best-fit redshift and the time when it was last active. For components which were best fit with a burst star-formation history I have adopted the instantaneous burst assumption and used the fitted age of the galaxy as the time for which the component has been quenched. The distribution of the length of time each component has been quenched is given in Fig. 4.32.

From this, it can be seen that the majority of components were last active $\simeq 1$ Gyr before the epoch of observation, therefore in order to best compare between the sizes of passive disks and their star-forming progenitors, the comparison should be conducted between passive disks at their current redshift and star-forming disks at redshifts which correspond to 1Gyr earlier. This is shown in Fig. 4.33, where the fitted $r_e \propto (1+z)^{-0.5}$ star-forming disk relation has been re-plotted for redshifts corresponding to ~ 1 Gyr earlier and can be directly compared to the sizes of the passive disks. From this plot it can be concluded that the sizes of the passive disks at $1 < z < 3$ are consistent with their star-forming progenitors. It is also worth

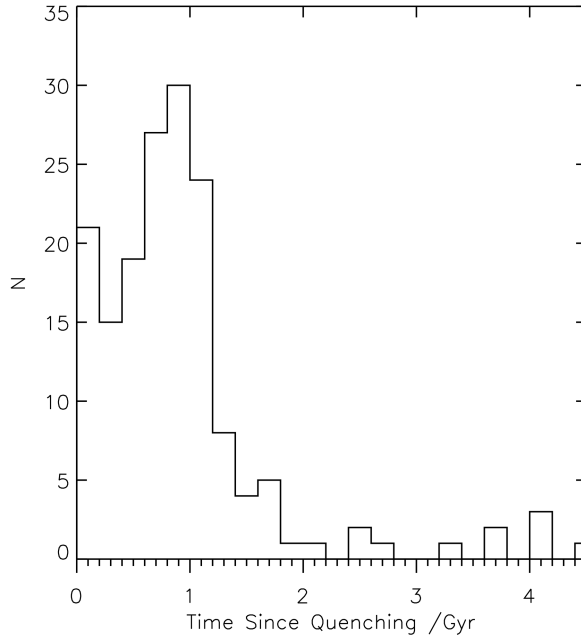


Figure 4.32 *Distribution of the time that each passive disk component has been quenched, as determined by evolving back the star-formation history of each component until the time when $sSFR = 10^{-10}\text{yr}^{-1}$.*

noting from Fig. 4.32 that the most recently quenched disks, < 0.5 Gyr ago, have a median size of $2.47^{+0.28}_{-0.2}$ kpc, which is larger than the median of $1.94^{+0.09}_{-0.14}$ kpc for the whole passive disk population. This lends further support to the assertion that the size offset between the passive and star-forming disks can be accounted for by the relation between size and the redshift of quenching.

The distribution of the masses in the disk components of these disk-dominated passive galaxies and their star-forming progenitors are shown in Fig. 4.34, alongside the distributions of the total galaxy masses. The disk component masses of the passive and star-forming disks have a $p = 0.06$ of being drawn from the same distribution from a K-S test, with the star-forming disks appearing to have a distribution centred on slightly higher stellar masses, while the total galaxy mass distributions are more comparable ($p = 0.66$). Any potential evidence for the star-forming disk components being more massive than the passive disk components which they evolve into is in fact consistent with the secular quenching scenario as the evolution of these systems may be accompanied by a transfer of mass from the disk to the bulge components (e.g. Bournaud et al. 2011), which would reduce the mass in the disk components but leave the total galaxy mass unchanged. Thus, the size and mass evolution of the star-forming and passive

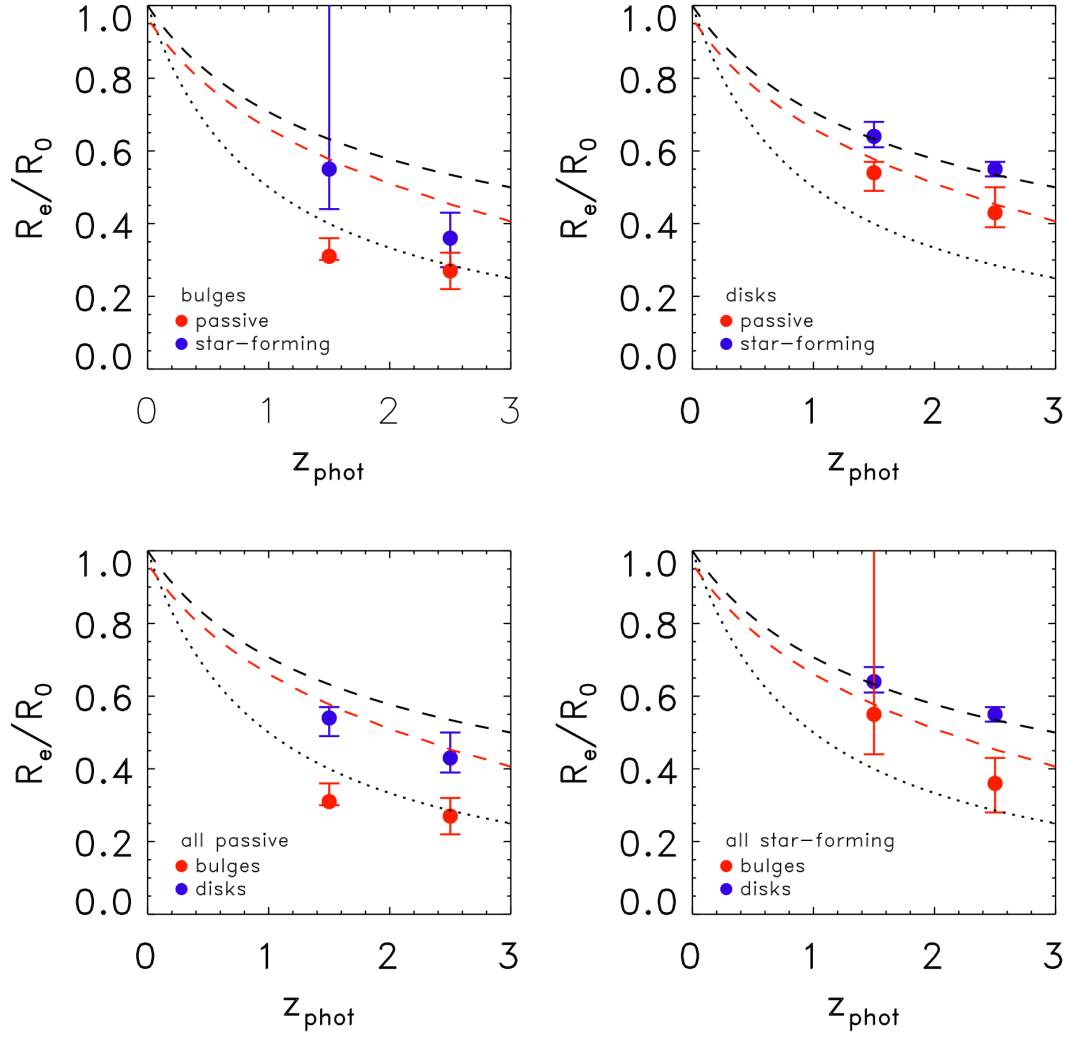


Figure 4.33 *Fractional bulge and disk component size evolution now over-plotted in the dashed red line by the relation for the progenitors of the passive disks to allow direct comparison between the sizes of the passive disks and their 1Gyr earlier star-forming progenitors.*

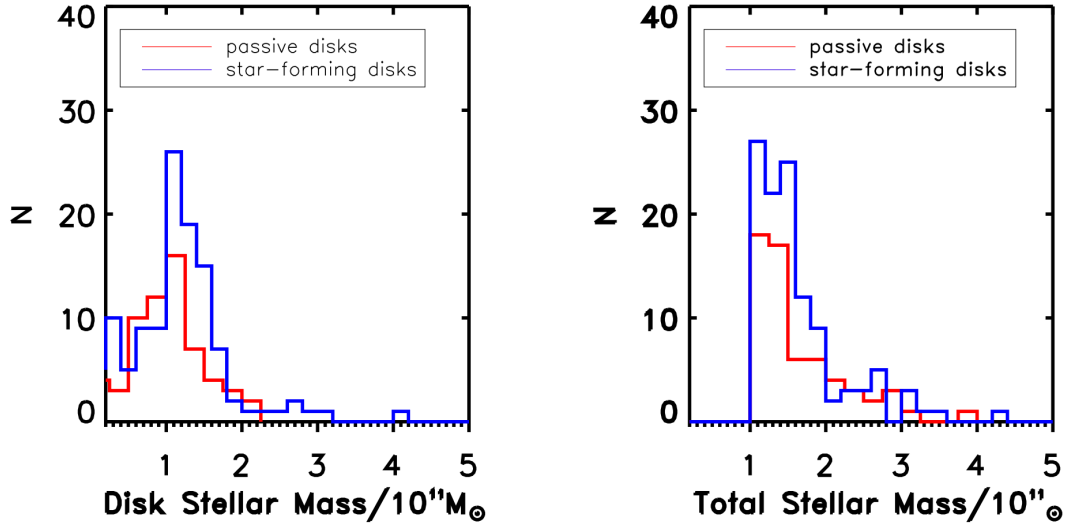


Figure 4.34 *The distribution of the disk component (left) and total (right) masses for the passive and star-forming disk-dominated galaxies. While the disk component masses have a probability $p = 0.06$ of being drawn from the same distribution, with the star-forming progenitors appearing to have a distribution centred on higher masses, the total galaxy masses for these passive and star-forming disk-dominated systems are more comparable with $p = 0.66$. This is consistent with the secular quenching scenario as the evolution of these systems may be accompanied by a transfer of mass from the disk to the bulge components, which would reduce the mass in the disk components but leave the total galaxy mass unchanged.*

disks are less compatible with the idea of major mergers quenching star formation and transforming morphologies, but are consistent with a model in which at high redshifts star-forming disks can quench through halo-mass quenching (Kereš et al. 2005, Dekel et al. 2009a). This is also consistent with the phenomenological model of Peng et al. (2010) which suggests that in this high-mass regime quenching is independent of environment and is a function of galaxy mass, or through violent disk instability models (Dekel et al. 2009b, Ceverino et al. 2010) and morphology quenching (Martig et al. 2009), and then evolve secularly, retaining their massive disks, and possibly shrinking in size by up to $\sim 30\%$ due to the dimming of the disks.

When considering the size evolution of the individual components it is interesting to address the current claims in the literature that the size evolution of passive galaxies from $z \approx 3$ to the present day can be better explained by the addition of newly-quenched, larger galaxies to this population with time (where the size of newly-quenched, younger, galaxies scales with the average density of the Universe at the epoch when they quenched) (e.g. Valentinuzzi et al. 2010b, Cassata et al. 2011, Poggianti et al. 2013, Cassata et al. 2013, Carollo et al. 2013), than by the evolution in size of individual galaxies. One of the natural predictions of this scenario is the star-formation dependent size of *both* bulge and disk components, as at any given epoch the star-forming components are expected to be larger, given the fact that they have not yet quenched but do so at later times. While there is evidence for this trend in the disk components, I do not find strong evidence for a size offset between the passive and active bulges, as has been previously reported by, for example, Carollo et al. (2013), albeit for smaller mass systems. However, as I have discussed, the star-forming bulge population is subject to significant contamination for sub-dominant active disks, and the scatter in the sizes of these components is large.

Finally, in addition to the size evolution of the individual components, this study also allows the evolution of the mass of each component to be explored across the $1 < z < 3$ redshift range covered. By plotting the bulge fraction of the total galaxy mass as a function of redshift in Fig. 4.35 it can be seen that these massive galaxies becoming increasingly bulge-dominated in terms of mass, with decreasing redshift. This relatively gradual emergence of increasingly bulge-dominated systems which retain a massive disk component (as seen from the results in Chapter 3) is perhaps more compatible with the evolutionary scenario of violent disk instabilities, in which it is proposed that as massive galaxies evolve

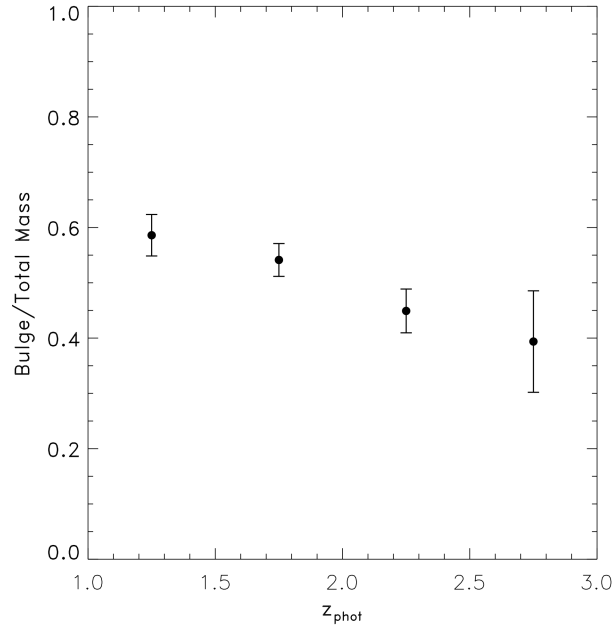


Figure 4.35 *The evolution in the mean Bulge/Total mass fractions of the galaxies in my combined UDS + COSMOS sample binned according to redshift, illustrating the gradual build-up of bulge mass with the retention of a massive disk component.*

there is a migration of mass to the centre of the system which acts to build-up a central bulge, whilst leaving a massive disk in place.

Chapter 5

Morphological and Star-formation Evolutionary Trends

5.1 Introduction

Following on from Chapter 4, which presented the results of the size evolution of the separate bulge and disk components of the massive galaxies in my CANDELS-UDS and COSMOS samples, in this chapter I discuss the evolutionary trends observed for the additional morphological properties. Particular emphasis will be placed on addressing the dominance of the bulge and disk fractions, the star-formation activity displayed by the individual components, and the axial ratio distributions of the bulge and disk components.

These properties have already been explored for the CANDELS-UDS sample in Chapter 3, where I found that in terms of overall galaxy morphologies, $z \sim 2$ marks a transition phase, above which these most massive galaxies become increasingly disk-dominated and below which they are mixed bulge+disk systems. In Chapter 3 I also reported that a significant fraction of passive galaxies are disk-dominated, as classified by either their single Sérsic and multiple-component fits ($40 \pm 7\%$ and $25 \pm 6\%$, respectively). This result has interesting implications for models of galaxy quenching, as it suggests that the processes responsible for star-formation quenching may in fact be distinct from those which drive morphological transformations. Moreover, the previous CANDELS-UDS analysis provided evidence that the axial ratios for high-redshift star-forming disks are

inconsistent with the flat distributions of passive disks within my sample, and with local disk-dominated galaxies, but are more comparable to the distributions peaked at $b/a \sim 0.6 - 0.8$ for bulge-dominated systems. This was interpreted as evidence for the more tri-axial nature of high-redshift star-forming disks, which could potentially be explained by star-formation processes “puffing-up” the scale-heights of active disks.

These results are re-addressed here, exploiting the multiple-component SED fitting results for both the UDS and COSMOS samples. As has been previously discussed in Chapter 4, the extension of the morphological decomposition to individual component SED fitting to provide separate component stellar masses did not significantly affect any of the reported trends in Chapter 3 (which adopted component masses based on the H_{160} decomposed light-fractions), thus re-enforcing the validity of adopting H_{160} flux as a reasonable proxy for mass. However, the more important advantage provided by the decomposed SED-fitting is the ability to determine star-formation rates for the individual components. Thus, by adopting the fully decomposed component properties, I can now better explore the trends in star-formation activity and morphology.

5.2 Morphological Evolution

In addition to studying the size evolution of massive galaxies, as has been discussed in Chapters 3 & 4, the evolution of the overall morphology of galaxies at $1 < z < 3$ can also provide insight into the physical processes which govern galaxy evolution. This is particularly pertinent in the redshift range covered by this study, as there is growing evidence from parametric and visual morphological studies, as well as dynamical surveys, that it is within this epoch that massive galaxies are undergoing dramatic structural transformations (e.g. Buitrago et al. 2008, Mortlock et al. 2013, Förster Schreiber et al. 2009).

For completeness, I first present the CANDELS-UDS and COSMOS samples, separately as well as combined, split by fractions into the different best-fit models, to allow direct comparison between the fields. Tables 5.1 and 5.2, which present the fractions of objects in each best-fit model category for the CANDELS-UDS field both from the sample of Chapter 3 and from the re-defined sample as discussed in Chapter 4, have been included to demonstrate that the adoption of the re-estimated stellar masses has not significantly affected the results from

the morphological analysis.

bulge	bulge +psf	disk	disk +psf	bulge +disk	bulge+disk +psf
$10 \pm 2\%$	$1 \pm 1\%$	$18 \pm 3\%$	$8 \pm 2\%$	$58 \pm 7\%$	$5 \pm 2\%$

Table 5.1 *The percentages of the original UDS sample of 192 objects with multiple-component best-fits corresponding to each of the six fitted models.*

bulge	bulge +psf	disk	disk +psf	bulge +disk	bulge+disk +psf
$10 \pm 2\%$	$1 \pm 1\%$	$17 \pm 3\%$	$8 \pm 2\%$	$59 \pm 7\%$	$5 \pm 2\%$

Table 5.2 *The percentages of the re-selected UDS sample of 184 objects with multiple-component best-fits corresponding to each of the six fitted models.*

From Tables 5.2 and 5.3, it can be seen that, overall, there is good agreement between the fractions of objects best-fit by the different models between the re-defined CANDELS-UDS and COSMOS samples. However, this direct comparison also highlights that there are fewer objects fitted with a bulge+disk model in COSMOS compared to UDS, but more have a bulge+disk+PSF best-fit model. Nevertheless, this difference is small, and while only part of the discrepancy can be attributed to cosmic variance (Newman & Davis 2002), the small number statistics involved do not provide significant evidence for any biases in the fitting of morphologies between these two fields. Moreover, it should also be noted from comparison of these two tables, that overall the fractions of “pure” bulge and disk galaxies are statistically comparable in both fields. The fractions for the overall combined sample are given in Table 5.4, where they can be seen to be consistent within the errors between both the UDS and COSMOS fields.

bulge	bulge +psf	disk	disk +psf	bulge +disk	bulge+disk +psf
$15 \pm 3\%$	$2 \pm 1\%$	$15 \pm 3\%$	$13 \pm 3\%$	$42 \pm 6\%$	$13 \pm 3\%$

Table 5.3 *The percentages of the final COSMOS sample of 163 objects with multiple-component best-fits corresponding to each of the six fitted models.*

bulge	bulge +psf	disk	disk +psf	bulge +disk	bulge+disk +psf
$12 \pm 2\%$	$2 \pm 1\%$	$16 \pm 2\%$	$10 \pm 2\%$	$51 \pm 5\%$	$9 \pm 2\%$

Table 5.4 *The percentages of the combined UDS+COSMOS samples of 347 objects with multiple-component best-fits corresponding to each of the six fitted models.*

5.2.1 Trends with redshift

In order to explore how the overall morphologies of these massive $1 < z < 3$ galaxies evolve with redshift I have binned the samples at $z < 2$ and $z > 2$ and have calculated the co-moving number densities of objects split according to the different morphology discriminators adopted in Chapter 3: $B/T > 0.5$ and $D/T > 0.5$; $B/T > 0.7$, $D/T > 0.7$ (where D/T is used to avoid confusion arising from a PSF component contributing a significant fraction) and intermediate objects; and $B/T > 0.9$ and $D/T > 0.9$ and intermediate objects. The results from this binning, determined based on the H_{160} light fractions, are shown in Fig. 5.1, where the three rows are split further into the UDS, COSMOS and combined samples. These number densities have been over-plotted with the total number density of galaxies in each redshift bin to demonstrate how the overall number of galaxies falls above $z = 2$. To first order these plots reveal that, as previously discussed in Chapter 3, in the UDS field the massive galaxy population is dominated by disk structures above $z = 2$ and becomes an increasing mix of bulge+disk morphologies below this, with no evidence even by $z = 1$ for the emergence of pure bulge systems. The rise in intermediate objects is similar in both the UDS and COSMOS fields. However, the COSMOS sample appears to show a less significant trend for the demise of dominant disks below $z = 2$ as the redshift evolution for the $D/T > 0.7$ and $D/T > 0.9$ cuts is much flatter within the errors, and actually increases with redshift for the $D/T > 0.5$ cut. These results appear to reveal significant evidence for a difference between the two fields.

This apparent inconsistency also extends to Fig. 5.2, which plots the co-moving number densities of the objects split into bulge and disk-dominated systems according to the multiple-component SED fitted masses. Compared to Fig. 5.1, these plots have a larger number of bulge-dominated systems, which, as previously discussed, is to be expected from the decomposed mass analysis due to the more evolved stellar populations and consequently higher mass-to-light ratios of bulge

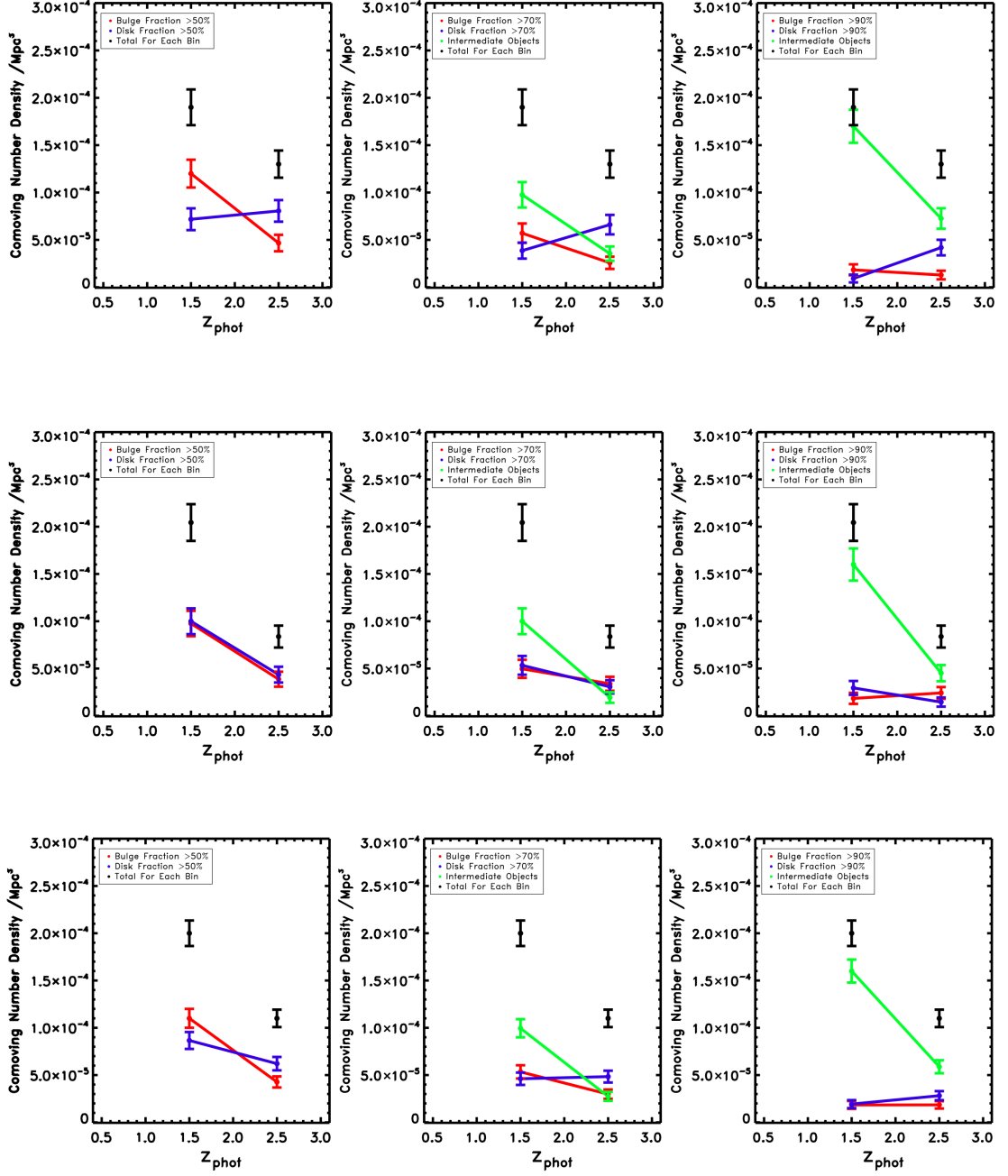


Figure 5.1 *The co-moving number densities of the samples split by the different bulge and disk-dominated criteria according to their H_{160} light fractions. The top panels show the UDS sample, the middle panels are the COSMOS sample and the bottom panels are for the combined UDS+COSMOS total sample. The blue data-points and lines are for the disk-dominated galaxies, shown in red are the bulge-dominated galaxies and in green are galaxies classified as intermediate bulge+disk systems. The left-hand panels split the populations according to $B/T > 0.5$ and $D/T > 0.5$, the middle panels adopt $B/T > 0.7$, $D/T > 0.7$ and intermediate objects, and the right panels use $B/T > 0.9$, $D/T > 0.9$ and intermediate objects.*

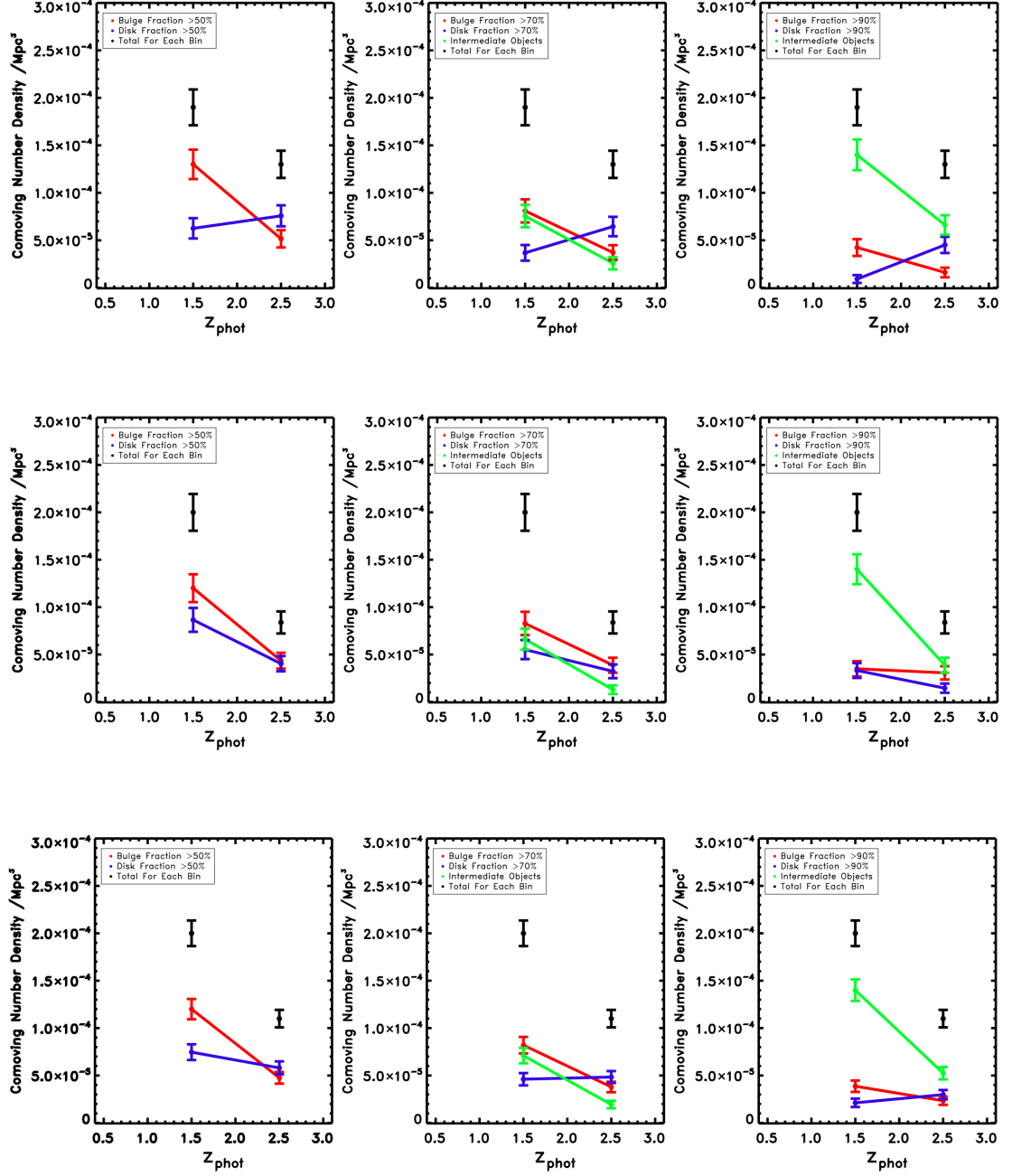


Figure 5.2 *The co-moving number densities of the samples split by the different bulge and disk-dominated criteria according to their SED-fitted individual component stellar-mass fractions. The top panels show the UDS sample, the middle panels are the COSMOS sample and the bottom panels are for the combined UDS+COSMOS total sample. The blue data-points and lines are for the disk-dominated galaxies, shown in red are the bulge-dominated galaxies and in green are galaxies classified as intermediate bulge+disk systems. The left-hand panels split the populations according to $B/T > 0.5$ and $D/T > 0.5$, the middle panels adopt $B/T > 0.7$, $D/T > 0.7$ and intermediate objects, and the right panels use $B/T > 0.9$, $D/T > 0.9$ and intermediate objects.*

systems compared to disks. Nevertheless, the same difference is observed between the disk evolution in the UDS and COSMOS samples.

However, when considering the evolution in the number of objects with disk and bulge-dominated morphologies in these plots, the overall evolution in the total number of galaxies in each redshift bin must also be taken into account, as it can clearly be seen that the total number of $z > 2$ galaxies is significantly less than the number of objects at $z < 2$. In order to better interpret these results, I have plotted the fraction of the total number of objects in each redshift bin which are split into bulge and disk-dominated according to the three different cuts in Figs. 5.3 and 5.4, again using the H_{160} light fractions and the decomposed stellar-mass estimates, respectively. From inspection of these plots, the variation between the disk-dominated trends with redshift between the fields is somewhat less prominent, although still present, and the evolution of the intermediate bulge+disk fractions remain consistent.

This discrepancy between the two fields is somewhat surprising given the results from Tables 5.2 and 5.3, which show that there are the same fraction of galaxies classified as “pure” bulges and disks in both fields. Further exploration of this issue revealed differences in the distributions of both the bulge and disk-dominated systems between the fields. These distributions are shown in Fig. 5.5 with the distributions for the UDS field on the left given in blue for the $D/T > 0/5$ galaxies and red for the $B/T > 0/5$, and the COSMOS fits on the right. It can be seen from these figures that there is a sharp peak in the redshift distribution of disk-dominated galaxies in the UDS at $z \approx 2$, which is perhaps indicative of a photometric redshift focussing effect. There is also a steeper decline in the number of bulge-dominated systems above $z \sim 2$ in the UDS field compared to COSMOS. These two effects act together to produce a flatter redshift evolution of disks compared to bulges in the COSMOS field.

The peaked redshift distribution of the disk-dominated objects in the UDS required further exploration to ensure that my results have not been biased by photometric redshift focussing effects. This issue is well-known for objects with relatively flat SEDs where there are no strong breaks for the SED template fitting approach to fit to and so may preferentially occur for the disk-dominated galaxies in my sample. Plausibly, this may also be more of an issue for the UDS sample due to the accompanying optical and near-IR photometry utilised for the SED fitting, as the UDS field makes use of much shallower Y-band data compared to the COSMOS field. This may partly explain the peak of objects with photometric

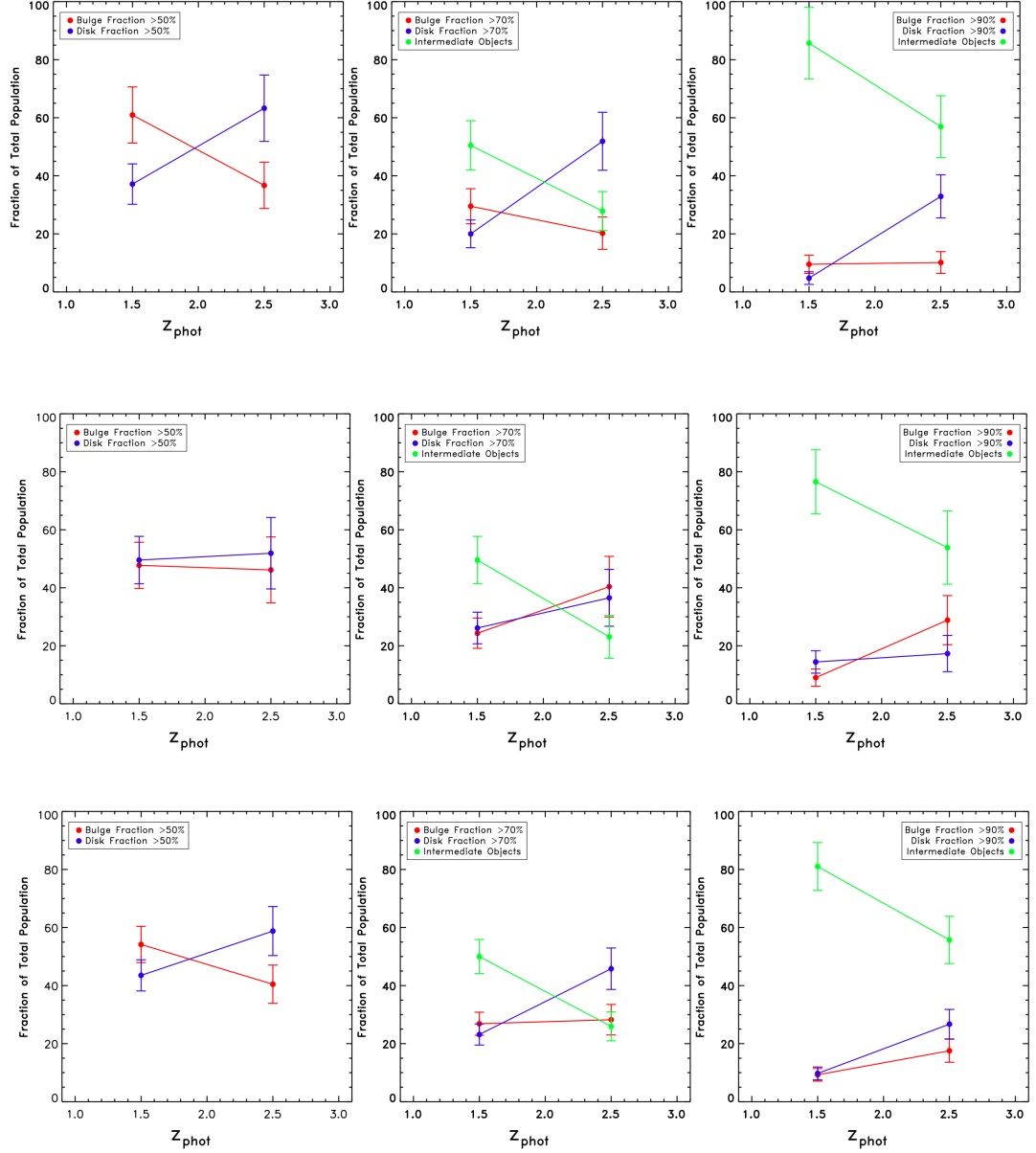


Figure 5.3 *The fraction of the total number of objects in each sample classified by the different bulge and disk-dominated criteria according to their H_{160} light fractions. The top panels show the UDS sample, the middle panels are the COSMOS sample and the bottom panels are for the combined UDS+COSMOS total sample. The blue data-points and lines are for the disk-dominated galaxies, shown in red are the bulge-dominated galaxies and in green are galaxies classified as intermediate bulge+disk systems. The left-hand panels split the populations according to $B/T > 0.5$ and $D/T > 0.5$, the middle panels adopt $B/T > 0.7$, $D/T > 0.7$ and intermediate objects, and the right panels use $B/T > 0.9$, $D/T > 0.9$ and intermediate objects.*

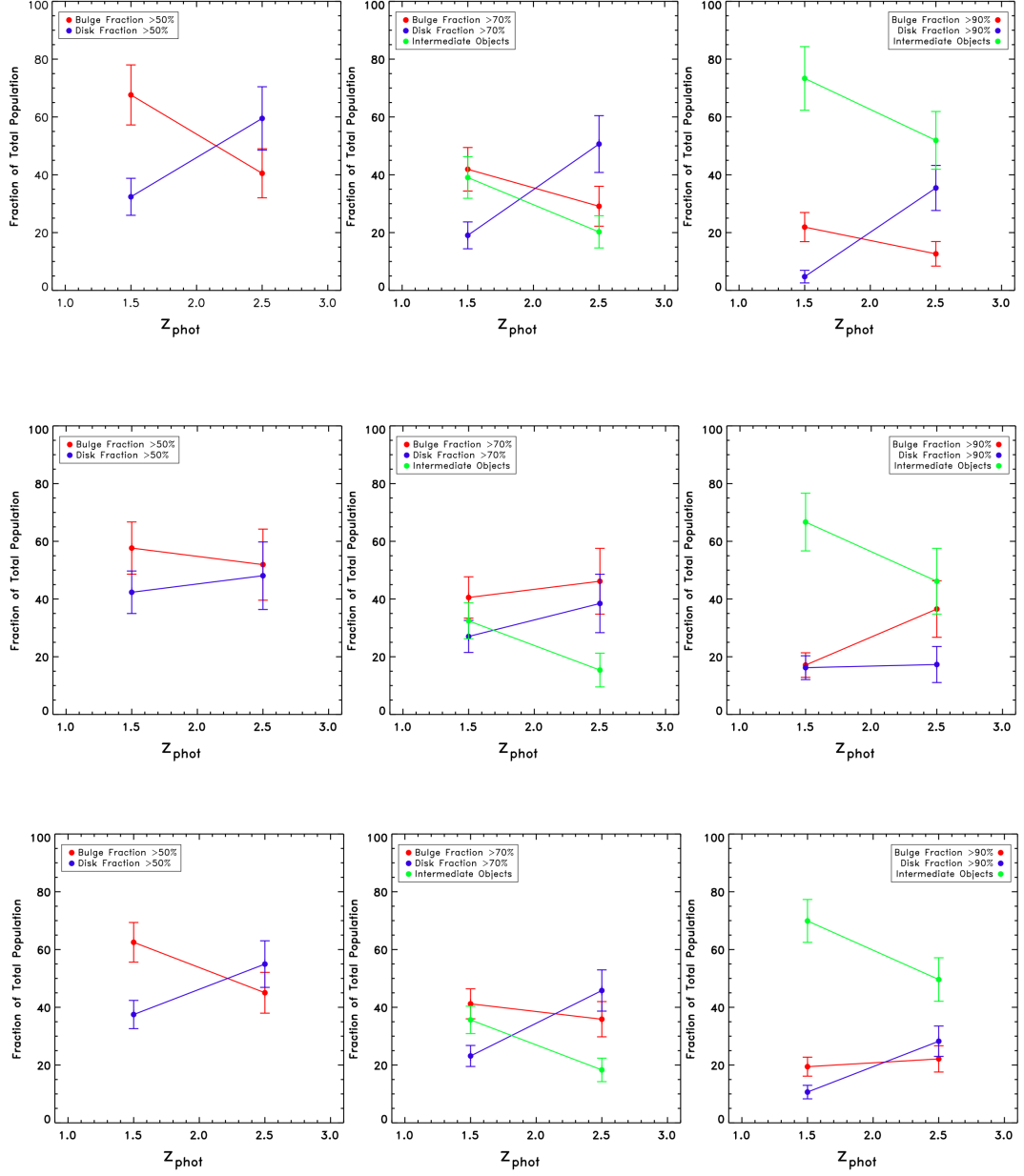


Figure 5.4 *The fraction of the total number of objects in each sample classified by the different bulge and disk-dominated criteria according to their decomposed SED-fitted stellar-mass fractions. The top panels show the UDS sample, the middle panels are the COSMOS sample and the bottom panels are for the combined UDS+COSMOS total sample. The same configuration is used as in Fig. 5.3. By adopting the fractions determined from the stellar-mass contributions and comparing them to those from the H_{160} light fractions, it can be seen that the most massive galaxies become increasingly mixed bulge+disk systems morphologically from $z \sim 3$ to $z \sim 1$, but their masses become even more bulge-dominated.*

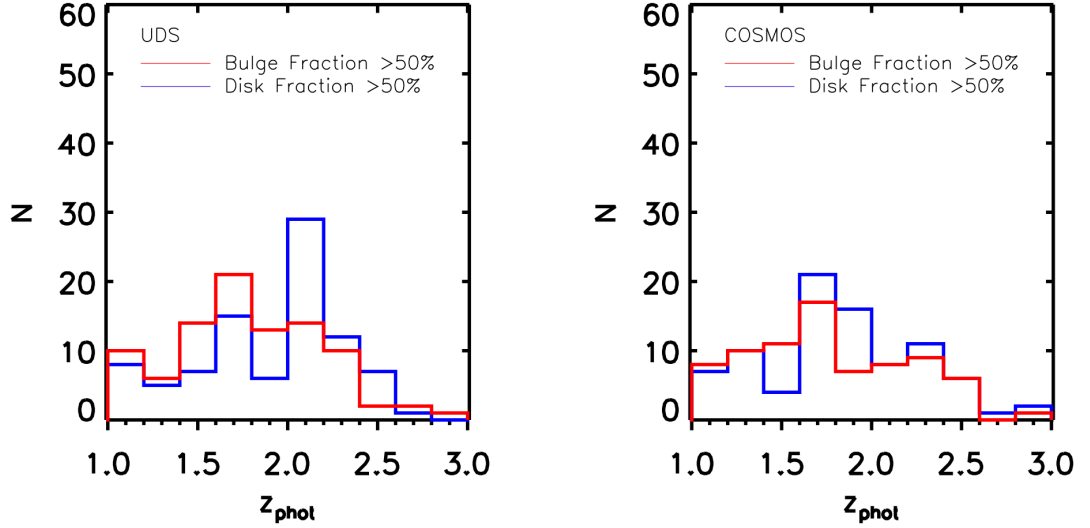


Figure 5.5 *Redshift distributions of the bulge and disk dominated components using the $B/T > 0.5$ and $D/T > 0.5$ criteria for the UDS and COSMOS samples separately. Comparison of these distributions reveals a peak in the redshift distribution of the disk-dominated galaxies in the UDS at $z \sim 2$, possibly indicative of redshift focussing in this sample. However, this comparison also shows that the number of bulge-dominated galaxies falls-off more steeply in the UDS than in COSMOS. This abundance of $z > 2$ bulge-dominated galaxies in COSMOS will also contribute to the flatter evolution of the fraction of disk-dominated galaxies in COSMOS.*

redshifts at $z \sim 2$ as the SED fitting code will try to fit the Balmer break in these galaxies at the longest wavelength possible until it is constrained by photometry. Thus, the shallow Y-band in the UDS may not be sufficient to constrain the fit and will result in the Balmer break ($\lambda \approx 4000\text{\AA}$) being placed up against the J-band at $\lambda \approx 1200\text{\AA}$, giving a photometric redshift of $z \sim 2$.

In order to test for this effect, I have cross-matched my sample with the CANDELS-UDS photometric redshift catalogue of Dahlen et al. (2013, in preparation) and have adopted their redshift estimates for my UDS sample. The Dahlen et al. photometric redshift catalogue is constructed using a Bayesian approach which uses the redshift probability distributions of six different photometric redshift fits from CANDELS team members using different photometric-redshift fitting codes. Adopting the Dahlen et al. redshifts for my sources does smooth out the redshift spike for the disk-dominated galaxies in my UDS sample, but does not affect the redshift distribution of the bulge-dominated objects, as can be seen in Fig. 5.6. Out of my $z > 2$ disk-dominated UDS sample, 14 objects are brought down to the $z < 2$ bin when adopting the Dahlen et al. photometric redshifts, but this number drops to 8 objects when considering the $1 - \sigma$ upper errors on the Dahlen et al. values. However, by comparing the morphological redshift evolution using both my photometric redshift cuts and the Dahlen et al. values, the overall effect on the fractional redshift evolution of the UDS and, moreover the combined sample, for disk-dominated objects is small.

For the objects for which the Dahlen et al. redshifts are $z < 2$, I have examined the SEDs and have over-plotted both my best-fit SED models and models corresponding to a fit at the Dahlen et al. photometric redshifts. This comparison for two representative objects is displayed in Fig. 5.7, which demonstrates that the SEDs for these two disk-dominated galaxies are in fact relatively flat and are arguably equally well fit by both photometric redshift models. Also worth considering, is that the Dahlen et al. redshifts are estimated based upon the redshifts fits of six other studies, some of which have redshift distributions for their overall samples that display peaks at lower redshifts, which are potentially no better physically motivated than my $z \approx 2$ peak. In light of this, and given the fact that adopting the Dahlen et al. photometric redshifts does not actually affect the trends for the combined UDS and COSMOS sample, I have concluded for this work that my overall results are not biased by this issue and so discuss the trends displayed by the combined UDS and COSMOS samples, simply noting that the separate UDS and COSMOS samples display some differences which are

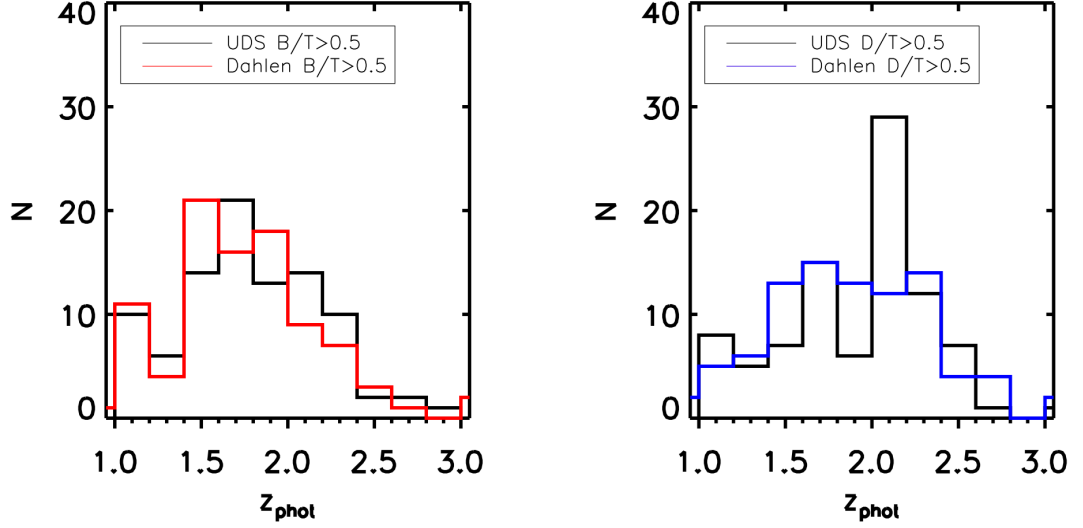


Figure 5.6 *Comparison of my redshift distribution in the UDS with the Dahlen et al. (2013, in preparation) redshift distribution. The redshift distributions have been split between the bulge-dominated objects in the left panel and the disk-dominated galaxies in the right panel. My UDS redshift distributions are given in black and the Dahlen et al. distributions are given in red and blue for the bulges and disks respectively. Examination of these distributions shows that the bulge-dominated galaxies do not appear to exhibit any strong evidence of redshift focussing, whereas adopting the Dahlen et al. redshifts for the disk-dominated galaxies smooths out the peak at $z \sim 2$. Eight of the disk-dominated galaxies have been fit with $z_{\text{phot}} > 2$ from my analysis and with $z_{\text{phot}} < 2$ from the Dahlen et al. catalogue within their $1 - \sigma$ upper errors. However, by comparing the morphological redshift evolution using both my photometric redshift cuts and the Dahlen et al. values, I find that any redshift focussing does not bias the morphological trends displayed by my combined UDS and COSMOS sample.*

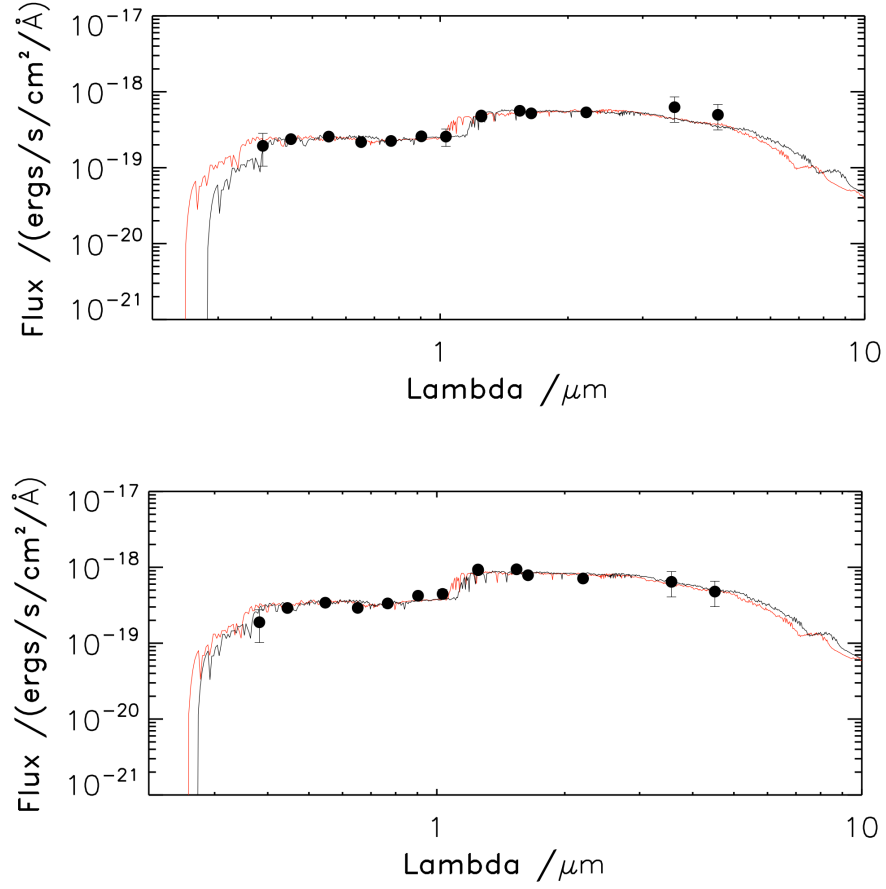


Figure 5.7 *Two examples of objects which have been fitted with $z_{\text{phot}} > 2$ from Cirasuolo et al., in preparation, and with $z_{\text{phot}} < 2$ from Dahlen et al. (2013, in preparation). The fits for the Cirasuolo et al. photometric redshifts are shown in black and the fits adopting the Dahlen et al. photometric redshifts are in red. The top panel shows an object which was best fit with $z_{\text{phot}} = 2.1$ from Cirasuolo et al., in preparation, and with $z_{\text{phot}} = 1.752$ from Dahlen et al. (2013), and the bottom panel shows an object which was best fit with $z_{\text{phot}} = 2.02$ from Cirasuolo et al., in preparation, and with $z_{\text{phot}} = 1.824$ from Dahlen et al. (2013). The SEDs for these two objects are relatively flat and these examples demonstrate the breaks between the Y and J-bands are fit reasonably well by both redshift models, however it should be noted that the points plotted are the photometry data-points which were used for the Cirasuolo et al. fits and will not be the same photometry used by the fits which were included in Dahlen et al.*

at least partly due to cosmic variance (Newman & Davis 2002).

Therefore, in conclusion, the combined UDS and COSMOS samples reveal that the fraction of bulge-dominated galaxies remains relatively flat across the $1 < z < 3$ redshift range covered by this study, particularly when considering the “pure” bulges with $B/T > 0.9$, where even at $z < 2$ these most massive galaxies are predominantly mixed bulge+disk systems and the significant fraction of “pure” bulges, comparable to the giant elliptical systems which dominate the massive galaxy population locally, are yet to emerge. In spite of the above discussion, there is still some evidence for the demise of disk-dominated systems below $z = 2$, both from the fractions determined from the H_{160} light fractions and the decomposed stellar masses. This becomes particularly evident when comparing the fraction of disk-dominated galaxies to not only the bulge-dominated, but also the intermediate objects, as it is clear that $z = 2$ still marks a key phase below which these most massive galaxies gain an increasing contribution from bulge components. The strongest trend witnessed from this analysis is the increase in the intermediate classification with decreasing redshift, which reveals the rise of S0 type galaxies within this redshift regime. This trend is noticeably stronger when cutting by H_{160} light fraction than decomposed mass. However, this is to be expected from the fact that bulge components are more dominant in terms of their contribution to the mass of the galaxy, so the decomposed mass trends show a weaker trend in the increase of intermediate systems but display a larger increase in the fraction of bulge-dominated systems.

Therefore, the extension of the morphological decomposition to the CANDELS-COSMOS field and across the 4-band photometry provided by HST has confirmed the main trends in the morphological evolution of the massive galaxies reported for the CANDELS-UDS sample in Chapter 3, strengthening the trend for the increase in the fraction of mixed bulge+disk systems, but weakening the trend for the demise of disk-dominated systems below $z = 2$.

5.3 Star-Formation Evolution

In the following sections I combine the information from the decomposed morphological analysis with star-formation activity estimates from both the overall galaxy, and the decomposed estimates for the separate bulge and disk components, to probe how the morphological transformations witnessed in this

$1 < z < 3$ redshift regime are linked to the process, or processes, responsible for star-formation quenching.

5.3.1 Star-formation and morphology

In Fig. 5.8 I have revisited the results presented in Chapter 3 for the updated UDS sample by plotting the total specific star-formation rate (sSFR) for each galaxy against both the single Sérsic index and the bulge/total light fraction. The differences in this plot from Fig. 3.9 are due to the updated star-formation rate estimates for galaxies which have $24\mu\text{m}$ counter-parts from SpUDS. In the new approach (following Wuyts et al. 2011), and due to the depth of the SpUDS imaging, any object which has a $24\mu\text{m}$ counter-part has a $sSFR_{UV+IR} > 10^{-10} \text{ yr}^{-1}$. There are also several objects which have been removed due to the re-evaluated mass estimates. Nevertheless, despite the movement of some galaxies into the higher star-forming region of this plot, there is still a significant population of passive galaxies which have disk-dominated morphologies and, moreover, star-forming objects which are bulge-dominated systems.

For comparison, Fig. 5.9 shows the same plot for the COSMOS sample, and both samples are combined in Fig. 5.10. The fraction of passive galaxies (from the overall galaxy sSFR) which are disk-dominated and star-forming galaxies which are bulge-dominated in each field are given in Tables 5.5 and 5.6. Reassuringly, despite the updated sample, the passive disk-dominated fraction in the UDS of $38 \pm 7\%$ using $n < 2.5$ or $30 \pm 7\%$ using $B/T < 0.5$, is still consistent (within the errors) with the results quoted in Chapter 3 which were $40 \pm 7\%$ using $n < 2.5$ or $25 \pm 6\%$ using $B/T < 0.5$. There is also a comparable fraction of both passive disk-dominated and star-forming bulge-dominated galaxies in both fields, judging morphology by either the single-Sérsic index cut at $n = 2.5$ or by the decomposed $B/T = 0.5$ measure, with $\sim 30\%$ of all passive or star-forming galaxies being disk or bulge-dominated, respectively.

However, one notable variation between the fields is the larger number of $B/T = 0$ passive disks in COSMOS than in the UDS. For the COSMOS field there are 5 objects within this range that are best-fit by a “pure” disk, and another 10 objects which are best-fit with a disk+psf model. The corresponding numbers for the UDS are 3 “pure” disks and 4 disk+psf objects. Given the low number statistics involved, and that overall, as shown in Tables 5.2 and 5.3, the same fraction of the population in both samples has been best-fit by disk and disk+psf models,

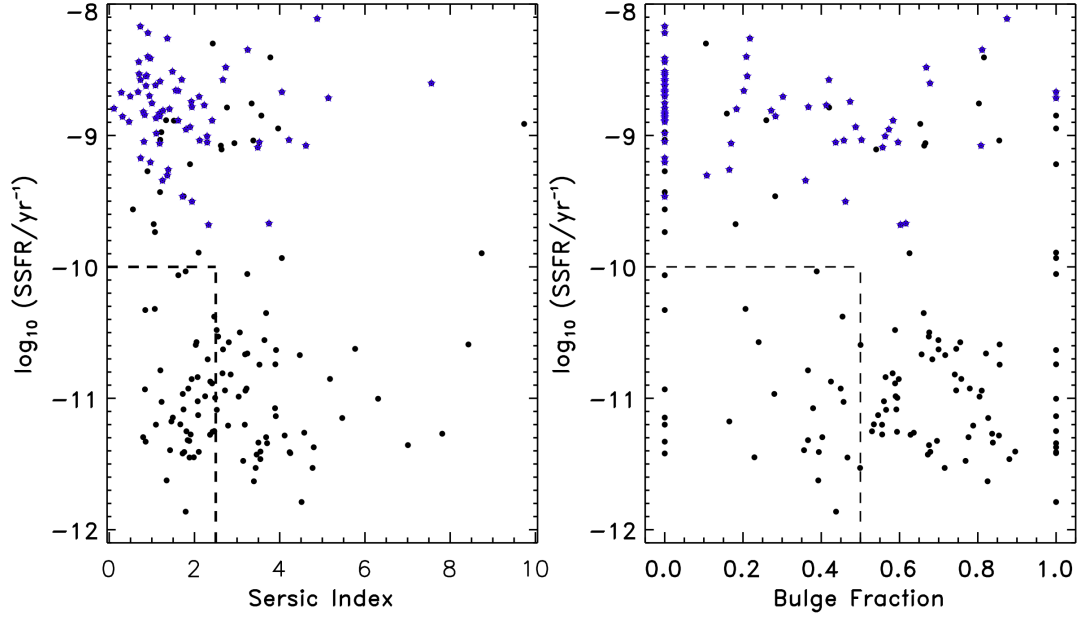


Figure 5.8 *Sérsic index (left) and bulge/total H_{160} light fractions (right) against sSFR for the UDS sample. Galaxies with a 24 μm counter-part from either SpUDS or S-COSMOS have been highlighted by the blue stars, and a box has been placed around the passive ($\text{sSFR} < 10^{-10} \text{ yr}^{-1}$) disk-dominated galaxies as judged by both $n < 2.5$ and $B/T < 0.5$. Comparison with the similar figure in Chapter 3 shows that the adoption of the re-evaluated star-formation rates for the UDS sample has removed objects which have a 24 μm counter-part from the passive region of the plot, but has still kept a significant number of passive disks and star-forming bulges.*

it is difficult to draw firm conclusions from these numbers. Moreover, as per the suggestion made in Chapter 3, given that the addition of a PSF component may indicate the presence of an AGN or nuclear starburst, I have tried to search for any evidence of AGN activity from the X-ray and radio catalogues available in both the UDS and COSMOS fields, but found no counter-parts within a 4 arcsec matching radius for the X-ray catalogues and 2 arcsec matching radius for the radio catalogues, for any of the “pure” disks or disk+psf fits. In addition to this, from examining the spatial positioning of these objects in both fields I find no obvious evidence of clustering. Thus, I simply conclude that the classification of these objects is equally robust and unbiased in both fields, and attribute the offset in the small numbers to shot noise.

The verification of a significant population of both star-forming bulge-dominated galaxies and passive disk-dominated objects is particularly scientifically interesting as they may suggest that the processes which quench star-formation are distinct from those which drive morphological evolution. At the time when the results presented in Chapter 3 were published in Bruce et al. (2012), this result remained controversial, (although see Stockton et al. 2008, McGrath et al. 2008, van der Wel et al. 2011, Cameron et al. 2011, Wang et al. 2012) but since then the presence of a significant passive disk-dominated population has been corroborated by studies such as McLure et al. (2013), Chang et al. (2013b), Fan et al. (2013), Lee et al. (2013) and Talia et al. (2013). However, these studies use a mixture of single-Sérsic, non-parametric and visual morphological classifications (with the exception of van der Wel et al. 2011 who perform double-component $n = 1 + \text{free}$ fits for 14 galaxies with $M_* > 10^{10.8} M_\odot$ at $z \sim 2$) and they all adopt star-formation rates for the galaxy as a whole. This approach may be prone to misclassification if, for example, the bulge component of the galaxy dominates in terms of stellar mass in which case the galaxy should arguably no longer be classified as disk-dominated and, moreover, the specific star-formation rate of the disk-only component may in fact be above the passivity threshold. This is clearly also a concern for the star-forming bulge-dominated galaxies, where one might expect the decomposition to reveal that, while the overall galaxy $sSFR < 10^{-10} \text{ yr}^{-1}$, the bulge component itself is passive and the star-formation activity is limited to the disk component. In order to explore how many of the passive disks and star-forming bulges in my sample may be prone to misclassification based on the adoption of the overall galaxy star-formation rate and morphological light-based bulge and disk fractions, I have examined the individual component stellar masses and star-formation rates for all objects within these

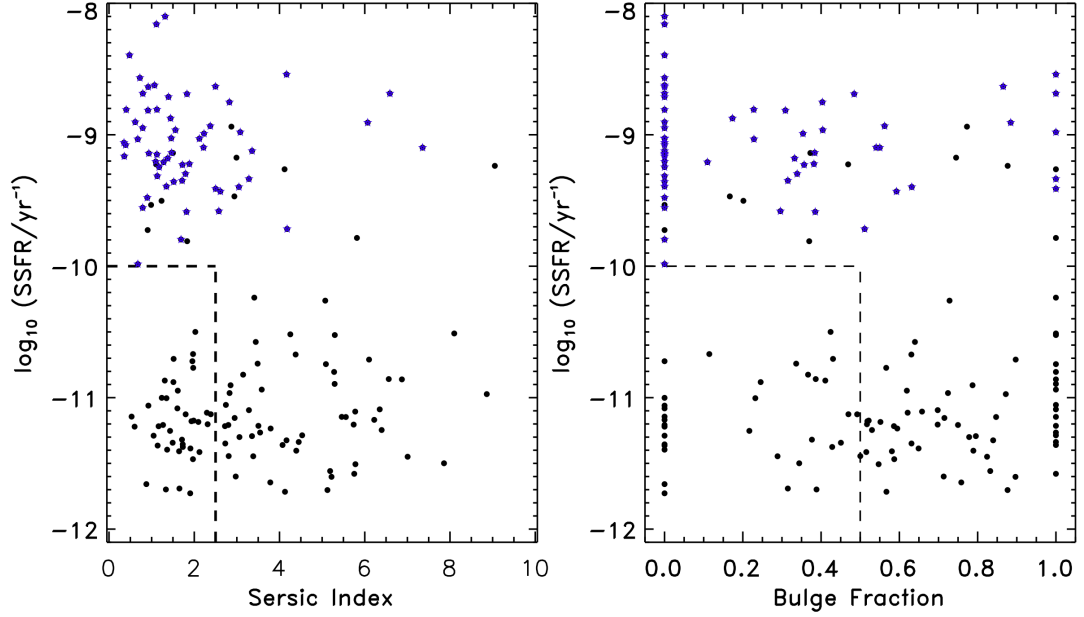


Figure 5.9 *Sérsic index (left) and bulge/total H_{160} light fractions (right) against sSFR for the COSMOS sample. Galaxies with a $24\mu\text{m}$ counterpart from either SpUDS or S-COSMOS have been highlighted by the blue stars, and a box has been placed around the passive ($\text{sSFR} < 10^{-10} \text{ yr}^{-1}$) disk-dominated galaxies as judged by both $n < 2.5$ and $B/T < 0.5$. In comparison to the UDS sample the COSMOS sample has the same overall number of objects in the star-forming bulge and disk-dominated and the passive bulge and disk-dominated subpopulations, however there do appear to be more passive $B/T = 0$ disks in COSMOS, but these numbers are very small and may be affected by cosmic variance.*

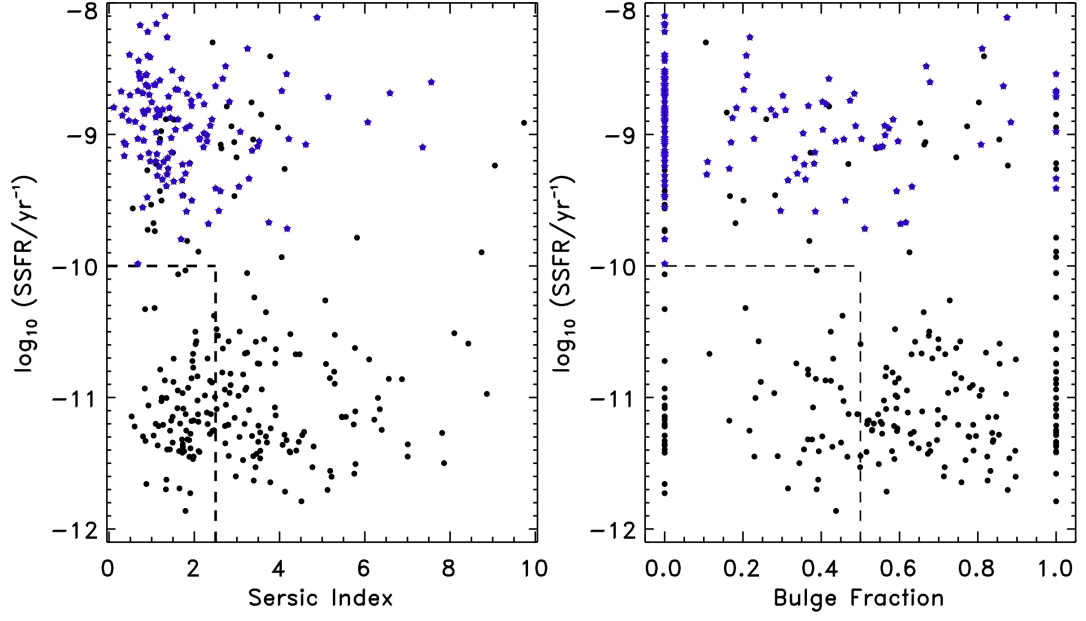


Figure 5.10 *Sérsic index (left) and bulge/total H_{160} light fractions (right) against sSFR for the combined UDS+COSMOS sample. Galaxies with a 24 μm counter-part from either SpUDS or S-COSMOS have been highlighted by the blue stars, and a box has been placed around the passive ($\text{sSFR} < 10^{-10} \text{ yr}^{-1}$) disk-dominated galaxies as judged by both $n < 2.5$ and $B/T < 0.5$.*

populations.

Field	$n < 2.5$	$B/T < 0.5$
UDS	$38 \pm 7\%$	$30 \pm 7\%$
COSMOS	$43 \pm 8\%$	$37 \pm 7\%$
Combined	$41 \pm 5\%$	$33 \pm 5\%$

Table 5.5 *The fractions of passive galaxies which are disk-dominated, split by field and using both the single-Sérsic and multiple-component classifications.*

Field	$n > 2.5$	$B/T > 0.5$
UDS	$33 \pm 8\%$	$31 \pm 6\%$
COSMOS	$26 \pm 7\%$	$26 \pm 7\%$
Combined	$30 \pm 5\%$	$29 \pm 5\%$

Table 5.6 *The fractions of star-forming galaxies which are bulge-dominated, split by field and using both the single-Sérsic and multiple-component classifications.*

5.3.2 Passive disks

I have first considered the case of the passive disk-dominated galaxies, where taking the 184 passive galaxies in the full sample, only 146 are covered by both the ACS and WFC3 pointings and so have been modelled by my decomposed SED fitting. In order to remain fully consistent, for the following analysis of the passive disk-dominated fraction I subsequently only consider objects which have been covered by both the ACS and WFC3 pointings.

Out of these 146 passive disk-dominated galaxies, 16 have been best-fit with either a “pure” disk or disk+psf model (13 in COSMOS and 3 in the UDS). These objects have therefore not been subjected to my decomposed SED fitting, and given the above discussion on the lack of any $24\mu\text{m}$, X-ray or radio counterparts for these systems, I have no reason to assume they have any obscured star-formation and/or AGN activity. Thus, I have adopted the overall galaxy star-formation rate for these galaxies and report them as genuine pure passive disks. For completeness, for the case of only the “pure” disks, there are 2 in the UDS and 4 in COSMOS.

In addition to the “pure” disk and disk+psf fits, there are 30 objects which are passive and disk-dominated which have been fit with a multiple-component

model. In order to report the most conservative and robust fraction of passive disk-dominated galaxies in my sample using the decomposed stellar-mass and star-formation rate estimates, I have adopted the criteria that these objects must be classified as passive with a total bulge+disk decomposed $sSFR < 10^{-10} \text{ yr}^{-1}$ and a decomposed disk $sSFR < 10^{-10} \text{ yr}^{-1}$ (where I have used the decomposed disk stellar-mass to calculate the specific star-formation rate). This leaves 26/30 candidates as passive, where these objects all additionally had decomposed bulge $sSFR < 10^{-10} \text{ yr}^{-1}$. Finally, to remain in the passive disk-dominated population, I required that the objects must be classified as disk-dominated by their decomposed disk/bulge+disk stellar masses. Imposing this criterion removed 15 galaxies and left 11 galaxies which are genuinely passive and disk-dominated by even my strictest definitions.

These 11 passive disk-dominated galaxies were then combined with the 16 “pure” disk and disk+psf objects and are taken as a fraction of the 146 passive galaxies. This provides the estimate that (27/146) $18 \pm 5\%$ of all passive galaxies are disk-dominated.

Two examples of the passive disk-dominated galaxies which are best-fit with a bulge+disk model and have been subjected to decomposed SED fitting are shown in Figs 5.11 and 5.12, where I have displayed the master H_{160} 6×6 arcsec images for the raw image, the best-fit bulge+disk model, the bulge component of the best-fit model, the disk component of the best-fit model, and the residual stamp. These images clearly illustrate that these are genuinely morphologically disk-dominated galaxies, the disk component is not some remnant of poor fitting, and that the model is a good fit to the galaxy. I have also included the best-fit model SED outputs for these two galaxies in the figures. As before, the blue data-points and line represent the disk component, the red data-points and line represent the bulge component, and the sum of the best-fit bulge and disk SED models is given in green. These SEDs demonstrate the quality of the fit to the photometry and the genuine passivity of the disk component. In order to provide the most conservative estimates of the passive disk-dominated fraction, I have also ensured that even by adopting the limited sub-set of SED models with $0.3 < \tau(\text{Gyr}) < 5$, which forces the galaxy to have at least some low-level of measurable on-going star-formation, the disk components of this population remain passive. The best-fit SEDs using this limited τ model sub-set are given in the bottom panels of Fig 5.11 and Fig 5.12 and serve to further confirm the classification of these objects.

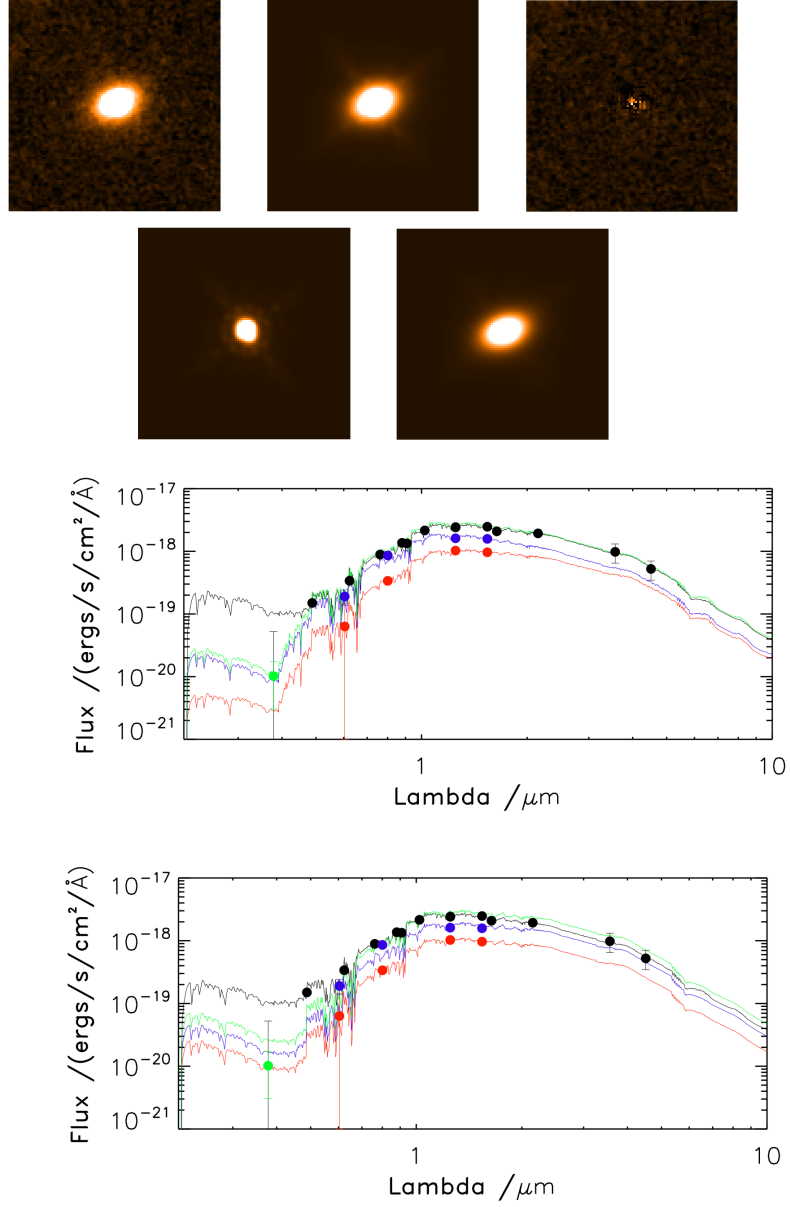


Figure 5.11 *One of the genuinely passive disk-dominated galaxies as judged by the most conservative criteria on the decomposed fits. The H_{160} 6×6 arcsec stamps are shown. The first row, from left to right, contains the image stamp, the best-fit multiple-component model and the residual map. The second row shows the best-fit bulge model component only on the left and the disk only component on the right. The third row displays the best-fit $0 < \tau(\text{Gyr}) < 5$ decomposed SED models. For completeness, the bottom row contains the $0.3 < \tau(\text{Gyr}) < 5$ SED fits which force the models to adopt a minimum low-level of on-going star formation.*

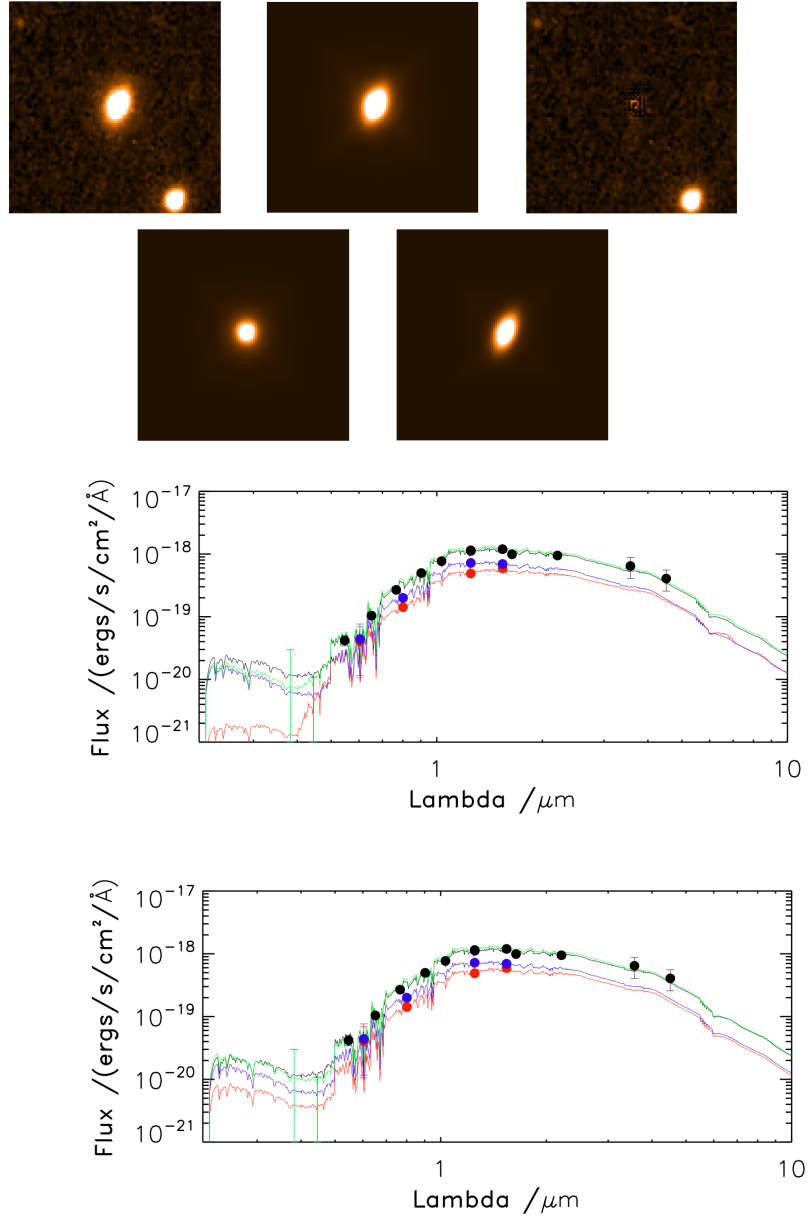


Figure 5.12 *A second example of another genuinely passive disk-dominated galaxies as judged by the most conservative criteria on the decomposed fits. The H_{160} 6×6 arcsec stamps are shown. This figure follows the same configuration as Fig. 5.11.*

Having looked at both the redshift and mass distributions for the passive disk-dominated galaxies I find no evidence that this population inhabits any distinct location in these distributions. In addition, due to the high stellar-mass cut of my sample I am unable to explore any correlation between the extrapolated halo masses of the passive disk-dominated galaxies and star-forming disk-dominated galaxies, which might have provided an indication of the viability of the halo quenching scenario.

5.3.3 Star-forming bulges

I have also examined the decomposed stellar-mass and star-formation rate estimates for the star-forming bulge-dominated systems. Again, only a limited sub-set of these objects have been covered by both WFC3 and ACS pointings, which gives a total of 136 star-forming galaxies. Out of these, 11 are best-fit by “pure” bulges (comprising 6 objects in COSMOS and 5 objects in the UDS) and there are an additional 2 objects best-fit by bulge+psf models. There are also 24 candidate star-forming bulge-dominated galaxies with best-fit multiple component models.

For these 24 candidate star-forming bulge-dominated systems I then impose that in order to remain in this sample they must be bulge dominated in terms of their bulge/bulge+disk decomposed stellar mass fractions, and that the bulge $sSFR > 10^{-10} \text{ yr}^{-1}$. Only 4 objects meet these criteria, as in the vast majority of cases the star-formation rate decomposition reveals that is the disk components which are active. For all four of these objects the disk component has a $sSFR < 10^{-10} \text{ yr}^{-1}$. As above, I also further restrict the sample to the most conservative fraction by requiring that, when the limited $0.3 < \tau(\text{Gyr}) < 5$ SED models are adopted, the bulge component remains star-forming. In one of the four cases the limited τ SED models fit both the disk and bulge components with $sSFR < 10^{-10} \text{ yr}^{-1}$. This suggests that this best-fit model is particularly degenerate so this object is removed from the sample and I have retained only 3 robust star-forming bulge-dominated galaxies.

Combining the 3 bulge-dominated systems with the 11 “pure” bulges and the 2 bulge+psf fits, and comparing them to the 136 star-forming galaxies also with ACS coverage, provides an estimate for (16/136) $12 \pm 3\%$ of all star-forming galaxies to be bulge-dominated systems.

These 3 star-forming bulge-dominated bulge+disk systems are shown in Figs 5.13, 5.14 and 5.15. These plots show the master H_{160} and blue v_{606} stamps for the images, best-fit models, separate model bulge and disk components and residuals, and justify that for the first two objects in Figs 5.13 and 5.14 these bulge-dominated morphologies are good fits to the objects. For these star-forming bulges I have also shown the best-fit SED models and below them the same best-fit models this time corrected for the modelled dust obscuration. These dust-corrected SEDs allow a direct comparison between the contribution to the flux of the galaxy at the blue end from the bulge and disk components and have been included as they support the classification of the bulge components as star-forming.

Of particular interest in these figures is the object shown in Fig. 5.15, which displays a PSF dominated image stamp. This object has clearly not been well-fit by the morphological decomposition and the best-fit SED is also a poor fit to the modelled disk photometry, as such it warranted further study. Visual examination of this object suggests that it could possibly be a mis-classified star or potentially an AGN, although the shape of the SED does not look stellar. This object is in the COSMOS sample and was determined to have a photometric redshift at $z_{phot} = 1.58$. By cross-matching with the available multi-wavelength catalogues in the COSMOS field this object was found to have both a $24\mu\text{m}$ and X-ray counter-part, but no radio counter-part. In comparison, the other two objects given in Figs 5.13 and 5.14 both have $24\mu\text{m}$ counter-parts, and one has an additional radio counter-part within a 2 arcsec radius. Given the X-ray flux of this source (Elvis et al. 2009), it would be classified as an AGN given the $L > 10^{42} \text{erg s}^{-1}$ criterion from Hasinger (2008) and adopting either the photometric or spectroscopic redshifts. It also has a hardness ratio of -0.2 which may suggest that it is obscured using the cut at $\text{HR} > -0.3$ (using $\text{HR} = \text{H-S}/\text{H+S}$, where $\text{H} = 2 - 7 \text{ keV flux}$ and $\text{S} = 0.5 - 2 \text{ keV flux}$) (Schmidt et al. 1998, Szokoly et al. 2004, Zheng et al. 2004). In fact, this object has been classified as a Type 1, unobscured, AGN by Trump et al. (2009), who determine a spectroscopic redshift of $z_{spec} = 2.458$, with $\geq 97\%$ confidence.

Therefore, given the classification of this object as an AGN, I have removed it from the star-forming bulge population, and the updated fraction of star-forming galaxies which are bulge dominated becomes (15/135) $11 \pm 4\%$.

Finally, I have also explored the mass and redshift distributions for the entire star-forming bulge-dominated galaxy population, using the overall $sSFR <$

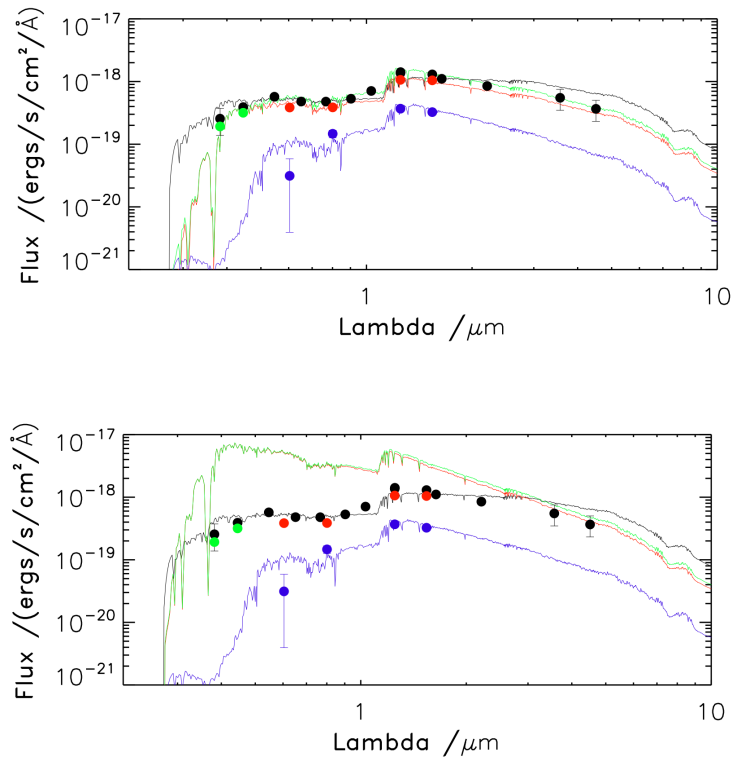
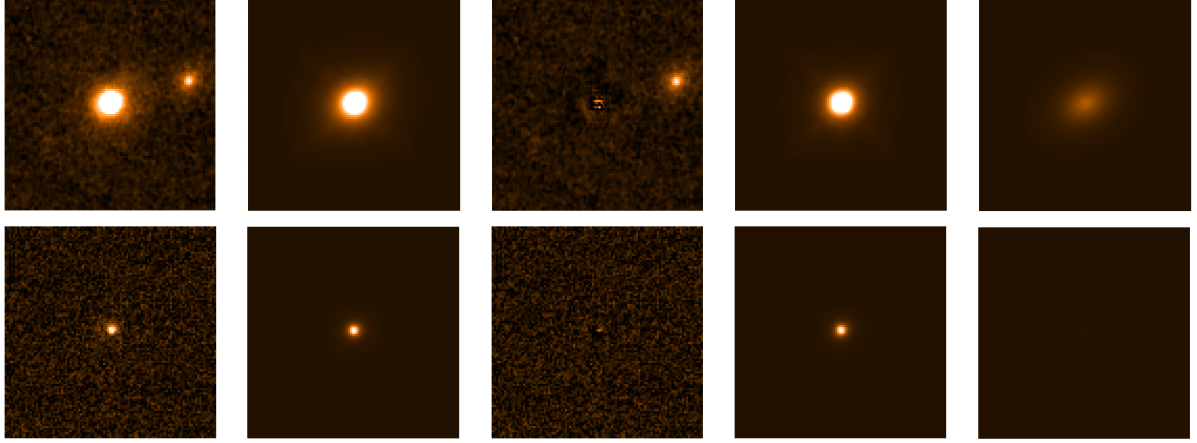


Figure 5.13 *The first of three genuinely star-forming bulge-dominated galaxies. The first row displays the 6×6 stamps for the H_{160} images. From left to right they are the image stamp, the best-fit multiple-component model, the residual, the bulge component of the best-fit model and the disk component of the best-fit model. The second row follows the same configuration for the blue v_{606} stamps. The third row show the best-fitting decomposed SED. The bottom panel shows the dust-corrected best-fit SED models to allow a direct comparison of the contribution from the bulge and disk components.*

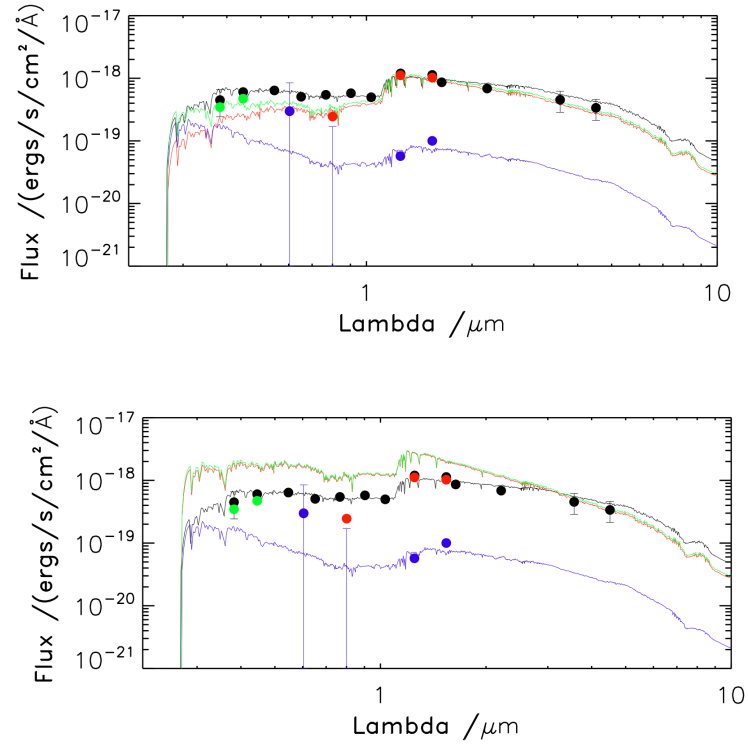
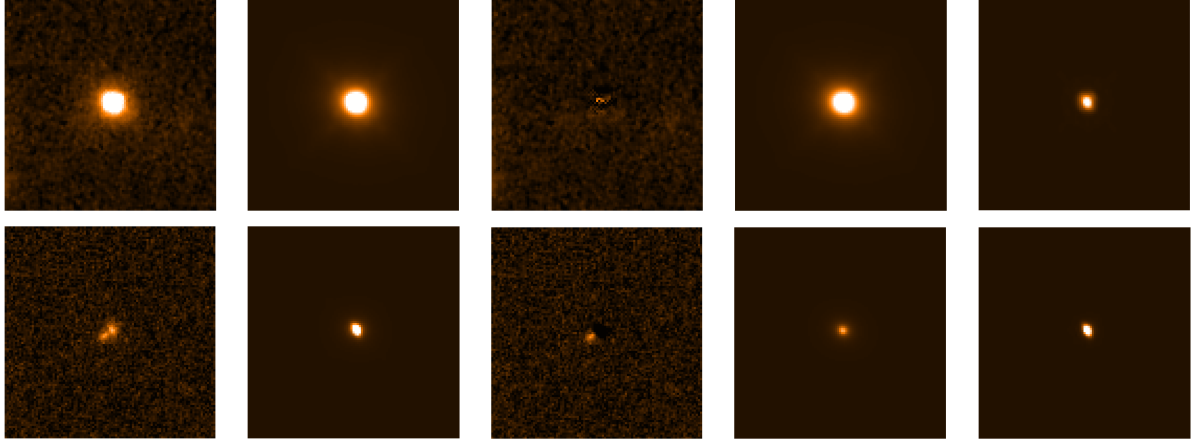


Figure 5.14 *The second of three genuinely star-forming bulge-dominated galaxies. This figure follows the same configuration as Fig. 5.13, where in the bottom panels, which illustrate the SED fits, the green data-points are the re-measured 2.5 arcsec radius aperture photometry in the u' and B bands, as discussed in Chapter 4.*

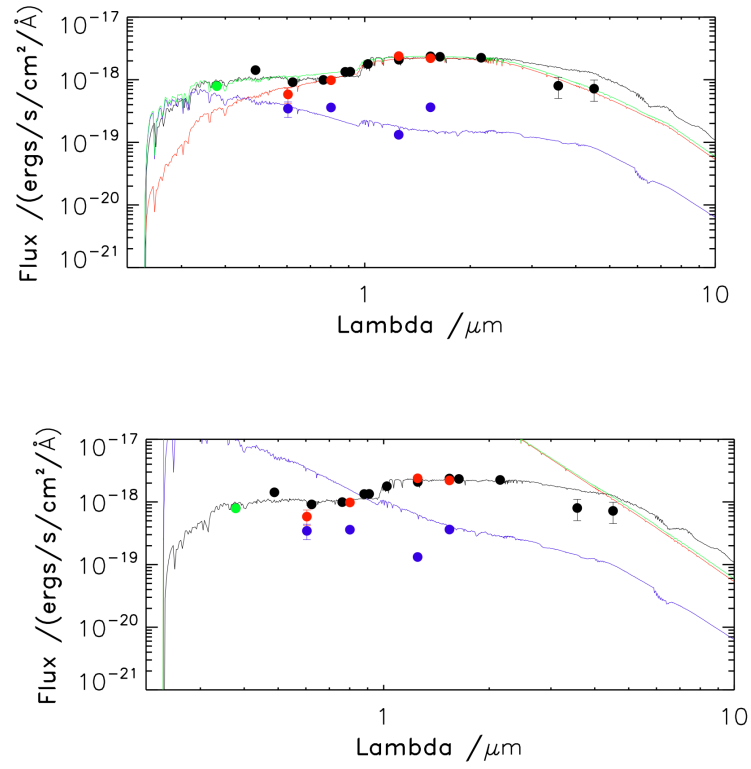
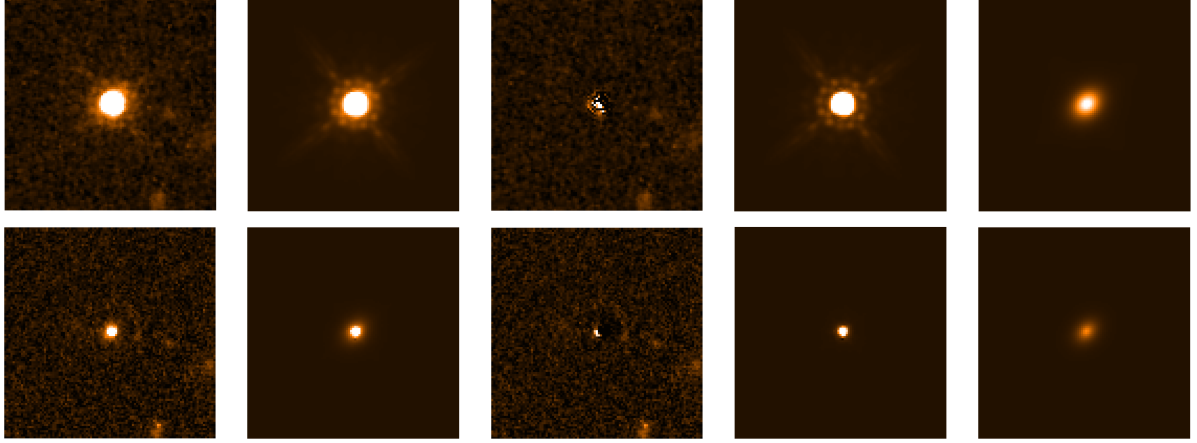


Figure 5.15 *The third genuinely star-forming bulge-dominated galaxy. The plot configuration follows Figs 5.13 and 5.14. In this case, the image stamps of this object clearly show that it is dominated by a point source, with large residuals from the best-fit multiple-component model. The SEDs for this object also reveal that the photometry for the disk component is more consistent with that of an AGN as it is flat. In fact this galaxy has been classified as Type1, unobscured, AGN by Trump et al. (2009).*

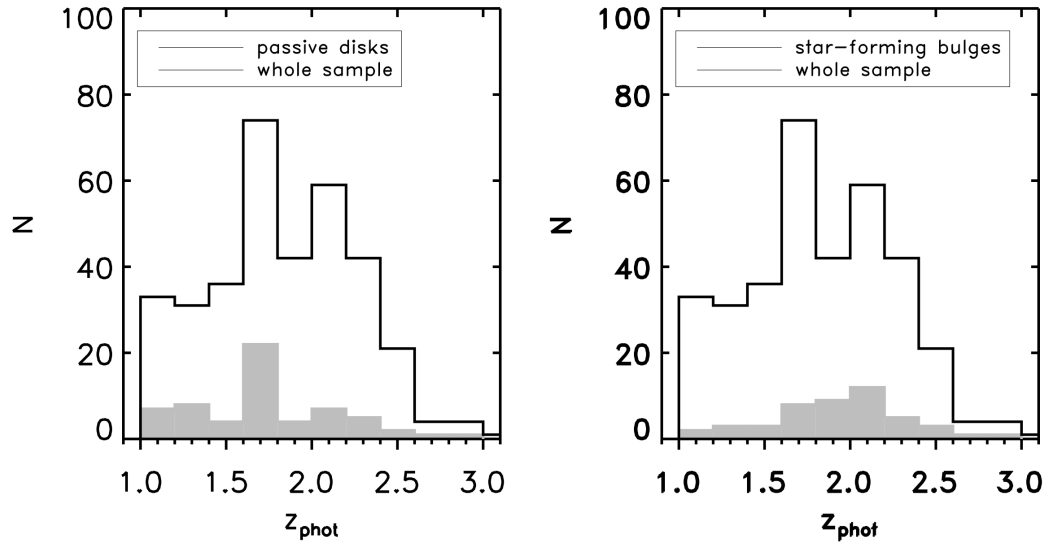


Figure 5.16 *The redshift distribution of all the $B/T < 0.5$ passive disks (left) and $B/T > 0.5$ star-forming bulges (right), compared to the whole sample of objects. This appears to show that the star-forming bulges preferentially lie at higher redshifts. This result is not statistically significant, which may be due to the small number of objects in the star-forming bulge sample, but a K-S test does reveal that the passive disks and star-forming bulges are not consistent with being drawn from the same distribution at the $3 - \sigma$ level.*

10^{-10} yr^{-1} and $B/T > 0.5 H_{160}$ light-fraction criteria to obtain larger numbers for comparison and find that the star-forming bulge-dominated galaxies appear to preferentially lie at higher redshifts compared to both the full $M_* > 10^{11} M_\odot$ sample and all bulge-dominated galaxies. This result is not statistically significant, which may be due to the small number of objects in the star-forming bulge sample, but a K-S test does reveal that the passive disks and star-forming bulges are not consistent with being drawn from the same distribution at the $3 - \sigma$ level. In fact, given the mass selection imposed for this study, this result is to be expected in the context of downsizing, where the most massive galaxies are observed to be more active at higher redshift and experience an accelerated evolution, quenching before less massive systems. This is further supported by the similarity in the redshift distributions of the star-forming bulges and all star-forming galaxies.

5.4 Axial Ratios

In addition to providing new insight into how the overall morphologies of the star-forming and passive components evolve, the detailed morphological analysis employed in this work has also allowed me to explore some of the axial ratio properties of the passive and star-forming populations. Axial ratio measurements provide key additional information about the structure of these components and any trends with redshift can offer further indicators of the physical processes which govern galaxy evolution within this epoch. The axial ratio distributions of the UDS sample have been discussed previously in Chapter 3, and are updated in the following section with the addition of the COSMOS sample.

The axial ratio distributions for the disk components of disk-dominated galaxies (as judged by H_{160} light fractions) and bulge components of the bulge-dominated galaxies are shown in Fig 5.17, where the samples have been split into passive and star-forming sub-populations using the total galaxy specific star-formation rate at $sSFR = 10^{-10} \text{ yr}^{-1}$, for simplicity. Similar to the results in Chapter 3, these distributions reveal that the axial ratios of both the star-forming and passive bulge components are peaked around $b/a \approx 0.7$, consistent with bulges in the local Universe (e.g. Padilla & Strauss 2008). However, visually the passive disks display a markedly flatter distribution to the star-forming disks, which look to be more consistent with the bulge components. However, based on the results from K-S tests, all four distributions shown in Fig 5.17 are actually consistent with

being drawn from the same underlying distribution. This includes the passive and star-forming disks which, despite appearing to be significantly different, are not statistically distinguishable at the $2 - \sigma$ level ($p = 0.11$).

The peaked distribution of the bulge components is consistent with a population of tri-axial objects, and similar distributions have been found for bulge-dominated systems at both low (e.g. Padilla & Strauss 2008) and high redshifts (e.g. Ravindranath et al. 2006). Similarly, the apparently flatter distribution of the passive disks is in agreement with expectations from a population of randomly oriented thin disks.

5.4.1 Passive disks

The apparently flat distribution for the passive disks provides further corroboration that the passive disk-dominated galaxies are genuine, and agrees well with other axial ratio studies at $z > 1$ such as Chang et al. (2013a). This paper used CANDELS photometry to explore the evolution of the axial ratios of early-type galaxies defined by low star-formation rates from rest-frame colours, where no additional morphological distinction was made. Chang et al. (2013a) found, from de-projecting the observed axial ratios of the galaxies in their sample, that both the local SDSS distribution and their $1 < z < 2.5$ distribution were not consistent with a single population of structures which are randomly oriented, but can be accurately modelled by two-components: a round tri-axial (bulge-like) population and a flatter oblate (disk-like) population. The Chang et al. (2013a) models and observed axial ratio distributions are displayed in Fig 5.18, in the bottom panels, and have been compared to the local SDSS results from Holden et al. (2012) in the upper panels. In their high-mass $M_* > 10^{10.8} M_\odot$ bin, they also found evidence that this oblate population increases as a fraction of the total number of objects from $20 \pm 2\%$ at $z = 0$ to $60 \pm 1\%$ at $1 < z < 2.5$. These results not only support the flat distribution that I find for the passive disks but also serve to independently substantiate the findings that, at higher redshifts, these most massive galaxies are increasingly disk-dominated, and that pure bulge galaxies emerge slowly within the $0 < z < 3$ epoch from a population of mixed systems.

Given that Chang et al. (2013a) used single-Sérsic morphological fits, to allow a more direct comparison I have included the single-Sérsic axial ratio fits from my passive disks in the left panel of Fig 5.19. Also included in the comparison in Fig 5.19 is the model distribution for the local SDSS galaxies from Holden et al.

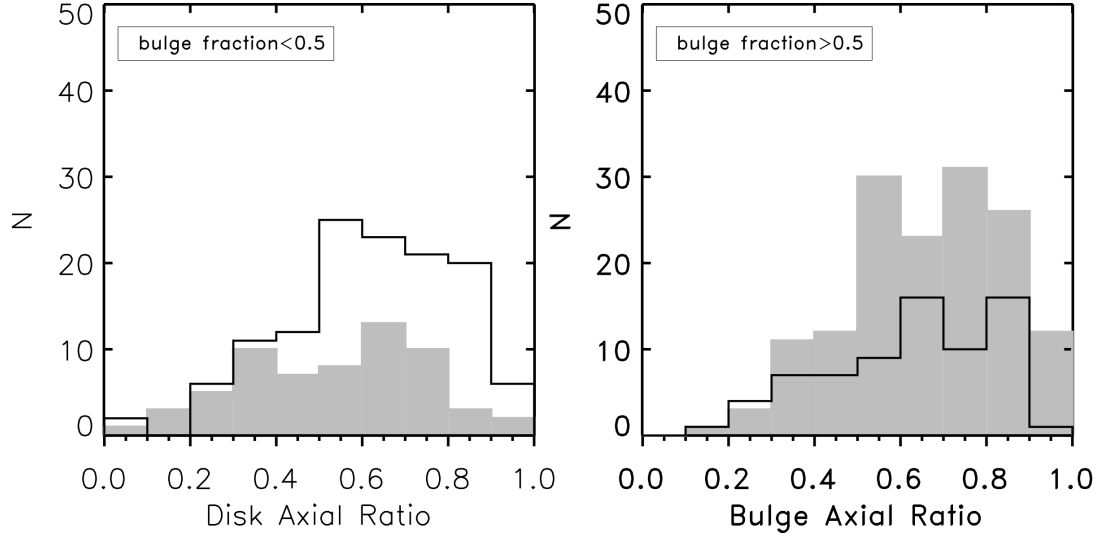


Figure 5.17 *Axial ratio distributions for the star-forming and passive bulge (right) and disk (left) components of the bulge and disk-dominated galaxies. In both plots the star-forming components are plotted in the black solid line, while the passive components are represented by the filled grey regions.*

(2012). From this comparison my passive disks appear to display a distribution which is somewhat intermediate between the peaked local distribution and the $1 < z < 2.5$ ETG sample, which has a more extended flat tail. By explicitly splitting the passive population into the bulge and disk-dominated samples there is a more discernible difference between the contribution of the oblate population to the overall axial ratio distribution in the Chang et al. (2013a) models, compared to the distribution of the passive disks in my mass-selected sample. From this comparison the extended flat tail from disks appears over-estimated in the Chang et al. (2013a) models with respect to my observed distributions, especially at $b/a < 0.35$. However, there are still visual indications that the passive disks have a flatter distribution than the star-forming disks, although these are not statistically significant. Thus, both my single-Sérsic and morphologically decomposed results broadly agree with the results of Chang et al. (2013a), especially given the difference in the mass ranges adopted.

Chevance et al. (2012) have also explored the axial ratios of 31 compact ($R_e < 2\text{Kpc}$), passive galaxies at $z > 1.5$ and find that while the single-Sérsic index distributions of their high-redshift sample are more consistent with local disks, the axial ratio distribution has only a 5% probability of being drawn from the same

population and is more consistent with the distribution of local ETGs. These results suggest that despite the passive galaxies having “disk-like” light profiles, their axial ratios are rounder. Chevance et al. propose that their high-redshift sample is either a mixture of bulges and disks or that the high-redshift galaxies are a genuinely distinct population with no real local analogues. By cutting my full sample at $z > 1.5$ and plotting the single-Sérsic index and axial ratio distributions of all the passive galaxies and just the most compact systems with $R_e < 2$ Kpc, I find agreement with the Chevance et al. (2012) results. The single-Sérsic index distributions are more similar to the distributions of local disks than ETGs, peaking at a value of $n \simeq 1.5 - 2$, while the axial ratio distributions are more peaked than the flat distributions observed for local disks. In fact, examining the bulge-to-total light fractions from my decompositions reveals that these passive, compact, objects are indeed a mixture of bulge plus disk systems with a median $B/T \sim 0.59$. These results are in line with my previous findings that within the $1 < z < 3$ era all massive galaxies become increasingly mixed systems, which gives rise to measured single-Sérsic indices which have intermediate values. Thus, despite the single-Sérsic index distributions being centred on lower, more disk-like, values than local ETGs, these compact $z > 1.5$ passive systems contain significant bulge and disk components and the axial ratio distributions for these systems remain more peaked as the flatter distributions for the passive disk components are overpowered by the contribution from the passive bulge components in the single-Sérsic fits. This further demonstrates the insights which can be gained from my decomposition analysis when considered with results from previous single-Sérsic studies.

In summary, it appears that there is some evidence that the passive disk components display the expected flatter axial ratios than passive bulges, but small number statistics stop me from rigorously demonstrating this with the current sample.

5.4.2 Star-forming disks

While the flat distribution of the passive disk components is supported by previous studies, the relatively peaked distribution of the star-forming disk components has been less well explored in the literature, and remains less understood. Although, as was discussed in Chapter 3, this peaked distribution does agree with the results of Law et al. (2012), who conducted a single-Sérsic

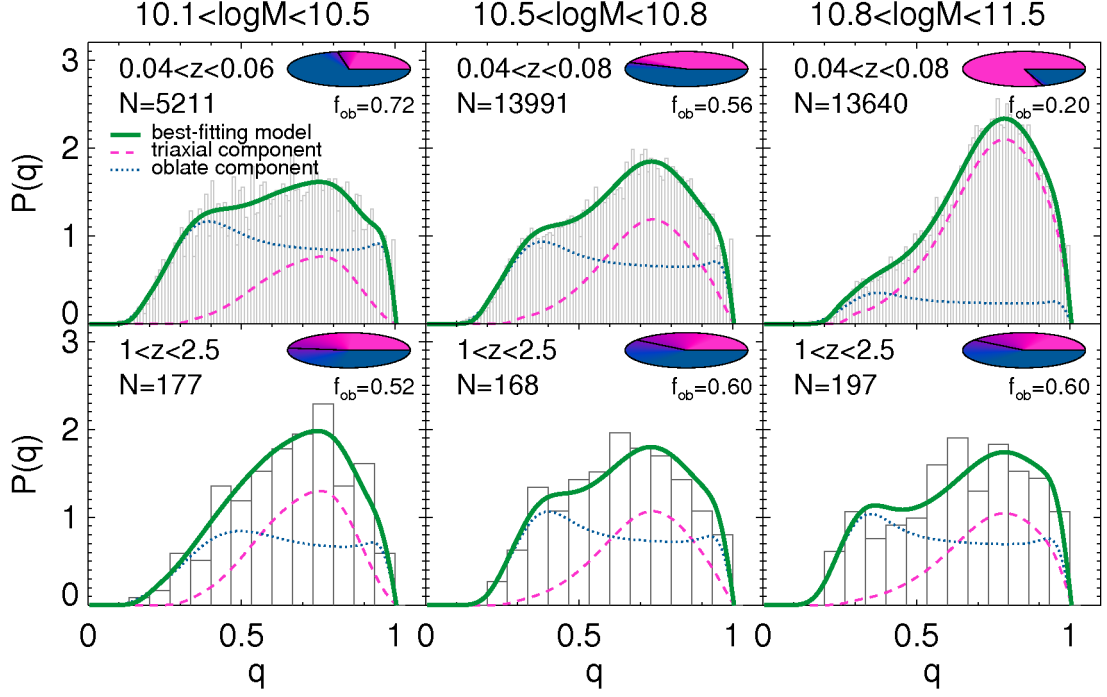


Figure 5.18 *The axial ratio distributions for low and high-redshift ETGs from Chang et al. (2013a). The top panels are for the local ETG population from SDSS (Holden et al. 2012) and the bottom panels are for their $1 < z < 2.5$ CANDELS ETG sample. The observed distributions are given by the black boxplots, and the best-fit double component population model is in green. This model is comprised of the tri-axial (pink) population and the flatter oblate (blue) population. The $10^{10.8} < M_*/M_\odot < 10^{11.5}$ bin provides an appropriate comparison sample for my analysis.*

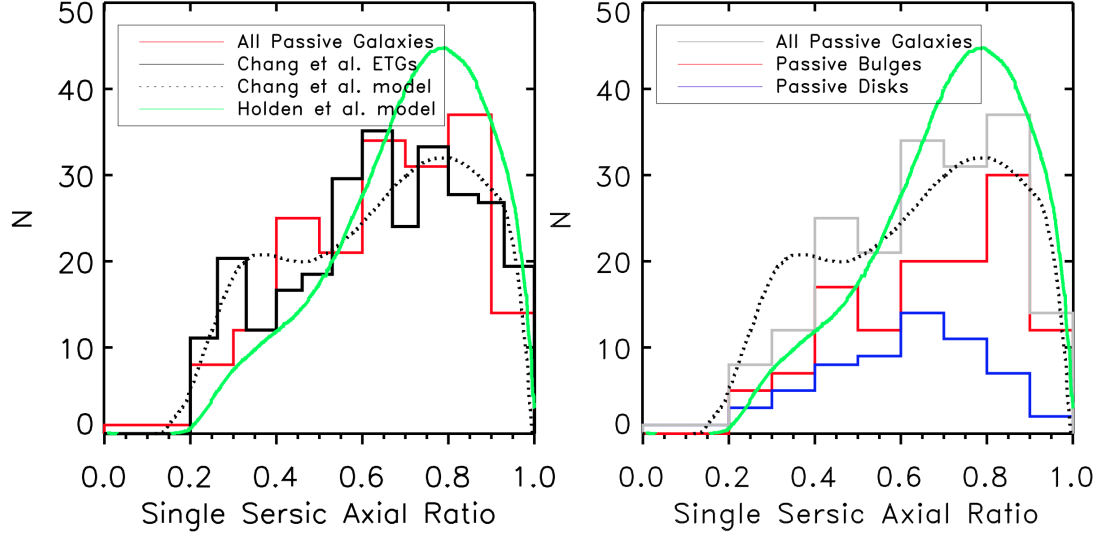


Figure 5.19 *Left: The single-Sérsic axial ratio distributions for the passive (red) galaxies in my sample over-plotted with the Chang et al. (2013a) observed distribution in black and their model in the dotted black line, where these distributions have been re-normalised to match the area under my histograms. Also included in this plot is the local SDSS model distribution from Holden et al. (2012). The passive galaxies in my mass-selected sample display a distribution which appears to be intermediate between the $1 < z < 2.5$ Chang et al. (2013a) ETGs, and the local SDSS sample. Right: the axial ratio distributions from the single-Sérsic fitting for the passive galaxies (grey) also split into the bulge (red) and disk-dominated (blue) populations. By splitting the passive galaxies into their morphological classifications I find that the single-Sérsic axial ratios also separate into a flatter distribution for the oblate disk-dominated objects and a peaked distribution for the tri-axial bulge-dominated galaxies. This is roughly consistent with the Chang et al. (2013a) results, although the contribution from the oblate population in the models of Chang et al. (2013a) to the flat tail of the distribution appears to be over-estimated in comparison with my sample.*

and non-parametric morphological analysis of $M_* = 10^8 - 10^{11} M_\odot$ star-forming galaxies at $1.5 < z < 3$ using HST/WFC3 imaging and reported an axial ratio distribution for $n < 2.5$ galaxies peaked at $b/a \approx 0.6$.

To better explore the origin of this peaked distribution, I have cut my star-forming, disk-dominated, disk component sample according to several different criteria. In the first case, I have cut the sample according to different indicators and measures of star-formation. I first compared the axial ratio distributions of the whole star-forming disk-dominated population with only those objects which also had a $24\mu\text{m}$ detection from either SpUDS or S-COSMOS. However, this was not informative as the majority of star-forming disk-dominated galaxies have a $24\mu\text{m}$ counter-part. I next compared the distributions for the sample split by their absolute and specific star-formation rates, as shown in Fig 5.20. The left-hand panel of Fig 5.20 displays the cuts made at increasingly higher absolute star-formation rates for the overall galaxy. The $SFR > 192 M_\odot \text{yr}^{-1}$ cut corresponds to the median absolute star-formation rate for the full star-forming disk-dominated galaxy sample, and the $SFR > 538 M_\odot \text{yr}^{-1}$ cut corresponds to the 90% quartile value. There is perhaps tentative evidence from this comparison that by imposing the extreme SFR cut, the distribution begins to flatten out, however the number of galaxies within this bin becomes very small, so this result is by no means robust. The right-hand panel of Fig 5.19 displays similar cuts made at increasingly higher specific star-formation rates for the overall galaxy. The $sSFR > 10^{-8.9} \text{yr}^{-1}$ cut now corresponds to the median specific star-formation rate for the full star-forming disk-dominated galaxy sample, and the $sSFR > 10^{-8.5} \text{yr}^{-1}$ cut corresponds to the 90% quartile value. These distributions agree with the results from splitting by absolute star-formation rate as they also display a weak trend for the most active disks defined by specific star-formation rate to have flatter axial ratios.

In addition to studying how the axial ratio distribution of the disk components varies with the star-formation rate of the galaxy, I have also examined how it varies with other properties of the galaxy. To do this, I first split the star-forming, disk-dominated, disk components above and below $z = 2$ to investigate if there was any redshift evolution evident. These distributions are given in the left-hand panel of Fig 5.21, and reveal that the star-forming disk components at $z > 2$ are peaked towards a higher b/a value compared to the $z < 2$ components. This is interesting as, naively the $z > 2$ disks would be expected to be more active than those at $z < 2$. Given that in the previous figure I reported that there might be

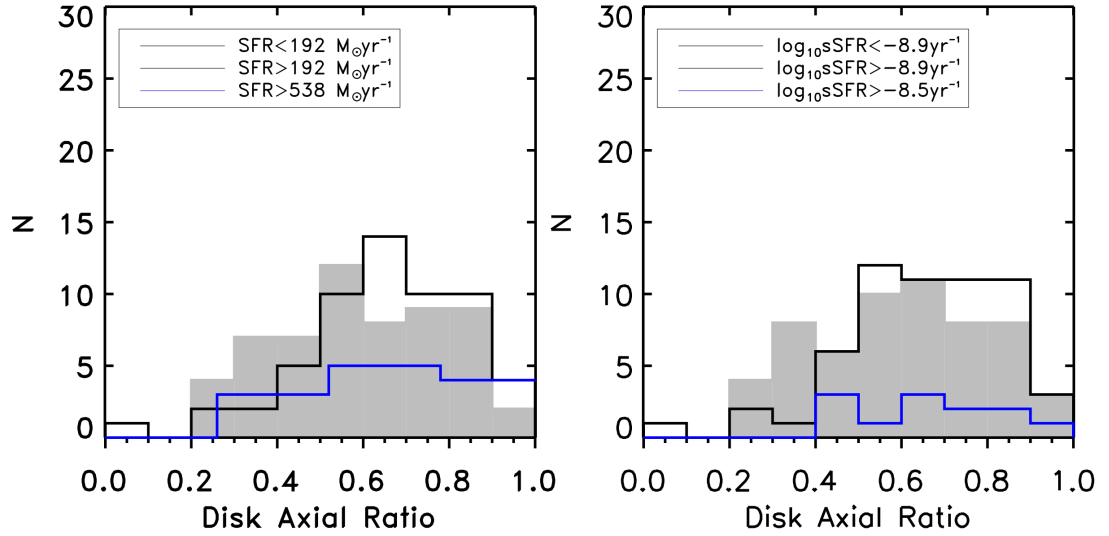


Figure 5.20 *Axial ratio distributions for the star-forming disks split by different measures of specific and absolute star-formation rate. On the left the star-forming disks have been split at the median absolute star-formation for the galaxies in this sub-population and the two distributions have been plotted with the less active star-formers in black and the more active disks in grey. I have also constructed an additional sub-sample of objects which have SFRs above the 90% quartile and have over-plotted the axial ratios of their disk components in blue. This comparison appears to show tentative evidence that the most active disks have a flatter axial ratio distribution. On the right the star-forming disks have been split at the median specific star-formation for the galaxies in this sub-population and the two distributions have been plotted with the less active star-formers in black and the more active disks in grey. I have also constructed an additional sub-sample of objects which have sSFRs above the 90% quartile and have over-plotted the axial ratios of their disk components in blue. This comparison appears to also show some weak evidence that the most active disks have a flatter axial ratio distribution.*

a potential trend for the distribution to flatten out for the most active disks, this results appears to be in direct conflict with this assertion. Moreover, I have also conducted a K-S test for these two redshift binned distributions and found that at the $2 - \sigma$ level ($p = 0.02$) they are inconsistent with being drawn from the same distribution.

However, in addition to a star-formation rate evolution with redshift, I have also extensively reported on the size evolution of the bulge and disk components with redshift, so in the right-hand panel of Fig 5.21 I have split the disks according to their median size. This clearly reveals that the largest disks have a flatter distribution and the smaller disks have a distribution peaked towards higher values. In this case the K-S test provides a value of $p = 0.03$, again making them formally different at the $2 - \sigma$ level.

This size trend has been further probed by splitting the star-forming disks at the 25% and 75% quartile sizes of the disks, as shown in Fig 5.22 , which confirms the previous trend that the most massive galaxies have the flattest axial ratios and the smallest galaxies are the roundest, where now $p = 0.50$ for the the distributions split at the 25% quartile sizes of 2.61 kpc, and $p = 0.03$ for the distributions split at the 75% quartile sizes of 5.21 kpc.

The trend for smaller star-forming disks to be rounder and larger disks to be flatter can be explained if at these redshifts star formation in disks depends only on the self-gravity of the disk, not on scale-length, and this intense star-formation phase induces feedback which “puffs up” the disk scale-height. In which case, the “puffiness” of the star-forming disk is independent of the disk size, and smaller disks will appear more tri-axial in structure than larger disks.

For completeness, I have also looked for any potential trends and biases for the axial ratio distributions by refining the sample to include only those objects which are classified as disk-dominated by their decomposed disk/bulge+disk masses, and have split the sample by disk decomposed mass at the median value of $M_{disk*} = 1.27 \times 10^{11} M_{\odot}$. These re-sampled distributions are displayed in Fig 5.23 and show that the distributions have not been biased by the disk-dominated by H_{160} light-fraction definition, and there are no significant conclusions that can be drawn from the mass cuts. However, in itself this result is at least worth noting as one might have expected from the size-mass relations, as smaller disks are rounder, the lower mass components would also display rounder axial ratios. The lack of a clear difference in the axial ratio distributions for the less and

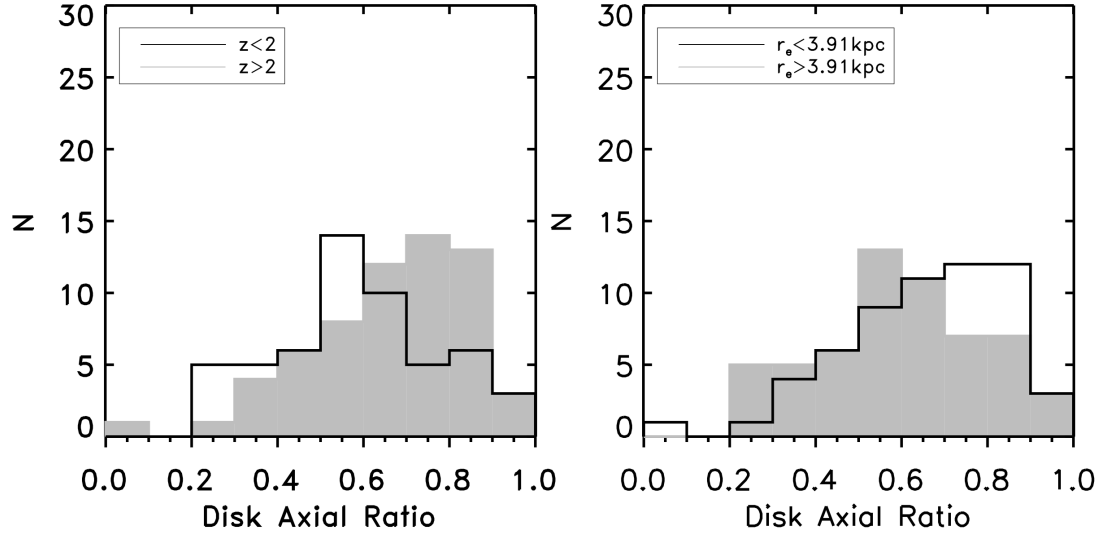


Figure 5.21 *The axial ratio distributions for the star-forming disks split by photometric redshift (left) and disk size (right), where the disks have been split according to the median disk size of 3.91 kpc. These distributions reveal a trend for lower redshift galaxies to have flatter axial ratios, although this can be explained by the redshift size evolution of the disks, and in fact, coupled with the right panel suggests that the smallest disks are the most tri-axial, which may be due to an absolute increase in disk scale-height due to star-formation at high redshift which would have a greater affect on the axial ratios of disks with smaller scale-lengths.*

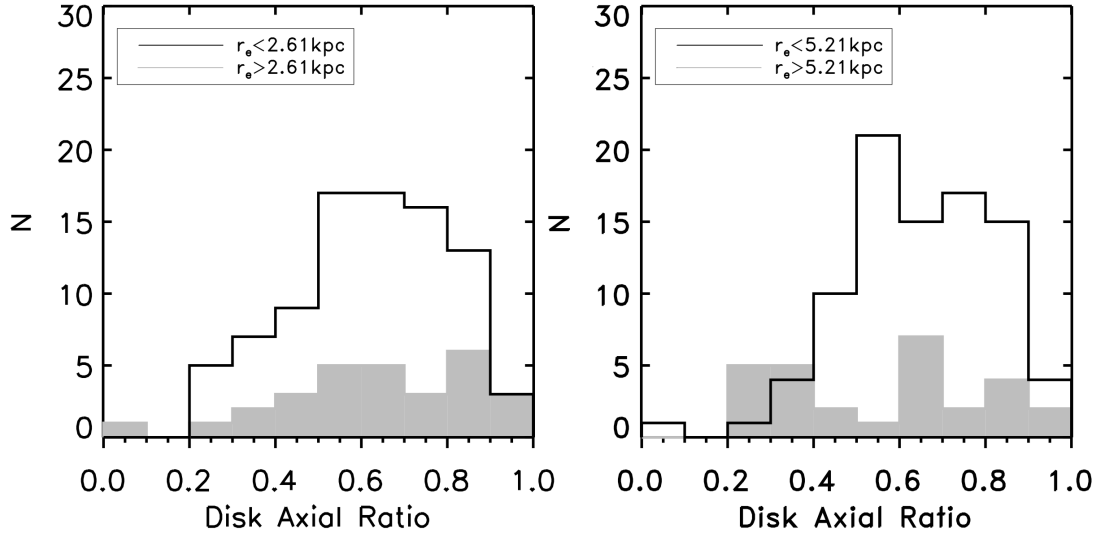


Figure 5.22 *Axial ratio distributions for star-forming disks split above and below 1st and 3rd quartile disk sizes to confirm the trend displayed in Fig. 5.21. The smaller disks are plotted in black and the larger disks in grey.*

more massive disks can be ascribed to the large, intrinsic, scatter in the size-mass relations for the disk components, as has been discussed previously.

It is worth discussing that there is some concern about the robustness of GALFIT results for small, flat objects due to the resolution limit, where $b/a \leq 0.1$ values of small objects result in scale-heights less than a single pixel. van der Wel et al. (2012) (and private communication) have conducted simulations, which reveal that in this case GALFIT tends to become confined to a restricted parameter space and returns accurate values for the other parameters but preferentially fits $b/a = 0.05$ values. This is clearly not the reason for the dearth of $b/a < 0.3$ values for the star-forming disks within my sample, as not only are the sizes of my objects too large to force the scale-heights of the majority of b/a fits to be less than a pixel, but if this were the case then I would have found an over-abundance of $b/a < 0.1$ values. This is not seen, as although I impose a $b/a > 0.1$ criterion for acceptable bulge fits, I do not apply this to the disks, so any components which were fitted with these values would be visible in the axial ratio distributions. Although the star-forming disks do have an H_{160} flux distribution centred on fainter magnitudes than the passive disks (Fig 5.24), the star-forming disks are still bright enough not to have GALFIT fits which are biased by low S/N . Hence,

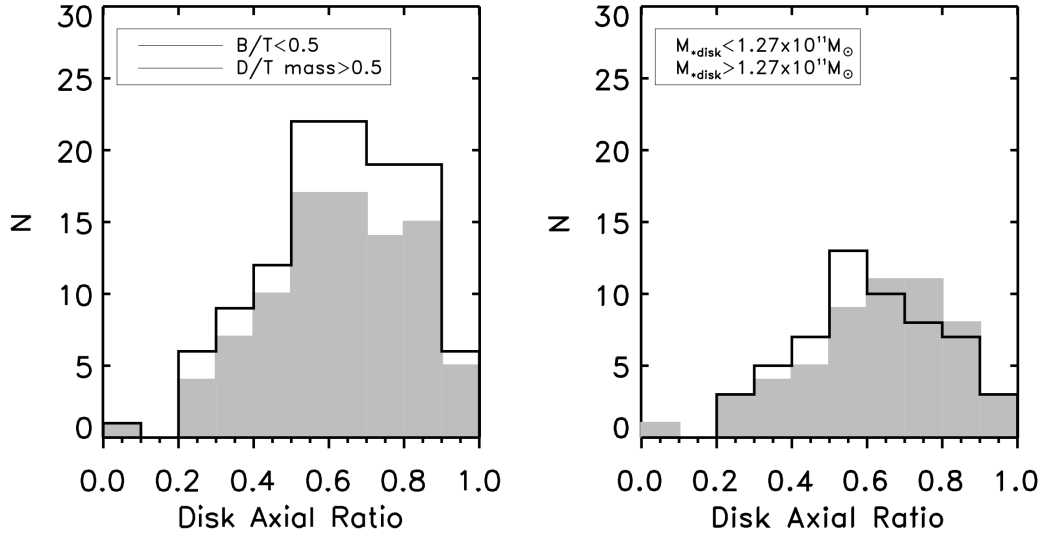


Figure 5.23 *Axial ratio distributions for star-forming disks split by the disk stellar-mass dominated sample (left) and by disk component masses from the decomposed SED fitting (right). These cuts do not influence the overall distributions for the star-forming disks, which is to be expected for the disk-mass dominated cut, but is itself interesting for the low and high stellar-mass cuts as one might have expected the size trends to manifest through the size-mass relation. The fact that there is no significant difference between these plots re-enforces the findings that the scatter in the size-mass relation is large.*

there is no reason to attribute the peaked axial ratios of the star-forming disks to bias in the GALFIT measurements as opposed to a genuine peak in the intrinsic distribution.

5.5 Comparison with Sub-mm Galaxies

In the previous section I have discussed the results from the axial ratio study of the galaxies in my sample. One of the main insights from this work is that the disk components of the star-forming disk-dominated galaxies have surprisingly peaked axial ratio distributions. I have explored the possible origins for this peaked distribution and in addition to finding that the smaller disks are rounder compared to the larger disks (albeit at only a $\sim 2 - \sigma$ statistical level), I have reported tentative evidence that the most active star-forming galaxies have the flattest distributions. However, in order to isolate the most active systems I restricted this cut to a very small number of objects, which prevented me from drawing any robust conclusions. As a result, this issue is clearly worthy of further investigation. To this end, in this section I have considered the mm/sub-mm AzTEC selected sample of Targett et al. (2013) in the GOODS-South field, which has been selected from sub-mm imaging at a uniform depth in a similar area as the CANDELS-UDS and COSMOS fields. Sub-mm selected galaxies are widely agreed to be extreme star-forming galaxies, although there is debate over whether this activity is triggered by major mergers or whether it is just the high-end tail of the normal star-formation main-sequence. One of the main conclusions of Targett et al. (2013) is that the (sub-)mm selected galaxies represent the extreme star-forming end of the morphologically disk-dominated population, thus they provide the ideal sample for extension of this axial ratio study.

First of all, in order to ascertain how valid a comparison is between my star-forming disks and the (sub-)mm galaxy sample, I have compared the properties of the samples in Fig 5.25. My entire mass-selected galaxy sample is plotted in black, my star-forming disks are plotted in blue, and the (sub-)mm galaxies are plotted in light grey. This colour scheme is adopted for all subsequent figures. The far-left panel of Fig 5.25 shows the photometric redshifts distributions of the samples, and confirms that the (sub-)mm galaxies span the full extent of the redshift regime covered by my study. The mass distributions of the samples are plotted in the middle panel of Fig 5.25, and reveal that the (sub-)mm selected sample provide a comparable sample for an extreme population with similar stellar masses to my

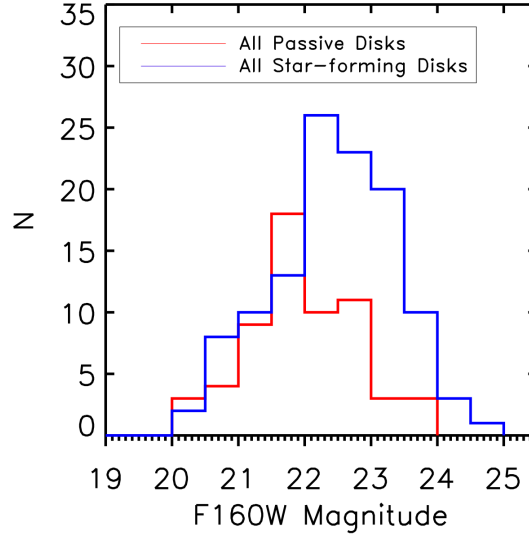


Figure 5.24 *Magnitudes of the passive (red) and star-forming disks (disks), which show that the star-forming disks do have a distribution centred on fainter H_{160} magnitudes, but are still bright enough to avoid biases introduced by low S/N .*

purely mass-selected sample. The final panel of Fig 5.25 shows the distribution for the single-Sérsic indices of the samples. It should be noted here that the study of Targett et al. (2013) was conducted using both a single-Sérsic index morphological fit and a detailed decomposition of the individual clumps in each (sub-)mm galaxy, but it is the overall single-Sérsic index results which are used here and compared with my single-Sérsic index fits.

Finally, as in the previous section I found that the axial ratios of the star-forming disks depends on the size of the disk components, I have also compared the size distributions for the overall galaxies, again to provide the most direct comparison of the whole galaxy I use sizes estimated from the single-Sérsic fits. Fig 5.26 shows that the (sub-)mm galaxies span roughly the same size range as my star-forming disk-dominated galaxies.

Having verified that the (sub-)mm selected galaxies provide a legitimate sample with which to conduct a direct morphological comparison between the “normal” star-forming galaxies in my CANDELS study and an extreme star-forming population, I have examined the axial ratio distributions for the different populations and have plotted them in Fig 5.27. For the above comparisons, which were included to establish the validity of the morphological comparison between

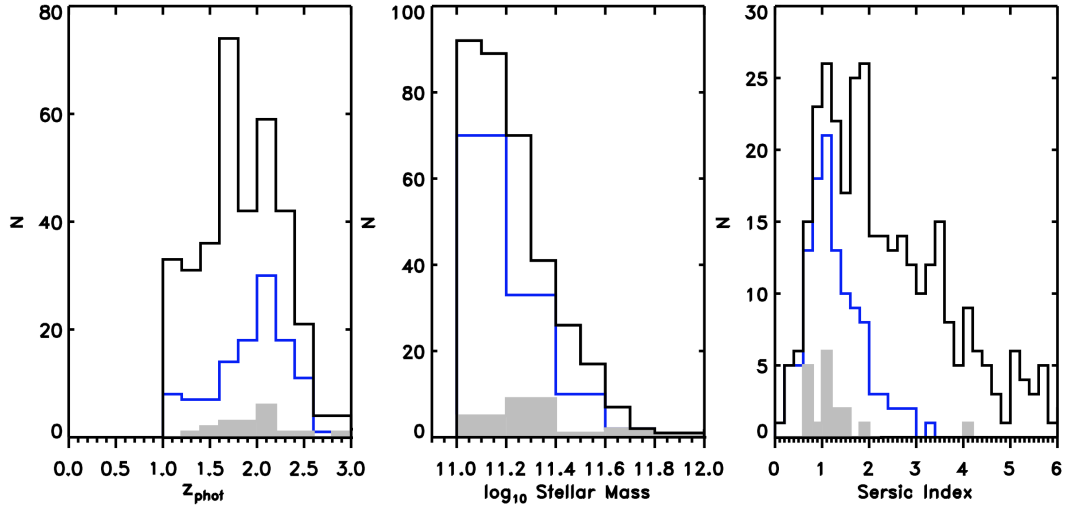


Figure 5.25 *Distributions for the properties of the (sub-)mm galaxies. The combined UDS and COSMOS CANDELS samples are always plotted in black and the star-forming disk-dominated galaxies in blue, where here the properties for the overall galaxies rather than for the disk components are used to allow a fairer comparison to the (sub-)mm selected samples. The Targett et al. (2013) (sub-)mm sample is in light grey. The left panel displays the redshift distributions, the middle panel shows the total galaxy stellar-mass distributions and the right panel shows the single-Sérsic index distributions. The comparison between these samples verifies that the (sub-)mm sample contains comparably massive, disk-dominated galaxies at similar redshifts to my CANDELS galaxies.*

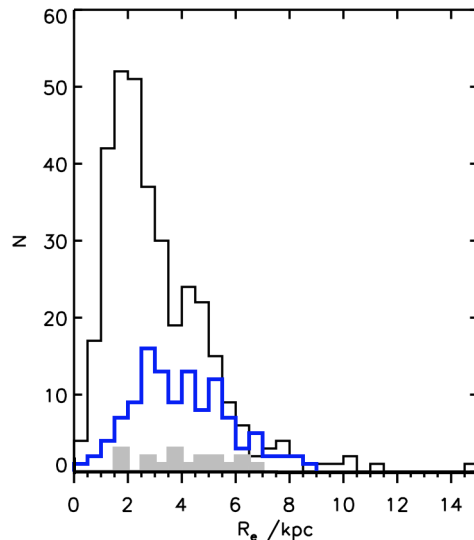


Figure 5.26 *Size distributions of the CANDELS galaxies, over-plotted with the size distributions of the (sub-)mm galaxies. This shows that the (sub-)mm selected galaxies span roughly the same size range as my star-forming disk-dominated galaxies.*

the near-IR and (sub-)mm selected samples, I have used the properties of the overall galaxies. In most cases these properties correspond to genuinely disk-dominated star-forming objects and so a direct comparison between the overall galaxy axial ratios for the (sub-)mm selected sample and the distributions for the disk components of my star-forming disk-dominated objects is justifiable. However, the analysis of Targett et al. (2013) conducted a decomposition of the individual clumps, so to be as thorough as possible in Fig 5.27 I have over-plotted the axial ratio distributions from the disk components of the star-forming disk-dominated CANDELS sample with the distributions from the single-Sérsic model of the (sub-)mm galaxies in the left panel, and with the primary (flux dominant) component of the decomposed model of the (sub-)mm galaxies in the right panel, even in the case where the primary clump was best-fit with an $n > 2.5$ profile (which will only result in a more peaked distribution).

In fact, using both of the axial ratio measurements reveals that the distributions for the (sub-)mm galaxies are flatter than for my star-forming disk components, which lends further support to my previous, tentative, findings that the axial ratio distributions of the most active star-forming galaxies appear to flatten out. The statistics for this comparison are weak, but this apparent trend allows speculation that if there is a maximum surface density of star-formation at high-redshift,

then the most star-forming disks, despite being the most puffed-up, will also be expected to be the largest, which agrees with the other observed trend between larger sizes and flatter axial ratio distributions and so goes some way to delivering at least a self-consistent picture of star-forming high-redshift disks.

Moreover, I have also explored cutting my sample at a star-formation rate that roughly matched the surface number density of the (sub-)mm galaxy sample. Allowing for the survey areas this match in surface number density is achieved at $SFR > 300 \text{ M}_{\odot}\text{yr}^{-1}$. A comparison between the axial ratios of my full star-forming disk sample, the $SFR > 300 \text{ M}_{\odot}\text{yr}^{-1}$ sub-set and the previously flat distribution for the extreme $SFR > 538 \text{ M}_{\odot}\text{yr}^{-1}$ (90% quartile) cut is given in the left panel of Fig. 5.28. The whole star-forming disk sample and the $SFR > 300 \text{ M}_{\odot}\text{yr}^{-1}$ sub-set are also directly over-plotted with the axial ratio distributions for the (sub-)mm selected sample in the right panel of Fig. 5.28. This further demonstrates that by selecting the most active star-forming disks, comparable to the extreme star-forming (sub-)mm selected sample, the axial ratio distributions appear, visually, to be equally flat (although statistics from a K-S test are inconclusive) and reconciles the observed structures of these two populations.

5.6 Summary & Discussion

Having better explored the evolution of the full range of morphological properties exposed by including the decomposed stellar-mass and star-formation rate estimates, I have been able to confirm and refine some of the trends which were reported in Chapter 3.

Perhaps the most fundamental measurement is the relative dominance of the bulge and disk components, as measured in terms of the galaxy morphology from the light fractions and by their contribution to the total galaxy mass. In this chapter I have re-determined these relations for the UDS sample and have compared and combined them with the results from the COSMOS sample. In doing this I found potential evidence for redshift-focussing in the UDS sample for the disk-dominated objects. Having compared my redshift distributions with various other estimates from CANDELS, I concluded that any bias in my photometric redshifts does not significantly affect my results. By combining the UDS and COSMOS samples, the redshift evolution of disk-dominated galaxies

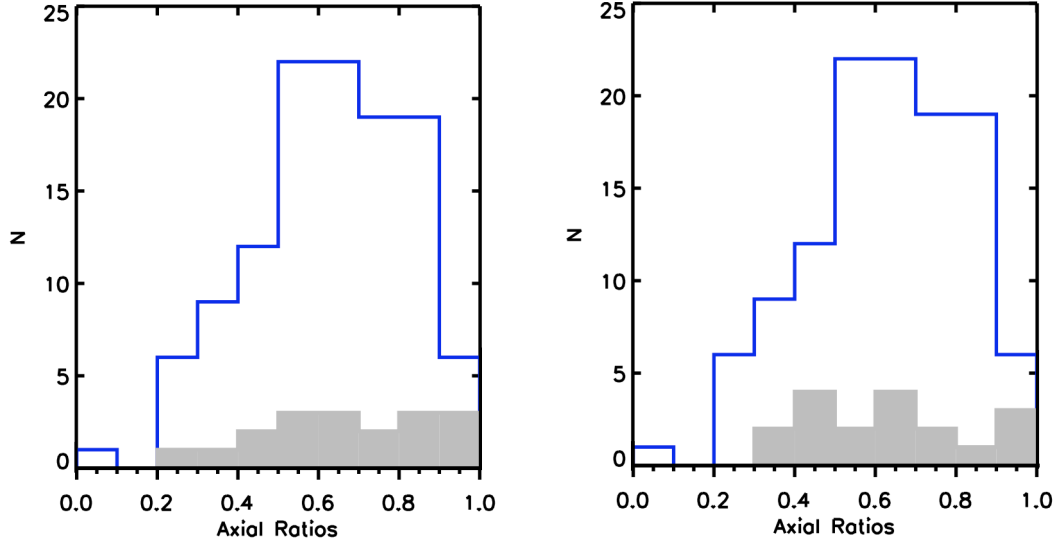


Figure 5.27 *The axial ratios of the (sub-)mm galaxies, where again the (sub-)mm selected is in light grey. The (sub-)mm selected sample was modelled in Targett et al. (2013) using both a single Sérsic fit and multiple component fits to each clump. Therefore, on the left I have plotted the axial ratio distributions from the single Sérsic fits and for completeness on the right plot the distributions for the axial ratios of the flux-dominant component/clump, even in the case where that component was best fit with $n > 2.5$ (which would only act to increase the axial ratios). However, from both plots the axial ratios for the (sub-)mm selected galaxies are considerably flatter than the distributions for the CANDELS star-forming disks. Although the numbers within the sample are too small for a robust statistical comparison, it does appear that the trend for the axial ratios of the most active galaxies to flatten-out also extends to the extreme star-forming (sub-)mm selected population.*

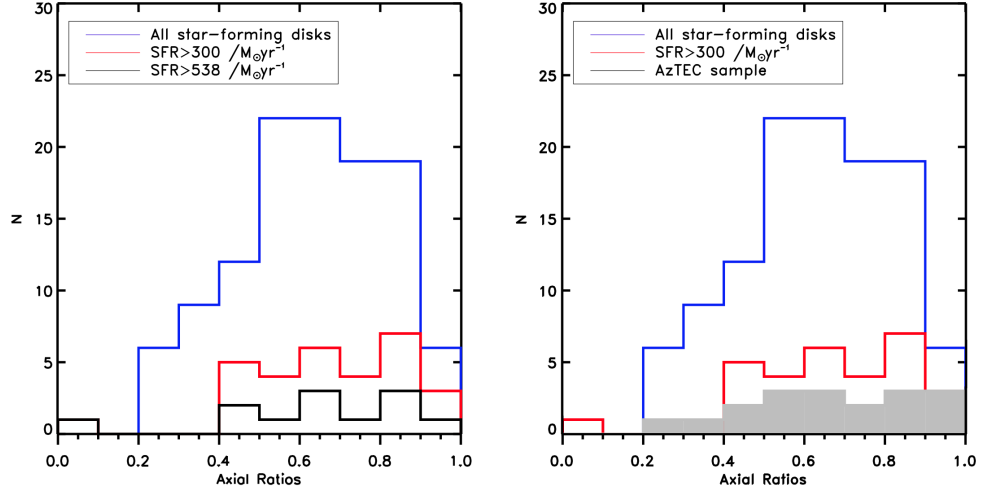


Figure 5.28 *Left: the axial ratio distributions of all the star-forming disks in my sample (blue), the sub-set cut at a similar star-formation rate ($SFR > 300 \text{ M}_{\odot}\text{yr}^{-1}$) as the (sub-)mm AzTEC selected sample (red), and the extreme 90th percentile cut imposed previously (black). Right: the axial ratio distributions of all the star-forming disks (blue) and the $SFR > 300 \text{ M}_{\odot}\text{yr}^{-1}$ sub-set (red), over-plotted with the distributions for the (sub-)mm AzTEC selected sample (grey). This further demonstrates that by selecting the most active star-forming disks, comparable to the extreme star-forming (sub-)mm selected sample, the axial ratio distributions appear, visually, to be comparably flat and reconciles the observed structures of these two populations.*

appears to be somewhat flatter than the trend witnessed for the UDS sample alone, discussed in Chapter 3, although there is still a decrease in the fraction of disk-dominated objects from $z = 3$ to $z = 1$. The combined sample also confirms that the evolution of bulge-dominated, and essentially “pure” bulges ($B/T > 0.9$), is relatively flat, which corroborates the previous findings. By including the COSMOS sample, the trend for an increase in mixed bulge+disk systems with decreasing redshift is strengthened, but by incorporating the decomposed stellar-mass results I find that this morphological evolution is accompanied by an increase in the bulge component mass of the objects. These results suggest that, instead of a clear transition at $z = 2$ when the most massive galaxies transform straight from disk to bulge-dominated systems, at $1 < z < 3$ there is a more gradual emergence of a mass-dominant bulge component while the galaxies still display a mixed bulge+disk morphology, but even by $z = 1$ these massive galaxies do not display the “pure” bulge morphologies exhibited by the ETGs in the local Universe, and in fact are more comparable to local S0 galaxies.

The presence of an increased fraction of disk-dominated galaxies is in agreement with previous studies, within similar mass and redshift regimes, such as Buitrago et al. (2008), Conselice et al. (2011) and Buitrago et al. (2013), who use IFU spectroscopy from SINFONI to kinematically confirm that $50 \pm 7\%$ of their $M_* > 10^{11} M_\odot$ $z \sim 1.4$ galaxy sample are rotationally supported disks, but also note evidence of interactions and mergers for galaxies within their sample. However, Conselice et al. (2011) report higher fractions of morphologically mixed objects at $1.5 < z < 2$ and find from adopting definitions based on combinations of visual, non-parametric, Sérsic and spectral classifications that only $\sim 3\%$ of massive galaxies are comparable to local bulge-dominated systems and $7 - 10\%$ are comparable to local disk-dominated systems. In addition to these studies, Mortlock et al. (2013) have conducted visual morphological classifications of $M_* > 10^{10} M_\odot$ galaxies at $1 < z < 3$ using CANDELS WFC3/IR imaging. For comparison, Mortlock et al. find that classifying bulges and disks by the $n = 2.5$ cut returns a morphological evolution for their highest mass ($M_* > 10^{10.5} M_\odot$) in agreement with my findings, whereby there is a transition from bulge to disk-dominate morphologies at $z \sim 2$. However, their visual classification suggests that, even for this high mass bin, the fraction of bulge and disk-dominated systems increases with decreasing redshift, and is accompanied by a fall in the fraction of “peculiar” morphologies. This result appears to be in conflict with both their Sérsic analysis and my findings and highlights the tension between the different measures of morphology. Mortlock et al. assert that this disparity

is due to the fact that at high redshift star-forming disks have not yet relaxed into stable disks and display disturbed and/or interacting morphologies. I note that although $\sim 80\%$ of the disk-dominated objects within my sample were well-fitted by the symmetric profiles, the remaining fraction required re-fitting with additional χ^2 masking to achieve acceptable fits. Despite the fact that the underlying profiles of these re-fitted objects were disk-like exponentials, the additional structure (whether clumps, spiral features or other asymmetries) may bias visual classifications.

In addition to the morphological trends witnessed with redshift, including information about star-formation activity has also delivered new insights into the evolution of the massive galaxies within my sample. One of the most interesting results from Chapter 3 was the discovery that a significant fraction of passive galaxies are in fact disk-dominated, and star-forming galaxies are bulge-dominated. Star-forming bulges and passive disks have been previously observed at both high and low redshift, however the large fractions found within my sample were unexpected. By effectively doubling the sample size, by combining the CANDELS-UDS and COSMOS samples, the reported fractions from Chapter 3, which use the overall galaxy star-formation rates, were further substantiated and I reported that $\sim 30\%$ of all star-forming and passive galaxies are bulge and disk-dominated, respectively.

More recent studies have also found higher fractions of passive disk-dominated galaxies, more comparable to the $\sim 30\%$ quoted here. In particular: Wang et al. (2012) report a passive disk-dominated fraction of $\sim 30\%$ for $M_* > 10^{11} M_\odot$ at $1.5 < z < 2.5$; Lee et al. (2013) publish broadly consistent results ($29 \pm 10\%$) for their 35 $1.4 < z < 2.5$ passive galaxies, although note the low S/N of these sources; McLure et al. (2013) find a passive disk-dominated fraction of $44 \pm 12\%$ for their $M_* > 6 \times 10^{10} M_\odot$, $1.3 < z < 1.5$ sample; van der Wel et al. (2011) extrapolate from the 14 galaxies with $M_* > 10^{10.8} M_\odot$, $1.5 < z < 2.5$ in their sample, based on visual, Sérsic decomposition and axial ratio results, that $64 \pm 15\%$ of all high-redshift passive galaxies are disk-dominated; and Fan et al. (2013) find that $68 \pm 24\%$ of the 19 passive $z \approx 3$ galaxies in their sample are disk-dominated with $n < 2$ and with consistently flat axial ratios.

However, I have also discussed how these statistics may be biased due to the use of star-formation rate estimates for the whole galaxy rather than for the individual bulge and disk components. To this end I re-evaluated the fractions of galaxies in my sample in each population using the strictest criteria possible in terms of

both star-formation rate and component dominance. This conservative approach revealed that only $\sim 18 \pm 5\%$ of passive galaxies are disk-dominated and $\sim 10 \pm 3\%$ of star-forming galaxies are bulge-dominated. The significant reduction in star-forming bulge-dominated galaxies brings my results into better agreement with previous, albeit single-component, studies such as Bell et al. (2012) at similar redshifts, which have suggested that the presence of a massive bulge correlates with quiescence but is not sufficient to solely signify quiescence.

The gradual emergence of a mixed bulge+disk (but increasingly bulge dominated) population at $1 < z < 3$, coupled with the discovery of a significant population of both star-forming bulges and passive disks, suggests that the physical processes which quench these massive galaxies, are not simply connected to the mechanisms which bring about the morphological transitions witnessed within this era. Moreover, these results are inconsistent with the idea that major mergers are solely responsible for both transformations as this would simultaneously quench the systems and transform their morphologies from disk to bulge-dominated. However, there are several competing quenching mechanisms which would not necessarily alter the morphologies of the systems or do so through a less stochastic processes than mergers. These include quenching through AGN feedback, the different modes of which have been discussed in Chapter 1, halo quenching (e.g. Birnboim & Dekel 2003, Kereš et al. 2005, Dekel et al. 2009a) and morphological quenching (e.g. Martig et al. 2009).

In addition to these theories for star-formation quenching, the model of violent disk instabilities (VDI) is also more consistent with the morphological evolution displayed by the galaxies within my $1 < z < 3$ sample. The VDI scenario has gained increasing support from both recent simulations and observations. This model proposes that in high-redshift star-forming disks, massive clumps form from gravitational instabilities within the disk. These clumps then migrate towards the centre of the disk transferring gas and stars to the centre of the system and build a bulge component. There is significant observational evidence of star-forming clumps within high-redshift disks from, for example, Elmegreen & Elmegreen (2005), Elmegreen et al. (2009), Guo et al. (2011b), Wuyts et al. (2012) and Mozena et al. (2013, in preparation). These studies agree that $\sim 70\%$ of massive $1 < z < 3$ star-forming galaxies have morphologies which contain at least a few kpc sized star-forming clumps. In fact Elmegreen et al. (2009) claim that, within these disks, the contribution to the total star-formation rate is split equally between the clumps and the diffuse disk. The formation and migration

of giant clumps within a gas-rich disk can be well modelled (e.g. Ceverino et al. 2010, Martig et al. 2012, Hopkins et al. 2012), as can the formation of a central bulge and the reshaping of the remaining disk to an exponential density profile (e.g. Bournaud et al. 2007a, Krumholz & Burkert 2010, Bournaud et al. 2011). However, there is some debate over the extent to which these clumps can survive or reform after disruption from feedback, and whether they can survive long enough to migrate to the centre of the disks (e.g. Genzel et al. 2011, Hopkins et al. 2012).

The latest simulations (for example Bournaud et al. 2013, Dekel & Krumholz 2013) address this issue by modelling the effects of photo-ionisation, radiation pressure and supernova feedback on the clumps and find that in their models the clumps can account for any momentum-driven mass outflows and tidal stripping of gas and stars by re-accreting from the gas-rich disk, so that they maintain constant masses and star-formation rates for a few hundred Myr, which is long enough to complete their migration to the centre and merge to form a bulge. However, there remains observational debate (e.g. Wuyts et al. 2012, Elmegreen et al. 2009) over whether the masses in these clumps are actually sufficient to build a central bulge.

The VDI model could plausibly account both for the morphological trends observed from my analysis and potentially the presence of passive disks if the clump migration which builds a central bulge, but leaves a massive disk in place, is accompanied by morphological quenching in the disk. However it is unclear what becomes of these star-forming central bulges, as this work has found evidence for only a small sub-set of star-forming galaxies which are bulge-dominated, where these systems also tend to be at higher redshifts. One possibility may be that the star-forming central bulges are quenched at later times via AGN feedback or halo quenching. The VDI model also reproduces compact sizes for the final quenched bulge stage, which may then undergo minor merging to increase their size from inside-out growth.

Finally, in addition to the bulge and disk dominance, and star-formation activity of the individual components, I have also explored the difference between the axial ratio distributions of the sub-populations comprising my sample. In Chapter 3 I found that the axial ratios of the passive disks of disk-dominated galaxies display a flat distribution, consistent with a population of randomly oriented thin disks, whereas the distribution for the star-forming disks is peaked at $b/a \sim 0.7$, consistent with a more tri-axial population. This is also the case for the new

combined sample.

The flat distribution for the passive disks agrees with both the distributions of local disks and the results from van der Wel et al. (2011) and Chang et al. (2013a). Chang et al. (2013a), explore the axial ratio distributions of local and $z \sim 2.5$ ETGs identified on the basis of low star-formation rates from rest-frame colours. By de-projecting the observed axial ratios Chang et al. (2013a) find that the low and high redshift ETG samples comprise of two populations: tri-axial objects, and flatter disk-like galaxies. The identification of disk-like galaxies within the Chang et al. (2013a) ETG sample by axial ratio distributions (which are similar to the distribution for my passive disks) independent of Sérsic index or bulge/disk ratios, helps to confirm that there is a significant population of passive, genuinely, disk-dominated galaxies at $z > 1$.

As well as the flat distribution for the passive disks, this sub-divided analysis also revealed that the star-forming disks have a distribution more similar to that of the bulges, which is peaked at $b/a \sim 0.7$ and displays a relative dearth of objects with $b/a < 0.3$. Having explored how the axial ratio distribution varies with size and star-formation rate, I found that the axial ratios of smaller galaxies tend to be rounder, and the distributions for the most star-forming galaxies are flatter. Due to the small number of objects in my most active star-formation rate cut I also compared my axial ratio distributions to those for (sub-)mm galaxies which are expected to be extreme star-formers, and found that this trend also holds for the more extreme (sub-)mm population. These results lead me to speculate that, at high redshift, feedback from star-formation in disks acts to “puff-up” their scale-heights, which accounts for the peaked axial ratio distribution of the disks with smaller scale-lengths and the flatter axial ratios of larger disks.

Chapter 6

Conclusions and Future Work

6.1 Conclusions

In this thesis I have constructed a sample of $\simeq 400$ galaxies in the CANDELS-UDS and COSMOS fields for which I have determined stellar masses $M_* > 10^{11} M_\odot$, and photometric redshifts in the range $1 < z < 3$. These objects are relatively bright, being selected from a parent sample with $H_{160} < 24.5$ (a factor of 10 brighter than the CANDELS WFC3/IR 5- σ detection limit of $H_{160} < 27$), and in practice virtually all objects have $H_{160} < 23$ (equivalent to 100- σ detections). I have compared the results from both fields, taking into account potential biases from photometric redshift focussing and cosmic variance, and have concluded that the findings reported in this thesis are robust to these issues. Thus, all trends are determined from the combination of the CANDELS-UDS and COSMOS results unless otherwise stated. Consequently, I have been able to exploit the exquisite CANDELS imaging to undertake a detailed analysis of their rest-frame optical morphologies, and have explored how these vary as a function of redshift, mass and star-formation rate.

Crucial to this work is proper control of both the random and systematic errors. In Chapter 2 I have undertaken a detailed study of the form of the adopted PSF, constructing and justifying the use of an empirical on-image PSF over that produced by the Tiny Tim modelling software. I also explored in detail the effect of errors in background determination on both the best-fitting values of, and errors in, the derived physical parameters such as Sérsic index and effective radius.

This led to the establishment of a robust procedure for the implementation of the GALFIT routine for determining the morphological properties of the massive galaxies within my sample.

In all subsequent chapters I have placed a high premium on the importance of obtaining formally acceptable model fits to as many objects as possible, in order to enable realistic error estimation. In the end, via careful object-by-object masking, and the use of models ranging from single-Sérsic fits to disk+bulge+point-source combinations, I achieved satisfactory structural models for $\simeq 90\%$ of the massive galaxies in my complete $1 < z < 3$ sample.

In Chapter 3 I have presented a procedure for the robust morphological decomposition of massive galaxies into their separate bulge and disk components using a multiple component $n = 4 + n = 1$ Sérsic light-profile fitting approach with GALFIT. This was first applied to the $M_* > 10^{11} M_\odot$ $1 < z < 3$ galaxy sample in the CANDELS-UDS field. Utilising the resulting unparalleled morphological information on massive galaxies during this key epoch in cosmic history, I have been able to reach the following conclusions.

My single-Sérsic results indicate that these massive galaxies at $1 < z < 3$ lie both on and below the local size-mass relation, with a median effective radius of ~ 2.6 kpc, a factor of $\simeq 2.3$ smaller than comparably-massive local galaxies. This median size is smaller than some previous reported results, however the scatter in the single-Sérsic purely mass-selected size-mass relation is large, which helps to reconcile some of the previous discrepancies between sizes reported for morphological or star-formation selected samples in the literature.

By decomposing the objects into their separate bulge and disk components I found evidence for a growing bimodality in the size-mass relation with increasing redshift for the bulge components; the fraction of bulges consistent with the local size-mass relation is $20 \pm 4\%$ at $1 < z < 2$, and $15 \pm 5\%$ at $2 < z < 3$, while the offset in size of the (dominant) compact population from the the local early-type relation is already a factor of 3.5 ± 0.5 at $1 < z < 2$ and rises to a factor 4.4 ± 0.3 at $2 < z < 3$. These trends appear to extend to the bulge components I have isolated from the disk-dominated galaxies, and I found evidence that the lower envelope of galaxy size is a function of mass which broadly parallels the local relation; no galaxies more compact than $R_e = 1$ kpc are found at masses $M_* > 2 \times 10^{11} M_\odot$, while bulges as small as $R_e < 0.5$ kpc are found at lower stellar masses $M_* \simeq 5 \times 10^{10} M_\odot$.

The changes for disks are less dramatic, with $42 \pm 4\%$ of disks still consistent with the relevant local size-mass relation over my full redshift range, and the offset of the compact population from the local late-type relation showing no significant evolution from a factor 2.4 ± 0.4 at $1 < z < 2$, to 2.5 ± 0.2 at $2 < z < 3$. I did, however, find that the objects which remain consistent with the present-day size mass relation are virtually all active star-forming disks, with the population of apparently passive disks confined to the more compact subset.

Even within the relatively limited redshift range of my study, I found evidence for dramatic changes in the morphologies of massive galaxies with redshift, with $z \simeq 2$ apparently marking a key transition epoch. While similarly massive galaxies at low redshift are generally bulge-dominated (and the expected more massive $M_* \simeq 3 \times 10^{11} M_\odot$ descendants of my high-redshift galaxies are virtually all giant ellipticals today), by a redshift of $1 < z < 2$ they are predominantly mixed bulge+disk systems, and by $z > 2$ they are mostly disk-dominated. Furthermore, at the lowest redshifts covered by this study while bulge-dominated objects are on the rise, pure-bulge galaxies (i.e. objects comparable to present-day giant ellipticals) have yet to emerge in significant numbers, with $> 90\%$ of these high-mass galaxies still retaining a significant disk component.

I found that the majority of the disk-dominated galaxies are actively forming stars, although this is also true for many of the bulge-dominated systems. Interestingly, however, while most of the quiescent galaxies are bulge-dominated (indicating early emergence of the red sequence), I found that a significant fraction ($25 \pm 6\%$ using a disk-dominated definition of $B/T < 0.5$, and $40 \pm 7\%$ using a disk-dominated definition of $n < 2.5$) of the most quiescent galaxies, with specific star-formation rates $sSFR < 10^{-10} \text{ yr}^{-1}$, have disk-dominated morphologies (including a small number (five) of “pure disk” galaxies with $B/T < 0.1$). I have shown that these passive disks appear to be “normal” disks in the sense that they display an axial-ratio distribution comparable to that displayed by present-day disks, while the more prevalent actively star-forming disks seem, on average, rounder and clumpier. I have considered various possible reasons for this, including selection effects, and have briefly discussed the theoretical implications in the context of galaxy quenching and morphological transformations.

Finally, I found evidence for a peaked axial ratio distribution for the star-forming disks in my sample. This distribution is not consistent with a population of randomly oriented thin disks and suggests that these high-redshift star-forming disks are more tri-axial in structure.

The results from Chapter 3 provided new insight into how the morphologies of these most massive galaxies evolve over this key era in cosmic time and highlighted interesting questions about how the processes which quench star-formation in these systems are connected to the mechanisms which transform their morphologies. These trends have been further explored in Chapters 4 and 5, where the morphological decomposition was applied to the CANDELS-COSMOS field in order to effectively double the sample size, and was extended across the 4 WFC3 and ACS (H_{160} , J_{125} , i_{814} , v_{606}) bands provided by the CANDELS survey. This extension to multi-wavelength bands provided individual photometric models for the separate bulge and disk components, which was then used to conduct decomposed component SED fitting. By exploring the effects of fixing the morphological parameters in the multi-band fitting procedure or allowing them to be fit as free parameters, I found that fixing all morphological model parameters except for the magnitude of each component at the best-fit H_{160} models provided acceptable fits at all wavelengths, and naturally produced realistic SEDs. Moreover, by adapting the SED fitting code to incorporate simultaneous fitting of both the bulge and disk photometry, I have found that the minimum age and limited star-formation history constraints imposed on the single component SED fitting to ensure physically meaningful fits are no longer required, as the addition of the degrees of freedom provided by the second component allow the fits to better account for a superposition of young and old stellar populations.

This decomposed SED fitting yielded individual stellar-mass and star-formation rate estimates for the bulge and disk components which allowed me to better probe both the morphological and star-formation evolution of the massive galaxies within my sample. Having conducted this analysis I confirm that the H_{160} light fractions provide a good measure for the underlying decomposed stellar-mass fractions, although the mass fractions tend to be more bulge-dominated, which is to be expected given the higher mass-to-light fractions in the bulge stellar populations. However, the decomposed star-formation rates provide significantly improved constraints for the star-formation evolution of the separate components, and by extension, to the overall evolution of the massive galaxies within this critical epoch.

Examination of the correlation between single-Sérsic indices and bulge/total H_{160} light fractions and decomposed stellar-mass estimates, confirms that in the majority of cases the single-Sérsic indices describe the overall morphologies of these most massive galaxies well, as $n = 2.5$ provides a good proxy for both

light and mass-based measures of $B/T = 0.5$. This strengthens the validity of the comparison between the size-mass relation of the decomposed bulge and disk components with the local ETG ($n > 2.5$) and LTG ($n < 2.5$) relations.

From examination of the size-mass relations from the combined UDS and COSMOS samples and utilising the new decomposed stellar-mass estimates, I found continued evidence that the bulge components display a stronger size evolution compared to similarly massive local galaxies than the disk components. This can be seen from both the fraction of bulge components which lie below the local relation and the median sizes of the bulge components split above and below $z = 2$. Using the combined UDS and COSMOS sample I found that, at $1 < z < 2$, $15 \pm 3\%$ of bulges have sizes consistent with the local ETG relation within its $1 - \sigma$ scatter, with the median bulge component sizes being a factor of 2.93 ± 0.32 smaller than similarly massive local ETGs. At $2 < z < 3$ this fraction of bulges with sizes comparable to the local ETG relation becomes $23 \pm 5\%$ and median bulge component size is a factor of 3.41 ± 0.58 smaller than local ETGs. In comparison, at $1 < z < 2$, $49 \pm 4\%$ of the disk components have sizes consistent with the local LTG relation and its $1 - \sigma$ scatter, and the median size is a factor of 1.65 ± 0.14 smaller. In the high-redshift bin these numbers become $43 \pm 5\%$ and the median size is a factor of 1.99 ± 0.25 smaller. The scatter in both the bulge and disk relations is larger than expected from measurement error and reflects the intrinsic scatter in the size-mass relations. As a result, the errors on these fractions are large and do not allow me to draw any robust conclusions about the evolution in the form of the relations between the two redshift bins adopted in my study. As a consequence, I do not find any additional support for a bi-modality in the size-mass relation of the bulge components. However, the new results confirm that there appears to be a minimum envelope in the size-mass relation.

By incorporating the new star-formation rate estimates from the decomposed SED fitting I do not find a clear distinction in the sizes of the passive and star-forming components. In order to further explore how the star-formation activity correlates with galaxy size I have examined the sizes of the galaxies in my sample as a fraction of local similarly massive galaxies, split into the passive and star-forming bulge and disk sub-populations and plotted above and below $z = 2$. By constructing these samples based on the $n = 2.5$ single-Sérsic fits with the overall star-formation rates, and using the decomposed morphologies and star-formation rates, I have highlighted the advantages in decomposing these galaxy properties. This analysis reveals that while the single-Sérsic fits would indicate

that the star-forming and passive bulges and the passive disks are equally compact in size (although the robustness of the star-forming bulge sample is called into question, as discussed in Chapter 5, by the high level of contamination from star-forming disk components) with the star-forming disks having larger sizes, the decomposed fits show that the passive disks have intermediate sizes. As the single-Sérsic fractional sizes are in broad agreement with results from previous studies, this clearly demonstrates that adopting the single-Sérsic fits presents a simplified view of the evolutionary processes involved, where for bulge-dominated systems morphology is the main indicator of compactness and for disks the main indicator is star-formation, whereas the decomposed fits reveal that compactness correlates with some combination of passivity and the presence of a significant bulge component.

Moreover, by assuming that the star-forming disks are the direct progenitors of the passive disks, and by evolving the star-formation histories of the passive disks back to the redshifts ~ 1 Gyr earlier, when the passive disks were still active, I have shown that the passive and star-forming disks have sizes consistent with a secular evolution scenario, where the size of newly quenched galaxies scales with the mean density of the Universe at the epoch of quenching.

Combining the CANDELS-UDS and COSMOS samples, I determined co-moving number densities for these most massive galaxies which are in agreement with the latest mass function studies, within the errors associated with stellar-mass estimation. By comparing the dominance of the bulge and disk fractions in terms of both the H_{160} light fractions and the stellar-mass contributions, I found that, within the $1 < z < 3$ redshift era, these most massive galaxies are more disk-dominated at higher redshifts and become increasingly mixed bulge+disk systems with decreasing redshift, where they are more bulge-dominated by mass than by light. However, even at $z = 1$ the “pure” bulges comparable to the giant ellipticals, which have been previously reported to comprise $\sim 60\%$ of the massive galaxy population locally, have yet to emerge.

One of the most interesting results from Chapter 3 was that despite confirmation that the colour-morphology bimodality is already well established at $1 < z < 3$, I identified that a significant fraction of passive galaxies are disk-dominated ($33 \pm 5\%$) and star-forming are bulge-dominated ($29 \pm 5\%$). These results challenge the idea that major mergers are the main mechanism for galaxy quenching as mergers would both quench these systems and transform their morphologies from disk to bulge dominated. In order to better probe this population I have

examined the decomposed stellar-mass and star-formation rate estimates for the passive disks and star-forming bulges and, adopting the strictest possible criteria, I conclude that $18 \pm 5\%$ of passive galaxies are genuinely disk-dominated and $11 \pm 3\%$ of star-forming galaxies are bulge-dominated. This passive disk-dominated fraction is significantly lower than the fraction determined from the overall galaxy specific star-formation rates and stellar-masses reported in Chapter 3, and by other studies at similar redshifts and masses, which clearly illustrates the superiority of the full SED decompositions over and above single model fits for this type of analysis. The fraction of star-forming galaxies which are genuinely bulge-dominated is also significantly reduced by examining the decomposed star-formation rates.

Finally, in addition to studying the overall morphologies and star-formation rates of the most massive galaxies at $1 < z < 3$, my decomposition technique has also allowed me to investigate how the axial ratio distributions for the passive and star-forming sub-populations of the bulge and disk components differ. The axial ratios of these components have provided another key indicator of the structure of these systems as they reveal that the passive disks have flattened axial ratio distributions consistent with the a population of randomly oriented thin disks, similar to disks in the local Universe, which further verifies that these are genuine disk-dominated passive galaxies. However, the star-forming disks have a distribution peaked at higher values of $b/a \sim 0.7$, more consistent with the distributions for the passive and star-forming bulges in this sample, and those for lower redshift bulge-dominated systems.

By exploring the trends within the star-forming disk population I found evidence that the smallest galaxies are the roundest and the largest galaxies are the flattest, and moreover, there is potential evidence that the most star-forming galaxies are the flattest, which has been supported by comparison with a (sub-)mm sample. I have discussed the robustness of the axial ratio estimates for the star-forming disks, in particular for the small disks, and have concluded that they are not subject to bias due to the resolution limit of GALFIT. These results are thus consistent with a scenario in which at high redshift feedback from star-formation increases the scale-height of disks, which affects the axial ratios of the smaller galaxies but has a lesser impact on the larger disks. If there is also a maximal surface-density of star formation in high-redshift disks, then the largest, flattest galaxies would also be expected to be the most star-forming, thereby reconciling both of these observations.

Moreover, the size evolution witnessed for both the bulge and disk components from my decomposition is consistent with the generally accepted competing mechanisms for galaxy growth, including major or minor merging or AGN driven adiabatic expansion. However, given the age arguments against the AGN driven expansion model (Ragone-Figueroa & Granato 2011) and constraints on the potential mass increase resulting from major mergers from the present day mass function (e.g. Baldry et al. 2012), at present minor-merger induced inside-out growth is the preferred process. The associated minor-merger size growth from the latest simulations, such as those by Oser et al. (2010) and Oser et al. (2012) can provide the required evolution for the bulge and disk components in my sample as they can produce a size evolution of the form $R_e(z)/R_0 \propto (1+z)^{-1.12}$ for all galaxies. In these models massive galaxy evolution occurs as a two-stage process, where at high redshift compact cores form rapidly from gas-rich mergers or through cold inflows Kereš et al. (2005), and the latter stage is dominated by minor mergers which accrete ex-situ stars to the outer regions of the galaxies.

By splitting my population into star-forming and passive bulges and disks I find evidence that the passive disks have sizes intermediate between the large star-forming disks and the smaller bulge components, and within the passive disk population I find that the disks which quenched most recently, less than 0.5 Gyr ago, have larger sizes. These results for the disk components support the scenario in which the disks evolve secularly and their sizes scale as $(1+z)^{-1}$, consistent with the mean density of the Universe at the time of quenching. However, I do not find strong evidence for a similar size separation between the passive and active bulges, as has been previously reported by studies such as Carollo et al. (2013) which further advocate this model, and suggest that the size evolution of passive galaxies is not predominantly driven by the growth of individual systems, but by the addition of larger, new quenched objects to the overall population. However, from examination of the decomposed star-forming bulge components of bulge-dominated galaxies, I find that this sub-population is very sensitive to contamination from sub-dominant active disks and the scatter in the sizes of components is large. Nevertheless, it is clear that the addition of newly quenched, larger galaxies, may play a role in the size of evolution of these massive galaxies.

The confirmation of a significant population of passive disks and star-forming disks, coupled with the observed gradual emergence of increasingly morphologically mixed bulge+disk systems, with larger bulge/total mass fractions, from $z = 3$ to $z = 1$ suggests that whilst some of these most massive galaxies

undergo major mergers which both quench their star formation and transform their morphologies, there must also be other physical processes which quench star-formation but leave a massive disk intact. This evolutionary scenario is more consistent with the models of AGN quenching, halo quenching (Dekel et al. 2009a) or violent disk instabilities (Ceverino et al. 2010), where there is mounting evidence for a scenario in which gravitational instabilities in gas-rich star-forming disks result in the formation of massive clumps, which then migrate to the centre of the galaxy transferring gas and stars, which builds a central bulge, but leaves a massive disk in place. This clump migration may also be accompanied by morphological quenching in the disk (Martig et al. 2009), where the star-forming central bulge is quenched at later times via AGN feedback or halo quenching. The VDI model also reproduces compact sizes for the final quenched bulge-dominated systems, which may then undergo minor merging to increase their size from inside-out growth. Such a scenario is consistent with the size, morphological and star-formation evolutionary trends revealed by this work.

6.2 Future Work

6.2.1 AGN hosts

In order to further explore the mechanisms responsible for star-formation quenching and size evolution in massive galaxies, I will next extend my multiple-component morphological and SED fitting analysis to AGN hosts. By exploring any correlations between morphology and star-formation rates with AGN activity, I aim to address how important a role AGN feedback plays in massive galaxy evolution. Previous high-resolution studies of the morphologies of AGN hosts suggest that they display morphologies similar to their non-active counter-parts where they lie in predominantly bulge-dominated systems at $z \leq 1.5$ (Kauffmann et al. 2003a, Sánchez et al. 2004, Grogin et al. 2005, Pierce et al. 2007) and are split between bulges and disks (Gabor et al. 2009) or in disk-dominated systems at $z > 2$ (Schawinski et al. 2011, Kocevski et al. 2012), although there remains debate about how disturbed the morphologies of the AGN hosts are. In addition to morphological trends, previous studies have explored the links between AGN activity and quenching from correlations between star-formation and galactic outflows, and the similar evolution of the AGN stellar mass function and the rate of star-formation quenching (e.g. Tremonti et al. 2007, Bundy et al. 2008),

as well as studies which reveal that AGN hosts preferentially lie in the “green valley” (e.g. Nandra et al. 2007, Schawinski et al. 2007), the transition region between the blue cloud and the red sequence. Furthermore, there is new evidence from the latest CANDELS studies of Barro et al. (2013) and Rangel et al. (2013, in preparation) from the prevalence of AGN in the high-redshift star-forming compact progenitors of local passive galaxies, that AGN may potentially both quench star-formation and facilitate size growth.

However, while previous AGN host studies have been conducted with high resolution HST data which have allowed detailed morphological studies using parametric fits and exploration of the asymmetries and concentrations of the hosts, the high-redshift AGN host galaxies have not yet been decomposed into their bulge and disk components. Thus, I will further explore the correlations between AGN activity and host star-formation rates and morphologies by implementing my decomposition analysis.

The CANDELS-UDS and COSMOS fields do not provide good samples with which to conduct this analysis as they have limited X-ray coverage from Chandra and XMM-Newton. The sample utilised in this paper has been cross-matched with accompanying multi-wavelength catalogues ranging from $24\mu\text{m}$ from SpUDS (PI Dunlop) and S-COSMOS (PI Sanders), and X-ray catalogues from SXDS (Ueda et al. 2008) and C-COSMOS (PI Elvis), to radio catalogues from VLA-SXDF (PIs Simpson & Ivison) and VLA-COSMOS (PI Shinnerer). However, adopting a 4arcsec matching radius for the X-ray catalogues and a 2arcsec matching radius for the radio catalogues, to take into account the PSF FWHM in both cases, I find only 8 objects in the UDS which have an X-ray counterpart, and 17 objects in COSMOS which have an X-ray counterpart. In addition to this, 20 objects in UDS have a radio counterpart (1 object has both X-ray and radio counter-parts) and 10 objects in COSMOS have a radio counterpart (2 objects have both an X-ray and a radio counterpart). Due to the small numbers involved I can draw no robust conclusions about the morphologies of these objects, or say anything about their preference for a centrally concentrated central component. However, the advantages of conducting a fully decomposed, detailed morphological analysis of the host galaxies are clear from the further insights which have been gained from the above work on massive galaxies. Thus, I will conduct a similar morphological study in the CANDELS GOODS-South field, which not only benefits from deeper WFC3 and ACS coverage ($5 - \sigma$ point-source depths of: $H_{160} = 27.6, J_{125} = 27.9, i_{814} = 29.4, v_{606} = 29.3$), but has also

been covered by the 4Ms Chandra imaging in the CDF-S field.

6.2.2 HST grism spectroscopy

The most massive galaxies at $1 < z < 3$ are also particularly well suited to exploring how dynamical and spatially resolved star-formation properties evolve throughout cosmic time, as they provide the best targets for detailed spectroscopic study. In the future, I will use the public 3D-HST (PI van Dokkum) data to further address the important outstanding issues for galaxy evolution, including the physical processes are responsible for the quenching of star-formation and how this changes with environment and downsizing effects. Upon completion of my morphological analysis of AGN hosts I will be able to combine the WFC3/G141 and ACS/G800L spectroscopy with existing bulge-disk decompositions in the CANDELS UDS COSMOS and GOODS-S fields. The spectral coverage of the WFC3/G141 and ACS/G800L grisms will allow me to provide upper estimates on star-formation rates of the extremely interesting population of passive disks and star-forming bulges identified at $1 < z < 3$ from observing H_α and $OII(\lambda 3727\text{\AA})$ emission lines. Moreover, the spatial resolution of the 3D-HST data will deliver age and metallicity gradients from $OII(\lambda 3727\text{\AA})$, $OIII(\lambda 5007\text{\AA})$, $H_\beta(\lambda 4861\text{\AA})$ lines and the Balmer break, along with spatially resolved star-formation information. I plan to combine this with colour-gradient information, determined from decomposed morphologies across the multi-band CANDELS data, in order to provide key insight into the mechanisms responsible for the quenching of star-formation in massive galaxies while still allowing a disk to remain intact. This will be done by directly probing the evolution of the disk components of galaxies. In addition to this, I will also be involved in conducting simulations based on the HST grism spectroscopy to prepare for the upcoming EUCLID mission, which will enable an SDSS comparable study at $1 < z < 3$.

6.2.3 KMOS follow-up

In addition to high resolution HST morphological and grism spectroscopy studies it would also be interesting to extend my work to wider ground-based surveys. By exploiting the area coverage of the VIDEO survey it would be possible to explore the stellar population and dynamical properties of the most massive, rarest galaxies, while the depth and area of UltraVISTA would allow me to probe

further down in mass to explore how these properties are affected by downsizing. The next generation of 3D near-infrared spectroscopy, such as that available soon with KMOS, will be ideal for this as it will simultaneously deliver spatially resolved star-formation, age and metallicity information while directly addressing the viability of minor merger driven growth as the dominant scenario for size evolution. This could be achieved by observing H_α at $1 < z < 2$ and $OII(\lambda 3727\text{\AA})$ emission lines at $1 < z < 3$ which would allow me to place upper estimates on the star-formation rates of the interesting population of passive disks and star-forming bulges identified at $1 < z < 3$. The full wavelength coverage of KMOS would also deliver age and metallicity estimates from $OIII(\lambda 5007\text{\AA})$, $H_\beta(\lambda 4861\text{\AA})$ lines and the Balmer break, and would break degeneracies in ages and dust from SED fitting. Moreover, KMOS is also capable of delivering crucial velocity dispersion measurements from the Ca H&K ($\lambda 3969, 3934\text{\AA}$) lines at $1 < z < 3$, which would add to the limited number of high-redshift velocity dispersion studies being used as powerful discriminators between the proposed size growth mechanisms for high-redshift galaxies.

References

- Abdalla F. B., Banerji M., Lahav O., Rashkov V., 2011, MNRAS, 417, 1891
- Abraham R. G., van den Bergh S., Nair P., 2003, ApJ, 588, 218
- Allen P. D., Driver S. P., Graham A. W., Cameron E., Liske J., de Propris R., 2006, MNRAS, 371, 2
- Alpher R. A., Bethe H., Gamow G. A., 1948, Physical Review, 73, 803
- Alpher R. A., Herman R., 1948, Nature, 162, 774
- Arnouts S., Cristiani S., Moscardini L., Matarrese S., Lucchin F., Fontana A., Giallongo E., 1999, MNRAS, 310, 540
- Baldry I. K. et al., 2012, MNRAS, 421, 621
- Baldry I. K., Glazebrook K., 2003, ApJ, 593, 258
- Baldry I. K., Glazebrook K., Brinkmann J., Ivezić Ž., Lupton R. H., Nichol R. C., Szalay A. S., 2004, ApJ, 600, 681
- Bamford S. P. et al., 2009, MNRAS, 393, 1324
- Barden M., Häußler B., Peng C. Y., McIntosh D. H., Guo Y., 2012, MNRAS, 422, 449
- Barro G. et al., 2013, ApJ, 765, 104
- Baugh C. M., 2006, Reports on Progress in Physics, 69, 3101
- Baugh C. M., Cole S., Benson A. J., Lacey C. G., 1999, in ASP Conference Series, Vol. 163, Problems of Extra-Galactic Research, P. Carral & J. Cepa, ed.
- Baugh C. M., Cole S., Frenk C. S., 1996, MNRAS, 283, 1361
- Baugh C. M., Lacey C. G., Frenk C. S., Granato G. L., Silva L., Bressan A., Benson A. J., Cole S., 2005, MNRAS, 356, 1191
- Baum W. A., 1962, in IAU Symposium, Vol. 15, Problems of Extra-Galactic Research, G. C. McVittie, ed., p. 390

- Behroozi P. S., Conroy C., Wechsler R. H., 2010, *ApJ*, 717, 379
- Behroozi P. S., Wechsler R. H., Conroy C., 2012, *ArXiv e-prints*
- Bell E. F., McIntosh D. H., Katz N., Weinberg M. D., 2003, *ApJS*, 149, 289
- Bell E. F. et al., 2012, *ApJ*, 753, 167
- Benson A. J., Bower R. G., Frenk C. S., Lacey C. G., Baugh C. M., Cole S., 2003, *ApJ*, 599, 38
- Benson A. J., Lacey C. G., Baugh C. M., Cole S., Frenk C. S., 2002, *MNRAS*, 333, 156
- Bernardi M., Meert A., Sheth R. K., Vikram V., Huertas-Company M., Mei S., Shankar F., 2013, *ArXiv e-prints*
- Bernardi M., Renzini A., da Costa L. N., Wegner G., Alonso M. V., Pellegrini P. S., Rit   C., Willmer C. N. A., 1998, *ApJL*, 508, L143
- Bertin E., Arnouts S., 1996, *A&A*, 117, 393
- Best P. N., 2007, *NAR*, 51, 168
- Bezanson R., van Dokkum P. G., Tal T., Marchesini D., Kriek M., Franx M., Coppi P., 2009, *ApJ*, 697, 1290
- Birnboim Y., Dekel A., 2003, *MNRAS*, 345, 349
- Blumenthal G. R., Faber S. M., Primack J. R., Rees M. J., 1984, *Nature*, 311, 517
- Bode P., Ostriker J. P., Turok N., 2001, *ApJ*, 556, 93
- Bolzonella M., Miralles J., Pell   R., 2000, *A&A*, 363, 476
- Bournaud F., Dekel A., Teyssier R., Cacciato M., Daddi E., Juneau S., Shankar F., 2011, *ApJL*, 741, L33
- Bournaud F., Elmegreen B. G., Elmegreen D. M., 2007a, *ApJ*, 670, 237
- Bournaud F., Jog C. J., Combes F., 2007b, *A&A*, 476, 1179
- Bournaud F. et al., 2013, *ArXiv e-prints*
- Bouwens R. J. et al., 2011, *Nature*, 469, 504
- Bower R. G., Benson A. J., Malbon R., Helly J. C., Frenk C. S., Baugh C. M., Cole S., Lacey C. G., 2006, *MNRAS*, 370, 645
- Brammer G. B., van Dokkum P. G., Coppi P., 2008, *ApJ*, 686, 1503
- Brinchmann J., Ellis R. S., 2000, *ApJL*, 536, L77

- Bruce V. A. et al., 2012, MNRAS, 427, 1666
- Bruzual G., Charlot S., 2003, MNRAS, 344, 1000
- Buitrago F., Conselice C. J., Epinat B., Bedregal A. G., Grutzbauch R., 2013, ArXiv e-prints
- Buitrago F., Trujillo I., Conselice C. J., Bouwens R. J., Dickinson M., Yan H., 2008, ApJL, 687, L61
- Buitrago F., Trujillo I., Conselice C. J., Haeussler B., 2011, MNRAS, submitted (arXiv:1111.6993)
- Bundy K. et al., 2008, ApJ, 681, 931
- Cacciato M., Dekel A., Genel S., 2012, MNRAS, 421, 818
- Calzetti D., Armus L., Bohlin R. C., Kinney A. L., Koornneef J., Storchi-Bergmann T., 2000, ApJ, 533, 682
- Cameron E., Carollo C. M., Oesch P. A., Bouwens R. J., Illingworth G. D., Trenti M., Labbé I., Magee D., 2011, ApJ, 743, 146
- Cameron E., Driver S. P., Graham A. W., Liske J., 2009, ApJ, 699, 105
- Cano-Díaz M., Maiolino R., Marconi A., Netzer H., Shemmer O., Cresci G., 2012, A&A, 537, L8
- Cappellari M. et al., 2005, in Nearly Normal Galaxies in a LCDM Universe. A conference celebrating the 60th birthdays of George Blumenthal, Sandra Faber and Joel Primack. 2005. Santa Cruz: UC Santa Cruz
- Cappellari M. et al., 2009, ApJL, 704, L34
- Caputi K. I., Dole H., Lagache G., McLure R. J., Dunlop J. S., Puget J., Le Floc'h E., Pérez-González P. G., 2006, A&A, 454, 143
- Carollo C. M. et al., 2013, ArXiv e-prints
- Cassata P. et al., 2010, ApJL, 714, L79
- Cassata P. et al., 2011, ApJ, 743, 96
- Cassata P. et al., 2013, ArXiv e-prints
- Cenarro A. J., Trujillo I., 2009, ApJL, 696, L43
- Ceverino D., Dekel A., Bournaud F., 2010, MNRAS, 404, 2151
- Ceverino D., Dekel A., Mandelker N., Bournaud F., Burkert A., Genzel R., Primack J., 2012, MNRAS, 420, 3490
- Chabrier G., 2003, PASP, 115, 763

- Chang Y.-Y. et al., 2013a, ArXiv e-prints
- Chang Y.-Y., van der Wel A., Rix H.-W., Wuyts S., Zibetti S., Ramkumar B., Holden B., 2013b, ApJ, 762, 83
- Chevance M., Weijmans A.-M., Damjanov I., Abraham R. G., Simard L., van den Bergh S., Caris E., Glazebrook K., 2012, ApJL, 754, L24
- Cicone C., Feruglio C., Maiolino R., Fiore F., Piconcelli E., Menci N., Aussel H., Sturm E., 2012, A&A, 543, A99
- Cimatti A. et al., 2008, A&A, 482, 21
- Cimatti A. et al., 2002, A&A, 381, L68
- Cimatti A. et al., 2004, Nature, 430, 184
- Cimatti A., Nipoti C., Cassata P., 2012, MNRAS, 422, L62
- Cirasuolo M. et al., 2007, MNRAS, 380, 585
- Clemens M. S., Bressan A., Nikolic B., Alexander P., Annibali F., Rampazzo R., 2006, MNRAS, 370, 702
- Cole S., 1991, ApJ, 367, 45
- Cole S., Aragon-Salamanca A., Frenk C. S., Navarro J. F., Zepf S. E., 1994, MNRAS, 271, 781
- Cole S., Lacey C. G., Baugh C. M., Frenk C. S., 2000, MNRAS, 319, 168
- Cole S. et al., 2001, MNRAS, 326, 255
- Cole S. et al., 2005, MNRAS, 362, 505
- Colless M. et al., 2001, MNRAS, 328, 1039
- Collister A. A., Lahav O., 2004, PASP, 116, 345
- Conroy C., Dutton A. A., Graves G. J., Mendel J. T., van Dokkum P. G., 2013, ArXiv e-prints
- Conroy C., van Dokkum P. G., 2012, ApJ, 760, 71
- Conselice C. J., 2003, ApJS, 147, 1
- Conselice C. J. et al., 2011, MNRAS, 413, 80
- Cooper A. P. et al., 2010a, MNRAS, 406, 744
- Cooper M. C., Gallazzi A., Newman J. A., Yan R., 2010b, MNRAS, 402, 1942
- Cowie L. L., Songaila A., Hu E. M., Cohen J. G., 1996, AJ, 112, 839

- Croton D. J. et al., 2006, MNRAS, 365, 11
- Daddi E., Cimatti A., Pozzetti L., Hoekstra H., Röttgering H. J. A., Renzini A., Zamorani G., Mannucci F., 2000, A&A, 361, 535
- Daddi E., Cimatti A., Renzini A., Fontana A., Mignoli M., Pozzetti L., Tozzi P., Zamorani G., 2004a, ApJ, 617, 746
- Daddi E., Cimatti A., Renzini A., Fontana A., Mignoli M., Pozzetti L., Tozzi P., Zamorani G., 2004b, ApJ, 617, 746
- Daddi E. et al., 2007, ApJ, 670, 156
- Daddi E. et al., 2005, ApJ, 626, 680
- Damjanov I. et al., 2011, ApJL, 739, L44
- Damjanov I. et al., 2009, ApJ, 695, 101
- Davé R., Oppenheimer B. D., Finlator K., 2011, MNRAS, 415, 11
- David L. P., Jones C., Forman W., Nulsen P., Vrtilik J., O’Sullivan E., Giacintucci S., Raychaudhury S., 2009, ApJ, 705, 624
- Davis M., Efstathiou G., Frenk C. S., White S. D. M., 1985, ApJ, 292, 371
- de Jong R. S., 1996, A&A, 313, 45
- De Lucia G., Blaizot J., 2007, MNRAS, 375, 2
- De Lucia G., Springel V., White S. D. M., Croton D., Kauffmann G., 2006, MNRAS, 366, 499
- de Vaucouleurs G., 1948, Annales d’Astrophysique, 11, 247
- Dekel A., Birnboim Y., 2006, MNRAS, 368, 2
- Dekel A. et al., 2009a, Nature, 457, 451
- Dekel A., Krumholz M. R., 2013, MNRAS, 432, 455
- Dekel A., Sari R., Ceverino D., 2009b, ApJ, 703, 785
- Djorgovski S., Davis M., 1987, ApJ, 313, 59
- Driver S. P. et al., 2006, MNRAS, 368, 414
- Driver S. P. et al., 2011, MNRAS, 413, 971
- Drory N., Fisher D. B., 2007, ApJ, 664, 640
- Drory N., Salvato M., Gabasch A., Bender R., Hopp U., Feulner G., Pannella M., 2005, ApJL, 619, L131

- Dullo B. T., Graham A. W., 2013, *ApJ*, 768, 36
- Dunlop J. S., 2013, in *Astrophysics and Space Science Library*, Vol. 396, *Astrophysics and Space Science Library*, Wiklind T., Mobasher B., Bromm V., eds., p. 223
- Dunlop J. S., Cirasuolo M., McLure R. J., 2007, *MNRAS*, 376, 1054
- Efstathiou G., 1992, *MNRAS*, 256, 43P
- Eggen O. J., Lynden-Bell D., Sandage A. R., 1962, *ApJ*, 136, 748
- Elbaz D. et al., 2010, *A&A*, 518, L29
- Ellis R. S., Colless M., Broadhurst T., Heyl J., Glazebrook K., 1996, *MNRAS*, 280, 235
- Ellis R. S. et al., 2013, *ApJL*, 763, L7
- Elmegreen B. G., Elmegreen D. M., 1978, *ApJ*, 220, 1051
- Elmegreen B. G., Elmegreen D. M., 2005, *ApJ*, 627, 632
- Elmegreen B. G., Elmegreen D. M., Fernandez M. X., Lemonias J. J., 2009, *ApJ*, 692, 12
- Elston R., Rieke G. H., Rieke M. J., 1988, *ApJL*, 331, L77
- Elvis M. et al., 2009, *ApJS*, 184, 158
- Erb D. K., Steidel C. C., Shapley A. E., Pettini M., Reddy N. A., Adelberger K. L., 2006, *ApJ*, 646, 107
- Faber S. M., Jackson R. E., 1976, *ApJ*, 204, 668
- Fan L., Fang G., Chen Y., Pan Z., Lv X., Li J., Lin L., Kong X., 2013, *ApJL*, 771, L40
- Fan L., Lapi A., Bressan A., Bernardi M., De Zotti G., Danese L., 2010, *ApJ*, 718, 1460
- Fan L., Lapi A., De Zotti G., Danese L., 2008, *ApJL*, 689, L101
- Fazio G. G. et al., 2004, *ApJS*, 154, 10
- Feain I. J., Papadopoulos P. P., Ekers R. D., Middelberg E., 2007, *ApJ*, 662, 872
- Ferreras I., La Barbera F., de la Rosa I. G., Vazdekis A., de Carvalho R. R., Falcón-Barroso J., Ricciardelli E., 2013, *MNRAS*, 429, L15
- Feruglio C., Maiolino R., Piconcelli E., Menci N., Aussel H., Lamastra A., Fiore F., 2010, *A&A*, 518, L155
- Flores R. A., Primack J. R., 1994, *ApJL*, 427, L1

Fontana A. et al., 2004, A&A, 424, 23

Fontana A. et al., 2006, A&A, 459, 745

Förster Schreiber N. M. et al., 2009, ApJ, 706, 1364

Franx M. et al., 2003, ApJL, 587, L79

Franx M., van Dokkum P. G., Schreiber N. M. F., Wuyts S., Labbé I., Toft S., 2008, ApJ, 688, 770

Frenk C. S., White S. D. M., Davis M., Efstathiou G., 1988, ApJ, 327, 507

Furusawa H. et al., 2008, ApJS, 176, 1

Gabor J. M. et al., 2009, ApJ, 691, 705

Gamow G., 1946, Physical Review, 70, 572

Genel S. et al., 2012, ApJ, 745, 11

Genzel R. et al., 2011, ApJ, 733, 101

Genzel R. et al., 2010, MNRAS, 407, 2091

Giacconi R. et al., 2002, ApJS, 139, 369

Glazebrook K. et al., 2004, Nature, 430, 181

Governato F. et al., 2012, MNRAS, 422, 1231

Graham A. W., 2011, in ‘Planets, Stars and Stellar Systems’, Springer (arXiv:1108.0997)

Granato G. L., De Zotti G., Silva L., Bressan A., Danese L., 2004, ApJ, 600, 580

Grillo C., Gobat R., Rosati P., Lombardi M., 2008, A&A, 477, L25

Grogin N. A. et al., 2005, ApJL, 627, L97

Grogin N. A. et al., 2011, ApJS, 197, 35

Guo Q. et al., 2011a, MNRAS, 413, 101

Guo Y., Giavalisco M., Ferguson H. C., Cassata P., Koekemoer A. M., 2011b, ApJ, submitted (arXiv:1110.3800)

Guo Y. et al., 2009, MNRAS, 398, 1129

Hartley W. G. et al., 2010, MNRAS, 407, 1212

Hartley W. G. et al., 2013, ArXiv e-prints

Hasinger G., 2008, A&A, 490, 905

- Häußler B. et al., 2013, MNRAS, 430, 330
- Häussler B. et al., 2007, ApJS, 172, 615
- Hogg D. W., Baldry I. K., Blanton M. R., Eisenstein D. J., 2002, ArXiv Astrophysics e-prints
- Holden B. P., van der Wel A., Rix H.-W., Franx M., 2012, ApJ, 749, 96
- Hopkins A. M., Beacom J. F., 2006, ApJ, 651, 142
- Hopkins P. F., Bundy K., Hernquist L., Wuyts S., Cox T. J., 2010a, MNRAS, 401, 1099
- Hopkins P. F., Cox T. J., Younger J. D., Hernquist L., 2009, ApJ, 691, 1168
- Hopkins P. F. et al., 2010b, ApJ, 724, 915
- Hopkins P. F., Hernquist L., Cox T. J., Di Matteo T., Robertson B., Springel V., 2006, ApJS, 163, 1
- Hopkins P. F., Kereš D., Murray N., Quataert E., Hernquist L., 2012, MNRAS, 427, 968
- Hopkins P. F., Quataert E., Murray N., 2011, MNRAS, 417, 950
- Hoyle F., 1948, MNRAS, 108, 372
- Hoyle F., 1953, ApJ, 118, 513
- Huang J., Glazebrook K., Cowie L. L., Tinney C., 2003, ApJ, 584, 203
- Hubble E., 1929, Proceedings of the National Academy of Science, 15, 168
- Hubble E. P., 1926, ApJ, 64, 321
- Hubble E. P., 1936, Realm of the Nebulae
- Ilbert O. et al., 2013, ArXiv e-prints
- Ilbert O. et al., 2010, ApJ, 709, 644
- Iverson R. J., Smail I., Le Borgne J., Blain A. W., Kneib J., Bezecourt J., Kerr T. H., Davies J. K., 1998, MNRAS, 298, 583
- Jeans J. H., 1928, Astronomy and cosmogony
- Johansson P. H., Naab T., Ostriker J. P., 2012, ApJ, 754, 115
- Katz N., Hernquist L., Weinberg D. H., 1992, ApJL, 399, L109
- Kauffmann G., Charlot S., 1994, ApJL, 430, L97
- Kauffmann G., Charlot S., 1998, MNRAS, 297, L23

Kauffmann G. et al., 2003a, MNRAS, 346, 1055

Kauffmann G. et al., 2003b, MNRAS, 341, 33

Kauffmann G., White S. D. M., Guiderdoni B., 1993, MNRAS, 264, 201

Kaviraj S. et al., 2012, MNRAS, submitted (arXiv:1206.2360)

Kennicutt, Jr. R. C., 1998, ARA&A, 36, 189

Kennicutt, Jr. R. C. et al., 2007, ApJ, 671, 333

Kereš D., Katz N., Weinberg D. H., Davé R., 2005, MNRAS, 363, 2

Khochfar S., Silk J., 2006, ApJL, 648, L21

Klypin A., Kravtsov A. V., Valenzuela O., Prada F., 1999, ApJ, 522, 82

Kocevski D. D. et al., 2012, ApJ, 744, 148

Kochanek C. S. et al., 2001, ApJ, 560, 566

Koekemoer A. M. et al., 2011, ApJS, 197, 36

Kormendy J., Kennicutt, Jr. R. C., 2004, ARA&A, 42, 603

Kriek M. et al., 2010, ApJL, 722, L64

Kriek M., van Dokkum P. G., Franx M., Illingworth G. D., Magee D. K., 2009, ApJL, 705, L71

Kriek M. et al., 2006, ApJL, 649, L71

Krist J., 1995, in Astronomical Society of the Pacific Conference Series, Vol. 77, Astronomical Data Analysis Software and Systems IV, R. A. Shaw, H. E. Payne, & J. J. E. Hayes, ed., p. 349

Kroupa P., 2001, MNRAS, 322, 231

Krumholz M., Burkert A., 2010, ApJ, 724, 895

Krumholz M. R., Leroy A. K., McKee C. F., 2011, ApJ, 731, 25

Lacey C., Silk J., 1991, ApJ, 381, 14

Lacey C. G., Baugh C. M., Frenk C. S., Benson A. J., Orsi A., Silva L., Granato G. L., Bressan A., 2010, MNRAS, 405, 2

Lackner C. N., Gunn J. E., 2012, MNRAS, 421, 2277

Larson D. et al., 2011, ApJS, 192, 16

Larson R. B., 1974, MNRAS, 169, 229

Larson R. B., 1975, MNRAS, 173, 671

- Law D. R., Steidel C. C., Shapley A. E., Nagy S. R., Reddy N. A., Erb D. K., 2012, *ApJ*, 745, 85
- Lawrence A. et al., 2007, *MNRAS*, 379, 1599
- Leavitt H. S., 1908, *Annals of Harvard College Observatory*, 60, 87
- Leblanc F., 2010, *An Introduction to Stellar Astrophysics*
- Lee B. et al., 2013, *ArXiv e-prints*
- Lemaître G., 1927, *Annales de la Societe Scietifique de Bruxelles*, 47, 49
- Lilly S. J., Le Fevre O., Hammer F., Crampton D., 1996, *ApJL*, 460, L1
- Lilly S. J., Longair M. S., 1984, *MNRAS*, 211, 833
- Lilly S. J., Tresse L., Hammer F., Crampton D., Le Fevre O., 1995, *ApJ*, 455, 108
- Longhetti M., Saracco P., 2009, *MNRAS*, 394, 774
- Lotz J. M., Primack J., Madau P., 2004, *AJ*, 128, 163
- Madau P., 1995, *ApJ*, 441, 18
- Madau P., Ferguson H. C., Dickinson M. E., Giavalisco M., Steidel C. C., Fruchter A., 1996, *MNRAS*, 283, 1388
- Madau P., Pozzetti L., Dickinson M., 1998, *ApJ*, 498, 106
- Magdis G. E., Rigopoulou D., Huang J., Fazio G. G., 2010, *MNRAS*, 401, 1521
- Mancini C. et al., 2010, *MNRAS*, 401, 933
- Maraston C., 2005, *MNRAS*, 362, 799
- Maraston C., Daddi E., Renzini A., Cimatti A., Dickinson M., Papovich C., Pasquali A., Pirzkal N., 2006, *ApJ*, 652, 85
- Marinacci F., Pakmor R., Springel V., 2013, *ArXiv e-prints*
- Martig M., Bournaud F., Croton D. J., Dekel A., Teyssier R., 2012, *ApJ*, 756, 26
- Martig M., Bournaud F., Teyssier R., Dekel A., 2009, *ApJ*, 707, 250
- Martin D. C. et al., 2007, *ApJS*, 173, 342
- Masters K. L. et al., 2010, *MNRAS*, 405, 783
- McCarthy I. G., Schaye J., Font A. S., Theuns T., Frenk C. S., Crain R. A., Dalla Vecchia C., 2012, *MNRAS*, 427, 379
- McCracken H. J. et al., 2012, *A&A*, 544, A156

- McCrady N., Gilbert A. M., Graham J. R., 2003, *ApJ*, 596, 240
- McGaugh S. S., 2005, *ApJ*, 632, 859
- McGrath E. J., Stockton A., Canalizo G., Iye M., Maihara T., 2008, *ApJ*, 682, 303
- McLure R. J., Dunlop J. S., Cirasuolo M., Koekemoer A. M., Sabbi E., Stark D. P., Targett T. A., Ellis R. S., 2010, *MNRAS*, 403, 960
- McLure R. J. et al., 2013, *MNRAS*, 428, 1088
- Michałowski M. J., Dunlop J. S., Cirasuolo M., Hjorth J., Hayward C. C., Watson D., 2012, *A&A*, 541, A85
- Moore B., Ghigna S., Governato F., Lake G., Quinn T., Stadel J., Tozzi P., 1999a, *ApJL*, 524, L19
- Moore B., Quinn T., Governato F., Stadel J., Lake G., 1999b, *MNRAS*, 310, 1147
- Mortlock A. et al., 2013, *ArXiv e-prints*
- Mozena M., Faber S. M., Koo D. C., Primack J. R., Dekel A., Moody C. E., Ceverino D., CANDELS, 2013, in *American Astronomical Society Meeting Abstracts*, Vol. 221, American Astronomical Society Meeting Abstracts, p. 112
- Muzzin A. et al., 2013, *ApJS*, 206, 8
- Muzzin A., van Dokkum P., Franx M., Marchesini D., Kriek M., Labbé I., 2009, *ApJL*, 706, L188
- Naab T., 2012, *ArXiv e-prints*
- Naab T., Burkert A., Hernquist L., 1999, *ApJL*, 523, L133
- Naab T., Johansson P. H., Ostriker J. P., 2009, *ApJL*, 699, L178
- Naab T., Johansson P. H., Ostriker J. P., Efstathiou G., 2007, *ApJ*, 658, 710
- Nandra K. et al., 2007, *ApJL*, 660, L11
- Navarro J. F., Steinmetz M., 1997, *ApJ*, 478, 13
- Navarro J. F., Steinmetz M., 2000, *ApJ*, 538, 477
- Newman A. B., Ellis R. S., Bundy K., Treu T., 2012, *ApJ*, 746, 162
- Newman A. B., Ellis R. S., Treu T., Bundy K., 2010, *ApJL*, 717, L103
- Newman J. A., Davis M., 2002, *ApJ*, 564, 567
- Nipoti C., Treu T., Leauthaud A., Bundy K., Newman A. B., Auger M. W., 2012, *MNRAS*, 422, 1714

Norberg P. et al., 2002, MNRAS, 336, 907

Nordon R. et al., 2010, ArXiv e-prints

Obreschkow D., Rawlings S., 2009, MNRAS, 400, 665

Oesch P. A. et al., 2010, ApJL, 709, L16

Oke J. B., 1974, ApJS, 27, 21

Onodera M., Arimoto N., Daddi E., Renzini A., Kong X., Cimatti A., Broadhurst T., Alexander D. M., 2010, ApJ, 715, 385

Onodera M. et al., 2012, ApJ, 755, 26

Oogi T., Habe A., 2013, MNRAS, 428, 641

Oser L., Naab T., Ostriker J. P., Johansson P. H., 2012, ApJ, 744, 63

Oser L., Ostriker J. P., Naab T., Johansson P. H., Burkert A., 2010, ApJ, 725, 2312

Padilla N. D., Strauss M. A., 2008, MNRAS, 388, 1321

Papovich C., Dickinson M., Ferguson H. C., 2001, ApJ, 559, 620

Partridge R. B., Peebles P. J. E., 1967, ApJ, 147, 868

Patel S. G. et al., 2013a, ArXiv e-prints

Patel S. G. et al., 2013b, ApJ, 766, 15

Peacock J. A., Heavens A. F., 1990, MNRAS, 243, 133

Peebles P. J. E., 1965, ApJ, 142, 1317

Peebles P. J. E., 1980, The large-scale structure of the universe

Peebles P. J. E., 1982, ApJL, 263, L1

Peng C. Y., Ho L. C., Impey C. D., Rix H.-W., 2002, ApJ, 124, 266

Peng Y.-j. et al., 2010, ApJ, 721, 193

Penzias A. A., Wilson R. W., 1965, ApJ, 142, 419

Percival W. J. et al., 2001, MNRAS, 327, 1297

Perlmutter S. et al., 1999, ApJ, 517, 565

Pierce C. M. et al., 2007, ApJL, 660, L19

Planck Collaboration et al., 2013a, ArXiv e-prints

Planck Collaboration et al., 2013b, ArXiv e-prints

- Poggianti B. M. et al., 2013, *ApJ*, 762, 77
- Poglitsch A. et al., 2010, *A&A*, 518, L2
- Pozzetti L. et al., 2007, *A&A*, 474, 443
- Press W. H., Schechter P., 1974, *ApJ*, 187, 425
- Quadri R. et al., 2007, *ApJ*, 654, 138
- Ragone-Figueroa C., Granato G. L., 2011, *MNRAS*, 414, 3690
- Ravindranath S. et al., 2006, *ApJ*, 652, 963
- Rees M. J., Ostriker J. P., 1977, *MNRAS*, 179, 541
- Renzini A., 2009, *MNRAS*, 398, L58
- Rettura A. et al., 2010, *ApJ*, 709, 512
- Rettura A. et al., 2006, *A&A*, 458, 717
- Rieke G. H., Alonso-Herrero A., Weiner B. J., Pérez-González P. G., Blaylock M., Donley J. L., Marcillac D., 2009, *ApJ*, 692, 556
- Rieke G. H., Loken K., Rieke M. J., Tamblyn P., 1993, *ApJ*, 412, 99
- Riess A. G. et al., 1998, *AJ*, 116, 1009
- Rix H.-W. et al., 2004, *ApJS*, 152, 163
- Robaina A. R., Bell E. F., van der Wel A., Somerville R. S., Skelton R. E., McIntosh D. H., Meisenheimer K., Wolf C., 2010, *ApJ*, 719, 844
- Roche N. D., Almaini O., Dunlop J., Ivison R. J., Willott C. J., 2002, *MNRAS*, 337, 1282
- Roseboom I. G. et al., 2012, *MNRAS*, 426, 1782
- Ryan, Jr. R. E. et al., 2012, *ApJ*, 749, 53
- Sachs R. K., Wolfe A. M., 1967, *ApJ*, 147, 73
- Salimbeni S., Fontana A., Giallongo E., Grazian A., Menci N., Pentericci L., Santini P., 2009, in *American Institute of Physics Conference Series*, Vol. 1111, American Institute of Physics Conference Series, G. Giobbi, A. Tornambe, G. Raimondo, M. Limongi, L. A. Antonelli, N. Menci, & E. Brocato, ed., pp. 207–211
- Salpeter E. E., 1955, *ApJ*, 121, 161
- Sánchez S. F. et al., 2004, *ApJ*, 614, 586
- Saracco P., Longhetti M., Andreon S., 2009, *MNRAS*, 392, 718

- Savaglio S. et al., 2005, *ApJ*, 635, 260
- Schawinski K., Thomas D., Sarzi M., Maraston C., Kaviraj S., Joo S.-J., Yi S. K., Silk J., 2007, *MNRAS*, 382, 1415
- Schawinski K., Treister E., Urry C. M., Cardamone C. N., Simmons B., Yi S. K., 2011, *ApJL*, 727, L31
- Schechter P., 1976, *ApJ*, 203, 297
- Schmidt M., Green R. F., 1983, *ApJ*, 269, 352
- Schmidt M. et al., 1998, *A&A*, 329, 495
- Scoville N. et al., 2007, *ApJS*, 172, 1
- Sekiguchi K., Akiyama M., Furusawa H., Simpson C., Takata T., Ueda Y., Watson M. W., Sxds Team, 2005, in *Multiwavelength Mapping of Galaxy Formation and Evolution*, A. Renzini & R. Bender, ed., p. 82
- Sérsic J. L., 1968, *Atlas de galaxies australes*, Sérsic, J. L., ed.
- Shankar F., Marulli F., Bernardi M., Mei S., Meert A., Vikram V., 2011, *MNRAS*, submitted (arXiv:1105.6043)
- Shapley A. E., Erb D. K., Pettini M., Steidel C. C., Adelberger K. L., 2004, *ApJ*, 612, 108
- Shapley A. E., Steidel C. C., Adelberger K. L., Dickinson M., Giavalisco M., Pettini M., 2001, *ApJ*, 562, 95
- Shen S., Mo H. J., White S. D. M., Blanton M. R., Kauffmann G., Voges W., Brinkmann J., Csabai I., 2003, *MNRAS*, 343, 978
- Silk J., 1977, *ApJ*, 211, 638
- Simard L., 1998, in *Astronomical Society of the Pacific Conference Series*, Vol. 145, *Astronomical Data Analysis Software and Systems VII*, Albrecht R., Hook R. N., Bushouse H. A., eds., p. 108
- Simard L., Mendel J. T., Patton D. R., Ellison S. L., McConnachie A. W., 2011, *ApJS*, 196, 11
- Slipher V. M., 1913, *Lowell Observatory Bulletin*, 2, 56
- Smail I., Ivison R. J., Blain A. W., Kneib J., 1998, *ApJL*, 507, L21
- Smith R. J., Lucey J. R., 2013, *ArXiv e-prints*
- Smoot G. F. et al., 1992, *ApJL*, 396, L1
- Somerville R. S., Primack J. R., Faber S. M., 2001, *MNRAS*, 320, 504

- Spergel D. N., Steinhardt P. J., 2000, *Physical Review Letters*, 84, 3760
- Spiniello C., Trager S. C., Koopmans L. V. E., Chen Y. P., 2012, *ApJL*, 753, L32
- Springel V., 2005, *MNRAS*, 364, 1105
- Springel V. et al., 2005, *Nature*, 435, 629
- Steidel C. C., Adelberger K. L., Giavalisco M., Dickinson M., Pettini M., 1999, *ApJ*, 519, 1
- Steidel C. C., Giavalisco M., Pettini M., Dickinson M., Adelberger K. L., 1996, *ApJL*, 462, L17
- Stockton A., McGrath E., Canalizo G., Iye M., Maihara T., 2008, *ApJ*, 672, 146
- Stolte A., Brandner W., Grebel E. K., Lenzen R., Lagrange A.-M., 2005, *ApJ*, 628, L113
- Szokoly G. P. et al., 2004, *ApJS*, 155, 271
- Szomoru D., Franx M., Bouwens R. J., van Dokkum P. G., Labbé I., Illingworth G. D., Trenti M., 2011, *ApJL*, 735, L22
- Szomoru D., Franx M., van Dokkum P. G., 2012, *ApJ*, 749, 121
- Szomoru D. et al., 2010, *ApJL*, 714, L244
- Talia M., Cimatti A., Mignoli M., Pozzetti L., Renzini A., Kurk J., Halliday C., 2013, *ArXiv e-prints*
- Targett T. A. et al., 2013, *MNRAS*
- Targett T. A., Dunlop J. S., McLure R. J., Best P. N., Cirasuolo M., Almaini O., 2011, *MNRAS*, 412, 295
- Taylor E. N., Franx M., Glazebrook K., Brinchmann J., van der Wel A., van Dokkum P. G., 2010, *ApJ*, 720, 723
- Taylor M. B., 2005, in *Astronomical Society of the Pacific Conference Series*, Vol. 347, *Astronomical Data Analysis Software and Systems XIV*, Shopbell P., Britton M., Ebert R., eds., p. 29
- Thomas D., Maraston C., Bender R., Mendes de Oliveira C., 2005, *ApJ*, 621, 673
- Thompson D. et al., 1999, *ApJ*, 523, 100
- Tinsley B. M., 1980, *FCP*, 5, 287
- Toft S., Gallazzi A., Zirm A., Wold M., Zibetti S., Grillo C., Man A., 2012, *ApJ*, 754, 3
- Toft S. et al., 2007, *ApJ*, 671, 285

Tremblay G. R. et al., 2012, MNRAS, 424, 1042

Tremonti C. A. et al., 2004, ApJ, 613, 898

Tremonti C. A., Moustakas J., Diamond-Stanic A. M., 2007, ApJL, 663, L77

Treu T., Koopmans L. V. E., 2004, ApJ, 611, 739

Trujillo I., Carrasco E. R., Ferré-Mateu A., 2012, ApJ, 751, 45

Trujillo I., Cenarro A. J., de Lorenzo-Cáceres A., Vazdekis A., de la Rosa I. G., Cava A., 2009, ApJL, 692, L118

Trujillo I., Conselice C. J., Bundy K., Cooper M. C., Eisenhardt P., Ellis R. S., 2007, MNRAS, 382, 109

Trujillo I., Ferreras I., de La Rosa I. G., 2011, MNRAS, 415, 3903

Trujillo I. et al., 2006, ApJ, 650, 18

Trump J. R. et al., 2009, ApJ, 696, 1195

Tully R. B., Fisher J. R., 1977, A&A, 54, 661

Ueda Y. et al., 2008, ApJS, 179, 124

Valentinuzzi T. et al., 2010a, ApJ, 712, 226

Valentinuzzi T. et al., 2010b, ApJL, 721, L19

van de Sande J. et al., 2012, ArXiv e-prints

van de Sande J. et al., 2011, ApJL, 736, L9

van den Bosch R. C. E., van de Ven G., Verolme E. K., Cappellari M., de Zeeuw P. T., 2008, MNRAS, 385, 647

van der Wel A. et al., 2012, ApJS, 203, 24

van der Wel A., Bell E. F., van den Bosch F. C., Gallazzi A., Rix H.-W., 2009, ApJ, 698, 1232

van der Wel A., Franx M., Wuyts S., van Dokkum P. G., Huang J., Rix H., Illingworth G. D., 2006, ApJ, 652, 97

van der Wel A., Holden B. P., Zirm A. W., Franx M., Rettura A., Illingworth G. D., Ford H. C., 2008, ApJ, 688, 48

van der Wel A. et al., 2011, ApJ, 730, 38

van Dokkum P. G., 2008, ApJ, 674, 29

van Dokkum P. G., Brammer G., 2010, ApJL, 718, L73

- van Dokkum P. G., Conroy C., 2012, *ApJ*, 760, 70
- van Dokkum P. G., Franx M., 1996, *MNRAS*, 281, 985
- van Dokkum P. G. et al., 2008, *ApJL*, 677, L5
- van Dokkum P. G., Kriek M., Franx M., 2009, *Nature*, 460, 717
- van Dokkum P. G. et al., 2013, *ArXiv e-prints*
- van Dokkum P. G. et al., 2006, *ApJL*, 638, L59
- van Dokkum P. G. et al., 2010, *ApJ*, 709, 1018
- Vika M., Bamford S. P., Haeussler B., Rojas A. L., Borch A., Nichol R. C., 2013, *ArXiv e-prints*
- Wang T. et al., 2012, *ApJ*, accepted (arXiv:1204.4194)
- White S. D. M., Frenk C. S., 1991, *ApJ*, 379, 52
- White S. D. M., Rees M. J., 1978, *MNRAS*, 183, 341
- Wise M. W., McNamara B. R., Nulsen P. E. J., Houck J. C., David L. P., 2007, *ApJ*, 659, 1153
- Wuyts S., Cox T. J., Hayward C. C., Franx M., Hernquist L., Hopkins P. F., Jonsson P., van Dokkum P. G., 2010, *ApJ*, 722, 1666
- Wuyts S. et al., 2012, *ApJ*, accepted (arXiv:1203.2611)
- Wuyts S. et al., 2011, *ApJ*, 738, 106
- Wuyts S., Labbé I., Schreiber N. M. F., Franx M., Rudnick G., Brammer G. B., van Dokkum P. G., 2008, *ApJ*, 682, 985
- York D. G. et al., 2000, *AJ*, 120, 1579
- Yuma S., Ohta K., Yabe K., Kajisawa M., Ichikawa T., 2011, *ApJ*, 736, 92
- Zheng W. et al., 2004, *ApJS*, 155, 73
- Zibetti S., Gallazzi A., Charlot S., Pierini D., Pasquali A., 2012, *MNRAS*, submitted (arXiv:1205.4717)
- Zibetti S., Gallazzi A., Charlot S., Pierini D., Pasquali A., 2013, *MNRAS*, 428, 1479
- Zirm A. W. et al., 2008, *ApJ*, 680, 224

Publication List

Bruce, V. A., et al., 2013, in preparation

Bruce, V. A., et al., 2012, MNRAS, 427, 1666

Bruce, V.A., et al., 2013, IAUS, 295, 49

Findlay, J. R., Sutherland, W. J., Venemans, B. P., Reyl, C., Robin, A. C.,
Bonfield, D. G., Bruce, V. A., Jarvis, M. J., 2012, MNRAS, 419, 3354

Jarvis, M. J., et al., 2013, MNRAS, 428, 1281

McLure, R. J., et al., 2013, MNRAS, 428, 1088

Targett, T. A., et al., 2013, MNRAS, 432, 2012

Willott, C. J., et al., 2013, ApJ, 145,4